Local structure of NBT-based piezoelectric materials

by

Anton Goetzee-Barral

Submitted in accordance with the requirements for the degree of

School of Chemical and Process Engineering

The University of Leeds

For the degree of

DOCTOR OF PHILOSOPHY

Date

28/03/2018

Intellectual Property and Publication Statements

The candidate confirms that the work submitted is his own, except where work which has formed part of jointly-authored publications has been included. The contribution of the candidate and the other authors to this work has been explicitly indicated below. The candidate confirms that appropriate credit has been given within the thesis where reference has been made to the work of others:

The synchrotron experiment described in Chapter 3 was conducted by Dr Alicia Manjon Sanz and Dylan Fast from the Michelle Dolgos group at the Oregon State University (OSU). Preliminary structure refinements were conducted by Dr Tim Comyn from Ionix Advanced Technologies ltd.

The synchrotron experiment described in Chapter 4 was completed with Dr Tedi-Marie Usher, Dr Giovanni Esteves and Alexandra Henriques from the Jacob Jones group at the North Carolina State University (NCSU). The pair distribution function peak shift analysis tool was provided by Dr Igor Levin from the National Institute of Standards and Technology (NIST). The following publication was used for this chapter: A. J. Goetzee-Barral, T.-M. Usher, T. J. Stevenson, J. L. Jones, I. Levin, A. P. Brown, and A. J. Bell, "Electric field dependent local structure of $(K_x Na_{1-x})_{0.5} Bi_{0.5} Ti O_3$" Phys. Rev. B, vol. 96, no. 1, p. 14118, 2017.

Acknowledgements

I am incredibly fortunate for all that I have learnt and experienced during my time as a PhD student. I have been lucky to have met a number of individuals who have influenced my time here.

First and foremost, I would like to thank my academic supervisors Andrew Bell, Andy Brown and Tim Stevenson for their constant mentorship, guidance and support. A special thanks to Tim Comyn who also provided significant academic support and mentorship throughout this period. They have all had a great influence over my development as a scientist and individual, and for all that, I am extremely grateful.

From the department, I thank Andy Mullis for his support when I first enrolled in the Centre for Doctoral Training. Clerical and technical staff have been invaluable to my time here and for that I would like to thank Rob Simpson, Diane Cochrane and Marie Gray, as well as Alastair Majoram from the Graduate School Office.

I must also thank several funding institutions for their financial support without which my attendance to multiple conferences, experiments and international secondments would have not been possible. For that I would like to thank EPSRC, IOM3, IEEE and the School of Chemical and Progress Engineering. Particularly I would like to thank Elaine Martin for her support of my proposal for an international two-month secondment.

Collaboration with internationally renowned research groups has been integral to my work. Thank you Jacob Jones, Tedi-Marie Usher and Giovanni Esteves from NCSU and Michelle Dolgos, Dylan Fast and Alicia Manjon Sanz from OSU. Additionally, thank you Katie Keiffer and Michelle Dolgos for your hospitality.

I would also like to thank the various friends and colleagues I have had the pleasure of meeting: Jim Bennett, Sam Parry. Tom Hooper, Laura Stoica, Rob Mathesson, Omar Matar, Stephen Collins and Richard Foster.

To my loved ones, the pillars of my life: Mum, Dad and Xan, thank you for your constant support. To my extended family, the Goetzees, Barrals and Morenos, and not forgetting the Lutchmans. Having you to rely upon was immensely important in me completing this. And last, through certainly not least, Josie, you have been through it all with me. Thank you for your everlasting patience, support and for being my source of inspiration.

Abstract

This thesis explores local structure variation in $(1-x)(Na_{0.5}, Bi_{0.5})TiO_3$-$xPbTiO_3$ (NBT-PT) and $(K_x, Na_{1-x})_{0.5}Bi_{0.5}TiO_3$ (KNBT) around the morphotropic phase boundary (MPB). Local structure alignment or ordering in NBT-PT was achieved through the addition of $PbTiO_3$ (PT), whilst in KNBT local ordering was induced by an applied electric field. Significant emphasis is placed on local structure analysis methods (up to 50 Å length scale) via pair distribution function (PDF) analysis.

In situ temperature X-ray diffraction was used to characterise the average structure of NBT-PT. A transition from a rhombohedral structure for $x = 0.08$ to tetragonal for $x = 0.18$ was observed (MPB $x = 0.13$). The ferroelectric-paraelectric transition temperature was corroborated by permittivity measurements which also showed a transition from relaxor to ferroelectric behaviour with increasing x. Whole profile PDF refinement revealed the presence of a monoclinic phase for $x = 0.14$ acting as a lower symmetry bridge between rhombohedral and tetragonal phases. Range dependent PDF analysis was used to measure the coherence length of nanoscaled regions which decreased in size from 40 to 20 Å with increasing x. These regions persisted at temperatures above the paraelectric transition, though reduced in size across all compositions. The measurements illustrate the order inducing properties of $PbTiO_3$, which suppresses nanoregions and promotes long-range ferroelectric order.

PDF analysis of unpoled KNBT at unit-cell length scale distances was used to measure the local Bi off-centre displacement direction. For $x = 0.10$, a rhombohedral distortion was observed. This transitioned to a monoclinic distortion for $x = 0.15$, further evolving into a complex mixture of various monoclinic distortions for $x = 0.20$ (MPB). A tetragonal distortion was observed beyond the MPB ($x = 0.30$). The improved piezoelectric properties at the MPB are attributed to the greater availability of displacement directions. Under an applied electric field, the suppression in diffuse scattering and sharpening of PDF peaks indicating field induced ordering. Changes in the peak area ratios corresponding to Bi-Ti distances indicate reorientation behaviour along the applied field vector. Local strain analysis was achieved by measuring the PDF peak shift. The onset of linear strain corresponding to piezoelectric response occurred at an electric field (E) $\approx$ 1000 - 1250 V/mm for $x = 0.20$ and at E $\approx$ 2000 – 3000 V/mm for $x = 0.15$ and 0.18. Non-zero strain below the threshold field indicates the presence of localised strain assumed to be incipient to the macroscopic strain.

Contents

List of Figures

List of Tables

List of Equations

Abbreviations

PZT	Lead zirconate titanate ($Pb(Zr_xTi_{1-x})O_3$)
PT	Lead titanate ($PbTiO_3$)
NBT	Sodium bismuth titanate ($Na_{1/2}Bi_{1/2}TiO3$)
KBT	Potassium bismuth titanate ($K_{1/2}Bi_{1/2}TiO_3$)
KNBT	Solid solution between KBT and NBT
NBT-xPT	Solid solution between NBT and PT
BT	Barium titanate ($BaTiO_3$)
PMN	Lead magnesium niobate ($Pb(Mg_{1/3}Nb_{2/3})O_3$)
PDF	Pair distribution function
XRD	X-ray diffraction
TEM	Transmission electron microscopy
RDF	Radial distribution function
RF	Radio frequency
C	Cubic
R	Rhombohedral
T	Tetragonal
M	Monoclinic
MPB	Morphotropic phase boundary
MPR	Morphotropic phase region
PNR	Polar nano region
WEEE	Waste from Electrical and Electronic Equipment

RoHS   Restriction of Hazardous Substances

APS   Advanced Photon Source

WEEE   Waste from Electrical and Electronic Equipment

RoHS   Restriction of Hazardous Substances

RoHS   Restriction of Hazardous Substances

APS   Advanced Photon Source

Symbols

Q Momentum transfer / Scattering vector

2θ Two theta scattering angle

k Wavevector

λ Wavelength

d d-space

a, b & c   Unit cell side lengths

α, β & γ Unit cell side angles

$G(r)$ Reduced pair distribution function

$g(r)$ Pair distribution function

$G*(r) / R(r)$ Radial distribution function

t Tolerance factor

r Atomic distance

$R*$ PDF peak shift residual

R_{wp} Weighted residual from structure refinements

$S(Q)$ Total scattering structure function

P Polarisation

P_r Remnant polarisation

X_{ij} Stress

x_{ij} Strain

d_{ij} Piezoelectric charge coefficient

s_{ij} Elastic compliance

p	Dipole moment
Q	Electric charge
χ_e	Dielectric susceptibility
E	Electric field
ε	Permittivity
ε_r	Relative permittivity
ε_0	Permittivity of free space $= 8.8542 \times 10^{-12}$ F m^{-1}
T	Temperature
T_c	Curie point
C	Capacitance
A	Area
V	Voltage

1 Introduction and Background

1.1 Chapter layout

This chapter serves to introduce the thesis topic and its associated scientific background, namely piezoelectric materials. In order to provide context to these materials a 'bottom up' approach is taken to this introduction beginning with the crystallographic basis for the origin of piezoelectric behaviour, followed by an examination of piezoelectric properties. Certain phenomena particularly pertinent to this study are discussed with a particular focus placed upon the atomic structure. The chapter is concluded with a review of the current literature and key example materials.

1.2 Introduction

Piezoelectric ceramics are a class of functional materials which have seen use in established technologies such as medical ultrasound, sonar and fuel injection [1]. Their function arises from their ability to act as transducers, exchanging between electrical and mechanical signals. An electrical charge is produced when the material is subject to stress and conversely by applying an electric field to the material a strain is induced [2]. In this way, they can be used as both sensors and actuators.

Current technologies are mainly lead (Pb) based, in particular the solid solution between $PbZrO_3$ and $PbTiO_3$, $Pb(Zr_x Ti_{1-x})O_3$ (PZT) is widely used due to its greater piezoelectric properties over its lead-free counterparts, and the ease with which its properties can be tailored to specific applications [1], [3]. The human health and environmental concerns associated with the toxicity of lead have motivated research into lead-free alternatives with competing properties, and is further spurred on by European Union legislation on the use of lead in technology such as the directives on the Waste from Electrical and Electronic Equipment (WEEE) (2003) and Restriction of Hazardous Substances (RoHS) (2003). Currently due to the high dependence of piezoelectric devices on Pb they are exempt from these restrictions. There is not yet a single lead-free material which could replace lead-based materials and be as pervasive as PZT, however there are several emerging lead free replacements for specific applications such as high frequency transducers for medical ultrasound [4].

The properties of piezoelectric materials are determined by sub-angstrom atomic displacements and atomic response to external stimuli such as electric-field, mechanical stress and temperature. With the development and improvement of structural characterisation methods including high energy X-ray diffraction and neutron diffraction techniques it has become apparent that the atomic structure will appear different depending on the coherence length of the measurement tool i.e. an averaged description of the structure may differ at the nanoscale. The understanding of well-documented and 'simple' materials such as $BaTiO_3$ (BT) and PZT has benefited from these analyses, leading to a new insight of their behaviour [5], [6].

1.3 Research Aims:

1) To describe the local structure of $(Na_{0.5}Bi_{0.5})TiO_3$ based piezoelectric materials and the behaviour under electric-field, temperature and with the incorporation of lead titanate into the solid solution.

2) To contribute to the understanding of the role played by the presence of Pb^{2+} ions in piezoelectric materials and the observed improvements to properties it imparts.

1.4 Research objectives

1) Characterise local structure by the pair distribution function (PDF) technique.

2) Measure local structure $(Na_{0.5}Bi_{0.5})TiO_3$-$PbTiO_3$ by pair distribution function (PDF) analysis as a function of $PbTiO_3$ content and temperature.

3) Measure local structure of $(Na_{0.5}Bi_{0.5})TiO_3$-$(K_{0.5}Bi_{0.5})TiO_3$ at the morphotropic phase boundary as a function of electric field magnitude and ramp rate.

1.5 Crystallography of materials

Piezoelectric properties are observed in several materials including quartz, Rochelle salt, bone and various polymers [7]. Here specifically ceramic piezoelectric materials are considered. As with many materials the properties of piezoelectric materials are determined by their atomic chemistry and structure. This is particularly important in piezoelectric materials whose crystalline structure is a significant determining factor in their properties [8]. This section covers a broad description of important aspects of crystallography with the aim to introduce to the reader the crystallography of piezoelectric materials and the origin of their properties. This description of crystallography is well established and has been extensively covered in a plethora of text books [9]–[12].

Crystal structure

A material is said to be crystalline when it is composed of atoms or molecules which are regularly arranged and form a lattice i.e. an array of points which periodically repeat in all three dimensions. A crystal structure provides a description of how atoms or molecules are arranged in the solid material. This periodicity can be represented by the *unit cell*, which contains all the atoms necessary to describe the repeating structure and serves as the simplest depiction of the entire structure. A two-dimensional array of lattice points is shown in **Figure 1.1**, showing how several unit cells can be constructed, including a square with lattice points on its corner positions (a), a parallelogram (b) and a square with a central point (c). There are a few rules which dictate which would be the preferred choice: The unit cell should be as small as possible, contain the least amount of lattice points, and generally be the simplest construction possible. In this example, the square (a) would be an adequate unit cell used to describe the whole structure.

Figure 1.2 shows a three-dimensional unit cell, with points at the corners of a cube. The main variables used to describe the unit cell are the side lengths (a, b & c), and the angles between them (α, β & γ). Additionally, all the atoms in the unit cell are given coordinates (x, y & z) corresponding to their position with respect to the unit cell dimensions and therefore expressed as fractions of the unit vectors a, b and c. An example is shown in red in the figure.
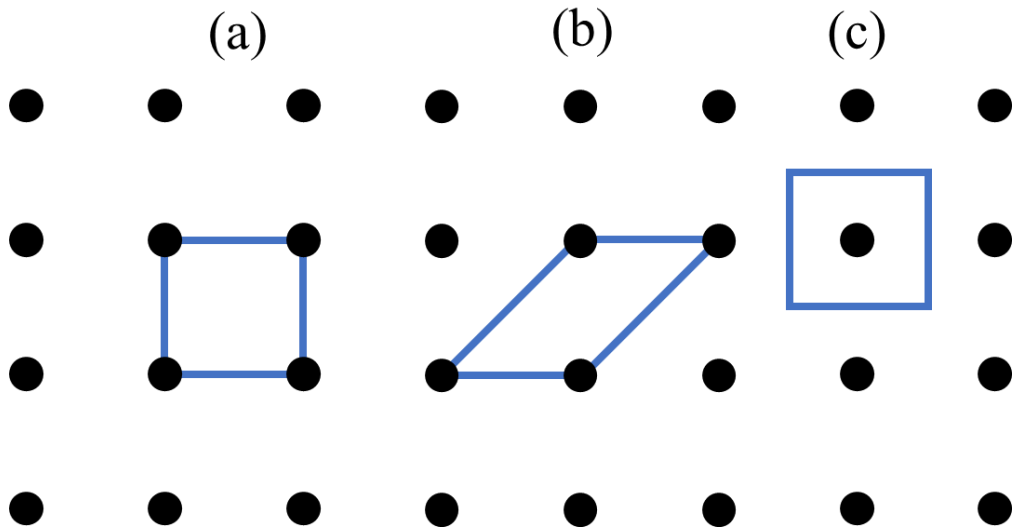
Figure 1.1. 2-dimensional array of points showing the various unit cells that can be used. The square with points in its corner positions (a)is the simplest description of the repeating structure and therefore the most adequate.
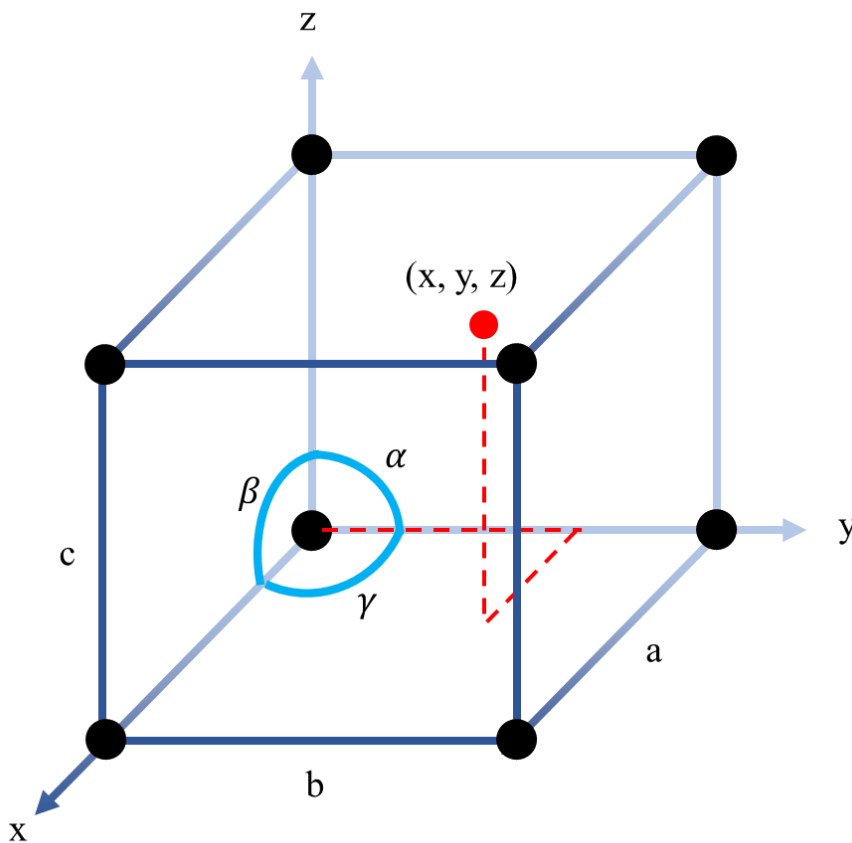
Figure 1.2. The unit cell provides a description of the crystal structure in the simplest manner possible. The main descriptor parameters are the side lengths (a, b & c) and angles between them (α, β & γ). The atomic positions in the unit cell are given by fractional coordinates (x, y & z)

Planes and directions

It is necessary to define some of the naming conventions used to define crystallographic directions and planes. Crystallographic directions are labelled with square brackets as shown in **Figure 1.3** (a). The directions [u, v, w] are simple vectors in the *x*, *y, and z* axes. Arrow brackets (⟨⟩) are used to denote a *family* of directions, in the example of a cubic structure [001], [010] and [100] (including the negative directions e.g. (00$\bar{1}$)) are identical and can be defined collectively as ⟨001⟩. Crystallographic planes (**Figure 1.3** (b)) are labelled with curved brackets and a family of planes are labelled with curly ({}) brackets. In the cubic system (see **Table 1-1**), planes are labelled by the inverse of the perpendicular vector emerging from the plane. For example, the vector [½½1] produces the plane (221) shown in the Figure. This is not the case for structures which deviate from the cubic system.
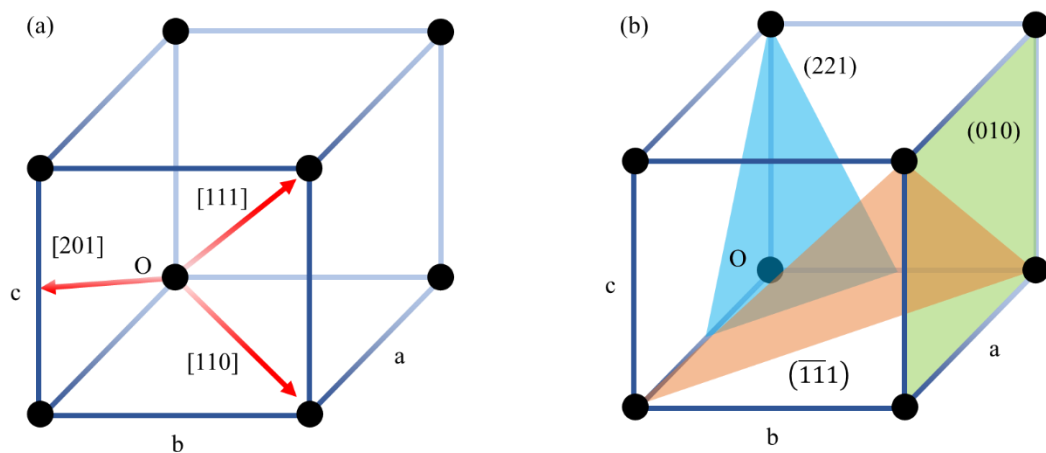
Figure 1.3 Examples of crystallographic directions (a) and planes (b). Crystal planes are denoted by the reciprocal of a vector perpendicular to said plane.

Crystal classes

There are several structures that arise from different unit cell side lengths and angles, which are classified into seven crystal systems. Combined with the available lattice centres they create the 14 Bravais lattices shown in **Figure 1.4** whose properties are described in **Table 1-1** [9] and are listed in order of decreasing symmetry. The cubic structure exhibits the highest symmetry where all side lengths are equals and all angles are at 90°, and as such contains several rotation axes and mirror planes. Conversely the

triclinic structure has the lowest symmetry, and if the conditions are such that all its angles and side lengths are unequal then it would have no symmetry. The non-equality symbol ($\neq$) is a requirement of the lower symmetry phases. However, in some circumstances equality can occur in a lower symmetry phase, for example a monoclinic phase where $a = b$, and can therefore be inscribed within an orthorhombic phase.
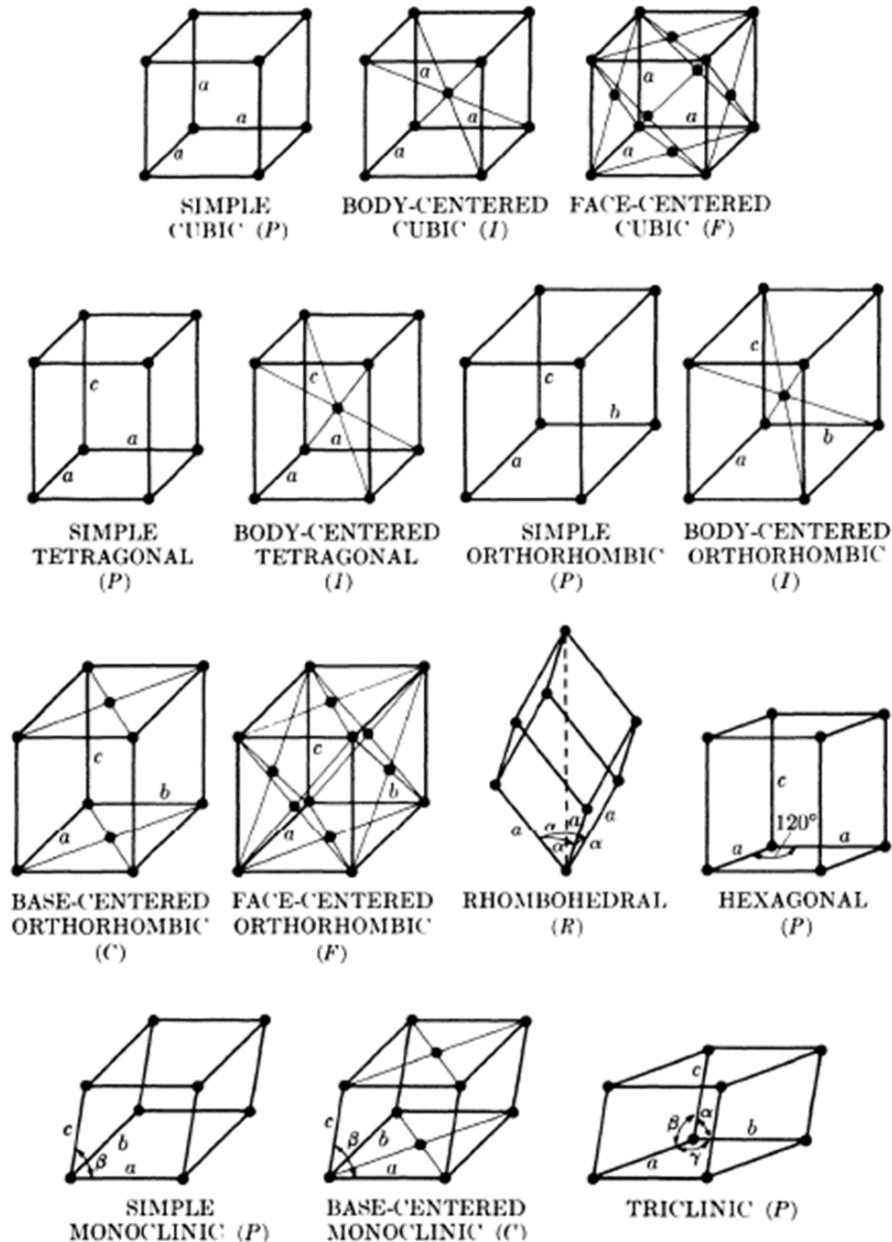
Figure 1.4 The 14 Bravais lattices describing all possible arrangements of atoms in a solid. From [9].

Table 1-1 Crystal systems, Bravais lattices, and parameters required by symmetry constraints.

System	Axis lengths and angles	Bravais lattice	Lattice symbol
Cubic	$a = b = c$	Simple	P
	$\alpha = \beta = \gamma = 90°$	Body-centred	I
		Face-centred	F
Tetragonal	$a = b \neq c$	Simple	P
	$\alpha = \beta = \gamma = 90°$	Body-centred	I
Orthorhombic	$a \neq b \neq c$	Simple	P
	$\alpha = \beta = \gamma = 90°$	Body-centred	I
		Face-centred	F
		Base-centred	C
Rhombohedral	$a = b = c$	Simple	R
	$\alpha = \beta = \gamma \neq 90°$		
Hexagonal	$a = b \neq c$	Simple	P
	$\alpha = \beta = 90°, \gamma = 120°$		
Monoclinic	$a \neq b \neq c$	Simple	P
	$\alpha = \gamma = 90° \neq \beta$	Base-centred	C
Triclinic	$a \neq b \neq c$	Simple	P
	$\alpha \neq \beta \neq \gamma \neq 90°$		

Polar structures and point groups

Combining the crystal systems with the symmetry operations such as mirror planes, rotation axes and inversion centre, yields the 32 point groups. Out of these, 21 are non-centrosymmetric, of which 20 are piezoelectric and have no inversion centre. The lack of central symmetry and inversion centre indicate a distorted i.e. non-cubic structure required of piezoelectricity, shown in **Figure 1.5**. In simple terms in a structure with an inversion centre an atom at position (x, y, z) should have an equivalent atom at position ($-x$, $-y$, $-z$).
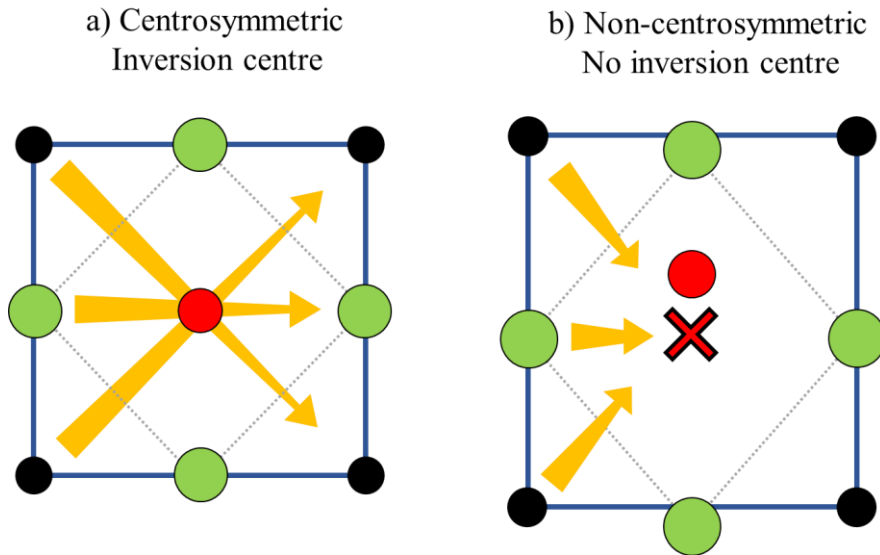
Figure 1.5 a) Centrosymmetric and b) non-centrosymmetric structures with centres of (or lack thereof) inversion highlighted by orange arrows.

Within this subset there are 10 polar point groups which possess a spontaneous dipole moment due to the separation of charge. This polarisation can be changed by changes in temperature and therefore these are termed pyroelectric. Some materials possessing the point groups in this subset also experience polarisation reversal by the application of an external electric field. The dipole moment in these structures is fundamentally tied to the piezoelectric properties and materials (Sections 1.7 and 1.8). This hierarchy of structure and properties is depicted in **Figure 1.6**.
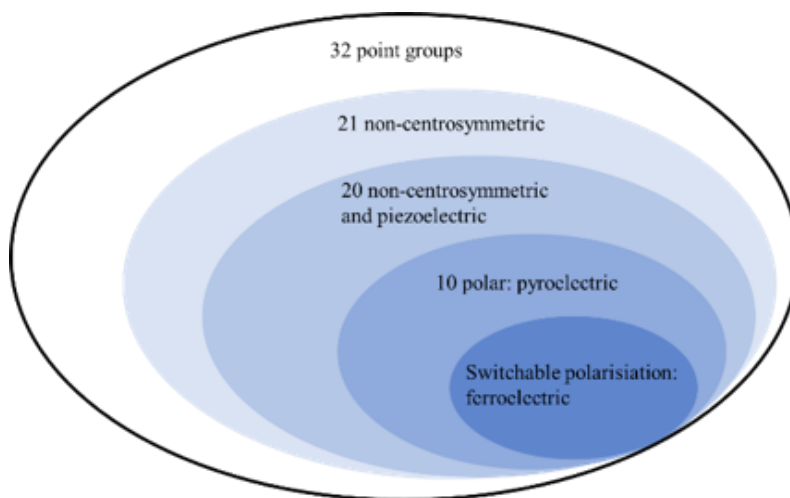
Figure 1.6 Classification of crystallographic point groups and their resultant properties

Symmetry operations

Before introducing space groups it is important to review the various symmetry operations that can be performed, shown in **Table 1-2** and the relevant nomenclature.

Table 1-2 Symmetry operations and their symbols used in nomenclature

Symmetry operation	Symbol
Rotation **360/R**	R = 2, 3, 4 and 6
Mirror plane	m
Glide plane: Mirror (m) + ½ **translation along direction**	a, b and c
Screw axis: Mirror (m) + rotation **R_T = rotation (360/R) + translation T/R**	$R_T = \ 2_1, 4_3, 6_2 \ ...$
Inversion centre	$\bar{2}, \bar{3}, \bar{4} \ and \ \bar{6}$

Space group nomenclature

A space group is used to describe the symmetry operations in a three-dimensional material. There are 230 space groups which are formed by combining the 32 point groups wherein are contained rotation, mirror and inversion symmetry operation, combined with the 14 Bravais lattices and furthermore with screw axis and glide plane symmetry operations. **Table 1-3** shows the rules as set by convention [13] for understanding the symmetry symbols when reading a space group. Shown in **Figure 1.7** are examples of

space groups with symmetry symbols described. **Figure 1.8** illustrates the structural origin for some of the symmetry operations discussed here. For clarity purposes coloured planes are used to highlight the operations.

Table 1-3 Convention rules of space group nomenclature. The rhombohedral crystal system is described in a hexagonal unit cell.

Crystal System	Order of viewing directions		
Cubic	a	[111]	[110]
Tetragonal	c	a	[110]
Orthorhombic	a	b	c
Rhombohedral / Hexagonal	c	a	[210]
Monoclinic	b (c in some literature)		
Triclinic	Only inversion centre exists (no viewing direction)		

Cubic

Mirror plane perpendicular to *a*

3-fold inversion axis around [111]

Primitive unit cell $\longrightarrow$ $Pm\bar{3}m$ $\longleftarrow$ Mirror plane perpendicular to [110]

Tetragonal

4-fold rotation around *c*

Mirror plane perpendicular to *a*

Primitive unit cell $\longrightarrow$ $P4mm$ $\longleftarrow$ Mirror plane perpendicular to [110]

Rhombohedral

3-fold rotation around *c* (hexagonal form)

Glide plane along *c* (hexagonal form)

Rhombohedral unit cell $\longrightarrow$ $R3c$

Figure 1.7 Cubic and tetragonal space groups with symmetry symbol descriptions. R3c symmetry is in its hexagonal form as discussed in Section 0.
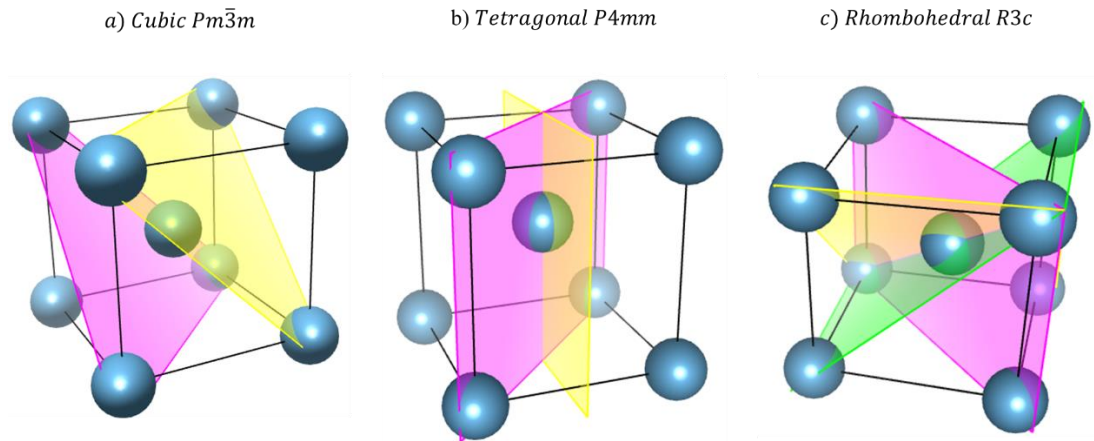
Figure 1.8 Examples of some of the symmetry operations present in different phases illustrated by planes. a) Inversion axis ($\bar{3}$) in the [111] direction of the cubic phase, b) mirror planes (mm) around the a axis and [110] direction in the tetragonal phase c) 3-fold rotation (3) and glide planes (c) in the rhombohedral phase.

Rhombohedral within hexagonal

The rhombohedral structure can be inscribed within a hexagonal unit cell as shown in **Figure 1.9**. In this example, the oxygen atoms have been removed for clarity. **Figure 1.9 a)** shows the view along the hexagonal c axis, and **Figure 1.9 b)** shows the view along the hexagonal a axis where atoms have been removed to show the two rhombohedral perovskite unit cells, which are stacked along their body diagonal correspond to the hexagonal c axis.
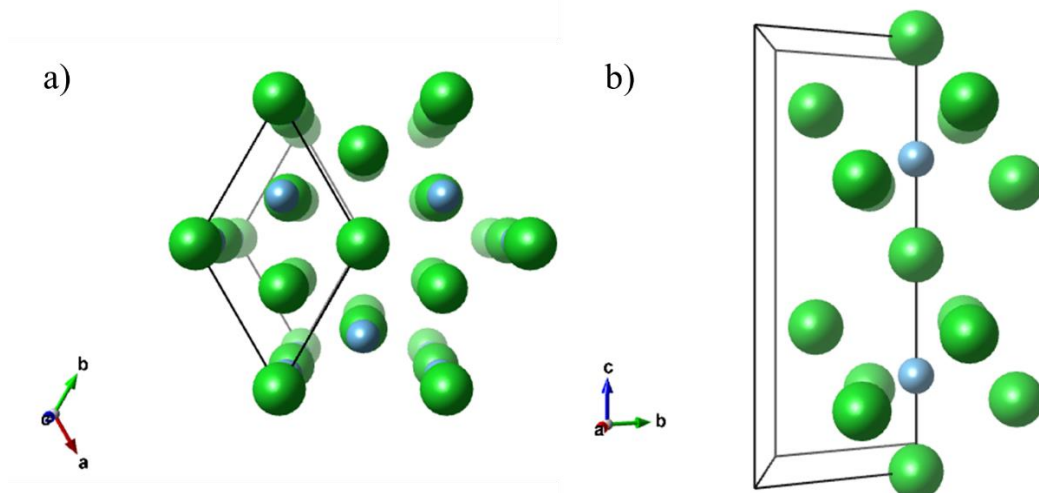
Figure 1.9 Rhombohedral structure inscribed in a hexagonal unit cell.. a) View along hexagonal c axis. b) View along the hexagonal a axis.

1.6 The perovskite structure

All the materials discussed here are characterised by a specific arrangement of atoms named the perovskite structure. The name perovskite stems from the mineral calcium titanate ($CaTiO_3$). Shown in **Figure 1.10** are three variations of the perovskite structure which are a) cubic, b) tetragonal and c) rhombohedral (or hexagonal). In these examples the perovskite atomic arrangement is maintained and denoted by the formula ABO_3, where A (green spheres) represents a corner cation, B (blue spheres) represents interior cation, and O_3 (red spheres) represents face oxygen anions. The tetragonal and rhombohedral structures can be considered as distortions of the cubic structure along one direction or the body diagonal respectively. It is these distortions that form the basis of piezoelectricity. There are of course many other structures which also exhibit piezoelectricity. For this work these are the most relevant.

a) *Cubic* $Pm\bar{3}m$ b) *Tetragonal P4mm*   c) *Rhombohedral R3c*
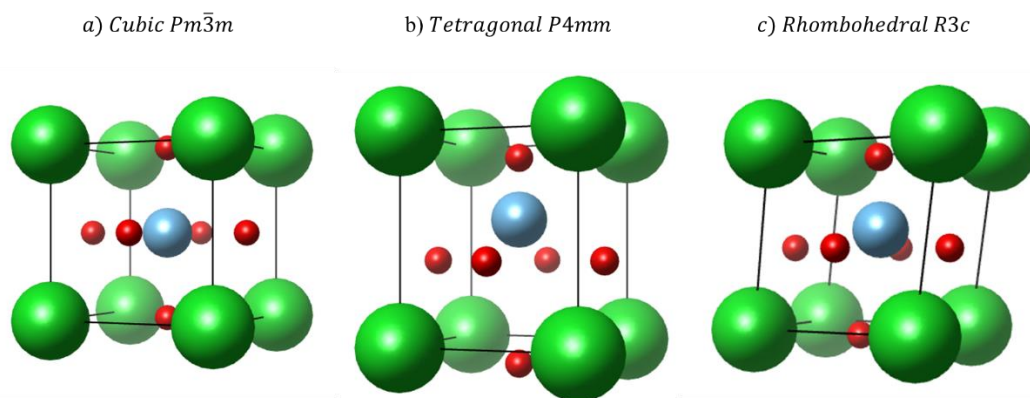
Figure 1.10. Perovskite unit cell for (a) cubic Pm-3m, (b) tetragonal P4mm and (c) rhombohedral R3c distortions with the ABO_3 structure where A = green corner cations, B = blue central cation and O = red face oxygen anions.

Octahedral tilt

There is another important distortion that can take place in some perovskite based materials which is the tilting of the octahedra formed by the eight face oxygen atoms shown in **Figure 1.11**. These tilts can occur about any of the orthogonal axes *a*, *b* and *c*. Since the face oxygen atoms are shared by two neighbouring unit cells a tilt in one direction will cause an *opposite* tilt in the other direction. Considering **Figure 1.11**, a clockwise octahedral tilt would cause the unit cells above, below and to either side to tilt

in the anti-clockwise direction. The unit cells in front and behind it however would be unaffected. A notation developed by Glazer [14] is useful to define the tilts. The notation is as follows: $a^+b^-c^0$, where a, b and c denote unique tilts about those axes, and the superscript indicates the tilt of subsequent layers, '+' if the tilt is the same, '-' if they are in the opposite direction and '0' if there is no tilt.

In **Figure 1.12** examples of tilt variations are shown. The front set of unit cells can be considered a 'layer' of octahedra. If the tilt occurs about the c axis, then the tilt extends across the layer as discussed above. For a lack of tilt a) the notation is $a^0a^0a^0$, if the subsequent layers along the c axis tilt in the same direction b) the notation is $a^0a^0c^+$, i.e. there is a unique tilt about the c axis which is in-phase (+). If the tilt of the subsequent layers alternates c) the notation is $a^0a^0c^-$, with the minus sign denotes the alternating or anti-phase tilt. These are examples of tilts around the single axis c, however there can be tilts about a and b, and combinations thereof, producing many more tilt variations outlined by Glazer [14].
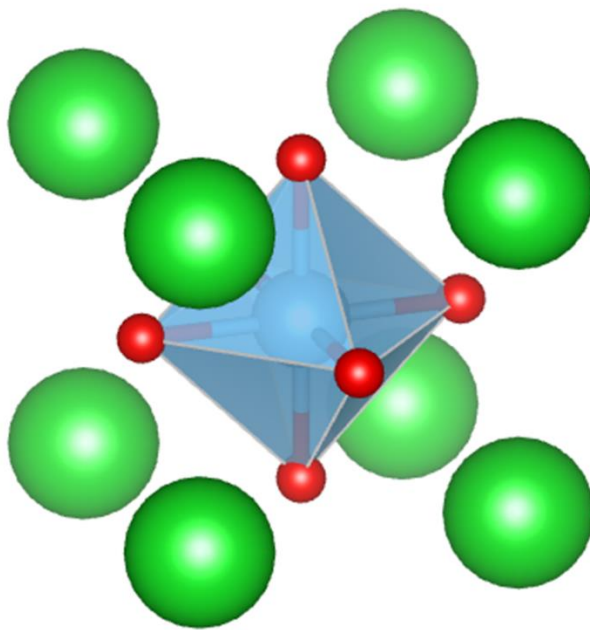
Figure 1.11 Perovskite unit cell with the oxygen octahedra unit highlighted.

a) No tilt $a^0a^0a^0$ b) In-phase tilt $a^0a^0c^+$ c) Anti-phase tilt $a^0a^0c^-$
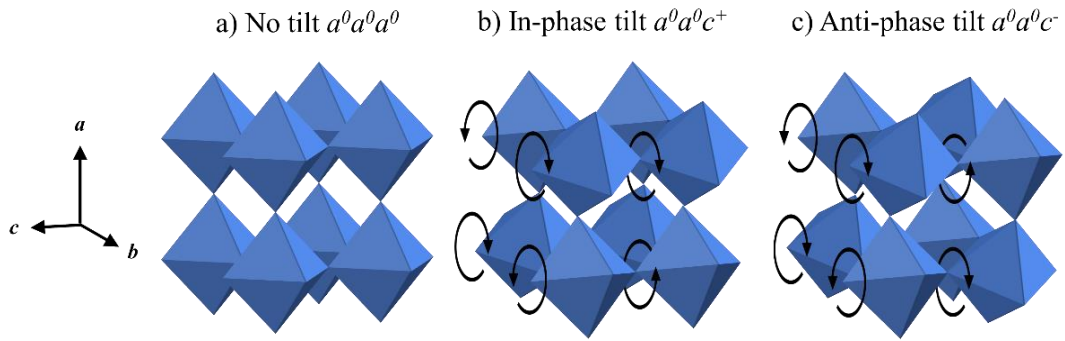
Figure 1.12 Examples of tilting variations along the c axis. a) No tilt, b) in-phase tilt, i.e. both layers tilt in the same direction, and c) anti-phase tilt, the layers tilt in opposing directions.

Tolerance factor

The Goldschmidt tolerance factor [15] can be used as an indication of the stability of a perovskite structure, and the phase it can adopt by its dependence on the ionic radii. The tolerance factor t is defined in **Equation 1.1** where r_O is the oxygen radius, r_B is the B-site atom radius and, r_A is the A-site ionic radius. For $0.9 < t \leq 1$ the structure is the ideal cubic perovskite. Here the B-site is the right size to fit within the oxygen octahedra. If the A-site is bigger or B-site smaller relative to the oxygen size, the B-site atom will have more space to displace towards its oxygen nearest neighbour, where $t > 1$, and the structure adopts a tetragonal or hexagonal structure. If the A-site ion becomes smaller or the B-site ion bigger relative to oxygen, the B-site ion will physically not have enough space to reside in. To accommodate this the entire structure experiences either a rhombohedral or an orthorhombic distortion where $0.71 < t \leq 0.9$. In some cases octahedral tilting also aides the stabilisation of the phase. Below 0.71 lower symmetry phases are adopted.

Equation 1.1

$$t = \frac{(r_O + r_A)}{\sqrt{2}(r_O + r_B)}$$

1.7 Dielectric materials

A dielectric material is one which displays extremely high electrical resistance and whose structure can exhibit polarisation or can have polarisation induced by an applied voltage. This section covers the description of dielectric materials from the following references [16], [17].

Polarisation occurs due to the separation of charges in a structure, for example displacements of cations and anions. The separation forms a dipole, where the centres of the positive and negative charges are displaced away from each other. The result is the formation of surface charge. In this manner, dielectric materials can act as capacitors in circuits as they are able to accumulate and store charge. There are several polarisation mechanisms illustrated in **Figure 1.13**. Every mechanism has an upper frequency response ceiling illustrated by the real and imaginary components of the relative permittivity (discussed in Section 0).

Space charge polarisation is associated with the movement of charge carriers which encounter barriers such as grain boundaries. As such this mechanism is a slow and low frequency process. The fastest mechanism is atomic polarisation, associated with the asymmetric distortion of electron clouds around atoms thereby producing a polarisation vector. The ionic and dipole polarisation mechanisms are the most pertinent to this work. As shown in Section 1.6 the ionic mechanism is associated with ionic displacements within the unit cell. In ferroelectric materials he dipole mechanism is associated with the formation of domains; regions or clusters in which the all the unit cells possess the same ionic polarisation vector. This is further elaborated in Section 1.8.3.
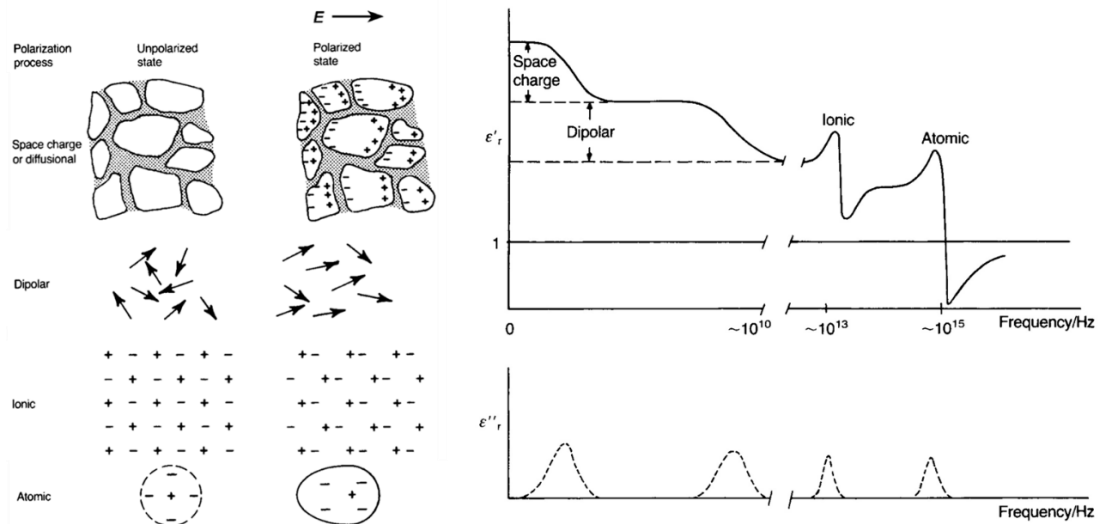
Figure 1.13 Polarisation mechanisms in dielectric materials, and the frequency dependence of the real and imaginary permittivity components. From [16].

Polarisation

The dipole moment p is calculated as the product of two equal and opposite charges Q, separated by a distance δx, shown in **Equation 1.2**.

Equation 1.2

$$p = Q\ \delta x$$

The polarisation P is calculated as the dipole magnitude per unit volume v of the material as described in **Equation 1.3**. For a linear dielectric, the polarisation is proportional to the inducing electric field E. It is related by the electric susceptibility χ_e, and the permittivity of free space $\varepsilon_0 = 8.85 \times 10^{-12}$ F/m. These are proportionality constants which determine the extent at which an applied electric field induces a polarisation.

Equation 1.3

$$P = \frac{p}{v} = \chi_e \varepsilon_0 E$$

The polarisation only accounts for bound charges. The total charge density D or charge Q per unit area A contains both bound and unbound charges, shown in **Equation 1.4**.

Equation 1.4

$$D = \varepsilon_0 E + \chi_e \varepsilon_0 E = (1 + \chi_e)\varepsilon_0 E$$

Permittivity

The extent by which a dielectric material can store charge (and thereby be polarised) by a given voltage is called the relative permittivity. The value of permittivity dictates the capacitance of the dielectric as shown in **Equation 1.5** where C is capacitance, Q is charge, V is voltage, ε_r is the relative permittivity which is the ratio of the material permittivity ε and the permittivity of free space ε_0, A is the area of the charged surface and d is the distance between the charged surfaces. The electric field E can also be expressed as volts V per metre (distance d).

Equation 1.5

$$C = \frac{Q}{V} = \varepsilon_0 \varepsilon_r \frac{A}{d}$$

Solving Equation 1.4 and Equation 1.5 for relative permittivity, its relationship with the susceptibility is shown in Equation 1.6.

Equation 1.6

$$\varepsilon_r = (1 + \chi_e)$$

Dielectric loss

For an ideal dielectric under an alternating field the current and the voltage are out of phase by 90°. As the voltage reaches its maximum value it charges the capacitor which becomes saturated and the current drops to zero. The voltage then returns to zero as the charge is released, observed as an increase in the current. This is illustrated in **Figure 1.14**.
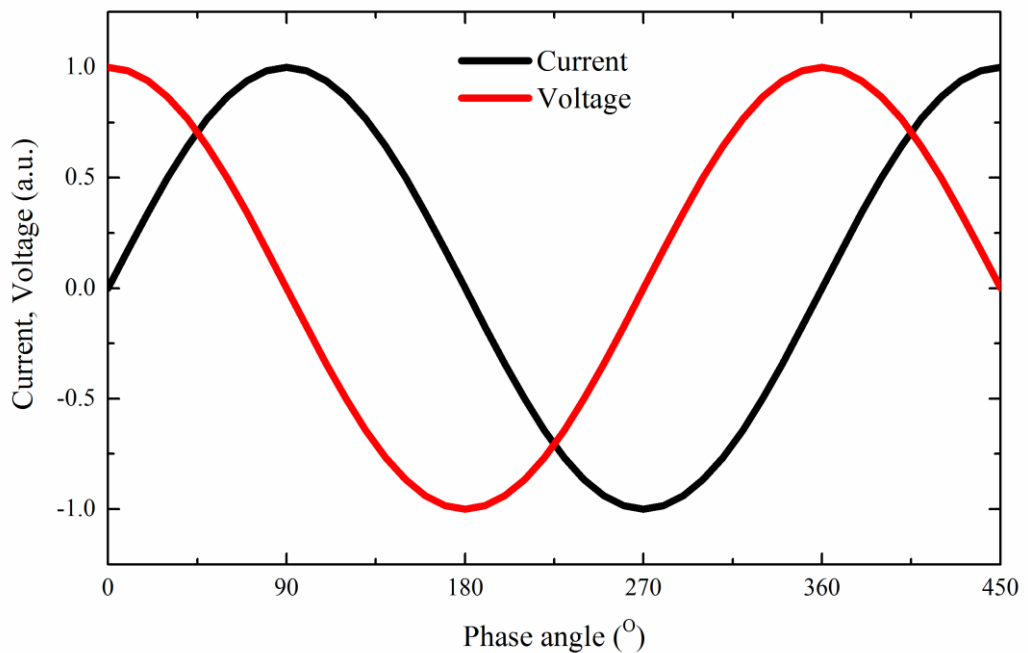
Figure 1.14 Voltage (black) and current (orange) traces for an ideal capacitor.

In reality however, there are always losses associated with current leakage and frequency response of the various polarisation mechanisms. As with any oscillating measurements be it mechanical or electrical, there are complex quantities with real and imaginary components. In this case measuring the complex permittivity can provide information on the dielectric loss of a dielectric. This is expressed in **Equation 1.7**, where $\varepsilon_r{}^*$ is the complex permittivity and $\varepsilon_r{}'$ and $\varepsilon_r{}''$ are the real and imaginary or capacitive and lossy components respectively.

Equation 1.7

$$\varepsilon_r^* = \varepsilon_r' - i\varepsilon_r''$$

The phase difference between the current and the voltage can be represented by a phasor diagram, shown in **Figure 1.15**. When the phase difference is less than 90° the current oscillations are split into two components, I_{cap} capacitive component, and I_{loss} is the loss component.
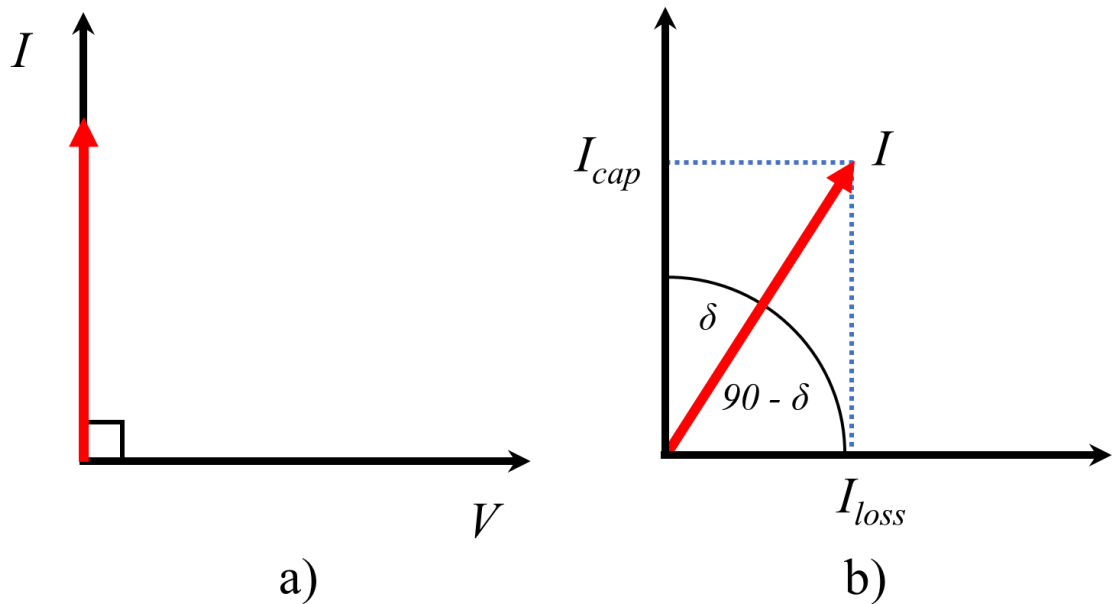
Figure 1.15 Phasor diagrams representing the current and voltage components in an a) ideal and b) non-ideal capacitor. The complex component emerges when the phase difference is less than 90°.

From the phasor diagram, it is apparent that the components can be calculated as shown in in **Equation 1.8**. These are in turn proportional to the capacitive and lossy components of the permittivity [16]. The ratio of these components is known as the loss tangent or dissipation factor and can therefore be obtained from the trigonometric equivalence shown in **Equation 1.9**. As stated earlier an ideal lossless capacitor has a 90° phase difference for which the loss tangent is zero. As the phase difference approaches zero the loss tangent tends to infinity. At this point there is no phase difference between the voltage and current and the material can be thought of as a classic resistor.

Equation 1.8

$$I_{cap} = I \cos \delta \propto \varepsilon'_r$$

$$I_{loss} = I \sin \delta \propto \varepsilon''_r$$

Equation 1.9

$$\frac{I \sin \delta}{I \cos \delta} = \frac{\varepsilon''_r}{\varepsilon'_r} = \tan \delta$$

1.8 Ferroelectricity

1.8.1 Introduction

As briefly described in Section 0, a pyroelectric material is one which displays a spontaneous polarisation due to its non-centrosymmetric and polar structure. If this polarisation can also be switched via an external electric field the material is also classed as ferroelectric. The emergence of this property is highly dependent on temperature; a material ceases to exhibit ferroelectricity above a temperature called the Curie point (T_c). Above T_c the structure becomes centrosymmetric (non-polar), and therefore the criterion required of ferroelectricity i.e. a non-centrosymmetric and polar structure, disappears. At this point the material becomes paraelectric. This occurs due to the high thermal energy of the ions whose off-centre thermal fluctuations average out to a cubic structure. As the Curie point is crossed upon cooling, the thermal energy decreases enough for the ions to settle into stable positions, resulting in the spontaneous polarisation. A mechanical strain accompanies the polarisation because of the ionic displacement.

In **Figure 1.16** a transition from cubic to tetragonal is shown. As the temperature decreases from above T_c (a), the ions in a centrosymmetric position displace into more energetically favourable positions (b) producing spontaneous polarisation and strain. The lattice extension along the polarisation vector also requires a contraction of ionic positions perpendicular to the vector to compensate for the anisotropic strain.
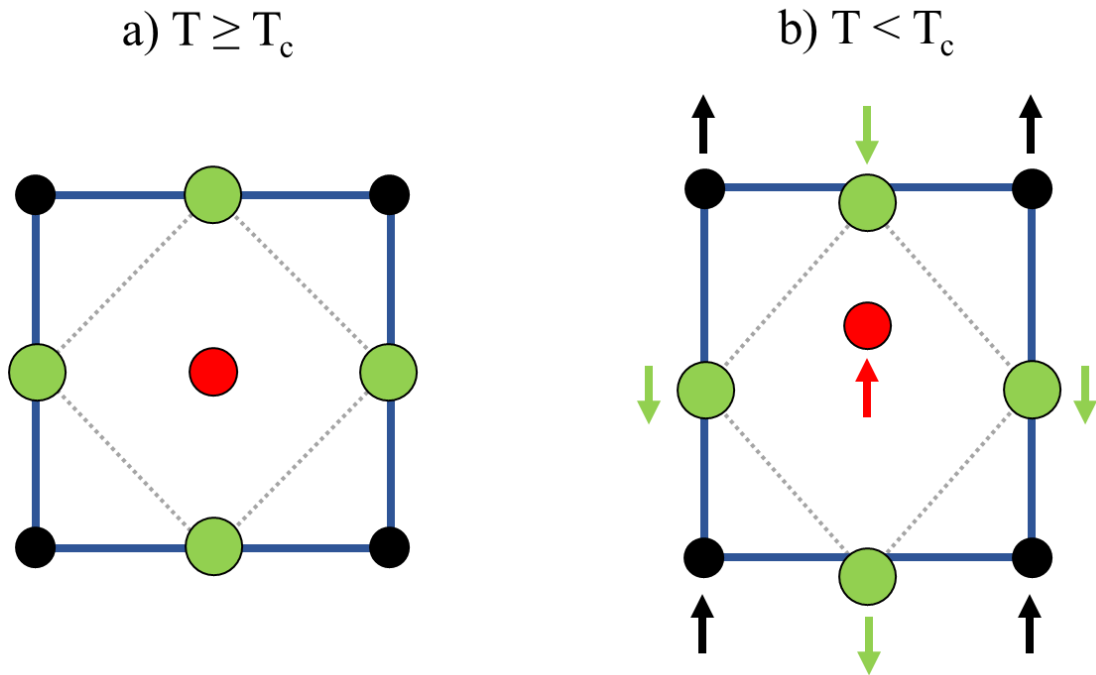
Figure 1.16. The perovskite structure depicted in two dimensions. Above its Curie point (a) the structure is cubic and paraelectric i.e. no dipole moment or separation of charge. Below the Curie point (b) there is a transition to (in this example) the tetragonal ferroelectric phase.

1.8.2   Curie-Weiss behaviour

The transition from paraelectric to ferroelectric can be modelled via the Landau model and the Curie-Weiss law [16]. The Landau model for energy density in a material (*G*), effectively the free energy in the system, can be approximated by the series expansion shown in **Equation 1.10** for the example of a tetragonal structure in which displacements are relatively simple. The coefficients α and β are temperature dependent. The coefficient α is particularly important and is described in **Equation 1.11** where *a* and *b* are experimentally determined constants. The simplified series expansion is shown in **Figure 1.17** for temperatures transitioning through T_C. Above T_C there is only one polarisation state which is zero. Below T_C two opposite polarisation states emerge, positive and negative.

Equation 1.10

$$G = G_0 + \alpha P^2 + \beta P^4 \cdots$$

Equation 1.11

$$\alpha = a(T - T_c)$$

$$\beta = b$$
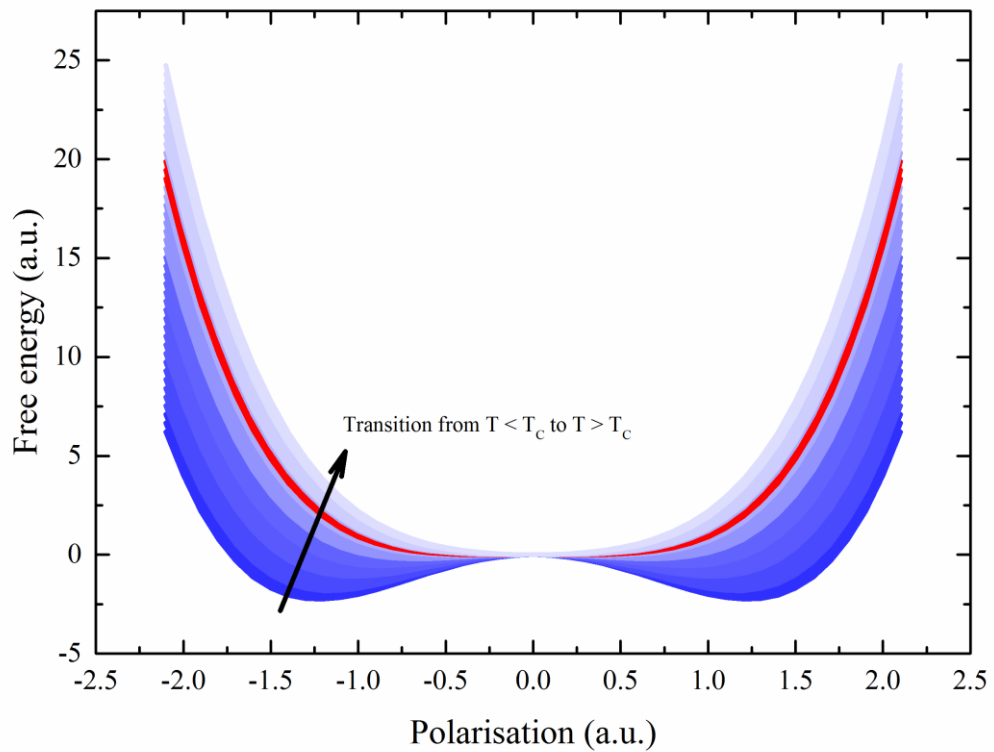
Figure 1.17 Landau model for free energy as a function of polarisation. The red trace corresponds to T = Tc

Differentiating the expansion and equating to zero can be used to determine the energy minima i.e. the polarisation state with respect to T, shown in **Equation 1.12**. This calculation is depicted in **Figure 1.18** showing polarisation as a function of T relative to T_C. The two polarisation states that emerge correspond to the ionic displacement in two different directions. As T_C is approached the energy in the system increases, reducing the potential barrier between the two states, finally combining into one where the structure no longer exhibits polarisation.

Equation 1.12

$$\frac{\partial G}{\partial P} = 2aP + 4\beta P^3 = 0$$

$$P = \pm \sqrt{\frac{a(T - T_c)}{2b}}$$
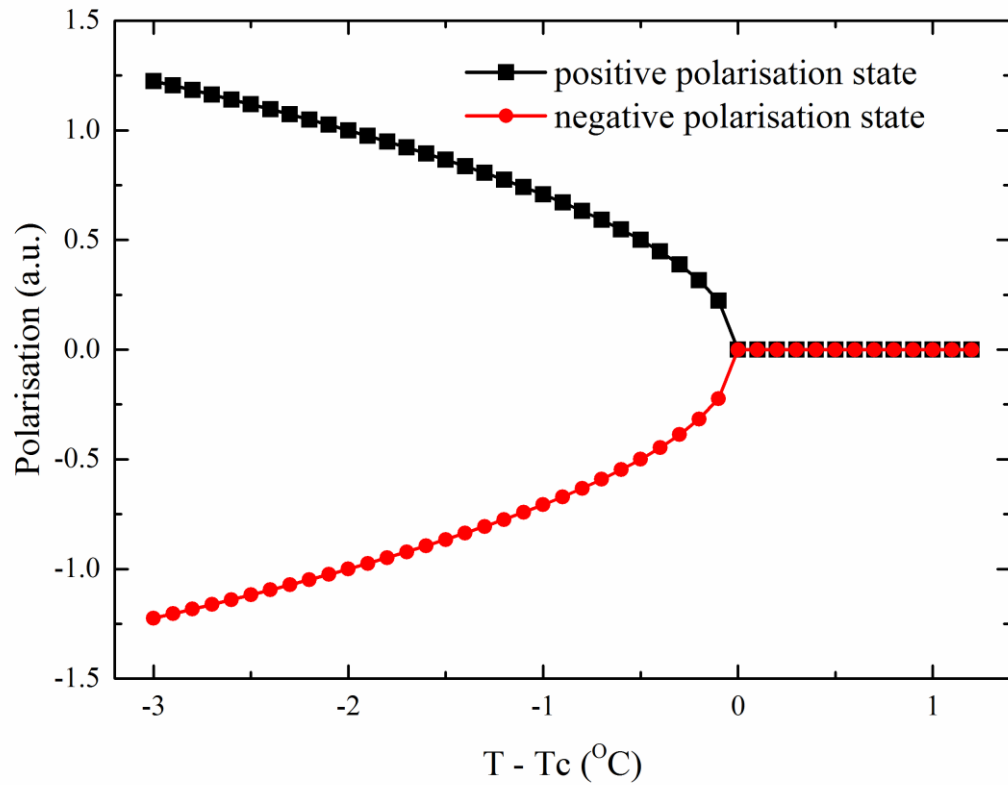
Figure 1.18 Polarisation states emerging from the Landau model.

Introducing an interaction energy in the form of an applied electric field into **Equation 1.12** and solving for the susceptibility in **Equation 1.3** produces the Curie-Weiss law described in **Equation 1.13**.

Equation 1.13

$$\varepsilon_r - 1 = \chi_e = \frac{1}{2a\varepsilon_0(T - T_c)}$$

1.8.3   Ferroelectric domains

Ferroelectric domains are regions within a ferroelectric material which are polarised in the same direction [2]. They arise in order to minimise the potential energy associated with surface charges and strains. In polycrystalline materials, neighbouring grains experience strain which further induces the formation of domains. **Figure 1.19** shows the formation of domains for a tetragonal material. If all the unit cells' spontaneous polarisation vectors are in one direction (a) an imbalance in the surface charges occurs. This creates an electric field gradient acting against the polarisation vector, and the high-energy state is reduced by the formation of 180º domains (b) which result in a net polarisation of zero. The spontaneous polarisation is accompanied by an associated mechanical strain (c) due to the ionic displacements. Again, this strain is highly directional and therefore produces high stresses produced by the elastic constraints of the surrounding grains in polycrystalline ceramics. This unfavourable state is reduced by the formation of 90º domains (d).

1.8.3.1   Domain behaviour

As discussed in Section 1.8.3, the formation of ferroelectric domains is motivated by the reduction of anisotropic polarisation and strain. As such the domain state becomes isotropic and no net strain or polarisation is produced. In order to make this material useful it must be forcibly polarised by applying a sufficiently high electric field. In doing so many of the domains will be aligned with the electric field. In a polycrystalline material, there will exist grains with unfavourable crystallographic orientations with respect to the electric field with domains which do not reorient as much as others e.g. 180º domains in grains aligned with the field vector. Additionally, domains oriented perpendicular to the field vector will require a greater magnitude of electric field to produce domain switching. Once this is achieved the material is polarised or 'poled' and will have a net polarisation. This polarisation is retained as a remnant polarisation after field removal. **Figure 1.20** shows a schematic of the domain behaviour in grains. Initially at zero-field (a) the domains are disordered. When a small field is applied (b) domains favourable orientated will grow at the expense of neighbouring domains. When a sufficiently large electric field is applied (c) the domains will be predominantly aligned with the field vector. At this point the material is considered 'poled'. These changes are

accompanied by elongation of the structure along the poling vector and a corresponding contraction perpendicular to the field vector. Applying a compressive stress (d) will align domains perpendicular to the stress vector.
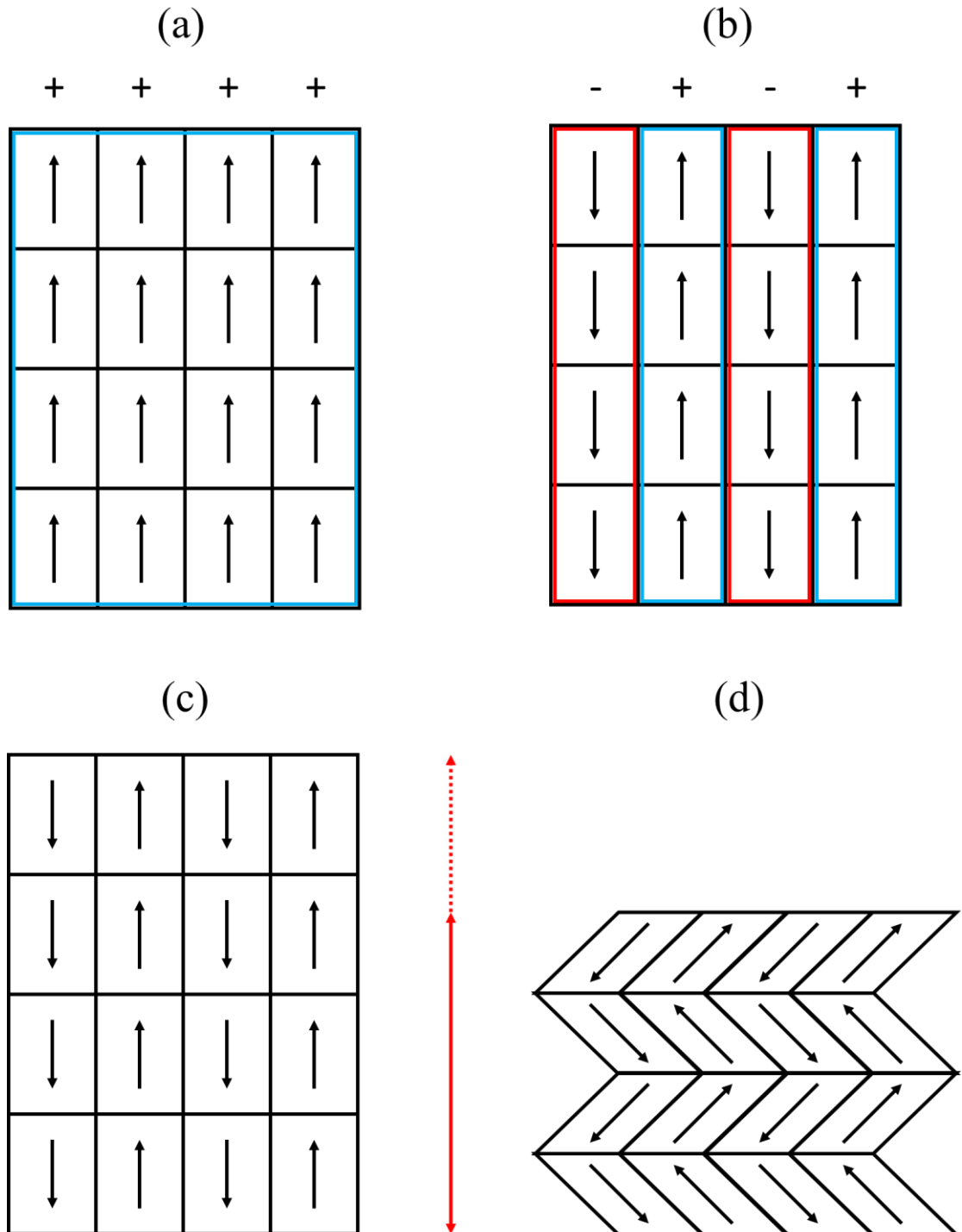
Figure 1.19. Formation of 180° domains (a-b) occurs to reduce the high electrostatic potential energy and results in a net zero polarisation (b). 90° domains (c - d) form to reduce the highly directional strain and high mechanical potential energy associated with the polarisation.
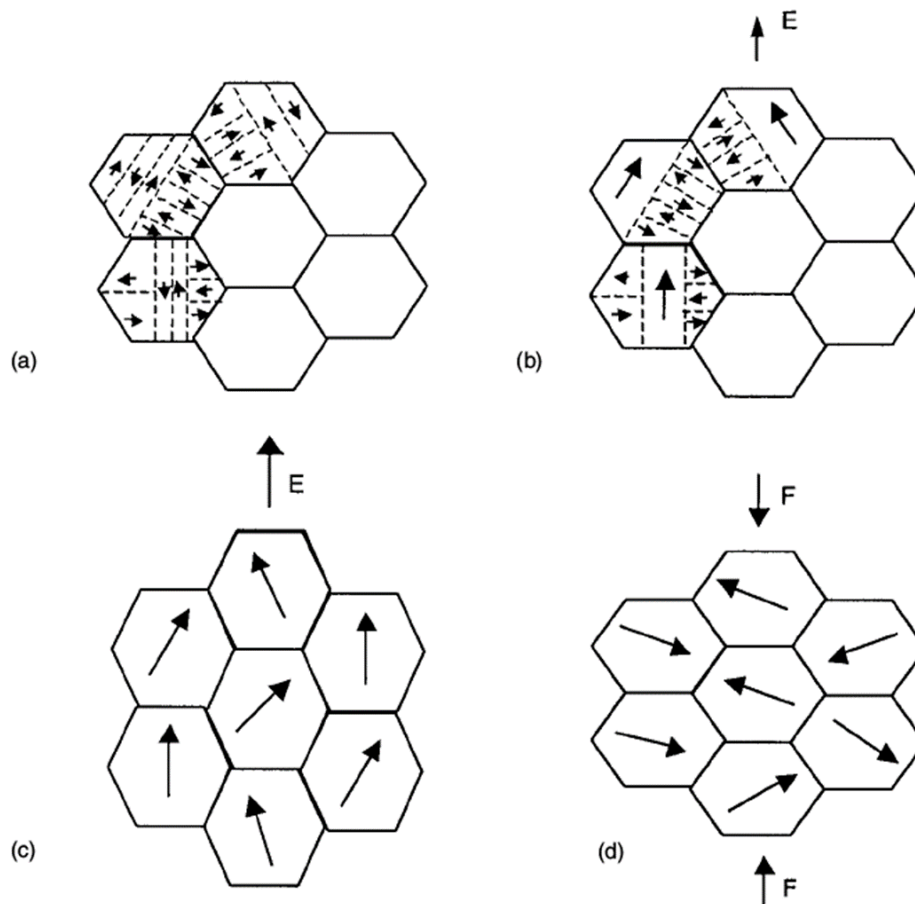
Figure 1.20 Domains within grains initially randomly orientated (a). Under an electric field those domains already favourable aligned will grow at the expense of their neighbours (b). With a greater field, domains not aligned are eventually switched (c) and a net polarisation is produced. Applying a compressive force (d) the domains rearrange perpendicular to the stress vector. From [16].

1.8.3.2 Ferroelectric hysteresis

When measuring polarisation as a function of electric field for ferroelectric materials, hysteretic behaviour emerges as shown in **Figure 1.21**. Initially the net polarisation is zero (*O*) requiring an electric field to align the domains in the positive direction. The rapid increase in polarisation is due to domain wall motion (growth of domains parallel to the field vector, and ionic polarisation. At high fields where the curve becomes linear the polarisation is said to be saturated i.e. there is no more domain wall motion. Here the polarisation mechanism is purely ionic and piezoelectric behaviour can be observed (see Section 1.10). This is represented in **Figure 1.20** (a), (b) and (c). Now if the electric field is removed the polarisation arising from the piezoelectricity decreases

following a linear trend. Here the hysteretic behaviour emerges as there is no restoring force on the domain walls and therefore. The intercept of the linear polarisation at zero-field is labelled the saturated polarisation P_s. In reality however some of the polarisation is lost due to domain walls relaxation. This polarisation value is called the remnant polarisation P_r. As the electric field is reversed the polarisation further decreases as the domains are being forcibly switched. $\pm E_c$ is the electric field required to switch the polarisation. Once the domains have been switched the process is repeated.
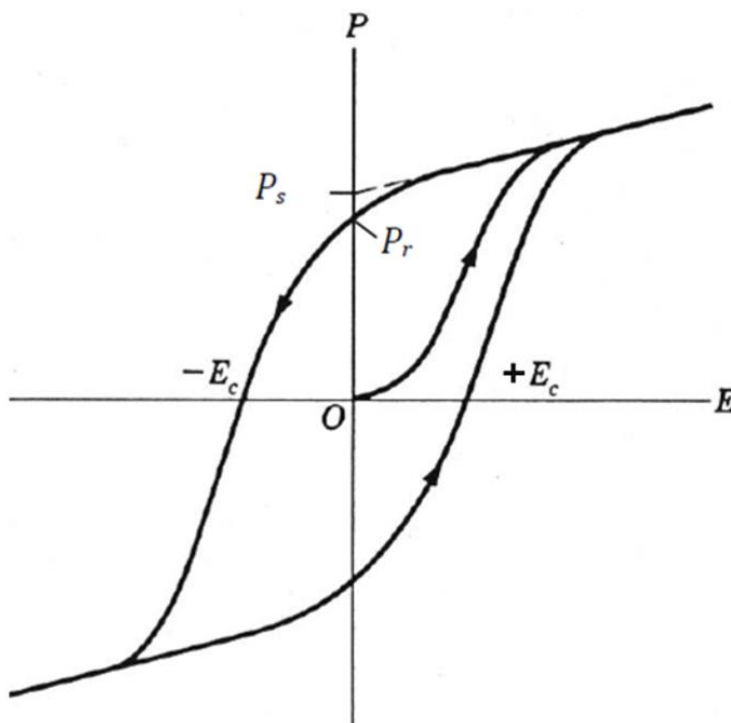
Figure 1.21 Typical hysteresis loop of polarisation (P) as a function of electric field (E) for a ferroelectric material. At zero-field (O) there is no net polarisation. Once polarised the field is removed and a remnant polarisation (P_r) remains. P_s is the saturated polarisation, extrapolated by a linear regression of the high field linear behavior of the polarisation. There are however some losses associated with domain wall dynamics. $\pm E_c$ is the electric field required to reverse the polarisation. Modified from [2].

1.8.3.3 Polycrystalline and single crystal materials

An essential feature of ceramic materials is whether they are a single crystal or polycrystalline **Figure 1.22**. A single crystal represents the 'purest' type of material as its structure is highly ordered and has translational order spanning the entirety of the

material. In many cases this produces anisotropic properties which are superior to a polycrystalline material [16].

Single crystal manufacturing methods are however far more difficult to perfect and are significantly more expensive than for polycrystalline counterparts. Polycrystalline ceramics are composed of millions of small crystals (or crystallites) with sizes of the order of 1μm-10μm and are relatively easy to produce. The result is a material with a random distribution of crystals in different orientations. The compromise for simpler and cheaper manufacturing are the inferior properties such as lower polarisation and field response. Several factors are responsible for this: Domain size and therefore high coherence of polarisation is inherently limited by the grain size. The random grain orientation means that many domains are unfavourable orientated with respect to the field vector. In these grains full domain switching is limited. Additionally the stresses associated to neighbouring grains act as restoring force to domain wall motion, producing a greater discrepancy between the saturated and remnant polarisation. Grain boundaries are regions of disorder, which coupled with the presence of defects further reduces domain mobility. These effects can be clearly measured as a significant decrease in the remnant polarisation and a significant increase in the coercive field. This is exemplified in **Figure 1.23** for barium titanate.

(a) Single crystal   (b) Polycrystalline
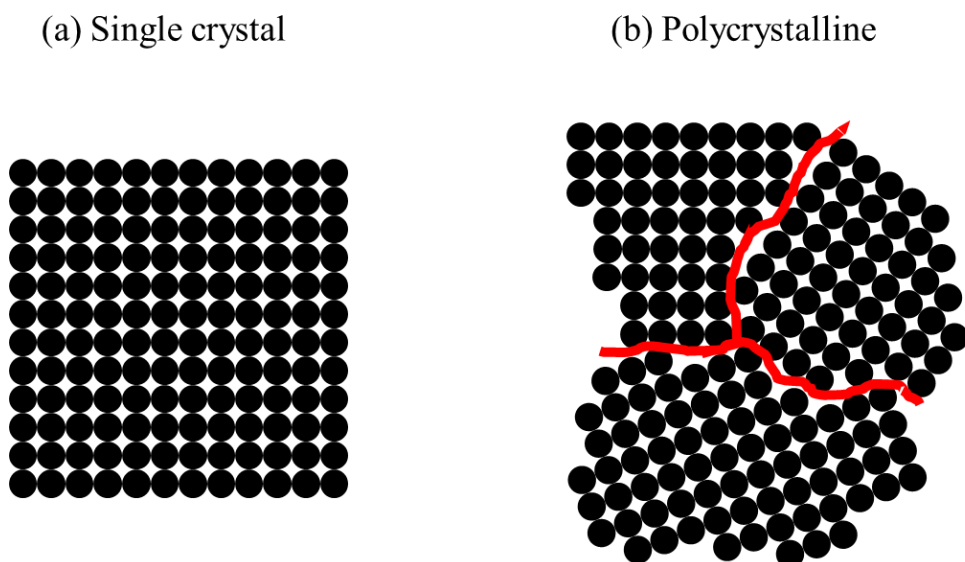
Figure 1.22 A single crystal material (a) has long range crystalline order with a single orientation across the entire material. In contrast a polycrystalline material (b) is comprised of many small crystals, or grains all of which are randomly orientated. This creates regions called grain boundaries (red line) which display disorder.
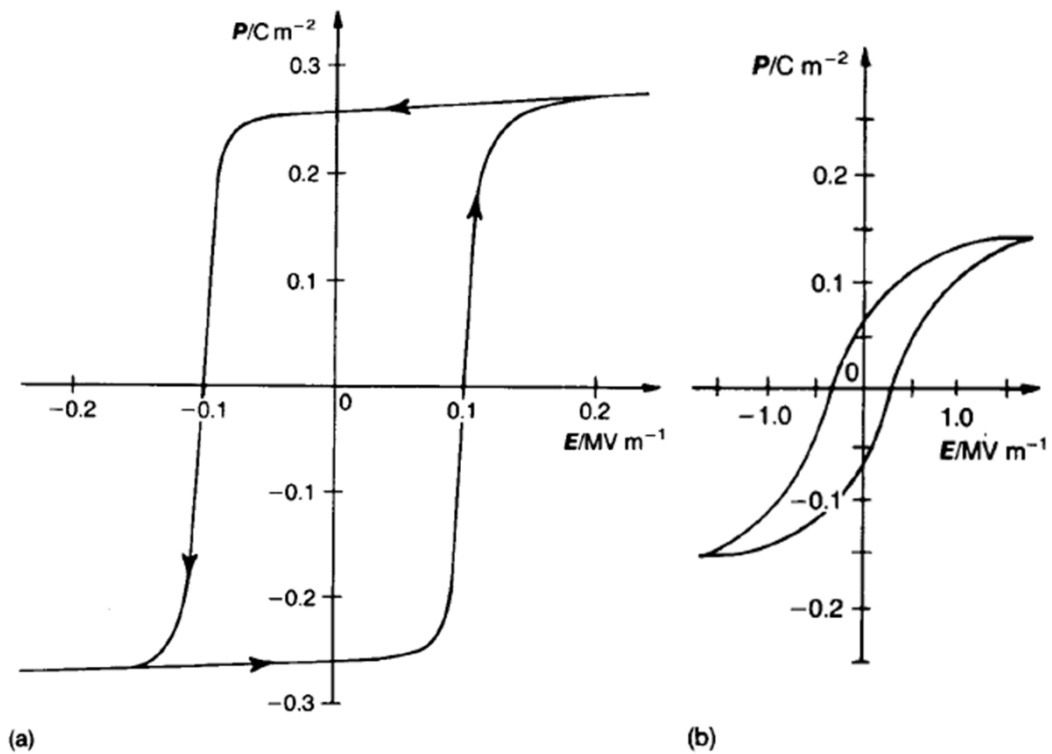
Figure 1.23 Polarisation measurements for barium titanate single crystals (a) and polycrystalline samples. The horizontal electric field axes are not to scale. From [16].

1.9 Phase transitions

1.9.1 Temperature dependent phase transitions

There are several temperature dependent phase transitions that can arise in ferroelectric materials in addition to the paraelectric transition at T_c. Barium titanate (BaTiO$_3$) is a widely studied ferroelectric material with many phase transitions as shown in **Figure 1.24**. The Curie point is at 130 °C below which it adopts a ferroelectric tetragonal structure with a polar distortion along the *c* direction. On further cooling to 0 °C there is a transition to an orthorhombic phase, whose distortion can also be described as a monoclinic face distortion. Then at -90 °C a further transition to a rhombohedral phase is observed where the distortion is along the body diagonal.

These phase transitions are apparent in permittivity measurements shown in **Figure 1.25** where the sharp peaks in the relative permittivity coincide with the phase transitions. The high temperature peak corresponds to the paraelectric to ferroelectric (Curie point) transition upon cooling, referenced earlier. At the transition temperature,

the thermal energy of the lattice provides sufficient mobility to be easily polarised by a small voltage but not too much so that the thermal vibrations surpass the polarising field. At cooler temperatures, more permittivity peaks are encountered due to the lattice flexibility afforded by other phase transitions, tetragonal to orthorhombic and orthorhombic to rhombohedral respectively.
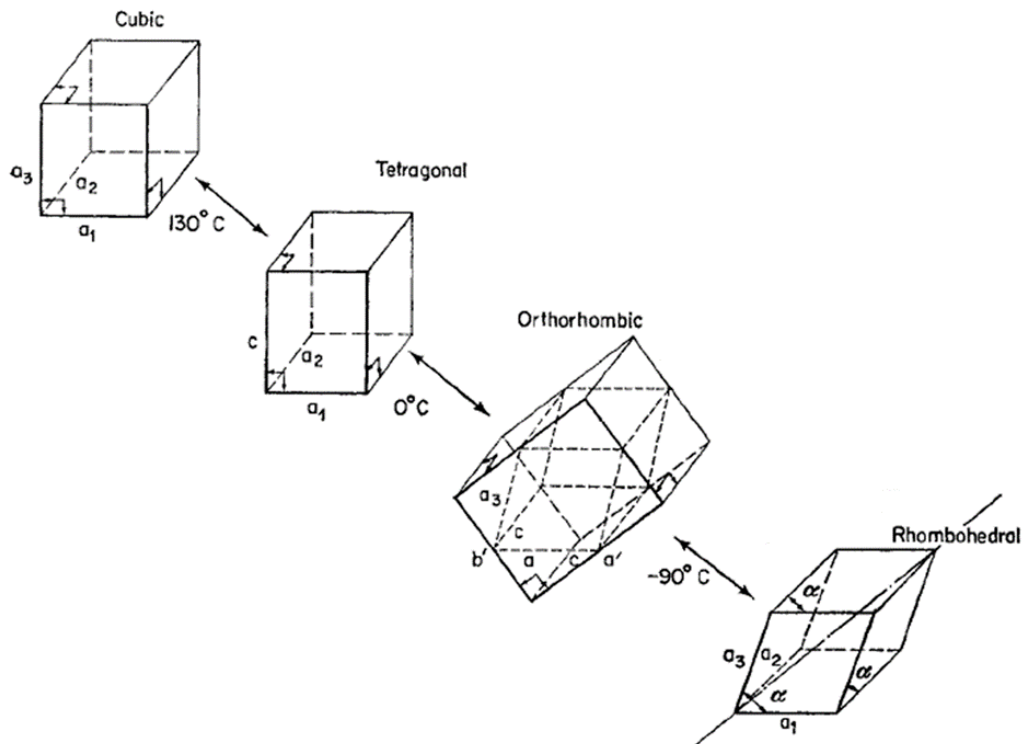
Figure 1.24 Phase transitions of BaTiO$_3$ as a function of temperature, from [2].
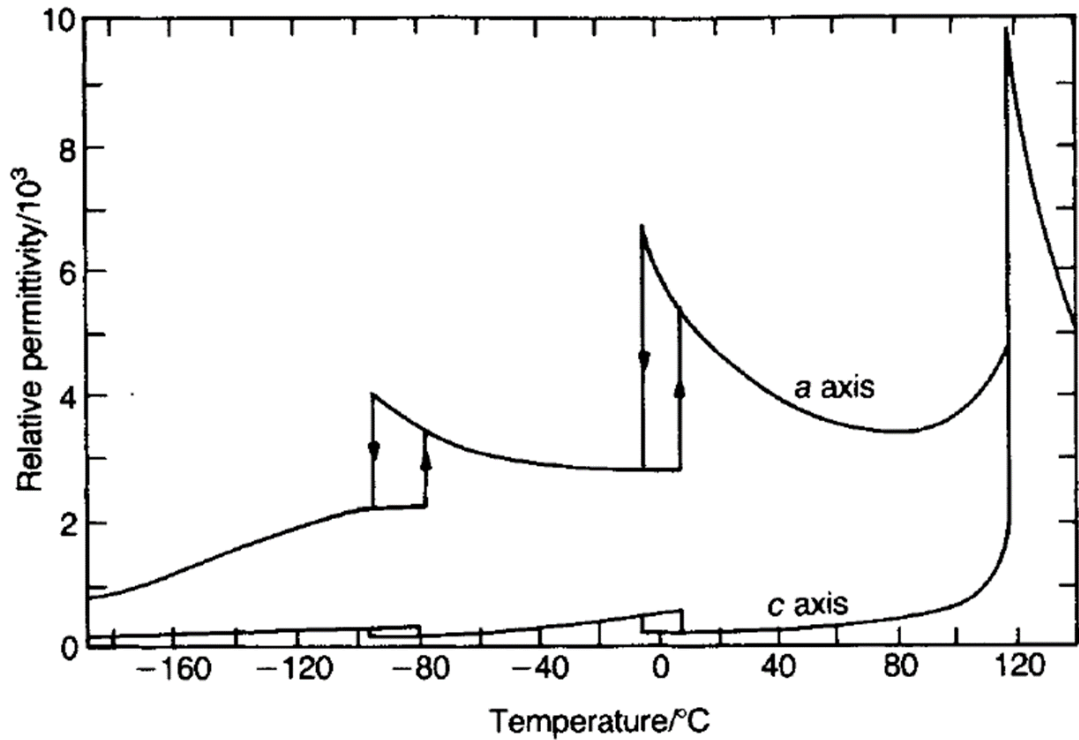
Figure 1.25 Relative permittivity of BaTiO₃ single crystal as a function of temperature in the a and c directions. Sharp peaks are in the vicinity of phase transitions shown in Figure 1.24. From [16]. Note that the figure does not represent the permittivity in the rhombohedral phase of a single crystal accurately as it would require the same permittivity values for a and c.

1.9.2   Composition dependent phase transitions

Phase transitions can also occur when two or more perovskite materials with different crystal phases are combined in a solid solution. Barium titanate, tetragonal at room temperature, can form a solid solution with barium stannate ($BaSnO_3$) which is cubic at room temperature. Shown in **Figure 1.26** is the phase diagram of $Ba(Ti_{1-x},Sn_x)O_3$ At 0% tin (Sn) the phase transitions of pure $BaTiO_3$ can be observed. With increasing Sn content the Curie temperature is significantly suppressed whilst the other phase transitions increase in temperature, resulting in a convergence of transitions into a single transition around $x = 12.5$. Above $x = 0.15$ the room temperature phase of the solid solution represents that of barium stannate i.e. cubic. As discussed in Section 0, variations in the relative size between A-site and B-site ions will induce distortions to the perovskite structure. An increase in Sn content increases the average B-site ionic size reducing the tolerance factor from $t > 1$ to $t = 0.9$-1. Above $x = 0.25$ the transition becomes diffuse due to dielectric dispersion. This behaviour is covered in Section 0.

Exemplified here is the ability to tailor material properties by atomic substitution. The addition of Sn can be used to reduce the Curie point to room temperature, thereby enabling the use of its high permittivity around T_c for capacitor applications, however at the cost of operating temperature for piezoelectric applications.
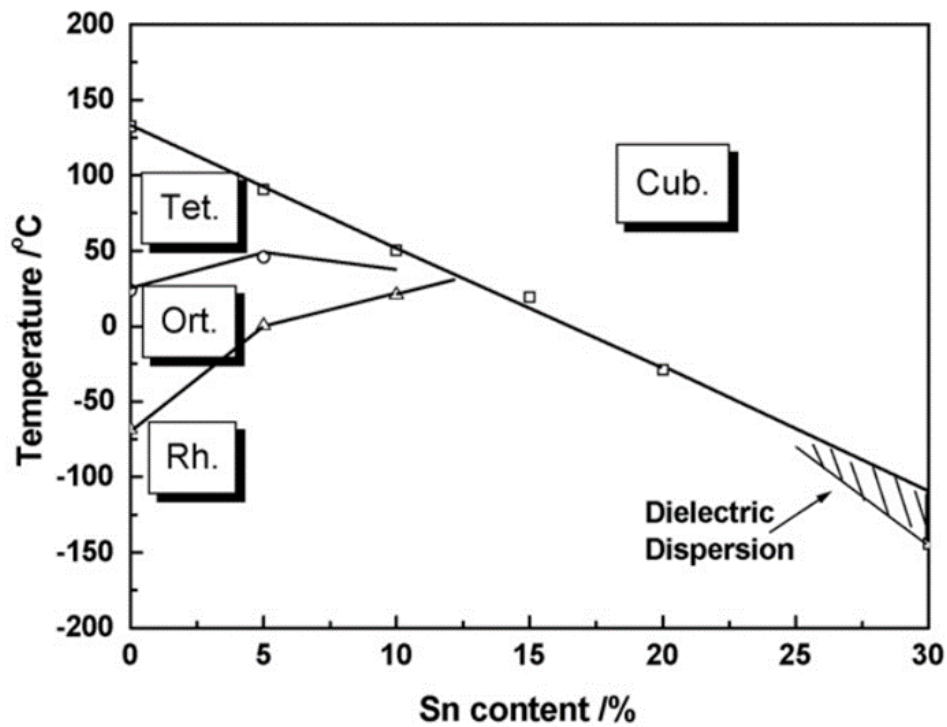
Figure 1.26 Phase diagram of the Ba(Ti$_{1-x}$,Sn$_x$)O$_3$ solid solution showing the phase transitions occurring with varying tin (Sn) content. From [18].

1.10 Piezoelectricity

Piezoelectricity is the effect by which the application of strain on a material produces a surface charge due to the strain induced polarisation of the atomic structure. Conversely an applied electric field produces a mechanical strain [2]. In this way, these materials can be used as sensors and actuators. A requirement of piezoelectricity is a non-centrosymmetric structure. Ferroelectric materials have the added benefit that they possess switchable spontaneous polarisation meaning that they can retain a net polarisation.

Piezoelectric behaviour can be divided into two related effects: The direct and converse piezoelectric effect. The direct piezoelectric effect is characterised by the formation of a surface charge in response to a mechanical stress and the converse effect is the manifestation of mechanical strain in response to an electric field.

There are several contributions defined in Equations 1-4 with their corresponding tensor notation (subscripts i, j, k, l, m, n, described in detail in the following section). The converse effect is defined in **Equation 1.14** where x is the induced strain, s is the compliance, X is the stress, d is the piezoelectric stress coefficient, M is the electrostriction coefficient and E is the electric field.

Equation 1.14

$$x_{ij} = s_{ijkl}X_{kl} + d_{mij}E_m + M_{mnij}E_mE_n$$

The first term is effectively Hooke's law and is equal to zero in an unclamped material. The final term describes electrostriction. All dielectric materials experience electrostriction, the physical deformation of a material due to an applied electric field [16]. Dielectrics contain ions with different electron affinities and therefore their response to an electric field is different. Positive and negative ions will also displace in opposing direction thereby creating a strain [16]. This effect is generally small and only observed at very high fields. Therefore, the piezoelectric stress coefficient d becomes a significant constant in determining the field induced stress. Removing the other terms a suitable approximation is shown in **Equation 1.15**. Symmetry constraints allow for the use of reduced tensor notation.

Equation 1.15

$$x_i \approx d_{mi}E_m$$

The direct piezoelectric effect is described by **Equation 1.16** where P is the polarisation and e^X is the permittivity at constant stress. In this case d is the piezoelectric charge coefficient. Again, this can be simplified as shown in

Equation 1.17 where higher order terms can be ignored, such as the permittivity term which can be set to zero in a short-circuit. Symmetry constraints again allow reduced tensor notation.

Equation 1.16

$$P_i = d_{ijk}X_{jk} + e_{ij}^X E_j + \cdots$$

Equation 1.17

$$P_i \approx d_{ij}X_j$$

In both cases, it is the piezoelectric coefficient d which determines the strain and polarisation and can be expressed as pm/V or pC/N respectively. This coefficient is equivalent for both effects.

1.10.1 Piezoelectric tensor notation

As with many physical properties, piezoelectric coefficients can be complicated and are fully described using tensor notation. The values of the tensor notation subscription range from 1 to 6. Values 1 to 3 refer to one of the three orthogonal directions, whilst 4 to 6 describe a shear around said directions. By convention in the field of piezoelectricity, polarisation is denoted along the '3' direction. These are shown in **Figure 1.27** The d coefficient determines the piezoelectric activity, and can be measured in various geometries:

A commonly used coefficient, d_{33} is the measure of strain or polarisation induced by an electric field or stress along the polarisation vector.

Transverse behaviour is measured with d_{31} where the polarisation is measured along the polar direction under a perpendicular stress, or perpendicular strain is measured under an electric field aligned with the polar direction.

Shear behaviour is defined by d_{15} where the polarisation is measured perpendicular (1 direction) to the polar direction under a shear stress about the 2 direction, or the shear strain is measured about the 2 direction under an electric field perpendicular to the polar direction (1 direction).
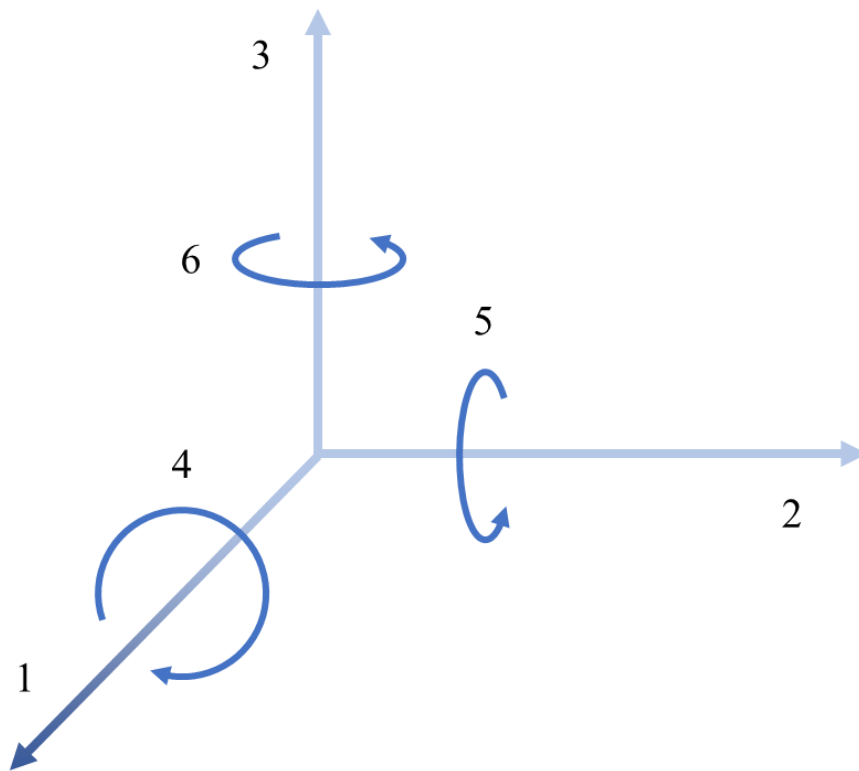
Figure 1.27 Depiction of piezoelectric tensor notation. Due to convention, the polarisation is defined to be along '3' direction.

1.11 Field-induced behaviour

Two important aspects of piezoelectric materials have been covered so far i.e. ferroelectric domains and electric field response behaviour, described in **Equation 1.15**, additionally **Figure 1.20** illustrates the ferroelectric domain behaviour under stimuli such as electric field or stress. *In situ* X-ray diffraction (XRD) methods have been used successfully to observe domain behaviour under stress and electric fields, particularly on Pb(Zr, Ti)O$_3$ (PZT) and related compositions [19]–[22]. This method of analysis relies on the fact that X-ray peaks correspond to domains. In a randomly orientated polycrystalline sample it is possible to observe X-ray scattering along different directions

relative to an electric field and by the observed changes determine the domain behaviour (X-ray diffraction and relevant techniques will be discussed in Section 2.2). **Figure 1.28** illustrates a typical experimental set up. The scattering range for the desired peak is measured as a function of angle (Ψ) relative to the applied electric field vector. It is important to note that 180° domain switching produces only a change in polarisation, not strain. This is evident from the depiction in **Figure 1.19**. Therefore measurements of domain reorientation via X-ray scattering are assumed to arise solely from non-180° domains.
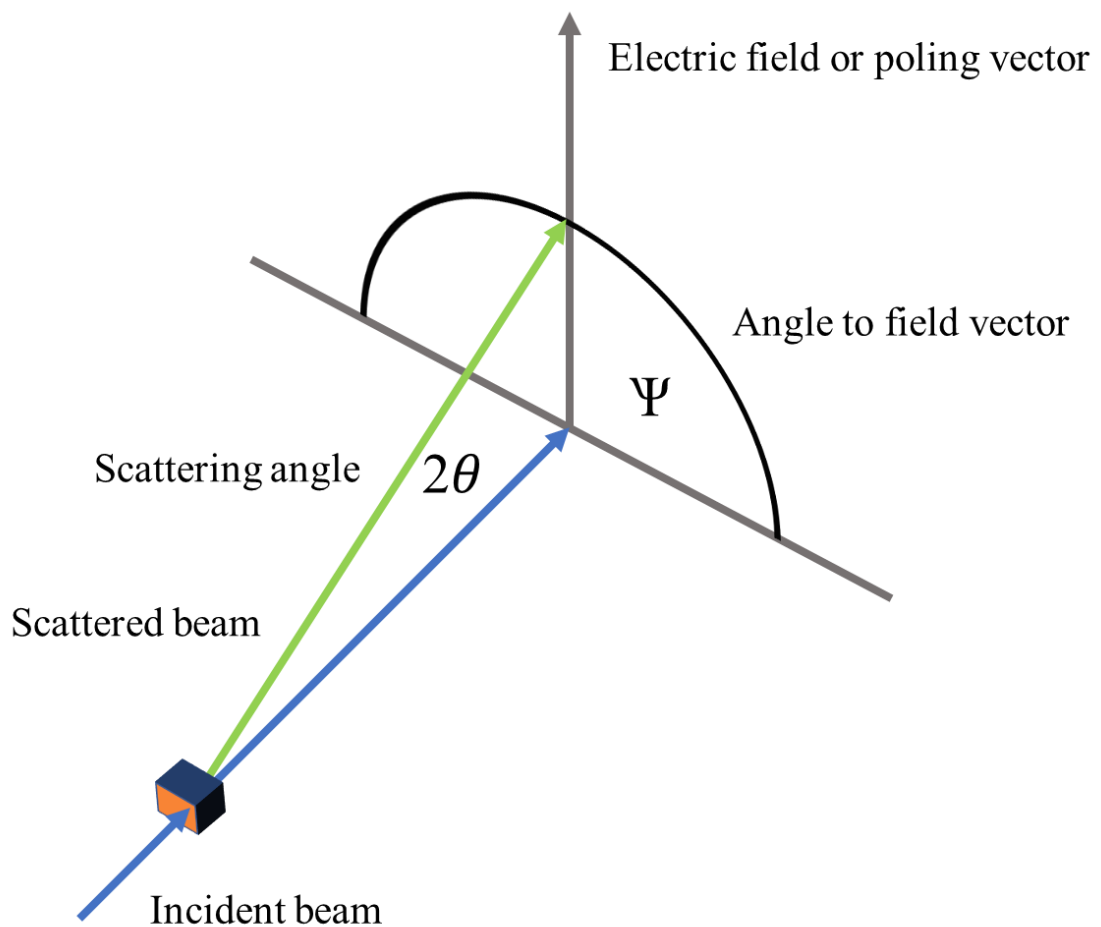
Figure 1.28 Typical in situ E-field experimental setup. With an applied electric field or a poled specimen, the scattering at a particular 2θ corresponding to relevant peaks is measured as a function of azimuthal angle Ψ.

In a tetragonal material the integrated intensity ratio of (002) to (200) is expected to be approximately 1:2 due to the multiplicity of (200) (including (020) peak). Similarly, in a rhombohedral material the ratio of (111) to ($\bar{1}$11) is approximately 1:3 as ($\bar{1}$11) also

includes $(1\bar{1}1)$ and $(11\bar{1})$. Due to the differences in the structure factor of different lattice planes however, the peak intensities do not fit these exact ratios. These peak ratios hold true when there is no anisotropy in the material and there is a randomised orientation of polycrystalline grains. When an electric field is applied, domain reorientation occurs. In the tetragonal example, a greater quantity of domains will become aligned to the electric field direction resulting in an increase in the contribution of (002) in turn decreasing (200) contribution parallel to the field, and vice versa perpendicular to the field. This is observed as a change in the peak ratios, illustrated in **Figure 1.29** for PZT showing the exchange of peak intensity as a function of electric field (a) and directional dependence (b).
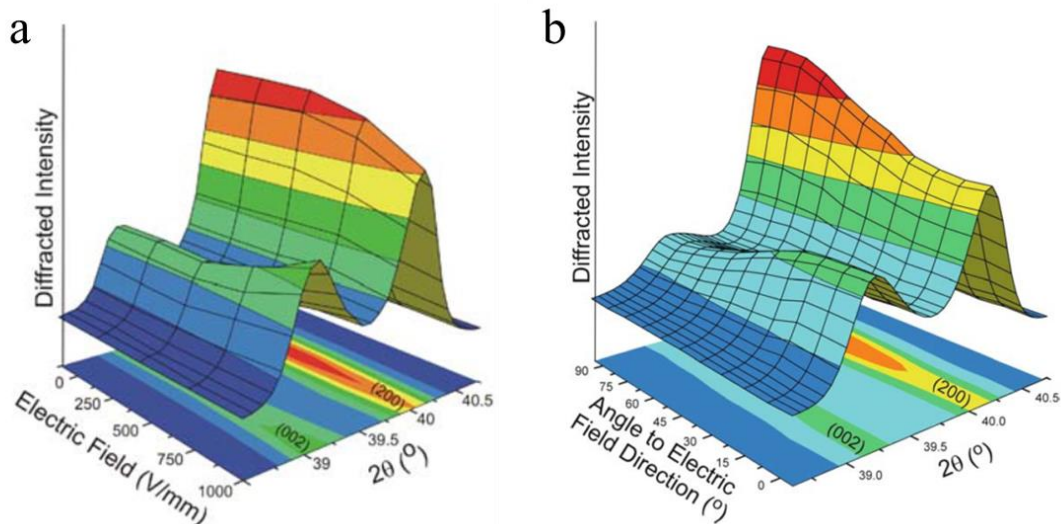
Figure 1.29 PZT (002/200) peaks as function of a) electric field magnitude (parallel to the electric field direction), and b) angle to electric field direction (at maximum field). From [23], [24].

This behaviour can be quantified in order to determine the fraction of reoriented domains, shown in **Equation 1.18** for tetragonal domains [25]. This is shown for PZT ceramic in **Figure 1.30** [26]. The dotted line represents a R(002) value of 1/3 expected of an unpoled material. Throughout the literature this ratio is shown to follow a $\cos^2$ trend, and several studies modelling this behaviour have indeed shown this relationship [19], [20], [26], [27].

Equation 1.18

$$R(002) = \frac{I(002)}{I(002) + I(200) + I(020)} \propto cos^2 \Psi$$
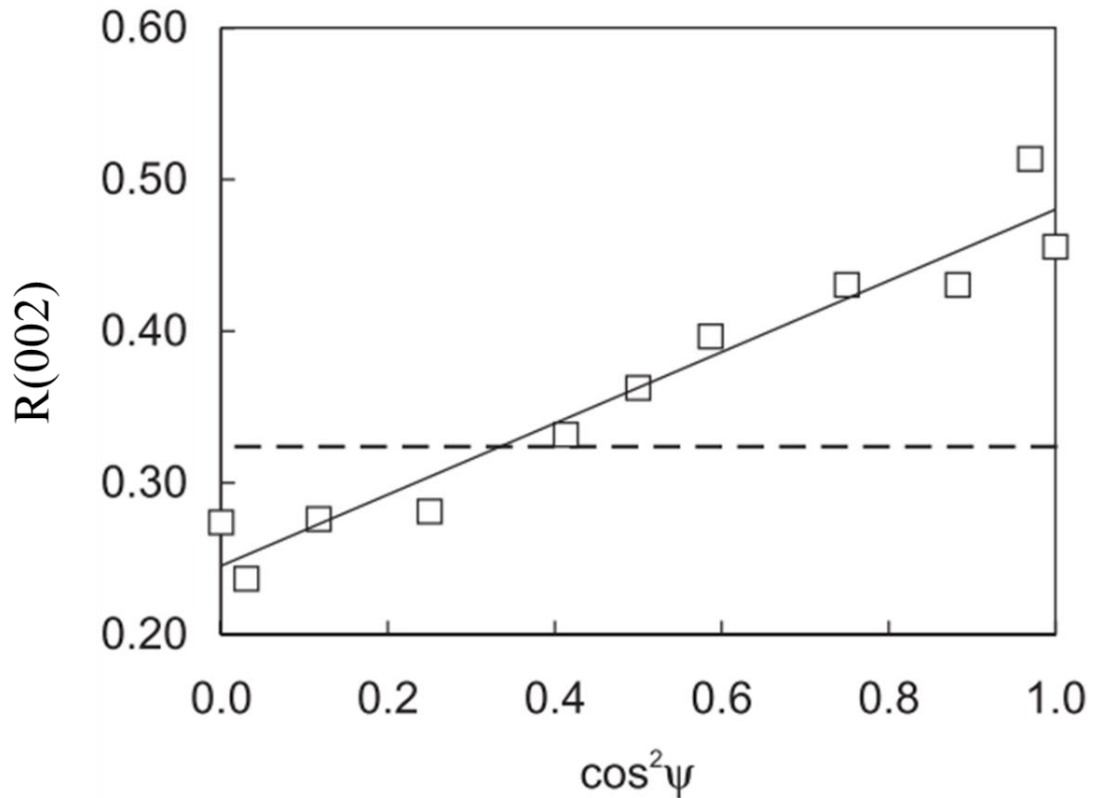
Figure 1.30 $R(002)$ of a poled PZT ceramic as a function of azimuthal angle Ψ which follows a cosine^2 trend. From [26]. The dashed line corresponds to $R(002) = 1/3$ representing unpoled values (1:2 peak ratio).

1.12 Morphotropic phase boundary

The definition of a morphotropic phase boundary (MPB) has changed over time. Initially it was the name given to a solid solution where a compositional phase transition which is temperature independent is observed [28]. Typically, piezoelectric properties (e.g. the d coefficient) are significantly higher at compositions at or around the MPB [28]. This prompted extensive investigation into its properties and it is still one of the principal subjects of interest when developing novel solid solutions.

Later, the requirement for temperature independence was less of a definite requirement, as several materials displaying improved properties at phase transitions did not display it, for example $(1-x)Ba(Ti_{0.8}Zr_{0.2})O_3 - x(Ba_{0.7}Ca_{0.3})TiO_3$ where the MPB varied from $x = 0.35$ to 0.55 in the $0 - 50\,°C$ temperature range [29]. Instead it was defined as a compositional transition between a rhombohedral and tetragonal structure as observed in PZT [30] where improved piezoelectric properties alone are observed. The term appears to have been generalised to a phase transition where improved properties are observed.

The reasoning for the improved properties is as follows: Two or more end members in a solid solution have different phases e.g. rhombohedral (R) and tetragonal (T). At some composition (the MPB), a transition from one to the other will occur, and at this point there is a coexistence between R and T phases. This provides a greater number of polarisation directions than R (8) or T (6) alone, and therefore polarisation is achieved with greater ease, i.e. the same can be achieved with a lower field and therefore the d coefficient increases.

More recently the most significant divergence from the standard definition of an MPB is in the changes in structure. Most significantly in many systems it has been shown that rather than a discrete boundary between two phases a gradual transition takes place, whose extent is greatly dependent on the material [31]. A more accurate term would be a morphotropic phase region (MPR). One of the more notable examples is lead zirconate titanate (PZT), whose MPB has previously been widely regarded to be a boundary between R and T [28]. The current established understanding however is that a monoclinic phase exists at the MPB acting as a lower symmetry parent structure to R and T [32] providing increased piezoelectric activity via the rotation of the polar axis in the monoclinic plane [33]. Further studies expand on this by suggesting the monoclinic structure is locally prevalent across the phase diagram becoming macroscopic at the MPB [34].

1.13 Average and local structure

At this point it is pertinent to introduce the importance of length-scale, both spatially and temporally, over which a structure is measured and described. The distinction and interaction between average and local structure is particularly crucial.

These terms are not specifically defined as their respective length-scales are dependent on the material. Additionally, it is not possible to refer to one without the other. Local structure describes the length-scale at which deviations or distortions away from the average or macroscopic structure begin to emerge. For example, at the unit-cell length scale a 'cubic' material may display a distorted local structure due to the chemical disorder creating a varying bonding environment. At greater length scales, however these distortions are smeared or averaged out. The point at which this occurs is dependent on the degree of distortion and the correlation of the distortion.

The structure of a hypothetical perfect crystal without any thermal atomic fluctuations can be exactly described by a few coordinates and some symmetry operations. Realistically however, all atoms have thermal energy, oscillating about a point (with a frequency around 10^{13} Hz and 10^{-11} m amplitude), which is to say at any given point in time an assemblage or a crystal of atoms would not be aligned in a perfect array but instead be slightly off the coordinate positions. Conventional structural characterisation techniques such as lab-based X-ray diffraction (XRD) measure over a period of minutes, lacking the temporal resolution to observe these effects. Therefore, the measurement would represent time-*averaged* structure.

The same can be said for spatial ordering, or the coherence length i.e. the distance over which atoms are ordered, can be of the order of nanometres in some materials. If the measurement probe is too large (e.g. a millimetre sized X-ray beam) these local differences would be obscured and measured instead as the collective average. In this case, there would be a disparity between the local and average structure. The local deviations from the average structure produce a diffuse and weak intensity diffraction signal due to their small coherence length and general disorder. Conventional data analysis techniques may overlook the diffuse signal, instead focusing on the strong diffraction peaks arising from the long-range spatially-*averaged* structure. However, novel methods such as total scattering analysis enable the measurement and interpretation of the diffuse signal to produce a description of the local structure.

A clear example of this disparity can be observed in the measurements of the Si-O bond distance in silica as it undergoes a phase transition from α-quartz to β-quartz **Figure 1.31** [35]. Distance measurements from Rietveld refinement of neutron powder diffraction (i.e. average structure measurements) show the bond distance initially at 1.612 Å, decreasing with temperature and abruptly changing to 1.587 Å at 850 K during the phase transition. This is in stark contrast to measurements obtained by the total-scattering analysis of the same neutron diffraction data, which also considers the diffuse scattering arising from crystalline disorder. It shows a general increase in bond distance due to thermal expansion. The illustration in **Figure 1.32** [35] demonstrates that the fluctuations of the Si-O bond produces a distribution of positions which are averaged out to produce an apparent shorter bond. With increasing temperature, the fluctuations increase causing the average distance to decrease.

The concept of average and local structure is a key theme in this work and will form an important part of the discussion of the current literature (Section 1.14). It is necessary to briefly introduce the concept of 'pseudosymmetry'. This is used to describe the *apparent* crystal structure, particularly when measured with techniques which only describe the average structure. A more specific term used is 'pseudocubic' used to refer to the structure of a ferroelectric perovskite which displays an apparent cubic structure. This is necessarily incorrect as ferroelectricity by definition requires a non-cubic structure. This is envisaged as small locally correlated distortions which may be rhombohedral, for example a rhombohedral angle very close to 90°.
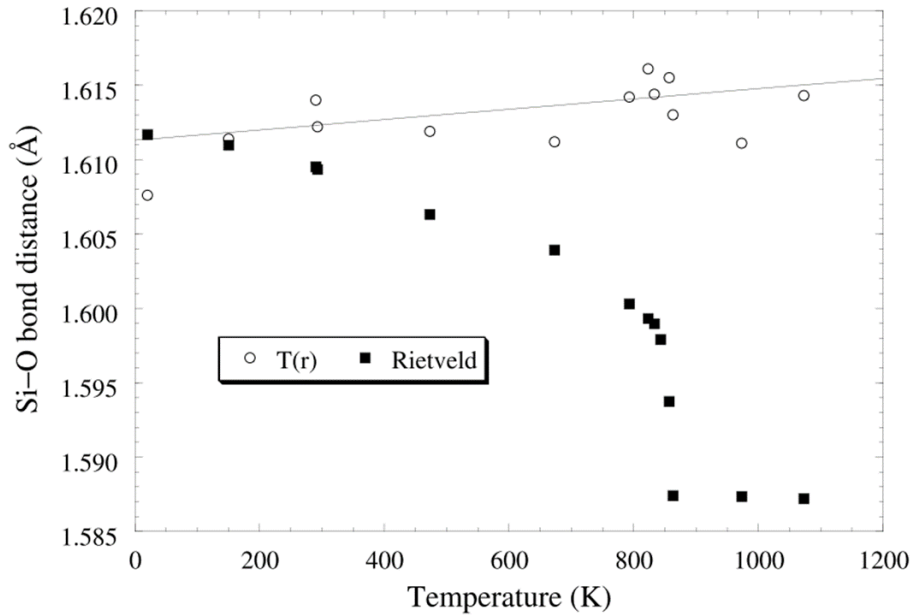
Figure 1.31 Measurements of the Si-O bond distance in silica as a function of temperature as measured by Rietveld refinement of neutron powder diffraction and neutron total-scattering (T(r)). A transition from α-quartz to β-quartz occurs around 850 K. From [35].
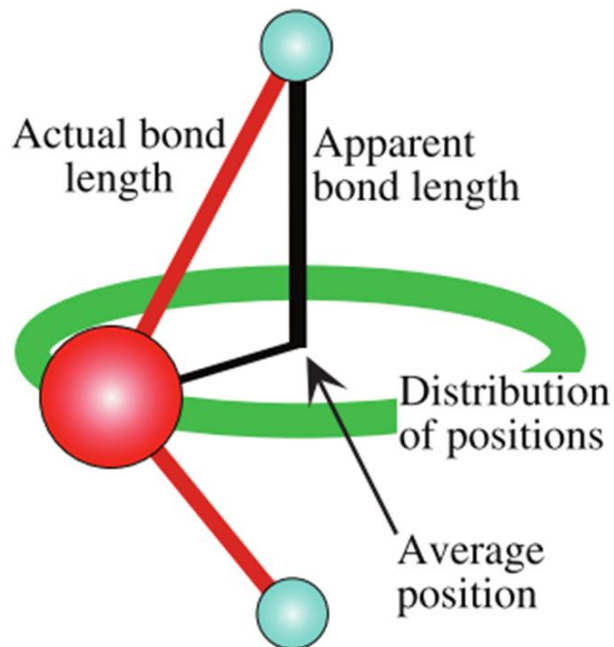
Figure 1.32 Illustration of the Si-O bond in silica whereby the local distortions of the bond produces a distribution of positions which average to an apparent bond length starkly different from the actual length. From [36].

1.13.1 Relaxor-ferroelectrics

Features such as structural disorder in many cases stem from chemical disorder arising in materials with multiple A or B-site species. These are not uniformly distributed across the entire material but instead form nano-scaled regions of chemical uniformity, which have been labelled as polar nano regions (PNRs). These features in ferroelectric materials has led to a classification of such disordered materials as relaxor-ferroelectrics [37].

As previously discussed (Section 1.9.1) the transition from paraelectric to ferroelectric produces a highly defined permittivity peak associated with a temperature at which the energy within the system is enough to allow facile polarizability i.e. high permittivity, yet not high enough to produce vibrations which overcome the polarisation inducing oscillating voltage. In this case the material can be said to exhibit 'classical' ferroelectric behaviour.

In a relaxor however, this transition is significantly different. As well as possessing chemical and structural disorder several further characteristics are used to define a relaxor [38], which are: a) The permittivity peak becomes broad and prohibits accurate placement of the Curie temperature. Often the transition permittivity maxima T_m is used to denote the paraelectric transition rather than the conventional Curie point T_C. b) The broad peak becomes frequency dependent in both its position in temperature and its maximum value, also termed frequency dispersion. A prototypical relaxor-ferroelectric is lead magnesium niobate (PMN), shown in **Figure 1.33** [39] for $Pb(Mg_{1/3}Nb_{2/3})O_3$ (Mg^{2+} and Nb^{5+} share the B-site) where the relaxor characteristics are readily apparent.
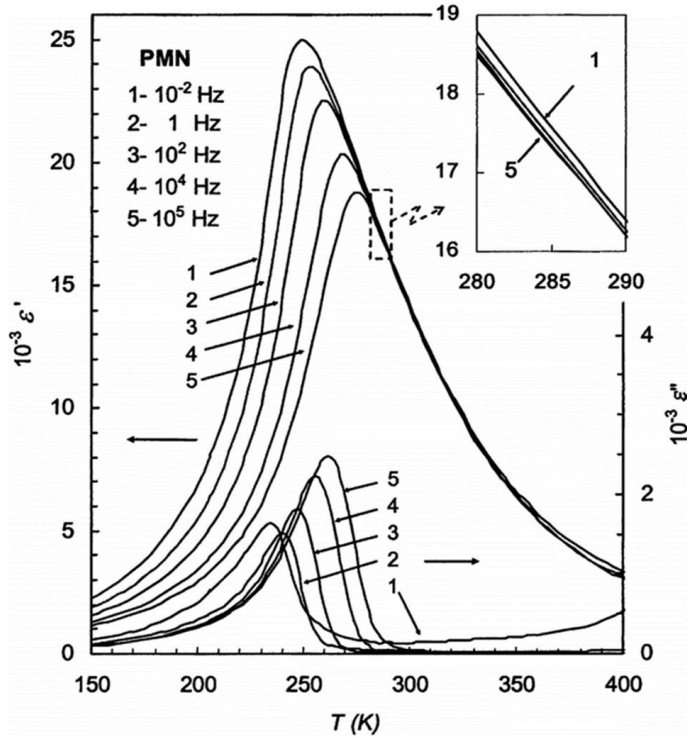
Figure 1.33 Temperature dependent permittivity components in relaxor-ferroelectric Pb(Mg$_{1/3}$ Nb$_{2/3}$)O$_3$ displaying characteristic behaviour in the paraelectric to ferroelectric transition namely a broad and frequency dispersive peak. From [39].

Several models have been proposed to explain this behaviour, all generally relying on the existence of polar nano regions (PNRs) or small volumes of structural and chemical coherence [40]. The Somlenskii model [41] suggests that the mixed B-site in PMN for example is not evenly distributed, producing small chemically ordered regions which are more polar than others. These regions will have different varying responses to an applied electric field depending on their composition and therefore the transition is spread out over a range of temperatures. Additionally, the variation in site species, and the PNR size will experience a variation in the frequency response and therefore produce the observed dispersion [42].

The currently accepted consensus is that PNRs exist above the conventional Curie point in relaxor materials and act as nucleation points for the formation of ferroelectric order below T$_C$. **Figure 1.34** shows a simulated model of PNR clusters of polar coherence existing within a largely disordered matrix [43]. These can persist below the T$_m$, to which the disordered nature of some materials is attributed. Studies have shown that long range ferroelectric order can be induced by prior poling by application of an electric field or

applied pressure [42], [44], [45]. **Figure 1.35** [45] illustrates this behaviour by the transition from a gradual to a discontinuous change in the permittivity, characteristic of classical ferroelectric behaviour.
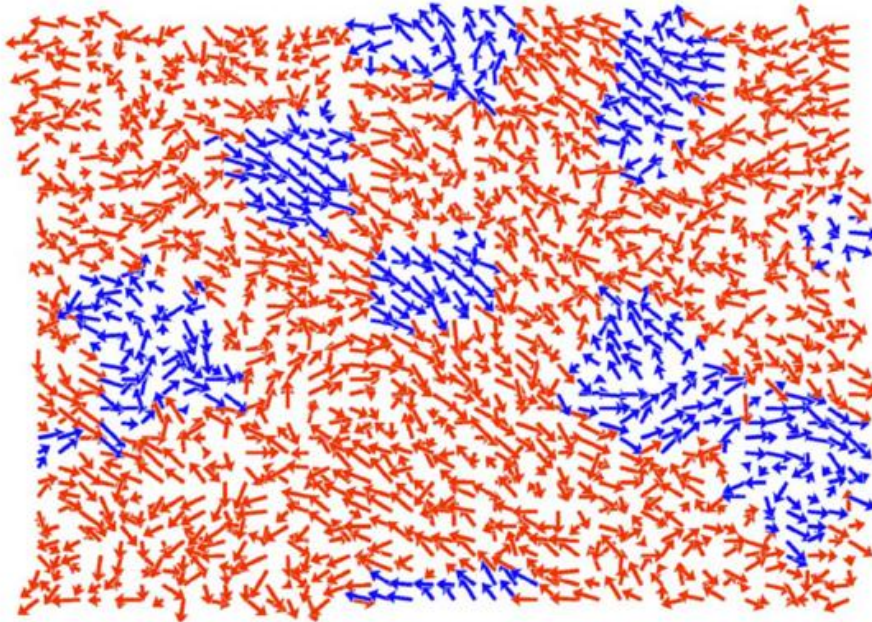
Figure 1.34 Simulation of PNRs as clusters of coherence (blue arrows) within a disordered matrix (red arrows). From [43].
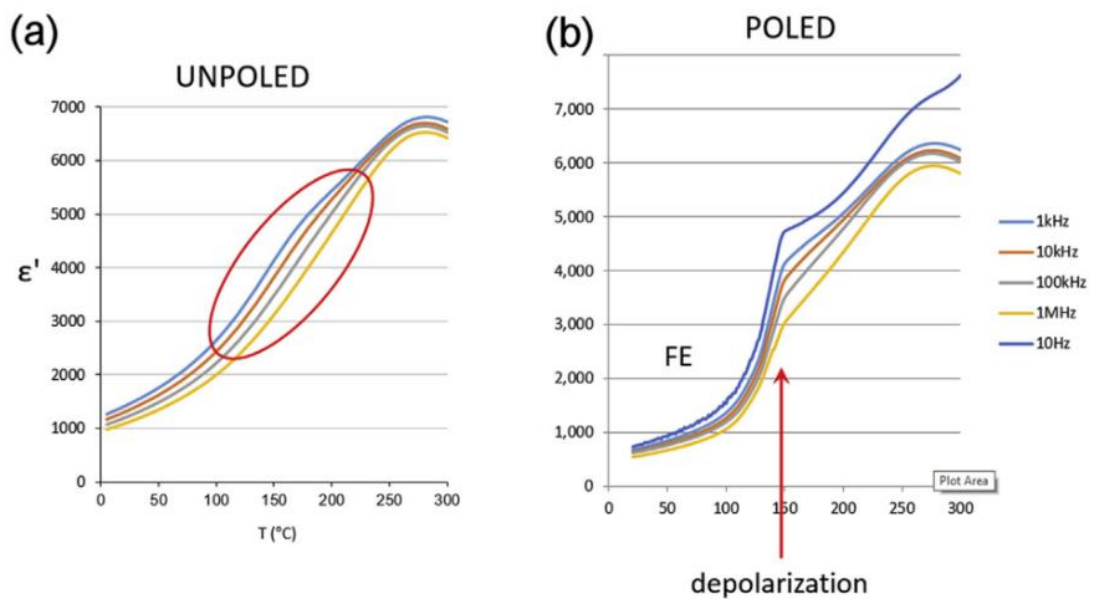
Figure 1.35 Permittivity of KNBT for unpoled and poled samples. Upon poling the relaxor like behaviour appears to more closely resemble classic ferroelectric behaviour from the discontinuity in the phase transition highlighted by the red ellipse. From [45].

1.14 Materials literature

The following section will examine specific piezoelectric materials for their historical and scientific significance, as well as discussing the materials studied in this work.

1.14.1 BaTiO$_3$

Barium titanate has been labelled the 'prototype ferroelectric' [16][1] as it is the first ferroelectric material to be widely used, whose characteristic properties largely define this material class. For example, the Curie point transition exhibits classic ferroelectric behaviour in its permittivity (Section 0) strongly following the Curie-Weiss law (Section 1.8.2). It was first discovered in 1945, and shown to exhibit far superior ferroelectric and piezoelectric properties to materials such as Rochelle salt [46], [47]. It exhibits a d_{33} around 190 pC/N [48] but suffers a relatively low T_C of 120 – 130 °C [49]. Though its piezoelectric properties were eventually superseded by materials containing PbTiO$_3$ such as Pb(Zr, Ti)O$_3$ (Section 1.14.3), it still one of the most used materials in capacitor applications due to its dielectric properties [4].

Several temperature dependent phase transitions have been observed (shown in Section 1.8.3), however, the nature of these transitions have been debated over several decades. Conflicts have arisen between theories of displacive transitions [49], [50], and order-disorder transitions [51], [52], all primarily supported by diffraction and spectroscopy techniques. Displacive transitions are characterised by displacement of the Ti^{4+} ion relative to the oxygen octahedra cage along the relevant polarisation direction for the given structure, shown in **Figure 1.24.** Order-disorder transitions are characterised by the interaction between local and average order. Local order regions which deviate from the average combine to produce the structures observed macroscopically. Neutron pair distribution function (PDF) studies (**Figure 1.36**) which examine structures at the nanoscale have shown that the local structure changes very little as a function of temperature, displaying a predominant rhombohedral distortion [53]. The PDF analysis technique is covered in depth in Section 2.3.
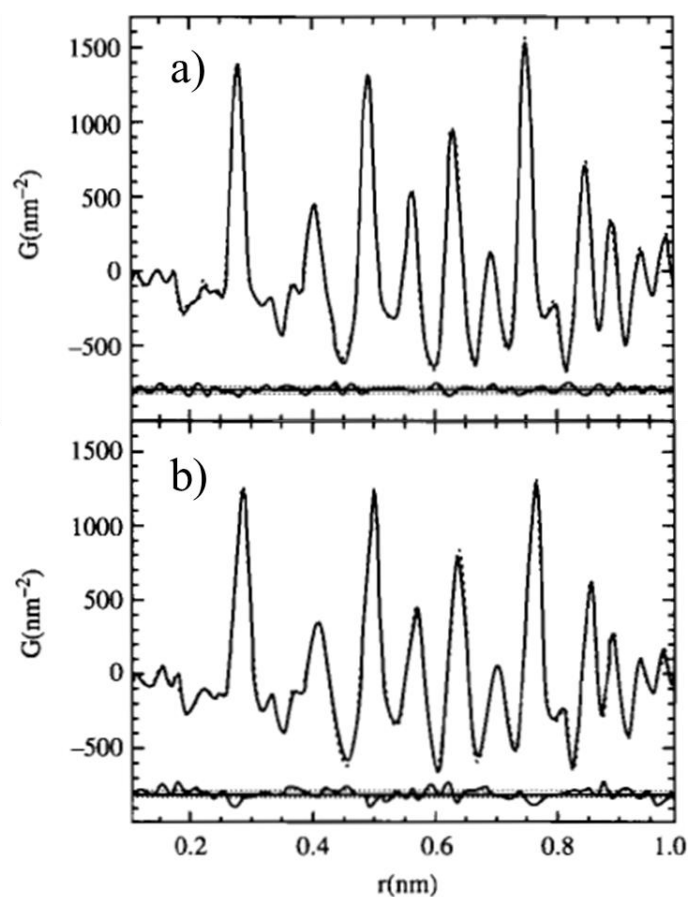
Figure 1.36 Neutron pair distribution function (PDF) data for a) rhombohedral and b) orthorhombic phases of BaTiO₃ illustrating the negligible local structural differences. From [53].

More recent studies strongly support the order-disorder theory using a combination of PDF analysis and Monte Carlo modelling. They show local Ti displacements occur along the rhombohedral ⟨111⟩ across all phases [5]. **Figure 1.37** (a) – (d) show how the polymorphic phase transitions emerge from a series of local transitions and disruptions of the long range rhombohedral order along various directions. A super cell contains a $5 \times 5 \times 5$ unit cells with a ⟨111⟩ polarisation vector. The white and black arrows illustrate the respective polarisation vector component for a given orthogonal direction. Bellow each diagram is the representative calculated diffraction pattern which illustrates the formation of diffuse scattering streaks from the disruption of the ordered rhombohedral state along various axes.

At low temperatures (a) the polarisation vectors are ordered in all axes, producing a macroscopic rhombohedral ⟨111⟩ polarisation. As the temperature increases (b) the disorder first increases along a single axis, producing a macroscopic orthorhombic phase with a lower average polarisation as some of the polarisation cancel out. With increasing

temperature (c) an additional polarisation axis becomes disordered, reducing the polarisation further and producing a macroscopic tetragonal phase. Finally (d), all axes become disordered resulting in a zero net polarisation and a cubic phase. Throughout these transitions the local ⟨111⟩ polarisation is maintained and can be observed as diffuse streaks in the diffraction patterns. These findings show that local scale phenomena can give rise to a rich variety of larger scale properties.
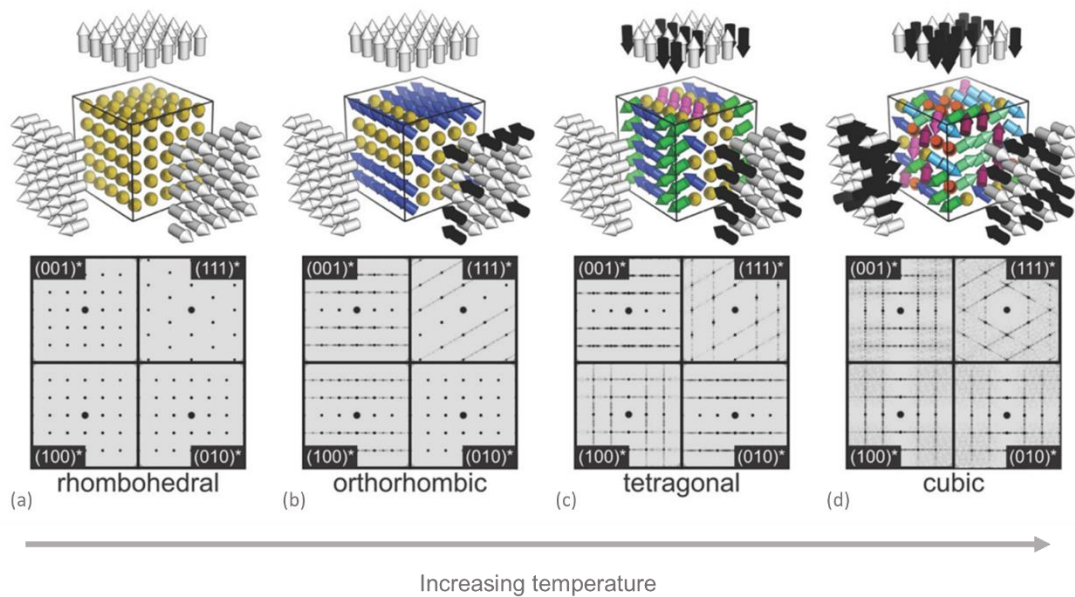
Figure 1.37 Local rhombohedral distortions. The white and black arrows indicate the polarisation vector for a given row. The arrows inside the box point in the direction of the summation of the white and black arrow vectors (a) – (d). From [5].

1.14.2 PbTiO$_3$

Lead titanate is structurally analogous to barium titanate with lead replacing barium on the A-site. At face value, it displays superior properties to BaTiO$_3$ such as a far higher Curie point ($\approx$ 490 °C vs $\approx$ 125 °C) and tripling in the single unit cell spontaneous polarisation (75 μC/cm^2 vs 25 μC/cm^2) [2]. These relatively extreme properties can be evidenced by the highly strained tetragonal structure with a spontaneous strain of 6%, shown in **Figure 1.38**, and are primarily produced by the displacement of the lead ion.

Lead cations experience hybridisation of the *6s* and *6p* orbitals, producing a polarisation of the outer core-electrons which in turn gives the atom an 'asymmetric'

structure, i.e. its ionic radius is much smaller on one side [54]. This permits a greater hybridisation between Pb^{+2} and O^{-2}, and Ti^{+4} and O^{-2} [55] producing stronger bonding with certain surrounding oxygen ions (depicted in **Figure 1.39**), producing a significant distortion and ferroelectric properties.
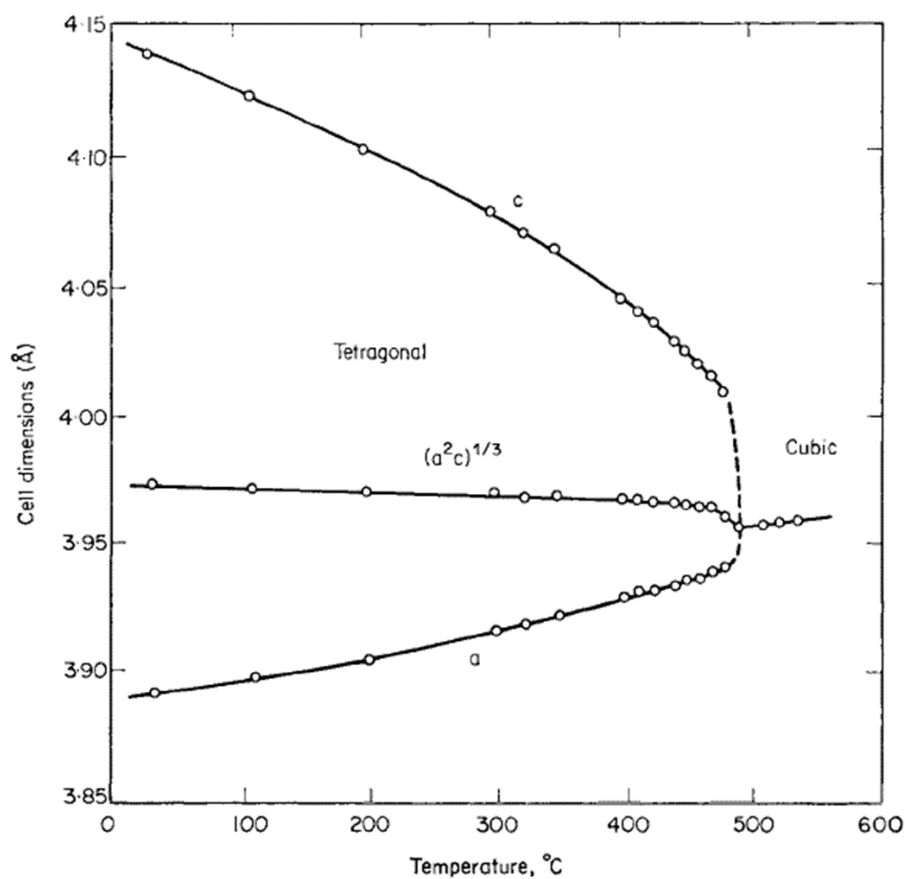
Figure 1.38 X-ray diffraction of cell parameters in PbTiO$_3$ as a function of temperature. Cooling through T$_c$ at 490 °C produces an abrupt onset of tetragonal strain. From [56].
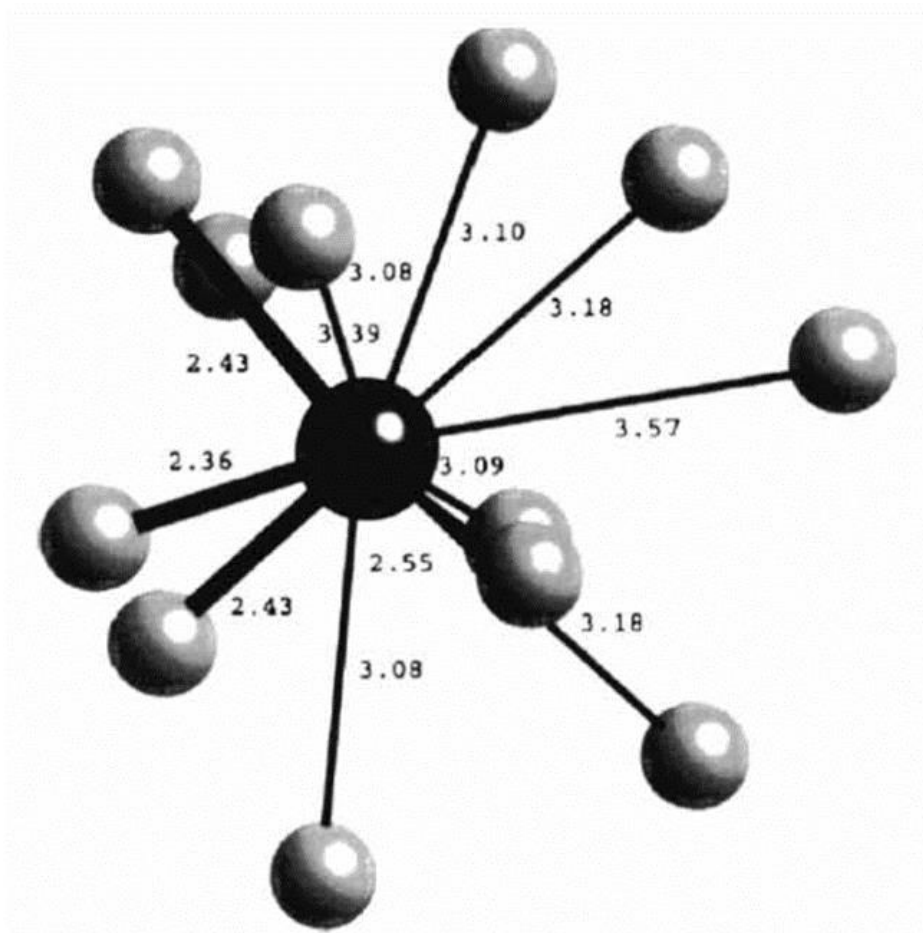
Figure 1.39 AO$_{12}$ cluster of Pb in PbTiO$_3$ showing the significant asymmetry in Pb-O distances producing a distortion. From [52].

Although it is apparent that lead imparts several ideal properties to the material, several practical problems are created. Namely, producing pure PbTiO$_3$ is not trivial due to the large strains in the structure, resulting in grain fractures and material degradation during processing.

1.14.3 Pb(Zr, Ti)O$_3$

Lead zirconate titanate (PZT) is a solid solution between tetragonal PbTiO$_3$ and rhombohedral PbZrO$_3$ giving Pb(Zr$_x$, Ti$_{1-x}$)O$_3$, first created in 1953 by E. Sawaguchi [57]. It has since become the most widely used piezoelectric material, surpassing the previously used barium titanate due to its highly favourable properties, namely greater piezoelectric coefficient, higher T$_c$ and therefore a higher operating temperature, and the variability of properties it offers by the addition of various dopants [1], [7]. This is owed primarily to

the existence of the morphotropic phase boundary (MPB) previously discussed in Section 1.12 that has been a topic of great debate in this system. In PZT the MPB occurs around $x = 0.48$ [28] above which the structure transitions from rhombohedral (R) to tetragonal (T). Here Jaffe defines this transition as discrete, where both phases coexist, shown in **Figure 1.40** [2]. However, this interpretation would eventually be superseded by novel discoveries. The improved properties were explained via the greater availability of polarisation directions.

Noheda *et al.* drastically changed the understanding of the MPB in 1999 with the discovery of a monoclinic ferroelectric phase spanning x = 0.46 – 0.51 using high resolution synchrotron X-ray powder diffraction [32], later supported by neutron diffraction [58]. At ambient temperatures a mixed phase is reported where local monoclinic distortions exist, condensing into the macroscopic phase upon cooling [59], shown in the updated phase diagram in **Figure 1.41** [60]. Further neutron diffraction studies show that the atomic displacement parameters obtained during structure refinement were unreasonably large in directions other than the polar R and T directions, thereby requiring a more complex displacement i.e. monoclinic, for a reasonable refinement [61].

These findings suggest the monoclinic phase acts as an intermediate phase between R and T and as an effective lower-symmetry 'parent' phase (Cm is a sub-group of both *R3m* and *P4mm*) thereby facilitating the transition. Thermodynamic modelling via free energy calculations has also shown this behaviour can occur by the coupling of the two end member polarisation vectors (R [111] and T [001]) [62], suggesting a far broader monoclinic phase region encroaching further into the neighbouring rhombohedral and tetragonal phase boundaries. X-ray absorption fine structure (XAFS) measurements further support this, showing that local Ti off-centre displacements rotate from [111] to [001] via the monoclinic ($\bar{1}$10) plane [63]. *In situ* XRD measurements with applied electric field show the stabilisation of the monoclinic phase under an electric field rather than one of the polar rhombohedral or tetragonal directions. [59]. In this updated understanding of PZT, the improved properties at the MPB emerge from the monoclinic phase enabling polarisation rotation.
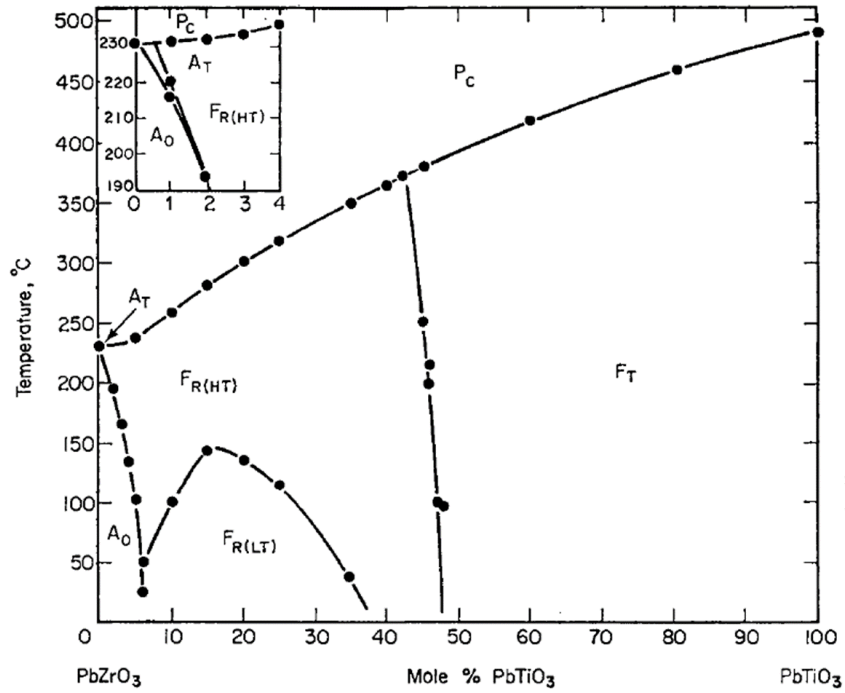
Figure 1.40 Phase diagram of PZT showing a discrete rhombohedral-tetragonal transition at 48% mol PbTiO$_3$. From [2].
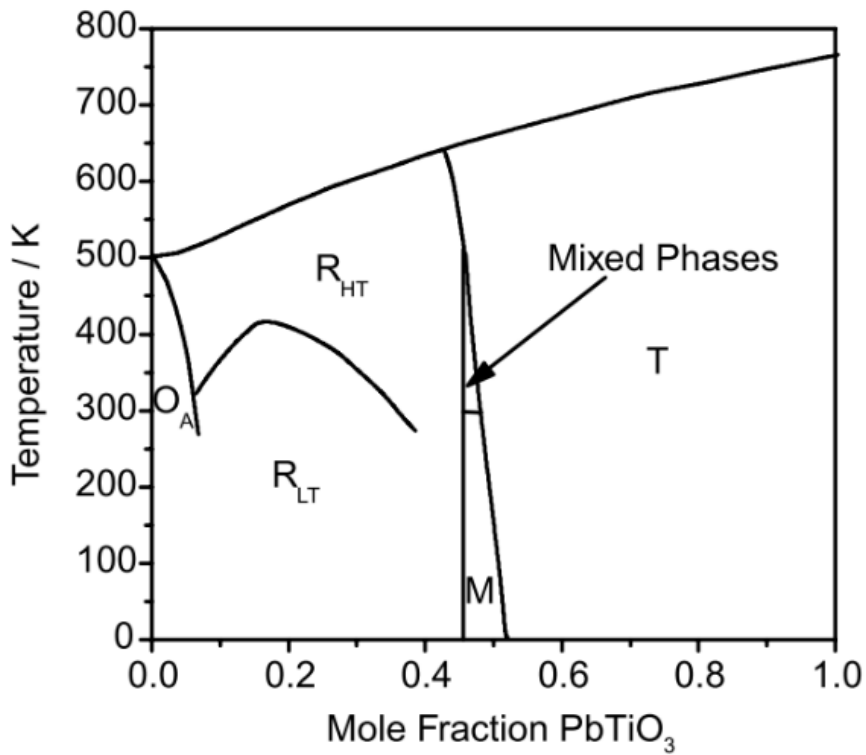
Figure 1.41 PZT phase diagram from Jaffe *et al.* updated to show the monoclinic structure discovered by Noheda *et al.* [32] in [60]. It is present at a MPB, that extends over a range, becoming mixed phase at higher temperatures.

The description of the structure of PZT would further change in 2004 when Glazer *et al.* used electron diffraction studies to suggest that the local monoclinic distortions of Pb persist throughout the entire phase diagram of PZT, and whose coherence length becomes macroscopic at the MPB [34]. This effectively forgoes the presence of any discrete transitions. Here the improved properties are suggested to arise from the long-range monoclinic order at the MPB, rather than polarisation rotation alone, as the peaks observed in piezoelectric coefficients and relative permittivity would have to be considerably sharper for the latter. Neutron diffraction studies suggest the behaviour is temporal rather than spatial i.e. fluctuations of Pb displacements are monoclinic at any given point which become 'frozen' at the MPB [61]. Theoretical approximations support the polarisation rotation theory of improved properties due to macroscopic monoclinic phase reducing the energy requirement for polar alignment [60]. Studies combining high resolution XRD and TEM [64] further support the rotation model suggesting that at the MPB domains become nanoscaled, are more flexible and have lower domain wall energies allowing the formation of long range order under an applied electric field.

In more recent neutron PDF studies monoclinic phases (M_A and M_B) are identified on the rhombohedral side of the MPB with a transition from M_B to M_A as the MPB is approached [6], where M_A offers greater deviation of Pb and therefore offers greater piezoelectric properties. Further TEM studies have even suggested that perhaps symmetries lower than monoclinic *Cm* may be present [31].

The understanding of the structure of PZT, namely at the MPB, has been continuously evolving over the past 60 years. As with $BaTiO_3$ many of the properties which were first observed in the 1950s have been observed to be directly related to the local dynamics of the atomic structure, revealed only by the use of more sophisticated experimental and analytical techniques that focus more on local structure.

1.14.4 (Na, Bi)TiO₃

Sodium bismuth titanate ($Na_{0.5}Bi_{0.5}$)TiO₃ (NBT) is a thoroughly studied material having formed the basis of many piezoelectric materials in the ongoing search for an alternative to Pb-based materials, both due to its elusive structure and ability to form several binary and ternary solid solutions with a variety of desirable properties [4], [65], [66]. It also boasts a relatively high remnant polarisation of 38 $\mu C/cm^2$, though it suffers

a low depolarisation temperature of less than 200 °C, as it becomes antiferroelectric, and has a low $d_{33} \approx 70$ pC/N [67]–[69].

First reported as a rhombohedral ferroelectric perovskite in 1961 [70], it was characterised by its unusual electrical and structural properties such as broad and frequency dispersed permittivity peaks, and diffuse temperature dependent phase transitions [67], [71], [72]. These properties are characteristic of relaxor materials (Section 0) and are associated with the presence of structural ambiguity and nano-scaled ordering and/or domains [37], [73], [74].

The greater sensitivity of neutron diffraction techniques over XRD to oxygen position prompted a Rietveld analysis study [75], exposing the complex phase transitions, primarily mediated by changes in octahedral tilting combined with A and B off-centre distortions. Shown in **Figure 1.42** [75] are the broad temperature ranges across which phase coexistence occurs. The rhombohedral to tetragonal transition commences around 250 °C and is particularly broad with a transition range exceeding 100 °C, whilst the tetragonal to cubic transition occurs around 500 °C, with a smaller 20 °C transition range. The depolarization temperature around 190 °C would conventionally be expected to coincide with a structural transition, however the rhombohedral-tetragonal phase transition begins around 250 °C. This discrepancy is thought to emerge from the decrease in the volume fraction of the monoclinic phase with increasing temperature. This in turn results in loss of long range ferroelectric order which subsequently gives rise to the antiferroelectric tetragonal structure [76].
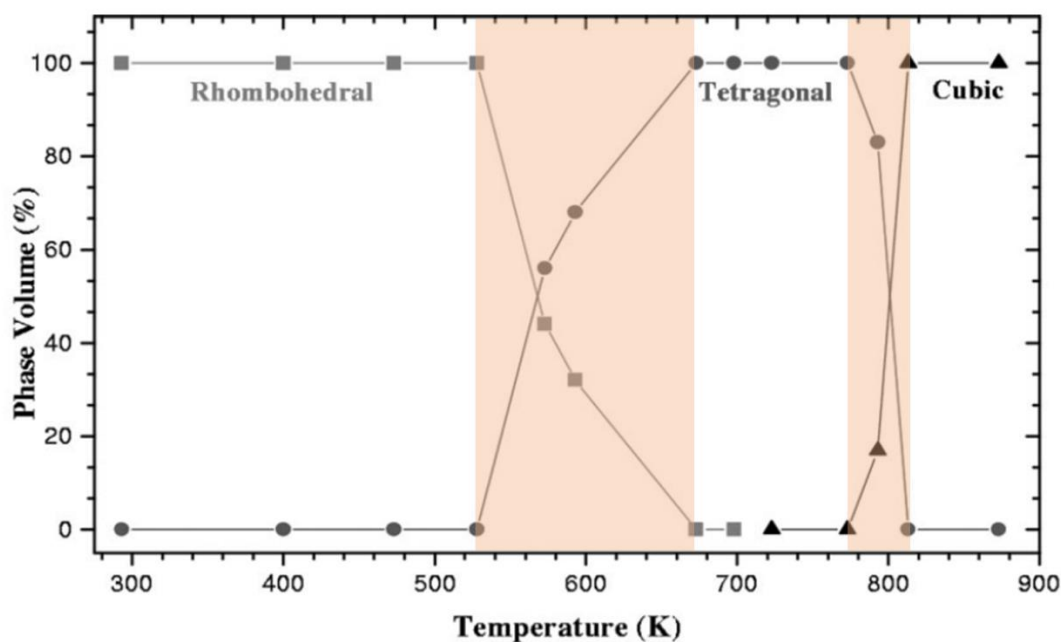
Figure 1.42 Phase volume obtained from neutron diffraction measurements by [75]. Regions highlighted in orange show the extended temperature range of the phase transitions.

Dorcet and Trolliard carried out extensive TEM studies focusing on the octahedral tilting during phase transitions [77], [78]. In a pure rhombohedral state the tilting is ordered and of the rhombohedral class. Within the matrix however, there are small regions or 'sheets' of tetragonal tilting between the rhombohedral tilting. As temperatures approach the tetragonal phase transition the rhombohedral tilts become increasingly disordered, i.e. individually correlated rhombohedral tilting regions become smaller, and therefore the tetragonal boundary regions grow [79]. With an increase in temperature the tetragonal tilt regions gradually encompass the entire structure. During this process, an anti-polar arrangement is induced producing the observed antiferroelectric state [67], [77]. Upon further heating the octahedral tilting experiences more tetragonal transitions, finally adopting a non-polar paraelectric state [78].

In the same manner as $BaTiO_3$ and PZT, the structure of NBT has been further investigated by more sophisticated experimental methods and subsequently redefined. High resolution X-ray synchrotron experiments on single crystal and polycrystalline NBT have defined the room temperature phase as monoclinic rather than rhombohedral; revealed by careful observation of subtle X-ray diffraction peaks, otherwise obscured in lower-resolution experiments [76], [80]. This was further supported by optical

birefringence studies [81]. Other studies suggest there is a room temperature monoclinic and rhombohedral ferroelectric phase coexistence, which can be forced into a single rhombohedral phase by external stimuli such as mechanical stress or an applied electric field [82].

Studies focusing more closely on the local structure have shown further diversion from the established structure. TEM studies describe the structure of NBT by a continuous octahedral tilt model with local scale in-phase tilts which are coherent over a few perovskite unit cells within an anti-phase tilt average structure, producing a pseudorhombohedral structure [83]. These nano-domains can also result in the average monoclinic symmetry shown by XRD. Neutron pair distribution (PDF) investigations have further elucidated the highly complex structure. A-site chemical disorder is shown to affect the structure by introducing two independent Bi distortions along the monoclinic plane between two $\langle 111 \rangle$ displacements, owing to the energy similarity between the distortions and the difference in Na and Bi ionic charges, shown in **Figure 1.43** [84]. Additionally there is a significant difference between the Na and Bi bonding environments, namely Bi is far more distorted than observed in the average structure [85]; suggested to arise from Bi attempting to achieve a bond valence sum (BVS) close to its oxidation state and accommodating its electron lone pairs.
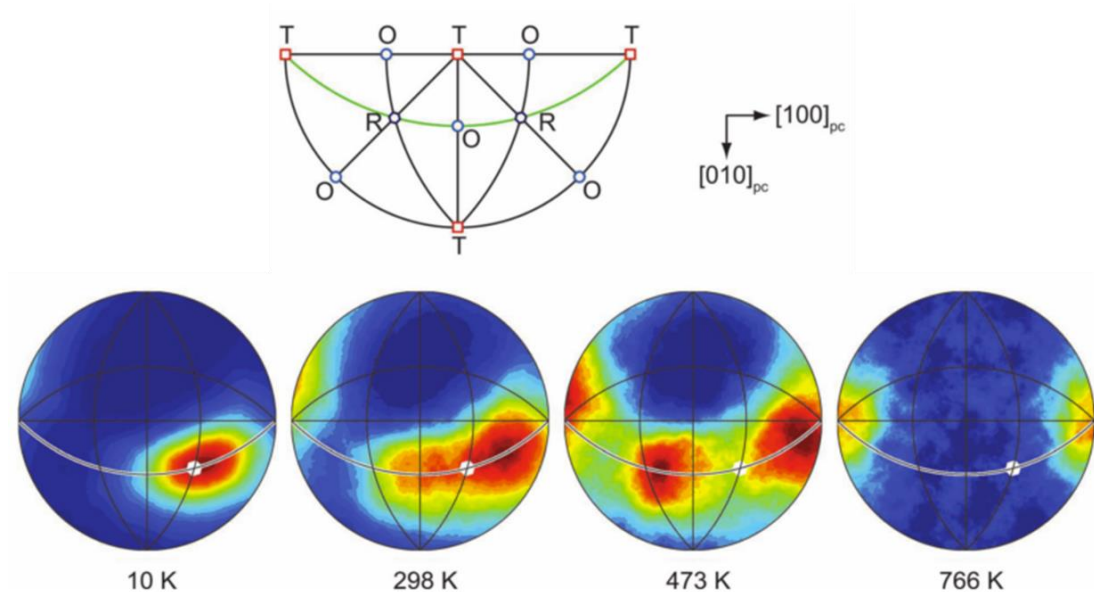
Figure 1.43 Stereographic projection of local Bi displacement directions in NBT as a function of temperature. As the temperature increases from 10 K the single Bi displacement in the rhombohedral direction bifurcates along the monoclinic plane (green line) resulting in coexisting discrete displacement directions. From. [84].

1.14.5 (Na, Bi)TiO₃ - (K, Bi)TiO₃

Potassium bismuth titanate (KBT) is a tetragonal material [86], able to form a solid solution with NBT forming $(K_x, Na_{1-x})Bi_{0.5}TiO_3$. A simpler nomenclature is KNBTx^*, where $x^* = 100x$. It has attracted interest as a potential lead-free piezoelectric material due to its promising properties at the MPB between rhombohedral (R3c) and tetragonal (P4mm) phases [87]. Shown in **Figure 1.44** [88] is the commonly accepted phase diagram of the average structure of KNBT. The transition to cubic is reported around 300 °C, however KNBT suffers a significantly lower depolarisation temperature around 130 °C which significantly impacts the maximum operating temperature.

The structure of KNBT has been reported as early as 1962 [89] though it is only in the last couple of decades that it has been thoroughly studied [45], [88], [90]–[92].
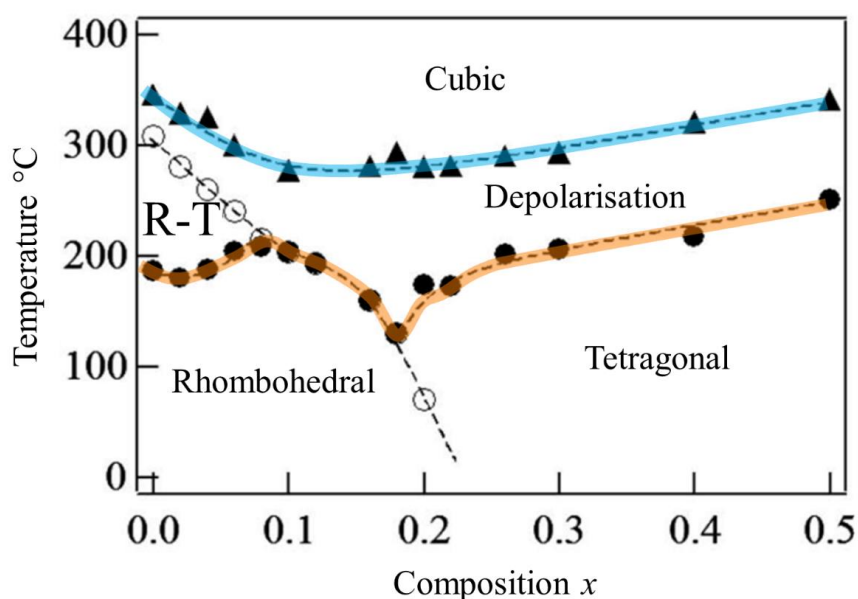
Figure 1.44 Phase diagram of KNBT from [93]. The depolarisation transition and ferroelectric-paraelectric transitions are shown in orange and blue respectively.

1.14.5.1 The structure of KNBT

To realise its piezoelectric potential, the compositional location of the MPB has to be precisely defined. This has not been trivial as the structurally disordered nature of the NBT end member is significant. Some studies suggest the MPB ranges from $x = 0.16$

– 0.20 [94], [95], whilst others indicate the range is $x = 0.17 - 0.25$ [96]. More recent studies suggest the transition is entirely smooth and mediated by gradual octahedral tilt transitions. Below $x = 0.20$ rhombohedral anti-phase tilting exists in which short range in phase tilting associated with the tetragonal structure emerges, whilst coupling between cation displacement and tilting decreases [92]. These behaviours occur in regions of nanoscaled coherence giving rise to 'pseudosymmetries'. In the same manner as NBT, KNBT displays a hierarchical structure, whereby the measured structure is entirely determined by the probing coherence length.

The overarching consensus however is that the peak in piezoelectric properties occurs near or at $x = 0.20$, where the d_{33} significantly exceeds that of NBT by over two to three times (>200 pC/N compared to ≈70 pC/N) [45], [97]–[99]. Shown in **Figure 1.45** is the d_{33} and relative permittivity for KNBT reported in [96]. It is apparent that for $x = 0.20$ properties desirable of a piezoelectric material are observed.
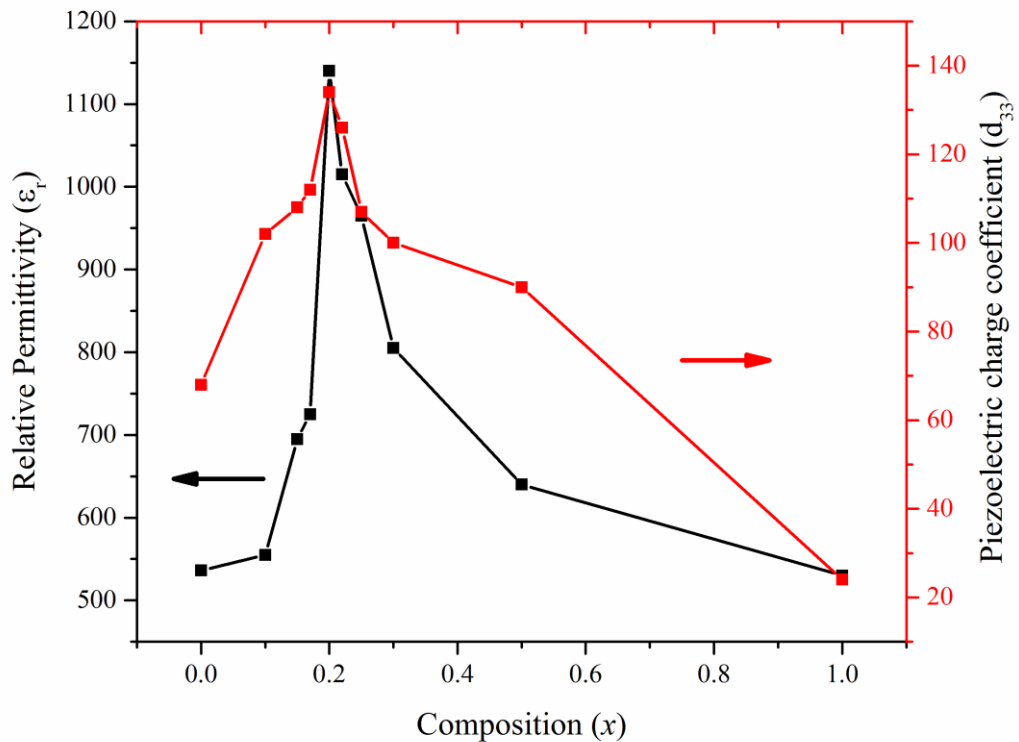
Figure 1.45 d_{33} and relative permittivity for KNBT. From [96].

1.14.5.2 Behaviour under fields

In situ electric field synchrotron X-ray diffraction measurements have identified a field-induced phase transition in the MPB composition at $x = 0.20$ [99]. Analysis of the {002} family of peaks showed a transition from a single (002) peak produced by the pseudocubic structure, which under an electric field produced the (200/002) doublet indicating a transition to a tetragonal structure. This occurred predominantly at 2 kV/mm (**Figure 1.47**). Additionally, further experiments revealed the same transition was dependent on the rate of the applied field up to 5kV/mm. **Figure 1.47** shows the same (200/002) peaks parallel (0) and perpendicular to the electric field. Above a rate of 0.25 kV mm^{-1} s^{-1} the tetragonal transition is observed.

More recent studies coupling *in situ* XRD with TEM analysis show that for the MPB composition at $x = 0.20$, compressive stresses induce the formation of rhombohedral domains whilst an applied electric field induces the formation of predominantly tetragonal domains [45], whose tilting arrangements coincide with previous TEM studies [92]. Additionally, the applied field induces ferroelectric order from the virgin relaxor-like state (Section 0).
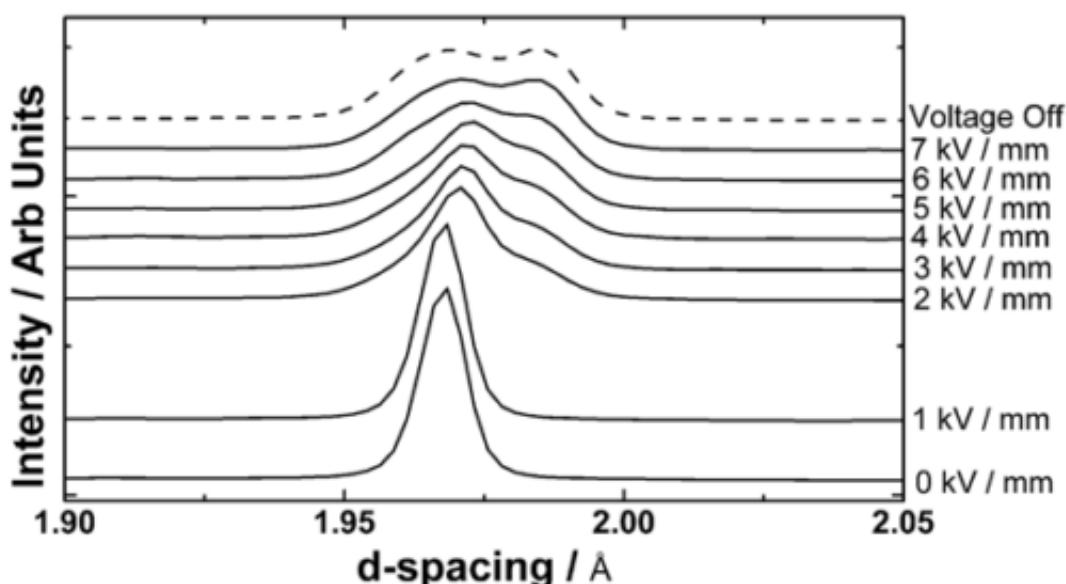
Figure 1.46 Effect of electric field magnitude on the (200/002) peaks in KNBT, producing a transition to tetragonal above 2kV/mm. From [99].
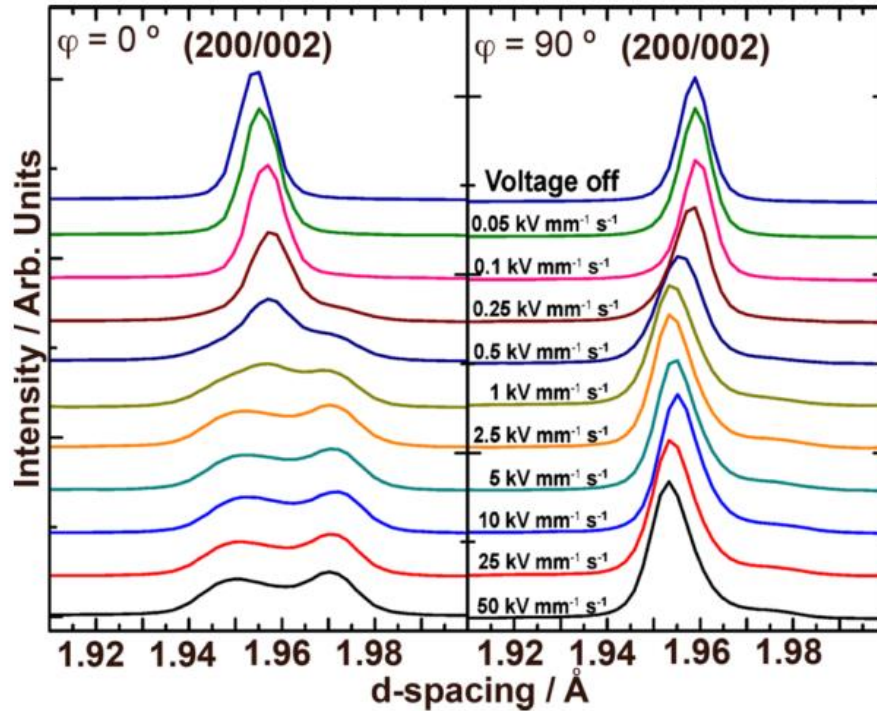
Figure 1.47 Rate dependent phase transition showing an induced tetragonal structure for rates above 0.5 kV mm^{-1} s^{-1}. The (200/002) peaks are shown parallel and perpendicular to the electric field vector. From [100].

1.14.6 (Na, Bi)TiO$_3$ - PbTiO$_3$

The addition of lead titanate to NBT to produce ((Na$_{0.5}$, Bi$_{0.5}$)$_{1-x}$, Pb$_x$)TiO$_3$ (NBT-PT) was envisaged to produce a viable low-lead content material, the presumption being that PT would induce long range piezoelectric order by its high polarisation and strain thereby improving its properties. However, this has not been realised due to poor piezoelectric properties $d_{33} \approx 100$ pC/N [101] and subsequently it has not attracted much scientific interest in comparison to other systems. Nevertheless, it offers an opportunity to observe the effects of the addition of lead on properties and structure and therefore can provide insight into the mechanism by which lead containing materials are typically superior. An MPB exists around $x = 0.13$, and synchrotron studies indicate a mixed phase region extended over $x = 0.10 - 0.15$, transitioning to mixed tetragonal and cubic phases shown to be antiferroelectric, and finally the cubic paraelectric phase as shown in **Figure 1.48** [102], [103]. Further addition of PbTiO$_3$ is shown to induce a high tetragonal strain [104] which appears to induce growth of nanoscaled domains originating from NBT and establish long range order [105].
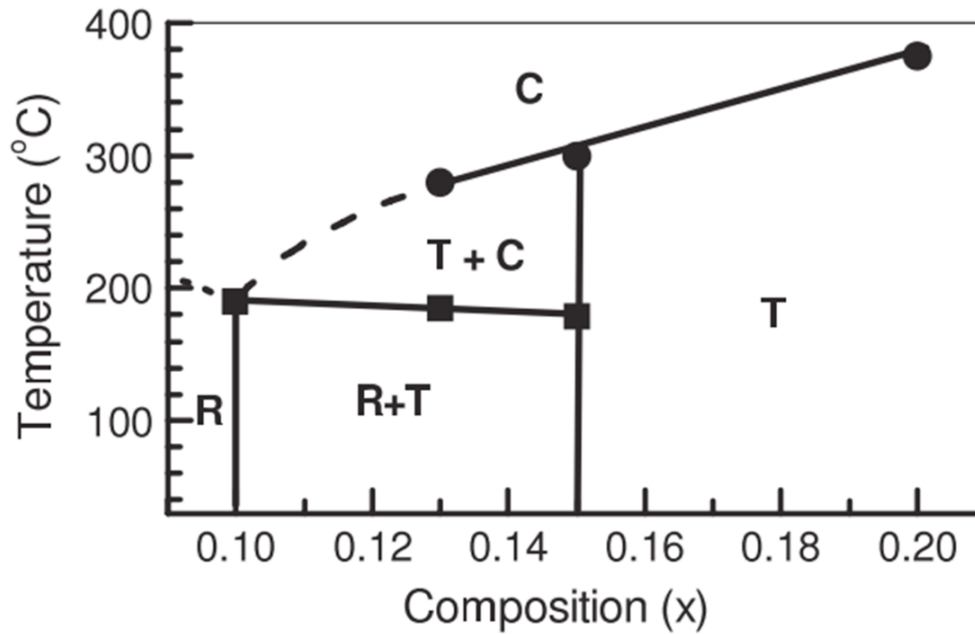
Figure 1.48 Phase diagram of NBT-PTx showing the mixed phase region x = 0.10 - 0.15 where an MPB resides. From [103].

1.15 Conclusions

This chapter has served to provide an introduction into the characteristics of piezoelectric materials and a review of some of the materials which have enjoyed significant interest from the research community. Focus was particularly placed on the structure of piezoelectric materials and the role of local and average structure behaviour. Increasingly it has become apparent that local and average structural behaviour must be considered in order to accurately attribute observed dielectric behaviour and is something present in many piezoelectric materials. Methods such as pair distribution function analysis have become increasingly prevalent in the literature and act as the local structure counterpart to average techniques such as high-resolution X-ray diffraction.

In this work materials which appear to exhibit local scale structural coherence are studied namely $(K, Na)_{0.5}Bi_{0.5}TiO_3$ (KNBT) and $(Na, Bi)TiO_3-PbTiO_3$ (NBT-PT). Both have exhibited behaviour which indicates local structure features strongly influence their properties and therefore the X-ray PDF technique is used with *in situ* variables such as electric field and temperature.

KNBT has been thoroughly studied using a wide range of techniques such as X-ray diffraction and electron microscopy methods coupled with *in situ* temperature, electric field and pressure measurements. E-field measurements in particular show phase transitioning behaviour and relaxor to ferroelectric transitions. The PDF method has not yet been applied *in situ* and therefore here the effects an applied electric field have on the local structure are investigated.

There is a scarce amount of literature on NBT-PT, especially in comparison to other NBT based materials. This is most likely due to its lacklustre piezoelectric properties. Studies do however show the effects of a high strain material such as PT on the disordered material NBT where relaxor-like to ferroelectric transition in behaviour is observed. Relaxor materials are characterised by the presence of local order and for this reason, the PDF analysis method has been used to further investigate the observed structural phenomena at room temperature and elevated temperatures.

2 Experimental techniques

2.1 Introduction

This chapter will detail the various methods used to describe the structure-property relationships of piezoelectric materials. The primary focus will be on structural characterisation techniques utilising the phenomenon of X-ray diffraction which relies on scattering of X-rays by atoms and planes of atoms which then produce an image or pattern that describes the atomic structure. The piezoelectric properties are measured via a variety of electrical measurements primarily describing the magnitude of polarisation within a sample, the piezoelectric activity, and the temperature dependent capacitance.

2.2 X-ray diffraction

2.2.1 Introduction

X-rays are a form of electromagnetic (EM) radiation with a wavelength in the 0.1 – 1 Ångstrom range, comparable to the distances between atoms and crystallographic planes, thereby suitable for studying atomic structure. X-ray diffraction (XRD) or more precisely wide angle X-ray scattering (WAXS) is a technique which uses the phenomenon of X-ray scattering and interference to produce a diffraction pattern from which the crystal structure of a material can be described. As the name suggests scattered X-ray intensities are measured over a large range of angles. And it is the relationship between the scattering angle and the intensity that provides structural information. This technique has a few principal assumptions: The X-rays are monochromatic and coherent, i.e. one wavelength and in phase; the interaction between X-rays and matter (scattering) is elastic i.e. there is no change in energy.

2.2.2 Interaction between X-rays and matter

Prior to discussing how X-rays are used to characterise atomic structure, it is first important to address their interaction with matter and at various length scales including a single electron, a single atom and a unit cell. Again, only elastic scattering is considered

here. The following description is adapted from Bernard D. Cullity's *Elements of X-ray Diffraction* [9] and Marc De Graef and Michael E. McHenry's *Structure of Materials: An Introduction to Crystallography, Diffraction and Symmetry* [11], both of which offer a far more thorough and complete mathematical derivation. However, a brief overview is still necessary.

2.2.2.1 X-rays and electrons

X-rays are electromagnetic waves i.e. oscillating electric and magnetic fields. These fields interact with charged particles such as electrons and induce an oscillation of the same frequency and wavelength. In turn the oscillation or continuous acceleration and deceleration of the electron produces an X-ray and in this manner the X-ray has been 'scattered'. X-rays are scattered in all directions; however, their intensity is direction dependent and is governed by Thomson scattering shown in **Equation 2.1**. Where I is the measured intensity, I_0 is the incident intensity, e is the electron charge, r is the distance at which I_0 is measured, m mass of the scattering particle (in this case the electron), c is the speed of light and 2θ is the angle between I_0 and I. The equation shows that the intensity is greatest in the forward and backwards scattering direction, and weakest in the plane perpendicular to the incident beam. The clue to this behaviour can be quickly inferred by the cosine term and is depicted in **Figure 2.1**.

Equation 2.1

$$I = I_0 \frac{e^4}{r^2 m^2 c^4}\left(\frac{1 + cos^2\theta}{2}\right)$$
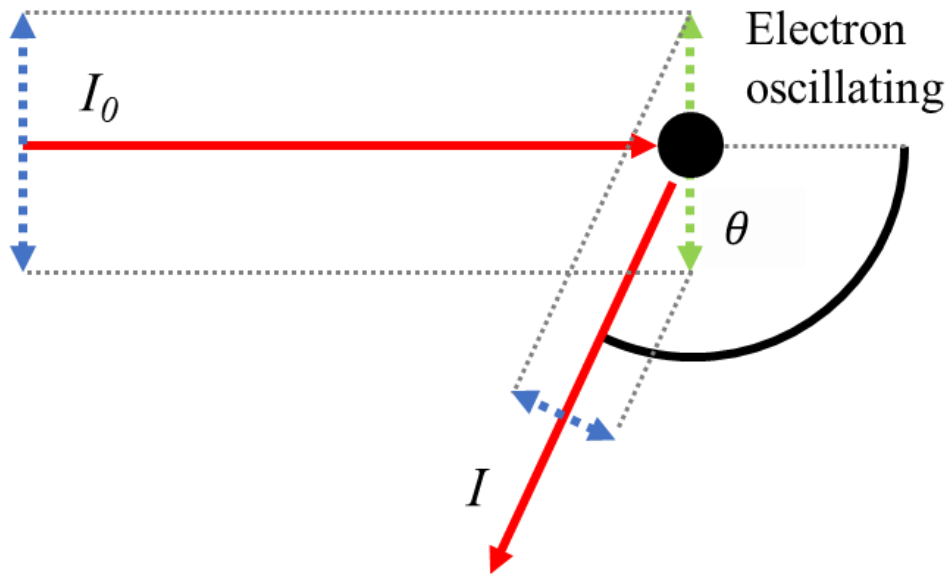
Figure 2.1 Simple depiction of Thompson scattering. The scattered intensity is proportional to the cosine of the scattering angle θ and therefore greatest for forward and backwards scattering, and lowest perpendicular to the incident vector.

2.2.2.2   X-rays and atoms

When scattering from an atom, only the scattering of X-rays from electrons require consideration, as the X-rays do not scatter from nuclei to any appreciable extent. This is evident from the inverse square relationship of the scattering particle mass and the scattered intensity in **Equation 2.1**. Since the mass of a single proton is a thousand times greater than an electron's, its scattering intensity will be 10^6 times smaller.

The scattering intensity is proportional to the number of electrons in an atom or the atomic number Z. This applies only in the forward scattering direction as all scattered X-rays remain in phase. Within an atom, electrons are in various positions, scattering at other angles will result in a loss of intensity from destructive interference due to the path difference travelled by the X-rays, shown in **Figure 2.2 a)**. The atomic scattering factor f is a quantity which describes how effectively a given atom scatters X-rays, described in **Equation 2.2**. **Figure 2.2 b)** shows the atomic scattering factor for copper as a function of scattering angle. The angle is in the form $\sin\theta/\lambda$ to represent wavelength independent values and so f is shown to decrease with increasing angle. Note that at the zero-scattering angle, f is equal to the atomic number of copper ($Z = 29$).

Equation 2.2

$$f = \frac{amplitude\ of\ an\ X-ray\ scattered\ by\ an\ atom}{amplitude\ of\ an\ X-ray\ scattered\ by\ an\ electron}$$

a)

b)
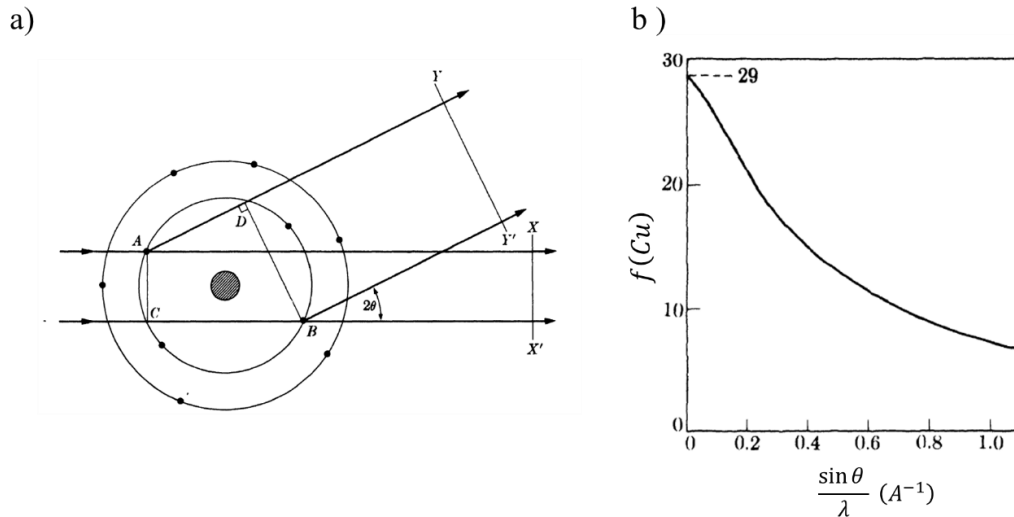
Figure 2.2 a) X-rays scattering of electrons within an atom. When scattering at angles other than 2θ = 0. b) Atomic scattering factor *f* for copper as a function of scattering angle in the form sinθ/λ. From [9].

2.2.2.3   X-rays and unit cells

It is now possible to consider X-ray scattering from a unit cell or crystal. Whilst a lengthy derivation can be elaborated the result is simply described by the structure factor *F* in **Equation 2.3**, the scattering arising from the contributions from all the atoms in the unit cell. The structure factor is computed by the summation of the atomic scattering factor *f* for *n* atoms in the unit cell at a coordinate *xyz* and for a given crystallographic plane *hkl*.

Equation 2.3

$$F_{hkl} = \sum_{1}^{N} f_n \, e^{2\pi i (hx_n k y_n l z_n)}$$

2.2.3   Diffraction from crystallographic planes

X-rays scatter off atoms in all directions as is described in Section 2.2.2.2. When arranged in a regular structure atomic planes are formed. This results in certain scattering directions constructively interfering whilst other destructively interfere and cancel out. **Figure 2.3** shows the geometry of X-ray scattering. X-rays (green arrows) scatter off two atoms (*A* and *B*) on equivalent crystallographic planes separated by a distance *d*. One X-ray will have to travel a longer path (red arrow $\overrightarrow{uBv}$) creating a path difference between the X-rays. Incident X-rays are in phase and therefore at most incident angles the path difference will result in scattered X-rays being out of phase because one is 'lagging' behind. This would result in destructive interference. However, at a specific angle or direction, the path difference will be an integer multiple of the X-ray wavelength and therefore the phases will be the same (i.e. X-ray crests and troughs are aligned) and the rays will constructively interfere producing a strong X-ray signal. This is called a Bragg angle, where Bragg's law is satisfied. When this condition is met the Bragg equation can be used to calculate the atomic plane spacing *d* (**Equation 2.4**) where *n* is an integer, λ is the wavelength, θ is the angle between the plane and the incident or reflected X-ray (2θ is the scattering angle). The success of this method to accurately define an atomic structure is wholly dependent on the long-range periodicity of crystallographic planes, each contributing to the X-ray intensity at a corresponding angle.

Figure 2.4 shows several crystal planes present in a hypothetical 2D arrangement of atoms separated by the parameter '*a*'. It is apparent that in this case the {10} *d*-space value will be exactly the distance between adjacent atoms along the axes and the {11} *d*-space will give information on the diagonal distance between atoms. In this way with a few measurements of atomic planes a picture of the structure can be identified. An important consideration which will be discussed later is that the smaller the d spacing the more planes there are per given distance i.e. the spatial periodicity is greater. It is important to note that for a given atomic plane to be observable it has to be orientated with respect to the incident X-ray beam in order to meet the Bragg condition.
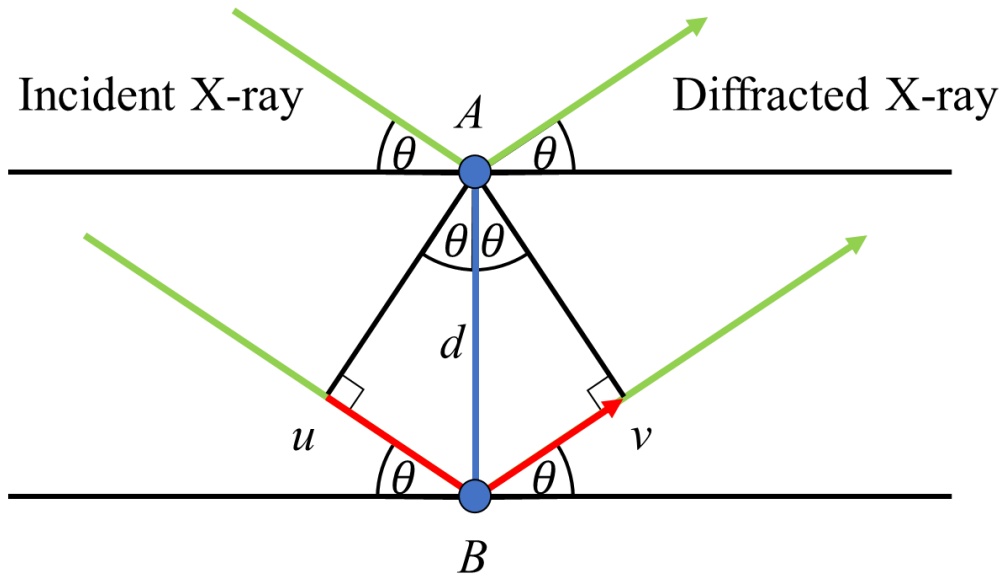
Figure 2.3 Geometry of X-ray scattering. The Bragg condition is met when the path difference created by two set of planes at a given angle is an integer multiple of the X-ray wavelength thereby giving constructive interference.

Equation 2.4

$$n\lambda = 2d \sin \theta$$
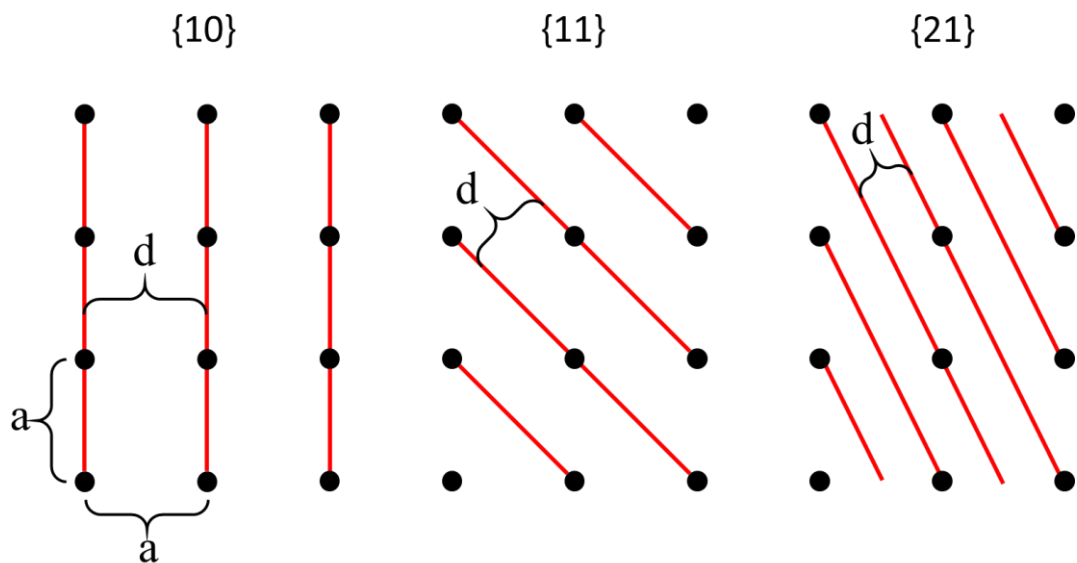
Figure 2.4 Depiction of crystal planes in a hypothetical 2D structure of atoms with periodicity 'a' in both dimensions.

In **Figure 2.5** a typical X-ray diffraction pattern is shown for a perovskite structure. The first five peaks of importance have been labelled *a – e* and are tabulated in **Table 2-1**, and indexed to the cubic Miller indices. Using **Equation 2.4** the d-spacing corresponding to the crystallographic plane which produces each peak can be calculated. This first naïve analysis of the peak positions can reveal a great deal of structural information. The peak splitting observed in the {001}, {011} and {002} peak groups, as well as the lack of splitting in the (111) peak can be used to deduce that this particular perovskite structure is tetragonal. More advanced methods are required to fully determine the space group, which would include analysis of the peak intensities and shapes (Section 2.5.1).
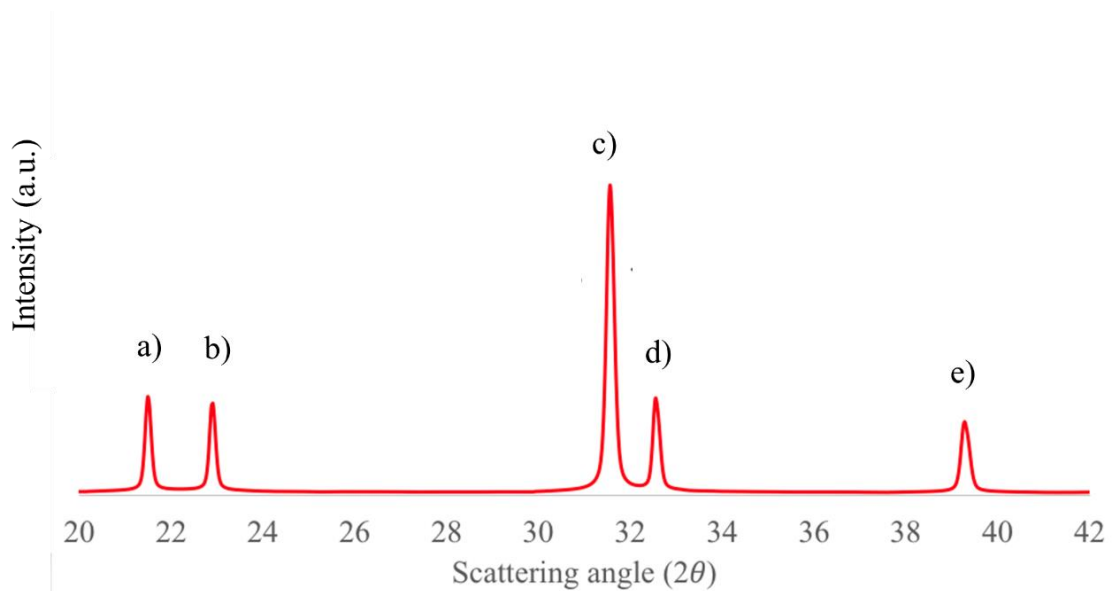
Figure 2.5 X-ray diffraction pattern for a perovskite structure. Incident wavelength $\lambda = 1.5406$ Å.

Table 2-1 XRD peaks in Figure 2.5 measured in 2θ, converted to d-spacing and indexed to the Miller indices of the cubic unit cell.

Label	(hkl)	2θ	d-space (Å)
a)	001	22.3	3.98
b)	100	22.8	3.9
c)	101	32.1	2.79
d)	110	32.6	2.74
e)	111	39.8	2.26

2.2.4 Scattering in Q-space

Previously discussed is X-ray scattering in terms of scattering angle and d-space between planes. Scattering can also be interpreted in terms of a scattering vector by considering the initial and final X-ray wavevectors k_i and k_f respectively, where the scattering vector Q or scattering momentum transfer is the difference between the initial and final wavevectors as shown in **Equation 2.5**. The wavevector k is defined in **Equation 2.6**. Here only elastic X-ray scattering is considered therefore the magnitude of the initial and final wave vectors are the same. This allows the use of simple trigonometry (**Figure 2.6**) to determine the magnitude of the scattering vector Q as shown in **Equation 2.7**, and by substituting **Equation 2.6** the 'Q' equation is obtained, shown in **Equation 2.8**. Q is wavelength independent and therefore advantageous when comparing different data sets.
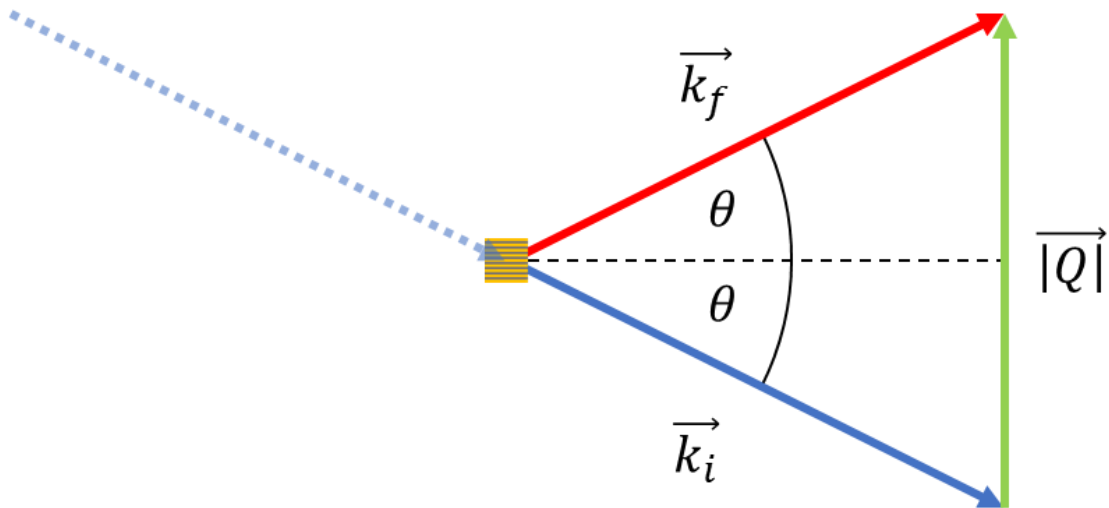
Figure 2.6 Geometry of the scattering vector Q. $|Q|$ is the magnitude of the difference between the initial and final X-ray wavevectors, and the vector describes the momentum required to scatter an X-ray in a different direction.

Equation 2.5

$$\overrightarrow{|Q|} = \overrightarrow{k_i} - \overrightarrow{k_f}$$

Equation 2.6

$$k = \frac{2\pi}{\lambda}$$

Equation 2.7

$$\frac{|Q|}{2} = k\ \sin\theta$$

Equation 2.8

$$|Q| = \frac{4\pi\ \sin\theta}{\lambda}$$

2.2.5 Size, order and thermal effects

So far when discussing X-ray scattering there are two important underlying assumptions: 1) all atoms are in fixed positions in space, and 2) a crystal structure extends in three dimensions to infinity. As expected, this is not true; atoms always possess some degree of thermal energy (even at 0 K) vibrating about their coordinate position, and are finite structures.

Figure 2.7 shows an example adapted from De Graef *et al.* [11] who uses the analogy of a marching band. In a marching band its members are initially in precise locations, throughout the march a highly disciplined band will retain its formation (a), whilst those less experienced would end up diverging from their original positions (b) and (c). In the case of atoms in a crystal, the increase in thermal energy induces vibrations in the atoms which distributes their position over a greater volume. The green box illustrates the range of possible interatomic distances resulting from these displacements.

a)   b)   c)
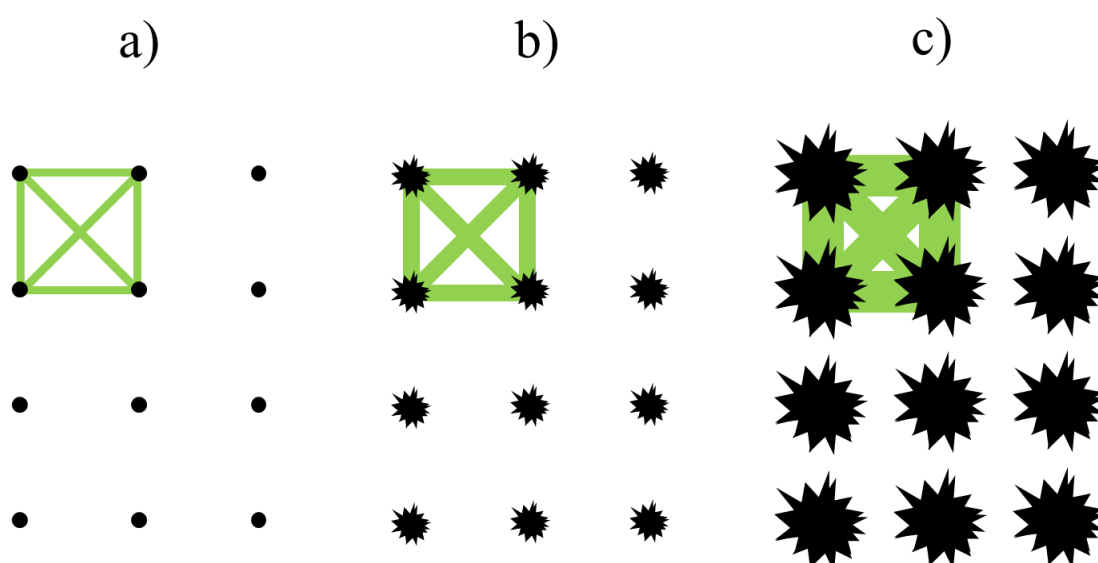
Figure 2.7 Positions of atoms (or a 'marching band') in crystals with increasing thermal energy a) with little to no energy, b) with some degree of thermal vibration c) a highly energetic system with large vibrations. The green boxes represent the range of possible interatomic distances. Adapted from [11].

The second important consideration is the coherence length of the structure, or the distance across which the structure and periodicity remains the same. The X-ray signal intensity at a Bragg angle is in part determined by the extent of the coherence. A highly

crystalline material produces high intensity peaks, whereas a poorly ordered material will have a greater distribution of atomic spacings and therefore the contribution to a given diffraction peak will be smeared out. **Figure 2.8** illustrates a crystalline material a) which produces a sharp intensity peak because the *d*-spacing is the same across the material. The peak is deliberately shown to have a small degree of broadness due to some of the thermal effects discussed earlier. An idealised perfect structure would be a Dirac delta function i.e. all the scattering signal is focused on a precise point *d*. Example b) shows a material with differing *d*-spacings which produce a broader less defined peak. It is important to note that the *average* of the *d*-spacings is still a peak at position *d*.

In a polycrystalline material, whilst every grain is one single crystal, the overall structure exhibits more disorder than a single crystalline material. The coherence length is bound by the grain size, and randomised orientation of grains reduces their contribution to a specific scattering angle. Additionally, the intergranular structure acts as a bridge between randomly orientated grains and therefore will typically have a disordered structure. All these effects contribute to interruptions in the crystal lattice reducing the intensity for a given scattering vector.
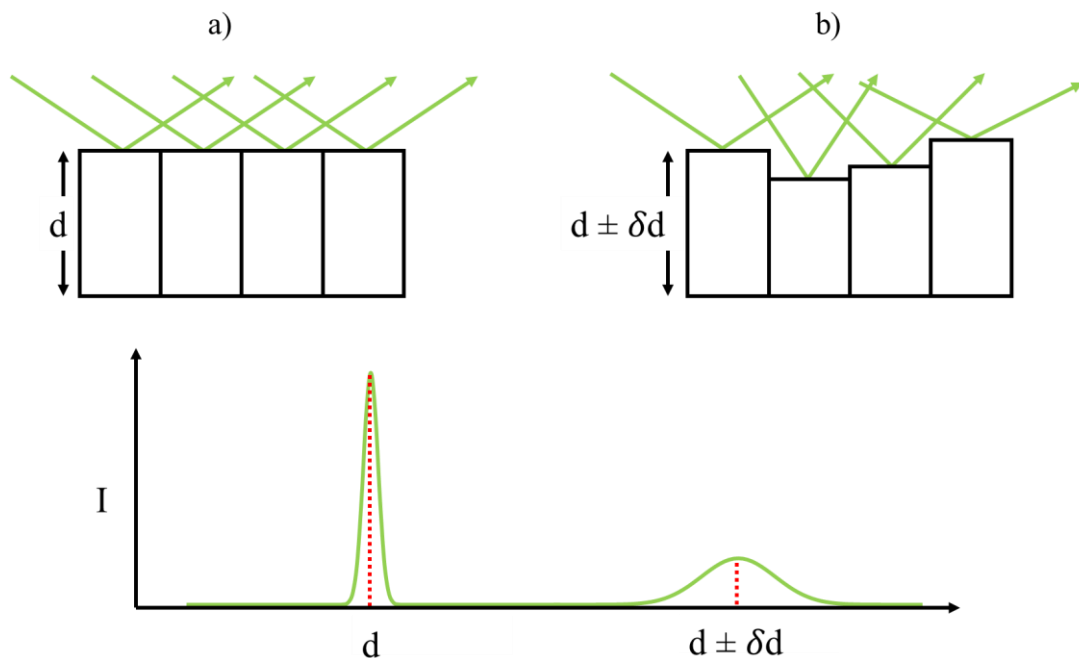
Figure 2.8 Effects of crystal ordering on the scattering signal. A highly-ordered structure (a). A structure which diverges from the ordered structure due to various factors e.g. local scale disorder (b).

2.3 The pair distribution function

2.3.1 Introduction

The technique so far could be described as 'conventional' X-ray diffraction as it employs methods which have been established across the global scientific community since its inception in 1913 [10]. There is no doubt that this technique has excelled, in part due to its wide-ranging applicability and multidisciplinary nature. As many as 29 Nobel prizes have been awarded to discoveries underpinned by crystallography, constituting more than 10% of prizes in the physics and chemistry categories [106]. As previously stated, the founding assumption of the technique is long range crystal periodicity. Indeed, the analysis methods currently used function primarily by determining scattering peak positions and intensities [10]. Structures such as glasses e.g. amorphous silica, do not display any long-range order producing diffuse peaks offering little structural information via this method.

Materials such as sodium bismuth titanate (Section 1.14.4) can be described as 'crystallographically challenged' due to an ambiguous structure and nanoscaled structural coherence. This is associated with its inherent chemical disorder associated with mixed A-site occupation (sodium and bismuth) which in turn creates local distortions which differ from the average structure. NBT's elusive structure has endured several decades study to accurately describe its structure [72], [80], [83], [84], [107], [108].

True nanocrystalline materials such as the C_{60} molecule or buckminsterfullerene possess length-scale-dependent structural coherence. The molecule itself is highly ordered as the carbon atoms form an array of pentagonal and hexagonal arrangements. However, beyond the molecular sphere diameter of around 6.9 Å the structure becomes less defined. The carbon spheres do however have a macroscopic face centred cubic (FCC) arrangement. **Figure 2.10** illustrates how the two types or ordering appear in pair distribution function (PDF) data. The sharp PDF peaks below 6.9 Å correspond to interatomic distances between carbon atoms in a single C_{60} molecule. As will be discussed later the peak width and amplitude describe the distribution of atom-pair distances. For carbon-carbon pairs within a single molecule these peaks therefore have a greater height and sharpness due to the high correlation of carbon-carbon pairs within the molecule. Above 7 Å the peaks are far less intense and a lot broader. These correspond to the distances between spheres, highlighted in the atomic models in the figure. The ordering

between atoms in adjacent molecules is much lower as the distances are not as well defined due to the molecules being able to rotate relative to each other.
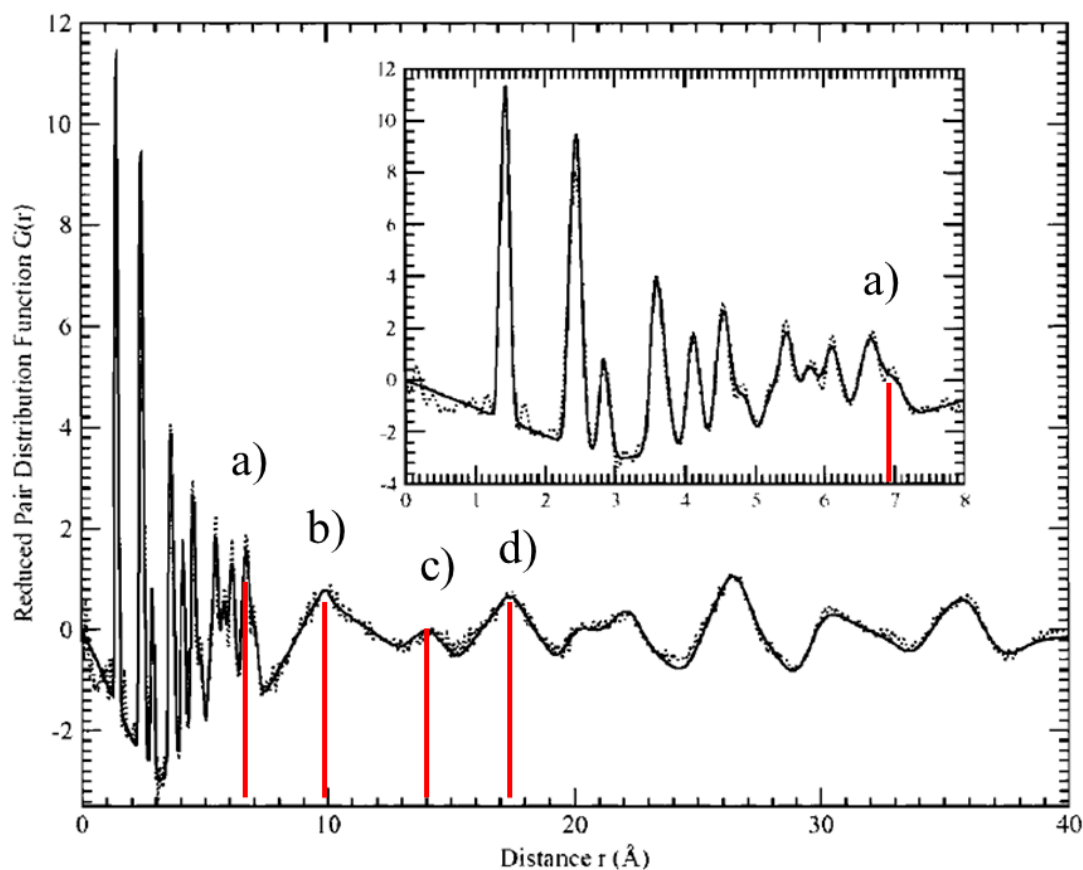
Figure 2.9 PDF of C_{60} molecules which pack in a face centred cubic structure as depicted. The highlighted peaks correspond to the distances between individual molecules. Modified from [109] in [52].
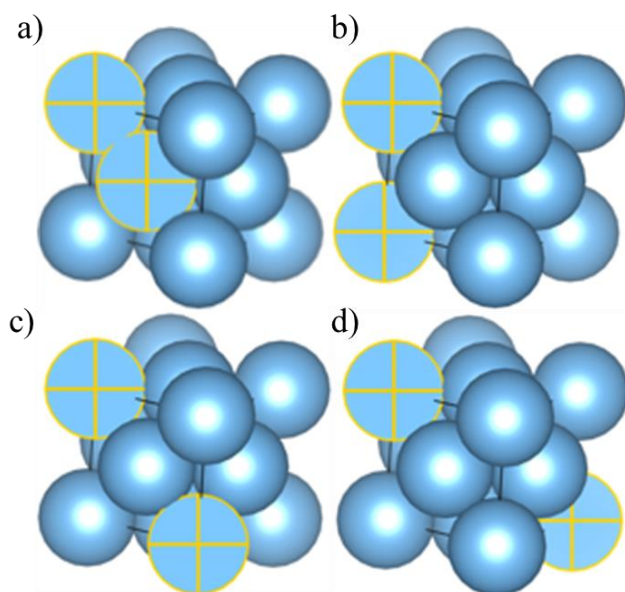
Figure 2.10 Schematic illustration of FCC packed C$_{60}$ molecules, whose inter-molecular distances correspond to PDF peaks labelled in Figure 2.9.

As early as the 1930s the pair distribution function (PDF) method of analysis was developed, and used to study the structure of liquids [110], [111]. The PDF is obtained by the Fourier transform (FT) of the total scattering structure factor, giving real space structural information on the separation of atom-pairs in a given structure at a wide range of length-scales [52]. The PDF considers all scattering information i.e. Bragg and diffuse scattering. Bragg scattering corresponds to the sharp X-ray peaks arising from the crystalline periodicity in a material. Diffuse scattering arises from small deviations from the crystalline order which produce far less intense X-ray peaks which can exist between or under the Bragg peaks and are therefore either obscured or ignored and considered part of the background in conventional diffraction analysis. Crucially much of the structural information associated with disorder in a material is contained within the diffuse scattering [112].

In its early years, PDF analysis was limited by the lack of computer technology to carry out Fourier transform operations. The development of both computers and high resolution scattering instruments has enabled the technique to flourish, seeing use in the study of complex structures such as in nanocrystalline, amorphous, and disordered materials [113]–[117]. The following sections will cover fundamentals of the PDF Fourier transform and total scattering before delving into pair distribution function analysis.

2.3.2   Fourier transform background

A Fourier transform (FT) is useful as it can be used to manipulate data and exchange the domain in which it is being represented aiding analysis. Scattering occurs as a function of angle or scattering vector in reciprocal space. A Fourier transform of the scattering would produce real space information.

A common example of the use of FT is in the analysis of the frequency content of acoustic signals to determine the frequency response of a speaker or microphone for example. These signals are measured as intensity as a function of time and via the FT are converted to the frequency domain [118]. The simplest signal would be a single sine wave, which would translate to a single peak in frequency space. Realistically however, the measured signal would contain a broad range of frequencies and intensities. For example, musical instruments produce notes which contain the fundamental frequency e.g. the note A4 (A above middle C) at 440 Hz as well as a rich quantity of harmonics, sub-harmonics and non-harmonics which give the instrument its unique sound or timbre. Analysing its frequency content would therefore be non-trivial, but possible by the FT approach.

Firstly, it is useful to recall Euler's formula shown in **Equation 2.9**, relating trigonometric functions (oscillations) to exponentials. In this case, it aids displaying by notation e^{ix} rather than the long trigonometric function. The frequency domain function $\hat{F}(f)$ is computed by the Fourier transform of the time domain function $F(f)$ shown in **Equation 2.10**, and the reverse transformation can be performed and is shown in **Equation 2.11**, called the inverse Fourier transform [118]. This is calculated by the summation of the cosine and sine contributions to a t or f function, from negative infinity to infinity. Note the similarity between the equations showing that they are effectively applying the same operation. A simple example is shown in **Figure 2.11**, in which a function in the time-domain is composed of three different sinusoidal signals (**Equation 2.12**) of varying amplitude and frequencies, shown in **Table 2-2**.

Equation 2.9

$$e^{ix} = \cos x + i \sin x$$

Equation 2.10

$$\hat{F}(f) = \int_{t=-\infty}^{t=\infty} F(t)\, e^{2\pi i t f}\, dt$$

Equation 2.11

$$F(t) = \int_{f=-\infty}^{f=\infty} \hat{F}(f)\, e^{-2\pi i f t}\, df$$

Equation 2.12

$$Function(a, b, c \ldots) = I_a * \sin(2\pi * f_a * t)$$

$$+ I_b * \sin(2\pi * f_b * t)$$

$$+ I_c * \sin(2\pi * f_c * t) + \cdots$$

Table 2-2 Function parameters

Function no.	Intensity I	Frequency f
a	2	1
b	4	2
c	1	3
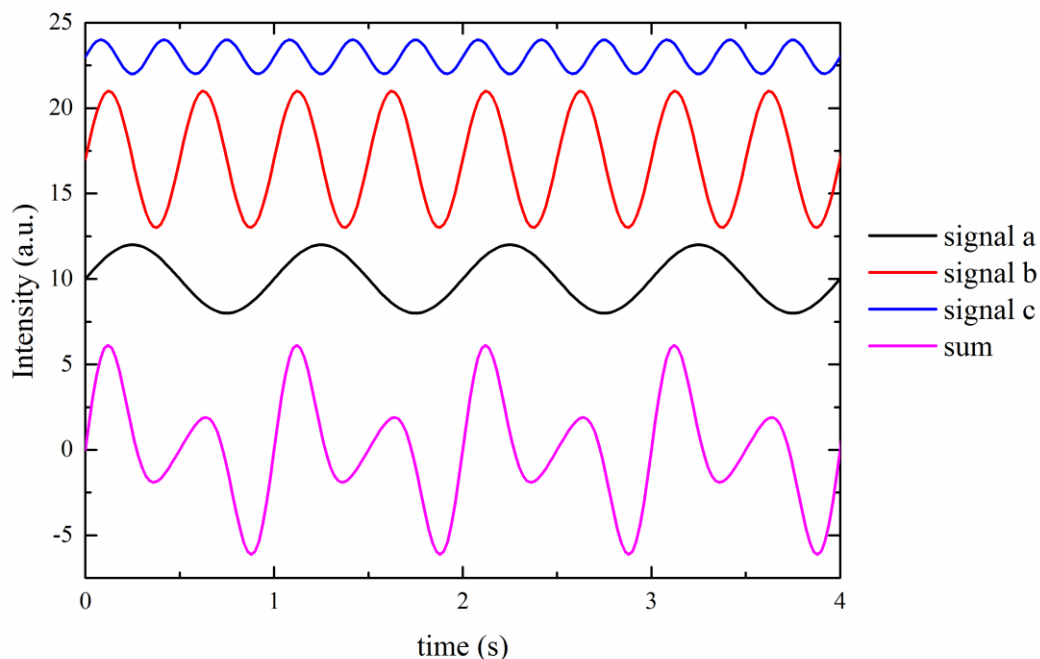
Figure 2.11 Signals (a), (b) and (c) of varying frequencies and intensities and their resultant sum.

For demonstration and simplicity, a pseudo-FT is performed where it is applied to just a sine function i.e. the imaginary or phase components are not considered. For every point on *x*, a sinusoid is produced with frequency *x* and amplitude *y*. In this case, there is a boundary to the integral between 0 and 8 seconds. All these newly formed sinusoids are summed producing the FT shown in **Figure 2.12**.

The intensity of the peaks show the frequency and amplitude of the contributing signals. Due to the simplicity of the method scaling factors were added to adjust the amplitude of the peaks, however it is apparent by the amplitude ratios of the peaks that they correspond to the original 3 signals. Applying this method to the results in **Figure 2.12** shows the reverse effect i.e. the inverse Fourier transform where the original signal is produced in **Figure 2.13**.
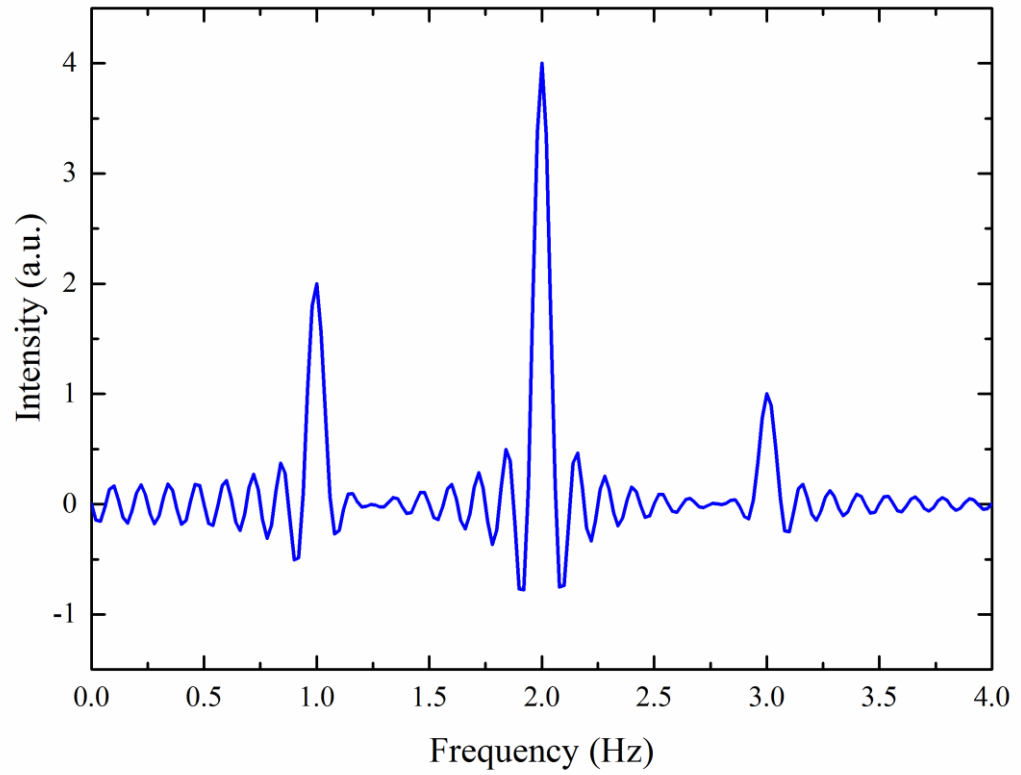
Figure 2.12 Fourier transform of the signal in Figure 2.11 showing the frequency content.
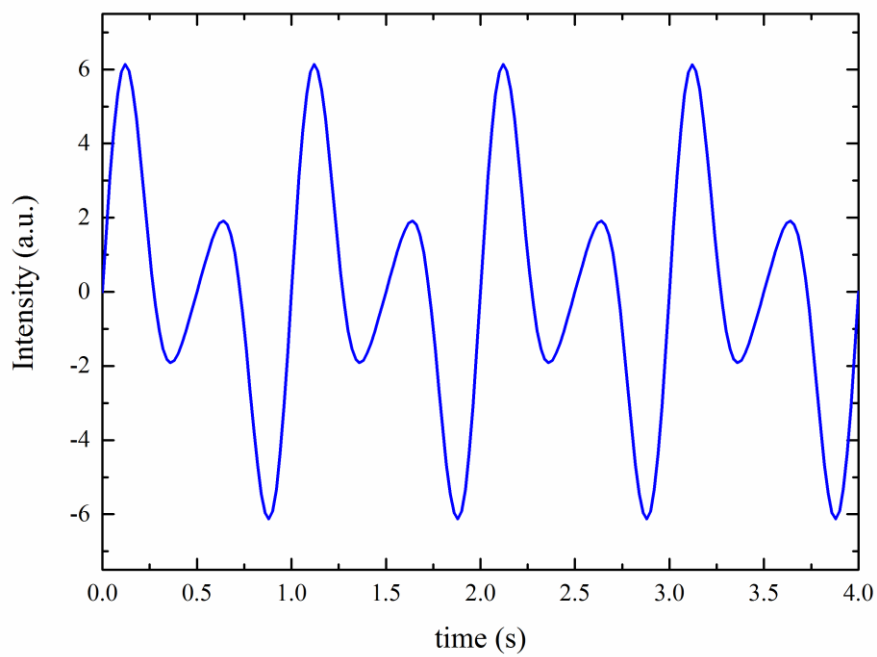
Figure 2.13 Fourier transform of Figure 2.12 showing the original functions. As this is a crude method the amplitude of the signal is off by some factor.

It is easier to envisage these operations by considering the function of the inverse Fourier transform. In the frequency-domain every point on the x axis corresponds to a frequency and therefore a sinusoid with said frequency can be formed. It can be seen that when applying the FT the high amplitude peaks will produce sinusoids with intensity y and frequency x.

It should now start to become apparent how this relates to crystallography. The Fourier function in this case transitions between real and reciprocal space. Every point from scattering data represents the periodicity or *frequency* of atomic planes. A high intensity peak for the (001) plane of a perovskite such as $BaTiO_3$ would (in *d*-space) lie around 3.9 Å which means it has a periodicity of 3.9 Å. Therefore, it is suitable to represent any point in Q-space as a sinusoid representing the periodicity in real space and showing the actual interatomic distances.

2.3.3 Total scattering

The total scattering structure function contains all the scattering information arising from the measured structure including the atomic species, species concentration and atomic position [119]. It is the Fourier transform of the total scattering structure function that generates the pair distribution function.

The atomic scattering amplitude (**Equation 2.13**) is calculated from the summation of the atomic scattering factor f_n (**Equation 2.2**), for every atom species n and for every concentration c_n. The arrow brackets indicate compositional average.

Equation 2.13

$$\langle f_n \rangle = \sum_n c_n f_n$$

The sample scattering $\psi(Q)$ is similar to the structure factor (**Equation 2.3**), where R_n is the position of atom n. The square of its magnitude is the sample scattering intensity (**Equation 2.14**). The coherent scattering intensity, $I_{coh}(Q)$ is the normalized scattering

with scattering originating from the background and experimental effects removed. It is added to the square of the mean minus the mean of the square of the atomic scattering factor, which is effectively the variance (standard deviation squared). The total scattering structure function is calculated as shown in **Equation 2.15** [52].

Equation 2.14

$$|\psi(Q)|^2 = \left| \frac{1}{\langle f_n \rangle} \sum_n f_n e^{iQR_n} \right|^2 = I_{coh}(Q) + \langle f_n \rangle^2 - \langle f_n^2 \rangle$$

Equation 2.15

$$S(Q) = \frac{|\psi(Q)|^2}{\langle f_n \rangle^2}$$

2.3.4 Pair distribution function

As stated earlier the PDF is obtained from the Fourier transform of the total scattering structure function $S(Q)$ shown in **Equation 2.16**. $G(r)$ is called the reduced pair distribution function, from which the pair distribution function $g(r)$ can be calculated shown in **Equation 2.17**. The reduced pair distribution function is obtained directly from the Fourier transform and so is most widely used. Therefore, any use of 'PDF' here will refer to $G(r)$ unless otherwise stated. The FT is technically a discrete Fourier transform since it is bounded by limits Q_{max} and Q_{min} rather than $\pm\infty$ (**Equation 2.11**). There are physical limits of Q imposed by the X-ray wavelength and angular coverage (**Equation 2.8**) so that Q_{min} cannot have a value of zero or lower and Q_{max} cannot have an infinite value. $\rho(r)$ is the atomic pair density function or microscopic density function (**Equation 2.18**) and ρ_0 is the atomic number density or average number density.

In **Equation 2.18** it becomes apparent that $g(r)$ can be represented as the probability of encountering two atoms separated by a distance r due to the fractional relationship of the microscopic/atomic (or local) density and the average density. A further Fourier transform of $G(r)$ produces $S(Q)$ as expected (**Equation 2.19**).

Equation 2.16

$$G(r) = \left(\frac{2}{\pi}\right) \int\limits_{Q_{min}}^{Q_{max}} Q(S(Q) - 1)\sin(Qr)\,dQ$$

Equation 2.17

$$g(r) = (G(r)/4\pi r \rho_0) + 1$$

Equation 2.18

$$g(r) = \frac{\rho(r)}{\rho_0}$$

Equation 2.19

$$S(Q) = 1 + \frac{1}{Q}\int\limits_{0}^{\infty} G(r)\sin(Qr)\,dr$$

The pair distribution function represents the probability of encountering an atom-atom pair at a distance r. This can be envisaged in two dimensions as shown in **Figure 2.14**. In this simple structure, the interatomic distances can be represented as concentric coordination rings centred on every atom. The PDF signal from a given ring is determined by the radius of the ring and the number of atoms it intersects.
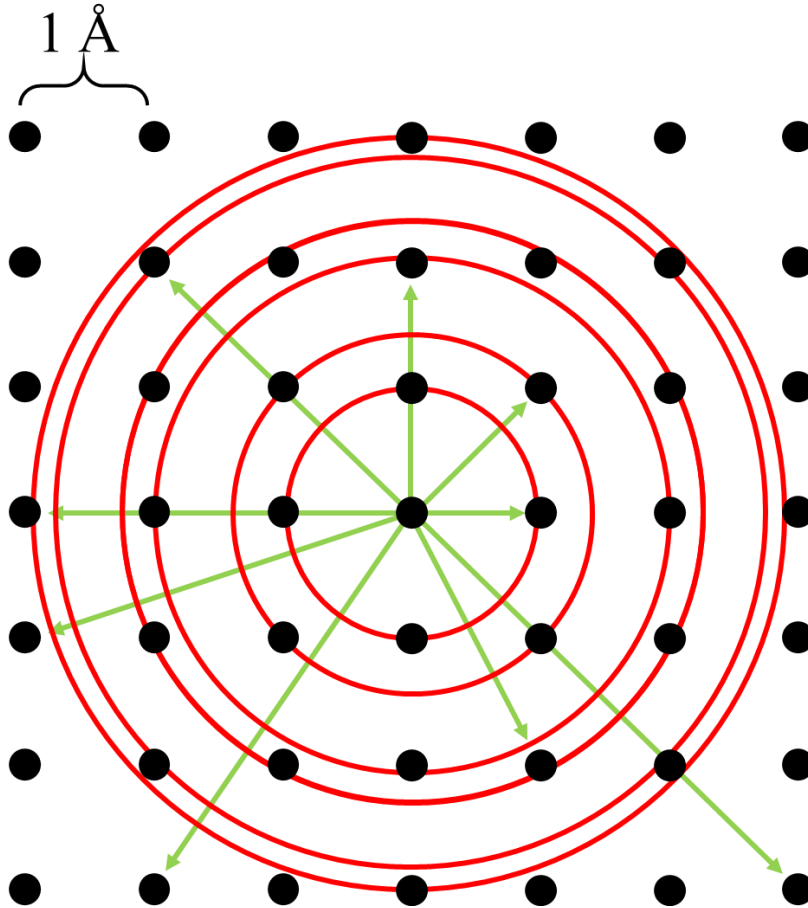
Figure 2.14 Two dimensional representation of a PDF in real space. The interatomic spacing, or unit cell parameter a = 1 Å.

To demonstrate this the square 2D structure in **Figure 2.14** was used to model a pseudo-PDF (**Figure 2.15**) purely for demonstration purposes. It is termed 'pseudo' as it is not calculated via the Fourier transform method but as described in the following: It is constructed by calculating the number of atoms at every distance r, for which a Gaussian peak with position r and height of a multiple of the number of atoms at distance r is calculated. All the contributions for a chosen distance r, are then summed. This simple pseudo-PDF construction is shown in **Equation 2.20** where r is the distance in angstroms, n is the atom at position p_n with amplitude N_n (number of atoms at position p_n), and w is the Gaussian peak width, set to show a realistic structure (rather than a Dirac delta function). In fact, the choice of a Gaussian peak here is appropriate as it closely approximates a realistic probability distribution of atomic positions about an equilibrium position. This is particularly relevant for the radial distribution function (RDF) discussed in Section 2.3.5.2.

Equation 2.20

$$PDF_{2D} = \sum_n N_n exp\left(-\frac{(r - p_n)^2}{w^2}\right)$$
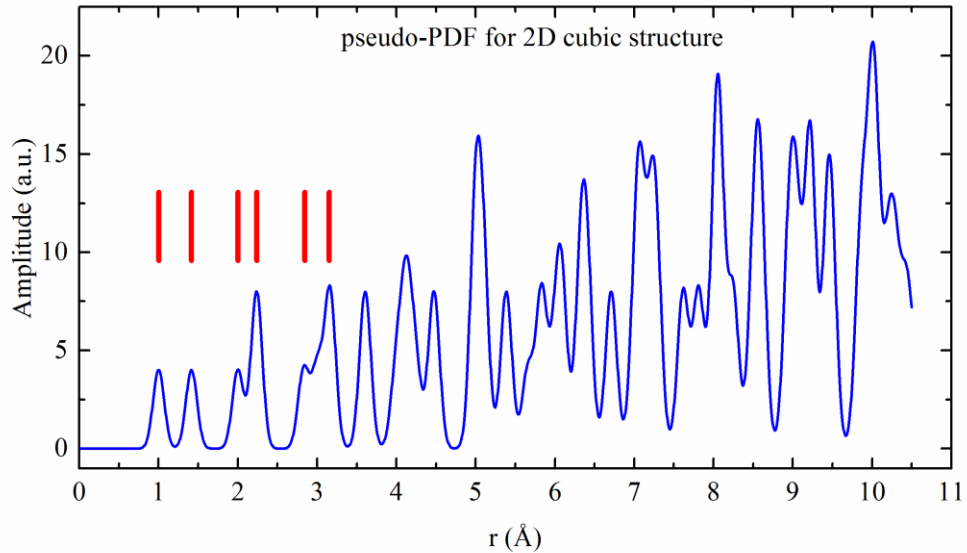
Figure 2.15 Pseudo-PDF for the structure shown in Figure 2.14. The red tick marks show the first 6 interatomic distances marked in the real space diagram of Figure 2.14.

A notable aspect of this construction is the increasing overlap of interatomic distances at greater r as shown by the constant increase in the number of peaks shown in **Figure 2.16 a)**, which follows an approximate square trend. This increases the difficulty of deciphering the structure at greater distances due to the contribution of multiple atom-pair distances to a single peak. **Figure 2.16 b)** shows the effective atomic number density ρ_0, or more precisely the areal density, which as expected tends to the average density which is 1 atom per unit area. This pseudo-PDF in fact more closely resembles a radial distribution function (RDF) which is related to the PDF. Section 2.3.5 expands more thoroughly on this and the various important aspects of PDFs.
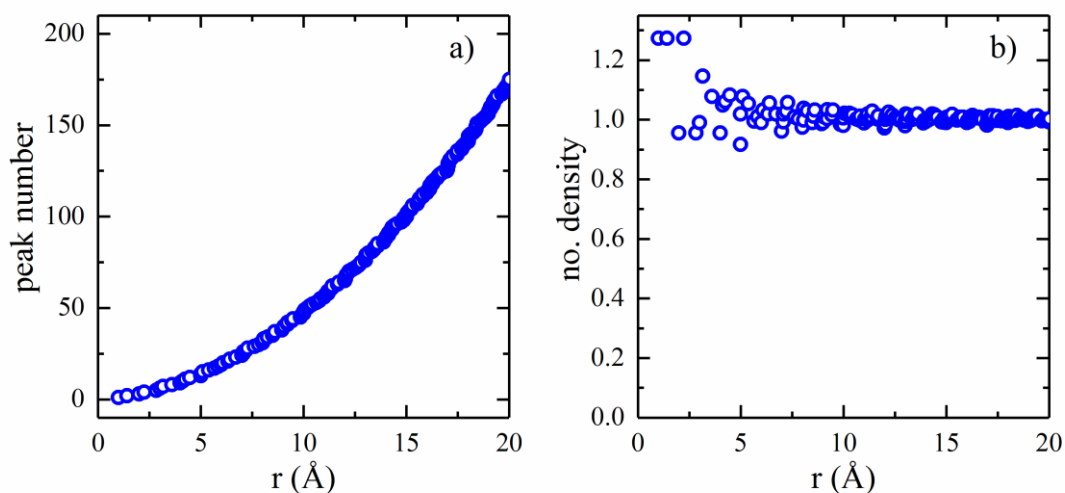
Figure 2.16 Peak number and atomic number density of Figure 2.15 as a function of distance *r*.

2.3.5   Important aspects of PDF analysis

In order to properly analyse PDF data there are several aspects which need to be explained, including the different forms of the PDF and the features of a PDF which can be used to extract useful information. A thorough review of these is published in Takeshi Egami and Simon Billinge's *Underneath the Bragg peaks: Structural Analysis of Complex Materials* [52].

2.3.5.1   Importance of *Q*-range

The Fourier transform operation is calculated over a set Q range (Q_{min} to Q_{max}) of $S(Q)$ which acts as an interruption in an ideal FT whose bounds are $\pm\infty$. These interruptions produce so called termination ripples, errors which take a sinusoidal form. Therefore, it is important to use as great a Q range as possible. Achieving a suitably small Q_{min} is typically simple, however the maximum Q_{max} is determined by the radiation wavelength and extent of the scattering angle (**Equation 2.8**) and so is highly dependent on the experimental setup. The effects of Q_{max} are shown for a calculated PDF of lead in **Figure 2.17** [120]. A marked dampening of the termination errors with increasing Q_{max} can be observed, negligible at 36 Å^{-1}. At $Q_{max} = 12$ Å^{-1} the termination errors cannot be distinguished from the scattering data, most notably at $r = 5$ Å. Generally, if $Q_{max} > 3/\sqrt{\langle\langle u^2 \rangle\rangle}$, where $\sqrt{\langle\langle u^2 \rangle\rangle}$ is the root mean square of the amplitude of lattice vibrations

the termination errors should become insignificant [112] i.e. Q_{max} should be sufficiently high to distinguish broadening errors from structural broadening. Extending the range of Q too far however, can present problems due to increased statistical noise [52] nonetheless this does not present as much of a problem. In the literature the general consensus is that $Q_{max} = 33$ Å^{-1} is ideal [121], though there are several studies which have used $Q_{max} \approx 24$ Å^{-1} [116], [117], [122]. As shown in **Figure 2.17** this range is still sufficient to distinguish the scattering data from the termination ripples.

Examples of the potentially highest Q_{max} obtainable from different X-rays sources are shown in **Table 2-3**, and calculated using **Equation 2.8**. This includes lab based tube X-ray generators such as copper and silver, X-ray synchrotrons and neutron sources. Realistically however detector coverage is physically limited e.g. lab-based diffractometers typically have a maximum 2θ of 150°, so the Q_{max} values would be somewhat lower. The resolution in r of $G(r)$ is also shown and approximated by $\delta r \approx \pi / Q_{max}$ [52]. Clearly in the case of the Cu X-rays both the available Q_{max} and resolution are not sufficiently high so as to obtain meaningful structural information from a PDF.
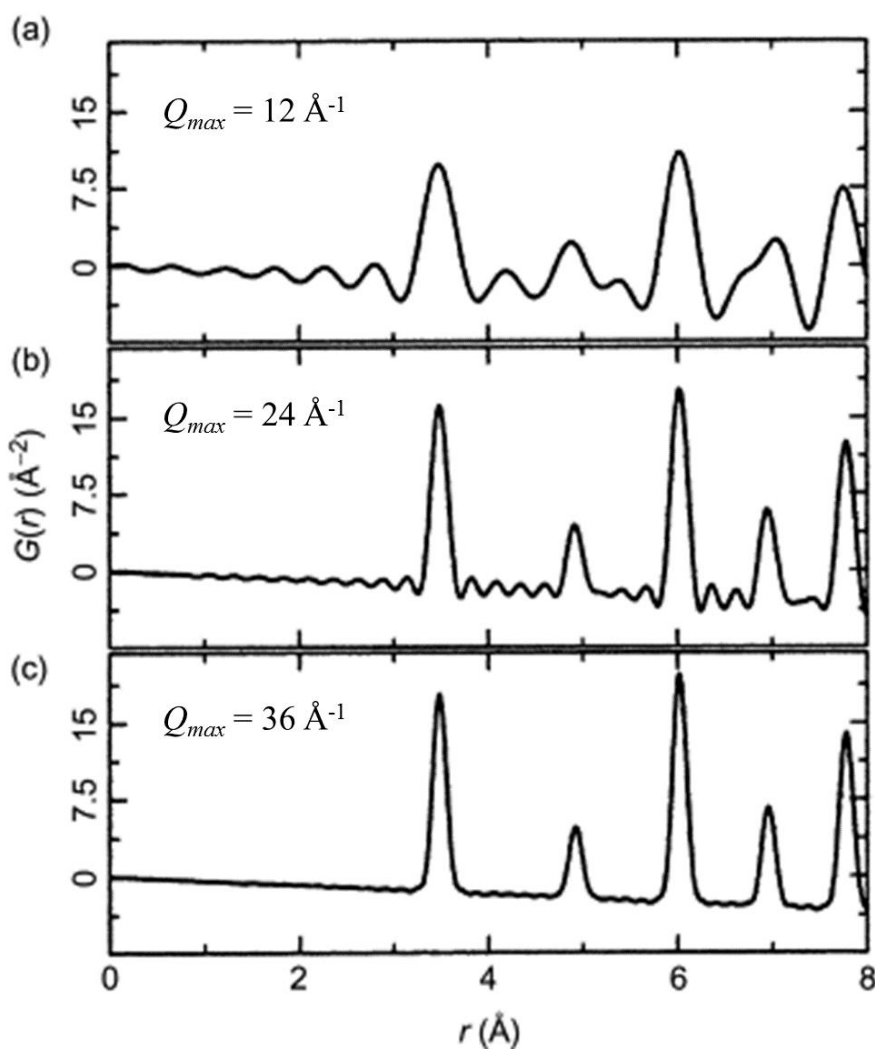
Figure 2.17 Calculated PDF of lead (Pb) showing the effect of Q_{max} on the quality of the PDF. Adapted from [120].

Table 2-3 Effects of probing radiation on Q_{max} and r resolution

Source	wavelength (Å)	Q_{max} (Å^{-1})	resolution in Δr r (Å)
Lab-based Cu X-ray	1.54	8	0.39
Lab-based Ag X-ray	0.56	22	0.14
Neutron	0.4	31	0.1
X-ray Synchrotron	0.2	63	0.05

2.3.5.2 PDF forms

Several correlation functions of the PDF have already been alluded to, namely the pair distribution function $g(r)$, the reduced pair distribution function (PDF) $G(r)$, the pair density function $\rho(r)$, and the radial distribution function (RDF) $R(r)$. All contain structural information and all have their own merits and drawbacks. There are many more '(r)' functions obtainable from total scattering. These originate from different formalisms used in the international community and various choices in the normalisation or multiplicative factors in the functions [123]. The limits of the various function as r approaches zero and infinity, are shown in **Equation 2.21**.

Equation 2.21

a) $$\lim_{r \to \infty} g(r) = 1$$

b) $$\lim_{r \to \infty} \rho(r) = \rho_0$$

c) $$\lim_{r \to \infty} G(r) = 0$$

d) $$\lim_{r \to \infty} R(r) = \infty$$

e) $$\lim_{r \to 0} \begin{Bmatrix} g(r) \\ \rho(r) \\ G(r) \\ R(r) \end{Bmatrix} = 0$$

Generally, $g(r)$ is more intuitive to interpret than $G(r)$, for example it fluctuates around and tends to 1 (**Equation 2.21 a)**), i.e. as infinity is approached the probability of encountering an atom-atom pair is 1. $\rho(r)$ on the other hand tends towards the average density ρ_0 (**Equation 2.21 b)**). These two functions also emphasise low-r distances, falling in amplitude in proportion $1/r$. However as discussed in the following this is not advantageous.

$G(r)$ offers far more advantages. As stated earlier it is directly obtained from the FT of $S(Q)$, whilst $g(r)$ requires prior knowledge of the atomic number density ρ_0, and therefore is considered 'cleaner' data which requires no further calculations. In fact, ρ_0 is

already contained within $G(r)$; the function generally follows a $-4\pi \rho_0 r$ slope at low-r. Both the PDF signal and statistical fluctuations or uncertainties in $G(r)$ are constant across r whilst all information content in $g(r)$ and $\rho(r)$ falls in proportion to $1/r$. Therefore, using $g(r)$ and $\rho(r)$ presents problems when assessing differences in PDFs caused by temperature for example, or comparing a PDF model to experimental data. The difference curves would be affected by the $1/r$ falloff making it non-trivial to determine if a structural model is more suited to low or high-r regions for example.

Another advantage of $G(r)$ is that the intensities of the peaks are related to the structural ordering or crystallinity of the material. It can therefore give an indication of structural coherence length by the decay of the $G(r)$ signal. A perfect crystal for example would have atom pairs extending to infinity, whereas a nanoparticle size determines the maximum coherence length. These effects are illustrated in **Figure 2.18 a)** for bulk and nanoparticulate gold. The decay of the nanoparticulate $G(r)$ occurs roughly at the particle size of 36 Å. Undoubtedly this offers a quick and simple way of assessing a material structure. However, instrument resolution is also an important factor as shown in **Figure 2.18 b)** for neutron PDFs of nickel powder measured with instruments of different resolution. This further emphasises the need for high Q_{max} measurements to push the PDF decay to greater r and reveal potential structural coherence effects [124].
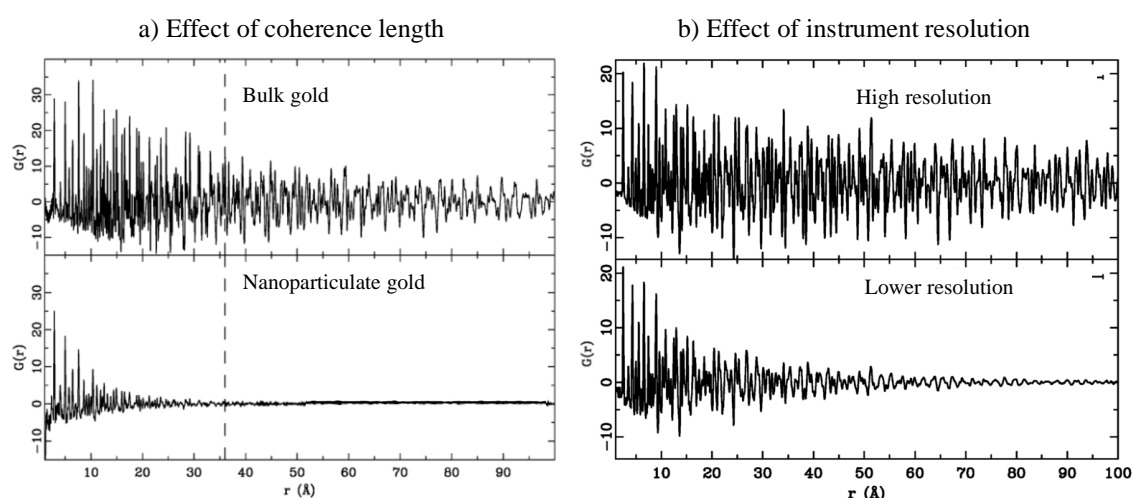
Figure 2.18 Effect of a) coherence length for bulk and nanoparticulate gold and b) instrument resolution on the decay of the PDF signal for Ni powder. Adapted from [124].

2.3.5.3   Radial distribution function

The radial distribution function (RDF) is perhaps the most intuitive to understand and calculated from $G(r)$ or $g(r)$ (**Equation 2.22 a)**). In a similar though more advanced manner to **Equation 2.20** the RDF can be calculated as shown in **Equation 2.22 b)**, where a and b are different atoms and r_{ab} is the magnitude of the distance between them, and f_n is the atomic scattering factor (**Equation 2.2**). It is the three-dimensional equivalent of **Figure 2.15**.

Equation 2.22

a)
$$R(r) = [G(r) + (4\pi r \rho_0)]r = 4\pi r \rho_0 g(r) r^2$$

b)
$$R(r) = \sum_a \sum_b \frac{f_{na} f_{nb}}{\langle f_n \rangle^2} (r - r_{ab})$$

It is useful because $R(r)dr$ gives the number of coordinating atoms in an annulus dr i.e. the area under a RDF peak will be proportional to the coordination number. Shown in **Equation 2.23** , where N_C is the coordination number and $r1$ and r_2 denote the range in r, for example the width of a given RDF peak. Another useful property is that the atom-atom pair peaks in $R(r)$ have a Gaussian shape and are therefore easier to fit unlike other correlation functions which are not exactly Gaussian. However, this function is only suitable to analyse at low-r distances as the function is proportional to r^2 meaning the signal rapidly increases in amplitude, which is not simple to plot.

Equation 2.23

$$N_C = \int_{r_1}^{r_2} R(r)\, dr$$

2.4 Diffraction instruments

2.4.1 Laboratory based XRD

2.4.1.1 Diffraction geometry

Lab based diffractometers typically use the Bragg-Brentano geometry which consists of an X-ray source and detector which revolve in a circular manner around a sample, shown in **Figure 2.19**. In this case the sample remains stationary, whilst the X-ray source and detector move in tandem in clockwise and anti-clockwise directions starting at the 0° line. This experimental set up is best suited to powdered samples which have a complete random orientation of crystallites thus enabling the measurement of all diffraction peaks. A single crystal in this case would only produce peaks related to its orientation relevant to the X-ray source and detector e.g. multiples of (00l): (001), (002) etc. In effect the X-ray pattern produced would be incomplete.
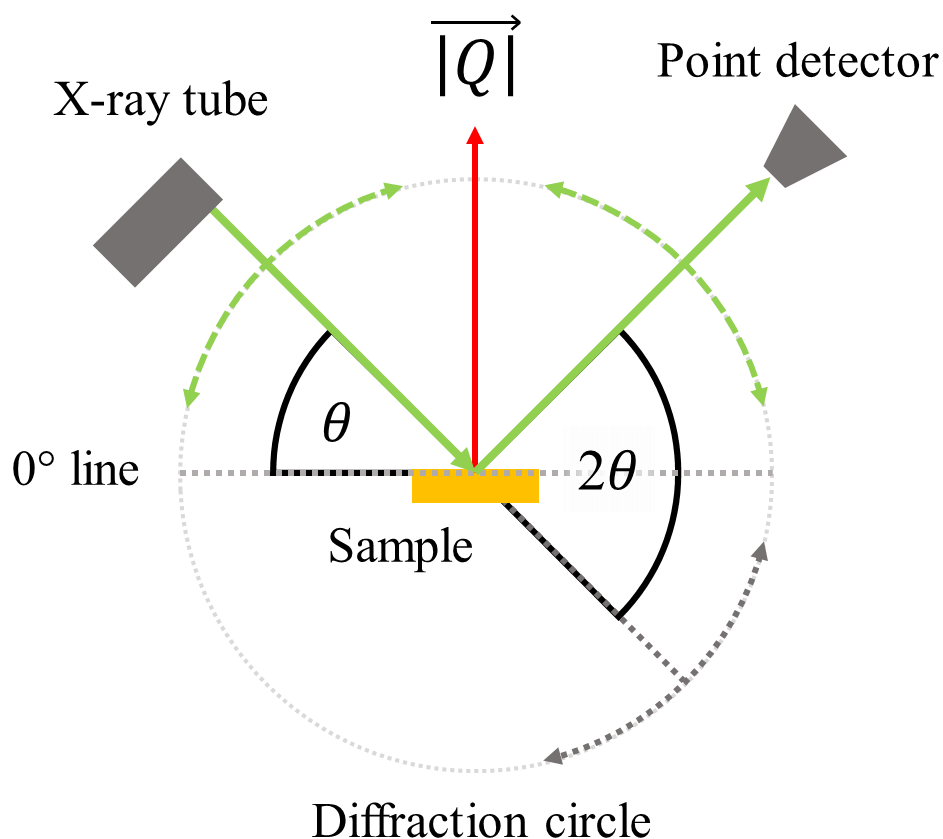
Figure 2.19 Bragg-Brentano geometry typically used in laboratory based XRD measurements.

A resulting feature of the combination of the diffraction geometry and a powder sample is that families of peaks are produced from different crystallites. For example, in lead titanate the following peaks (100), (001), (110), (101) and (111) each belong to a crystallite orientated in a different direction as shown in the case of $PbTiO_3$ (tetragonal) in **Figure 2.20**. The unit cell depictions are orientated in such a way that the scattering vector Q is vertical. This becomes important when subjecting a sample to anisotropic fields e.g. electric or strain, as the orientation of the grains will determine its response to the field.

Figure 2.20 Powder XRD pattern for $PbTiO_3$ showing the crystallite orientation corresponding to different peaks if the scattering vector Q were vertical.

2.4.1.2   Production of X-rays

The production of X-rays begins with electrons produced at a cathode filament via thermionic emission. The electrons are accelerated towards and strike an anode target, typically copper, and in doing so eject an inner shell electron which is promptly replaced by an outer shell electron. This transition is from a higher energy L level to a lower energy inner K level, and via the laws of the conservation of energy a photon of the same energy is produced. Every element has a characteristic L-K transition energy difference, and by equivalence between photon energy and photon wavelength this creates a characteristic X-ray wavelength [9]. In this way, the X-ray wavelength used during diffraction can be

tuned by using different targets as shown in **Table 2-4**. **Figure 2.21** displays this in more detail, illustrating the various energy levels present in copper. As shown there are several X-ray wavelengths that can be emitted depending on the energy levels involved in the electron transitions. The $K\alpha$ X-ray is preferred as it has the greatest intensity and therefore provides the best signal to noise ratio [9]. The other X-rays are also produced at lower intensities and can be removed using absorbing filters, collimators or by data processing.
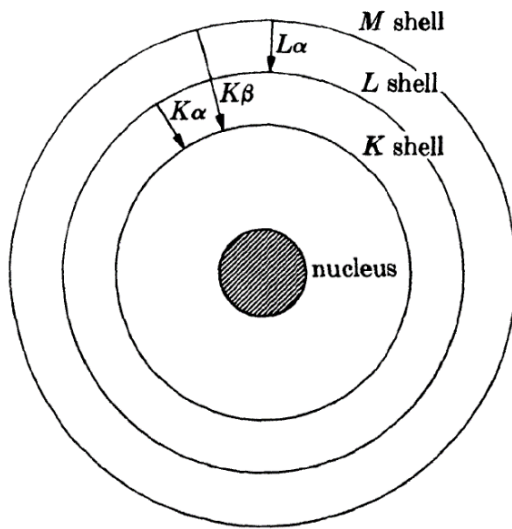
Figure 2.21 Electron energy levels present in copper. Various X-ray wavelengths can be generated, however *Kα* produces the greatest intensity and is therefore preferred. From [9].

Table 2-4 Target elements and the corresponding *Kα* wavelength.

Target element	*Kα* wavelength (Å)
Cr	2.29
Fe	1.94
Co	1.79
Cu	1.54
Mo	0.71
Ag	0.56

2.4.2   Synchrotron XRD

2.4.2.1   Background

A synchrotron is a class of cyclic particle accelerator which accelerates electrons in a circular path and produces high brilliance radiation. Brilliance is a term which describes the radiation via a combination of factors shown in **Equation 2.24** [125]. A high brilliance source will therefore consist of a beam of light which has a well-defined wavelength, narrow size and high intensity. The principal advantages offered by such devices is that high energy (sub-Angstrom wavelength) X-rays enable far higher resolution measurements, and a high X-ray flux reduces the measurement time required significantly.

Equation 2.24

$$Brilliance = \frac{no.\,of\,photons}{time\,\times\,angular\,divergence\,\times\,cross\,section\,\times\,band\,width}$$

Using magnets and radio frequency (RF) electric fields, electrons are forced to travel in a circular path subjecting them to a constant acceleration and reaching relativistic velocities (99% speed of light). When an electron is subjected to these conditions it emits light (synchrotron radiation) in the direction of travel, which takes the form of a radiation cone. Shown in **Figure 2.22** is the general structure of synchrotrons. These contain a source of electrons, typically obtained by thermionic emission, which are then accelerated into an initial storage ring where a controlled injection into the main ring can be carried out. The depicted production of X-rays represents the early generation technology using bending magnets. More modern generations utilise *undulators* and *wigglers* to obtain greater radiation brilliance. The differences between bending magnets, undulators and wigglers are illustrated in in **Figure 2.23**, including the impact on angular divergence of the beam and subsequent radiation spectrum.
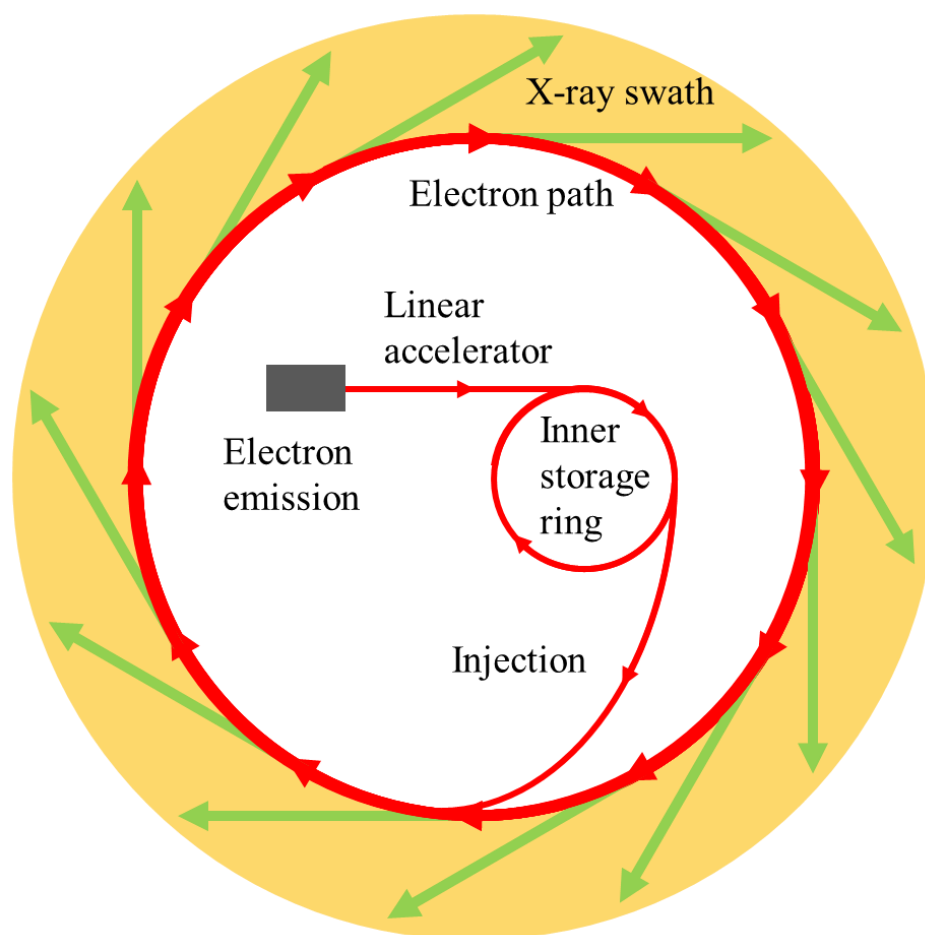
Figure 2.22 General depiction of the production of X-rays in synchrotrons. Electrons accelerated in a circular path produce X-rays radiating tangential to the path.

2.4.2.2 Production of X-rays

2.4.2.2.1   Bending magnets

The radiation wavelength produced by an electron in synchrotron conditions is shown by the proportionality in **Equation 2.25**, where B is the magnetic field, and γ is the Lorentz factor (**Equation 2.26**), v is the speed of the electron and c is the speed of light. The first synchrotrons utilized this phenomenon in a straightforward manner using bending magnets to continuously force a circular path on the electrons. The result is a broad radiation spectrum which includes hard X-rays (0.1 – 2 Å) for crystallographic analysis. The resulting radiation cone has a divergence inversely proportional to the electron speed. A schematic illustration of a bending magnet and subsequently discussed synchrotron sources is shown in **Figure 2.23**.

2.4.2.2.2 Undulators

Undulators include periodic magnets around the circumference of the synchrotron applying weak magnetic fields (around 1 T) to induce oscillations which are smaller than the normal bending magnet divergence cone. This divergence cone is narrow and inversely proportional to the square root of the number of magnets per unit distance (*N*). The resulting oscillations are harmonics producing highly defined radiation wavelengths, proportional to the magnet periodicity.

The expression of the radiation wavelength produced by an undulator is shown in Equation 2.27 [126], where λ_u is the 'wavelength' or period of the magnets, and *K* is described in Equation 2.28, and is the product of several fundamental constants, the applied magnetic field and magnet period. Undulator radiation is produced when the value $K \leq 1$.

2.4.2.2.3 Wigglers

Wigglers differ from undulators in that periodic magnets apply greater magnetic fields (of the order of 4 T) so that the oscillations are greater than the natural divergence cone. In this regime, $K > 1$. The result is an increase in the number of harmonics to the extent that a continuum in the spectrum is formed again, rather than the discrete harmonics formed by the undulator. However, the spectrum is significantly higher in intensity and shifted towards smaller radiation wavelengths [126].

Equation 2.25

$$\lambda \propto B\gamma^2$$

Equation 2.26

$$\gamma = \frac{1}{\sqrt{1 - \frac{v^2}{c^2}}}$$

Equation 2.27

$$\lambda = \frac{\lambda_u}{2\gamma^2}\left(1 + \frac{K^2}{2} + \gamma^2\left(\frac{1}{\gamma\sqrt{N}}\right)^2\right)$$

Equation 2.28

$$K = \frac{e\,B\,\lambda_u}{2\pi mc}$$
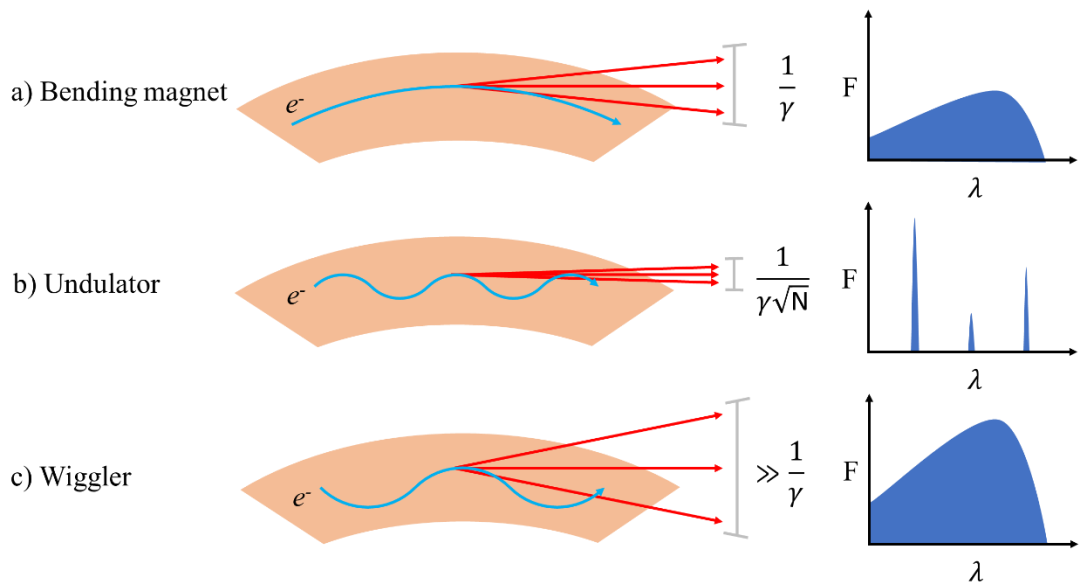
Figure 2.23 Various sources of synchrotron radiation at the corresponding beam's angular divergence and wavelength spectrum. Adapted from [126].

Figure 2.24 shows schematics of first generation synchrotrons (a) using bending magnets, and modern synchrotrons (b) which use undulator and wigglers, requiring the use of several straight sections instead of a continuous circular path.
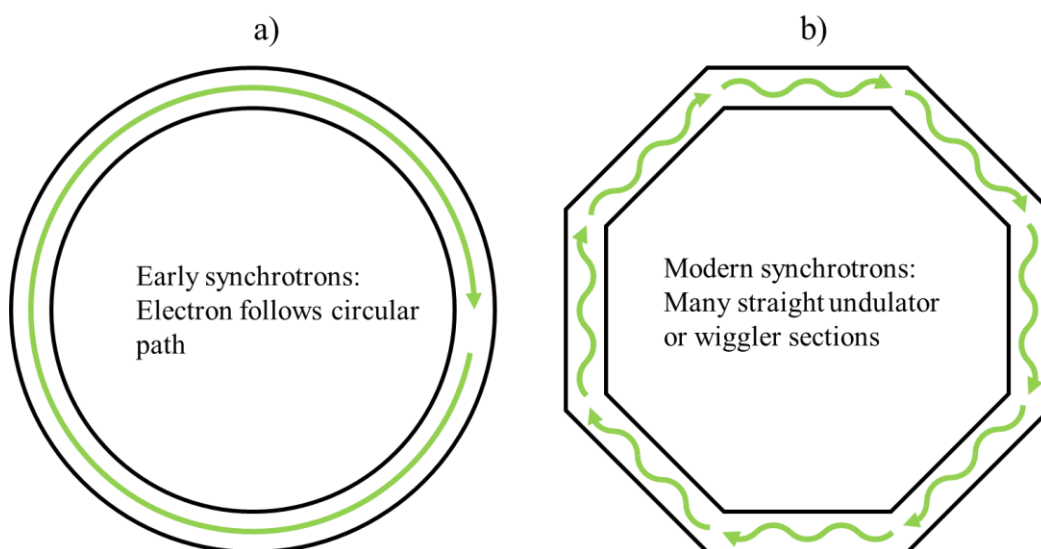
Figure 2.24 a) Early synchrotrons using bending magnets, and b) modern synchrotrons using wiggler or undulator magnets. Adapted from [126].

2.4.3 Flat plate diffraction geometry

Flat plate geometry offers several advantages over a single point detector setup such as the Bragg-Brentano geometry because the scattering vector exists in a 360° plane parallel to the detector plate. For a polycrystalline material, it is particularly beneficial as it contains scattering information from many more grains and is therefore more representative of the entire material. The 360° coverage also enables measurement of anisotropic behaviour such as an electric field or a stress field applied in a specific direction. Response to the field can be measured along or perpendicular to it. **Figure 2.25** shows an example of a diffraction pattern measured on a PerkinElmer flat plate detector.

A possible experimental setup is shown in **Figure 2.26**, which enables the application of perturbing forces such as applied stress, electric field and temperature among many others. In the case of an anisotropic field such as an electric or stress field, different detector sectors will correspond to structural changes with respect to the field vector. For a polycrystalline tetragonal material, each sector will correspond to grains aligned in a specific direction as shown in **Figure 2.27**. In this example selecting the 0° sector will correspond to structural changes along or parallel the field vector and the 90° sector corresponds to changes across or perpendicular to the vector. For a piezoelectric material which experiences strain parallel to the electric field vector one might observe

positive strain parallel due to the structure being extended in proportion to the field (Section 1.10), and the opposite effect perpendicular to the field.

PerkinElmer flat panel detector
1024 by 1024 200μm pixels

Diffraction rings

Shadow from 0° scattered beam-stop
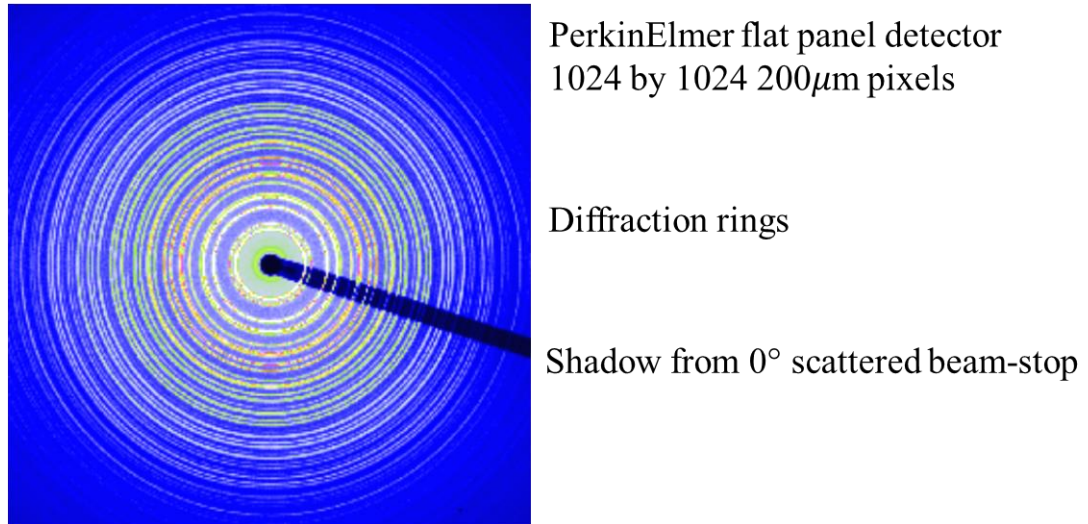
Figure 2.25 Example of a polycrystalline diffraction pattern on a PerkinElmer flat panel detector. The dark shadow is caused by the direct beam-stop which protects the centre pixels from the direct non-scattered X-rays.

Flat panel 2D detector

Debye-Scherrer rings

Applied perturbation:
Temperature, electric field,
stress field etc.

Scattered X-rays

Incident X-ray
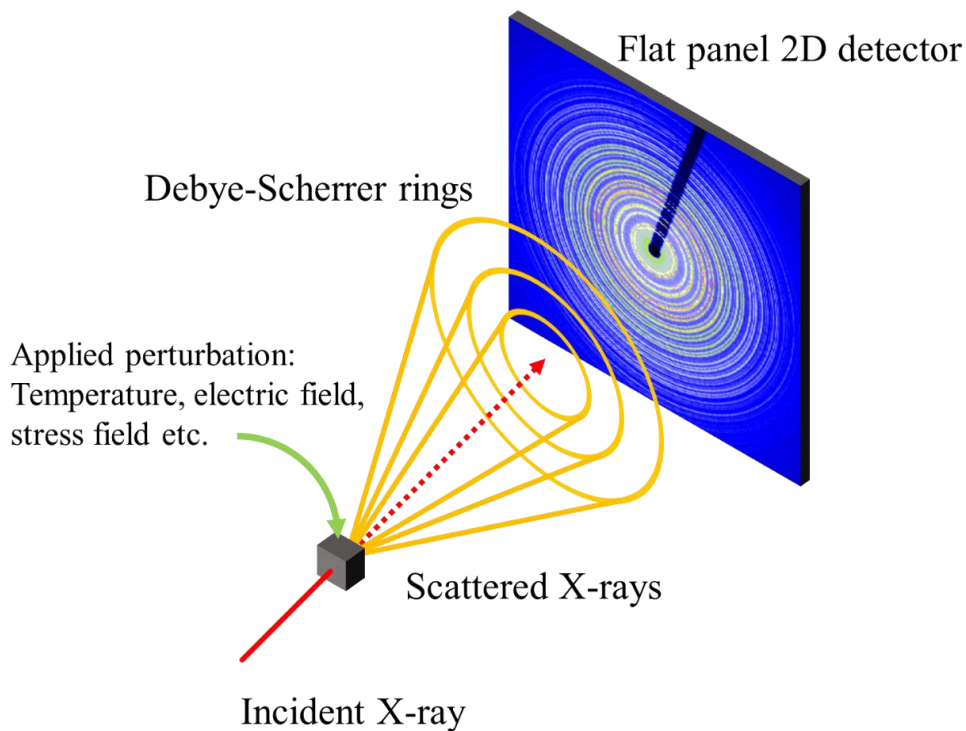
Figure 2.26 Experimental setup for transmission geometry (Debye-Scherrer), with examples of *in situ* parameters which could be used such as an applied electric field or temperature change.
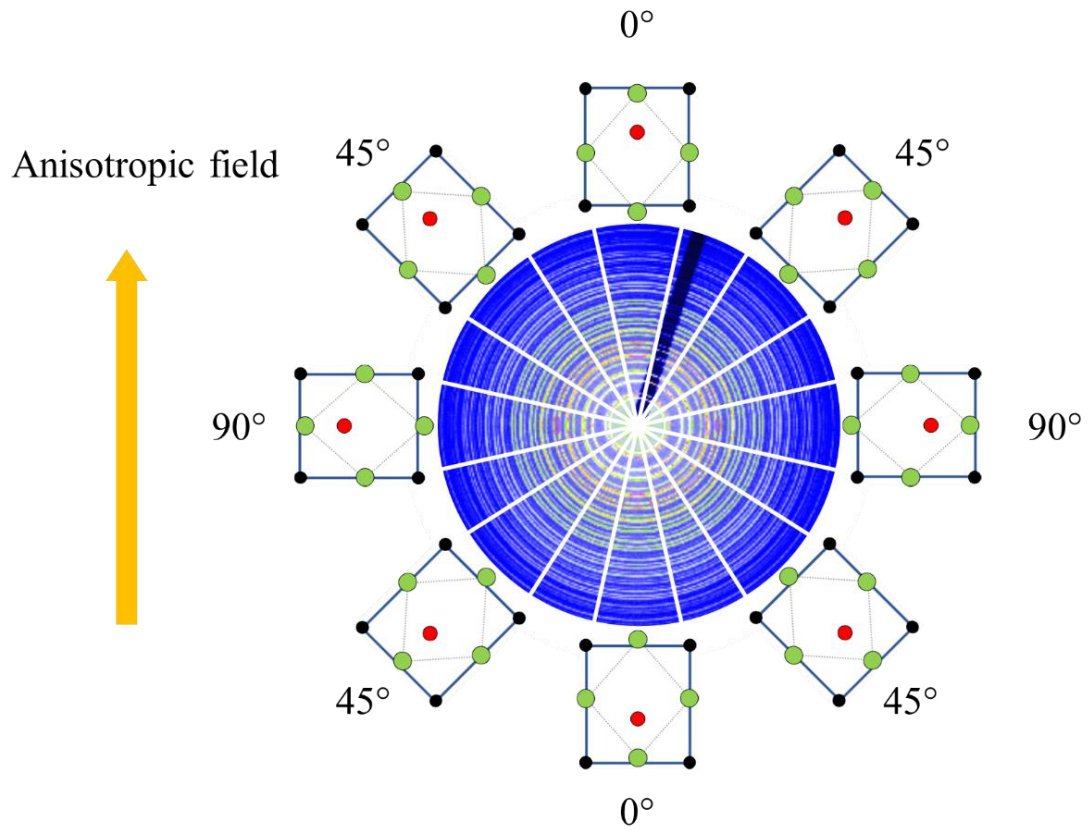
Figure 2.27 For a tetragonal material each flat-plate detector sector corresponds to a differently orientated grain. With the application of an anisotropic field the different sector signals can be isolated to measure directional differences on the diffraction pattern.

2.4.4 *In situ* measurements

An obvious advantage of the synchrotron combined with the 2D plate diffraction geometry is that it enables the coupling of *in situ* measurements (**Figure 2.26**). For example: under applied electric field, pressure and/or temperature measurements. **Figure 2.28** is a cross section diagram of an electric field stage which enables the application of an electric field on a sample where the X-ray beam passes into (X) or out of (O) the page.
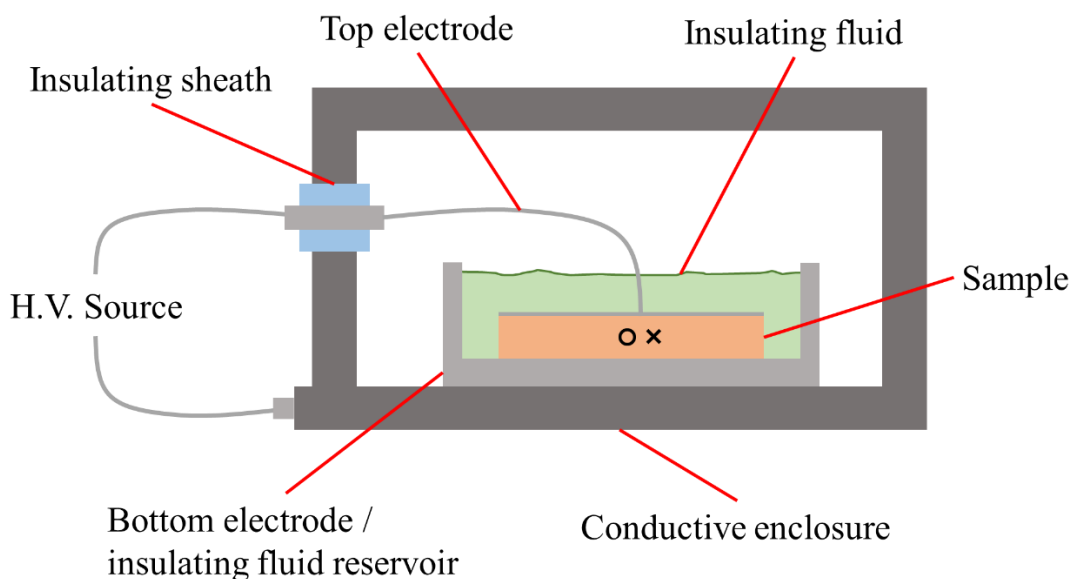
Figure 2.28 Schematic of a transmission diffraction stage enabling the application of an in situ electric field. The 'X' and 'O' symbols denote the path (into or out of the page respectively) that an X-ray beam takes through the sample.

2.5 Data analysis methods

2.5.1 Rietveld refinement

Rietveld refinement is a technique used for the analysis and structural determination of X-ray and neutron diffraction data. It was first developed by Hugo Rietveld [127] and is now a staple tool used to analyse powder diffraction data. The refinement method uses a least squares method (described in Section 2.5.1.1) to obtain the best fit between a theoretical or modeled diffraction profile and the measured scattering data. The theoretical scattering profile is composed of various peak shape functions and backgrounds, whose parameters such as position width and position are altered to fit the scattering data by reducing the residual. The residual between the model and data can be considered by an agreement index or R value [128]. The weighted profile R_{wp} calculation is shown in **Equation 2.29** where $y_i(obs)$ is the measured diffraction profile and $y_i(calc)$ is the calculated or modeled profile at step i, and w is the weight. The statistically expected value R_{exp} is shown in **Equation 2.30**, where N is the number of observations or data points, and P is the number of parameters. The ratio of the two R values is χ^2 or 'goodness of fit' and is shown in **Equation 2.31**. In the literature R_{wp} and χ^2 are typically quoted [128].

Equation 2.29

$$R_{wp} = \sqrt{\frac{\sum_i w_i \left[y_i(obs) - y_i(calc)\right]^2}{\sum_i w_i \left[y_i(obs)\right]^2}}$$

Equation 2.30

$$R_{exp} = \sqrt{(N - P) \Big/ \sum_i^N w_i y_i(obs)^2}$$

Equation 2.31

$$\chi^2 = \frac{R_{wp}}{R_{exp}}$$

2.5.1.1 Least squares method

The least squares regression method is used to fit a function to a data set in order to extract useful information. In this demonstrative example, the method is used to determine the parameters or coefficients which determine the linear trend of a set of data points which follow an approximate linear response i.e. line slope and y intercept (**Figure 2.29**). The calculations are detailed in **Equation 2.32**. Where x and y are the data points, $\bar{x}$ and $\bar{y}$ their mean values, $\hat{y}$ is the calculated linear regression model **a)**, a and b the coefficients or slope and y-intercept respectively. These are calculated in **b)** and **c)**. R^2 is the residual between the data and the fit **d)**, and σ the standard error or deviation of the data **e)**.

Equation 2.32

a)
$$\hat{y} = ax + b$$

b)
$$a = \frac{\Sigma(x-\bar{x})(y-\bar{y})}{\Sigma(x-\bar{x})^2}$$

c)
$$b = \bar{y} - \left(\bar{x}\,\frac{\Sigma(x-\bar{x})(y-\bar{y})}{\Sigma(x-\bar{x})^2}\right)$$

d)
$$R^2 = \frac{\Sigma(\hat{y}-\bar{y})^2}{\Sigma(y-\bar{y})^2}$$

e)
$$\sigma = \sqrt{\frac{\Sigma(\hat{y}-y)^2}{n-2}}$$
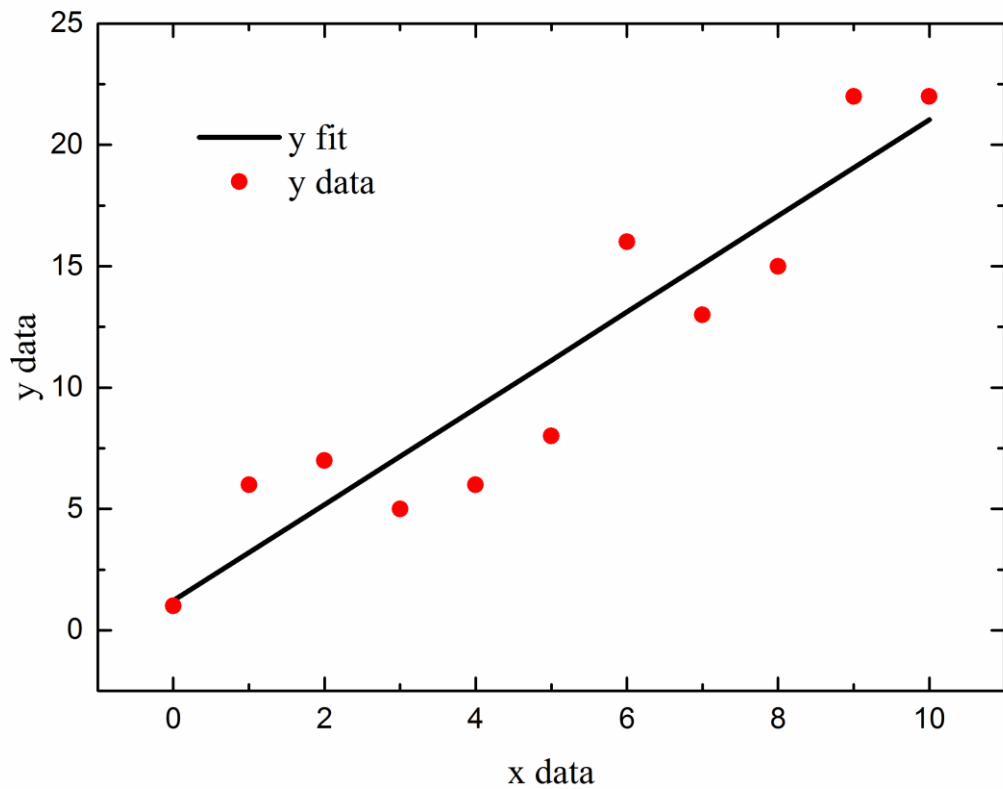
Figure 2.29 Plot showing data with a linear trend and the linear fit obtained by the least squares method.

2.6 Electrical characterisation

One of the fundamental goals of materials science is to improve the understanding of materials via the development of structure-property relationships. So far, the structural measurement techniques have been covered. Here the methods of understanding the electrical properties of piezoelectric ceramics are covered.

2.6.1 Permittivity-Temperature

The permittivity-temperature measurement enables the observation of temperature dependent phase transitions which are useful to determine the operating range of a piezoelectric material, or determine if a material is suitable for capacitor applications. It can also provide insight into other behaviours, for example whether the material is a classical ferroelectric or a relaxor material. The equations defining permittivity and the loss tangent have been covered previously (Section 0). A small oscillating voltage is applied to the ceramic sample at a broad range of frequencies. The induced current through the sample is then measured as a function of frequency and temperature. The permittivity is calculated from these parameters and the sample dimensions and is outputted as a function of temperature. A simple schematic of the circuitry used is shown in **Figure 2.30**.
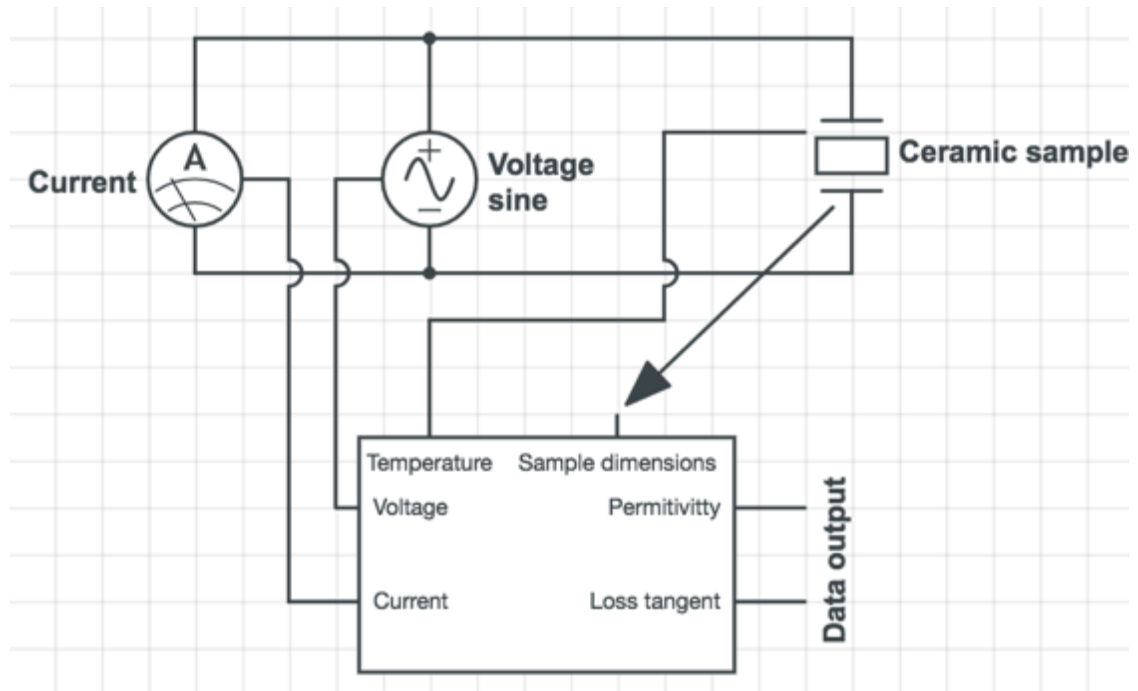
Figure 2.30 Simplified circuit diagram of permittivity-temperature measurements.

2.6.2   Strain-field

Strain is typically measured as a function of an applied electric field. A setup consisting of two optical fibers, one transmitting light and one receiving light is used as shown in **Figure 2.31**. The illumination and receiving cones (A and B respectively) overlap (C) depending on the sample to fiber optic distance. When a high voltage is applied the sample will become strained and extend so it is closer to the receiver and the overlapping area decreases. Two competing effects emerge. The light intensity is proportional to the overlapping area but inversely proportional to the distance, illustrated in **Figure 2.32**. As the distance increases the cone overlap increases and therefore so does the light intensity. However, light intensity decreases with distance and this effect becomes dominant at a critical distance. The initial regime is preferred as the measurement is more sensitive to small changes in distance.
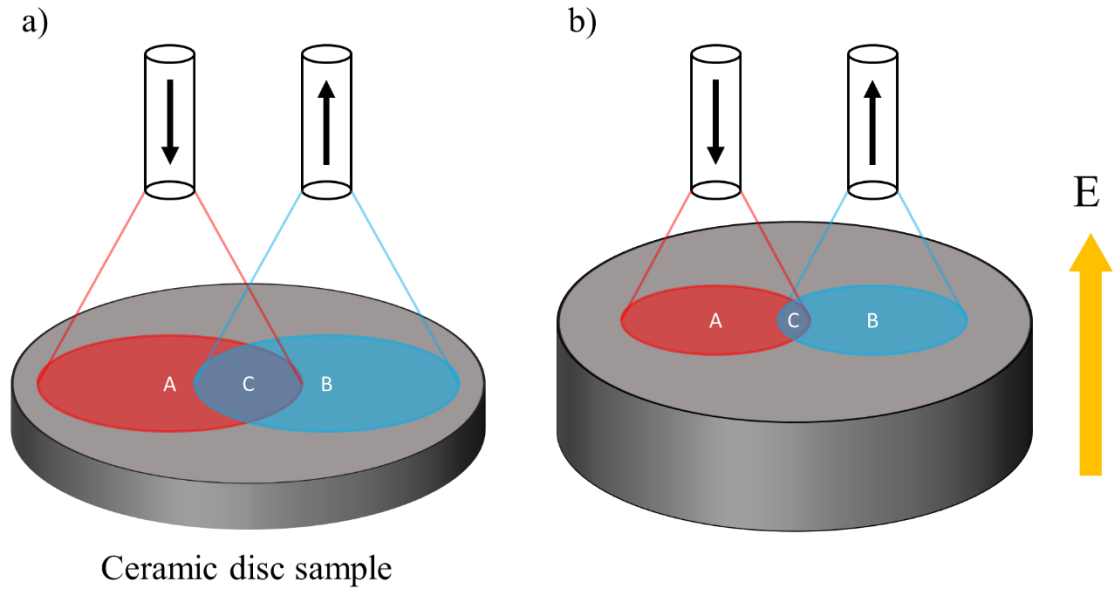
Figure 2.31 Schematic of fiber-optic displacement sensor displacement. a) Piezoelectric sample at zero-field, and b) under an applied electric field. Modified from [44].
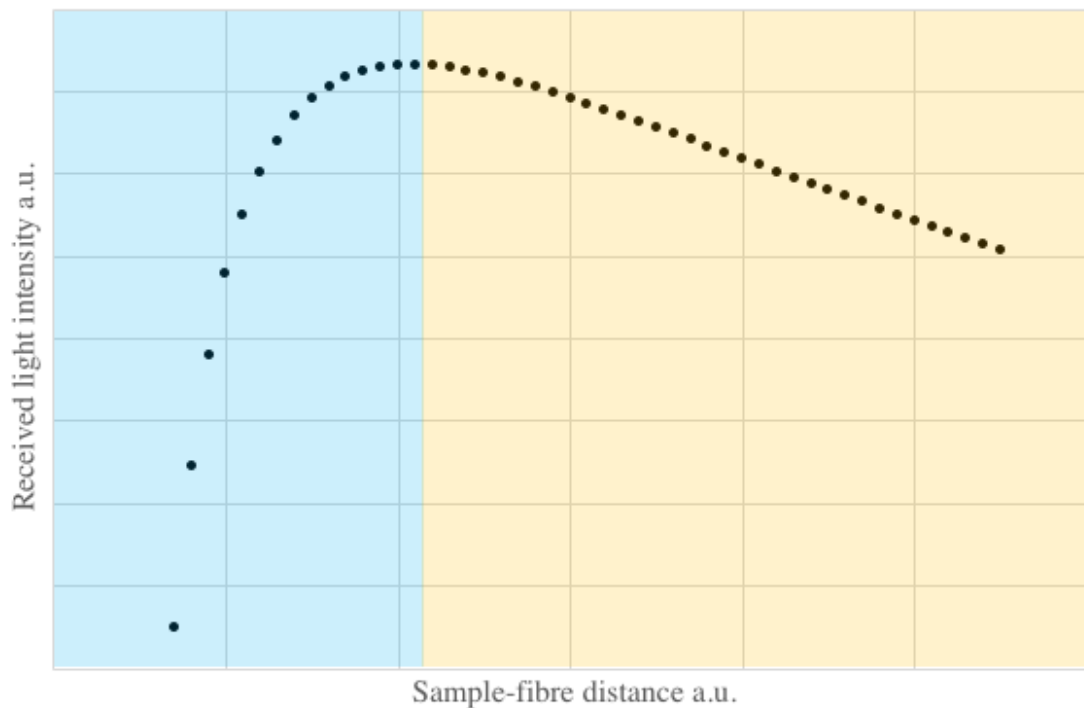
Figure 2.32 Measured light intensity as a function of sample to fiber distance. The two regimes previously explained are highlighted.

Figure 2.33 shows a strain-field or 'butterfly' loop showing characteristic piezoelectric behaviour. From an initial state of zero-net strain (a) an electric field with sufficient magnitude is applied to induce domain reorientation and ionic displacement (b) until the contribution from domain wall motion saturates (c) and the strain adopts a linear behavior described by the converse piezoelectric effect (**Equation 1.15**). At this point the high-field d_{33} can be measured by the strain-field gradient. When the field is removed the strain decreases to a remnant value (d) where the domain orientation is maintained. Some domain relaxation occurs at lower fields, shown as a deviation from the linear piezoelectric trend. At this point the high strain-field gradient at low fields enables exploitation of both ionic displacement and domain wall motion to achieve a higher d_{33}. Reversing the electric field (e) results in a reduction of the strain as the prior domain reorientation is reversed. At a critical field (f) the domains are fully switched and aligned domain growth commences with a resultant strain.
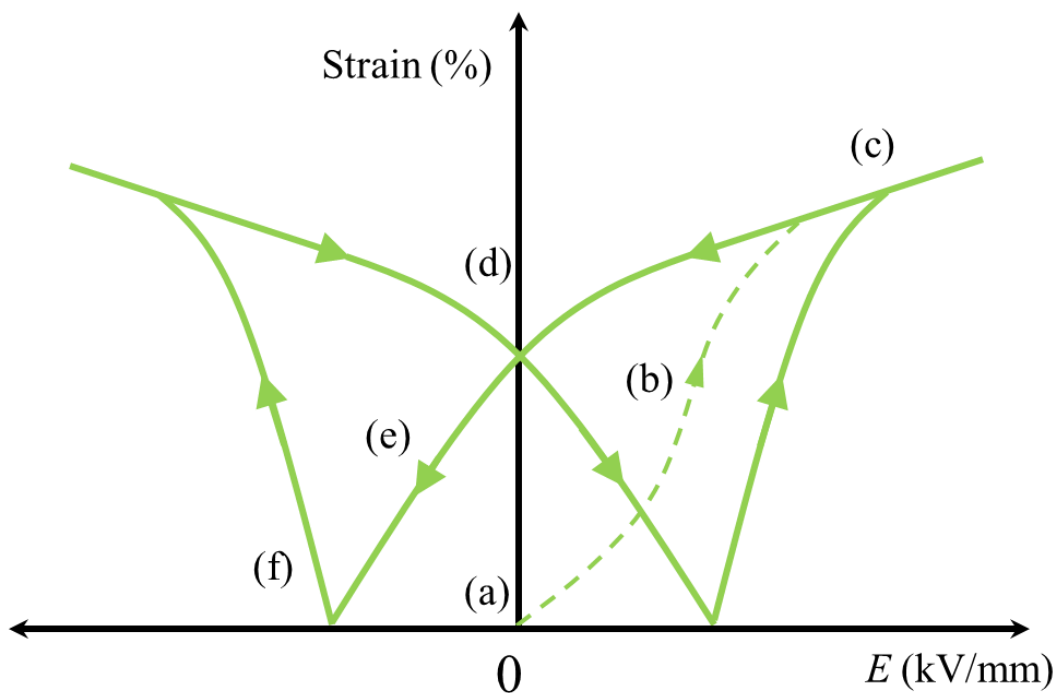
Figure 2.33 A typical strain-field loop for a piezoelectric material. Various key points around the loop are labeled and described in the text.

3 Local and average structure of (1-x)(Na$_{0.5}$, Bi$_{0.5}$)TiO$_3$-xPbTiO$_3$

3.1 Introduction

The solid solution (1-x)(Na$_{0.5}$, Bi$_{0.5}$)TiO$_3$-xPbTiO$_3$ (NBT-PT) has been previously discussed in Section 1.14.6. NBT-PT has an extended morphotropic phase boundary (MPB) around x = 0.13 – 0.15 which exhibits a mixed phase of *R3c* and *P4mm* corresponding to its two endmembers [102], [103]. Due to the endmembers (Na$_{0.5}$, Bi$_{0.5}$)TiO$_3$ and PbTiO$_3$, properties which reflect both relaxor behaviour (such as frequency dispersion of the permittivity), and, depending on the composition, classical ferroelectric behaviour can be observed [101]. The presence of nano-scaled domains or regions of structural coherence have been reported, which disappear with greater PbTiO$_3$ content giving rise to macroscale domains [102], [105]. This is inferred from permittivity measurements of relaxor-like behaviour which suggests nano regions, however no direct measurements of the domains have been demonstrated. It is apparent that this is a material rich in structural and property diversity, reflecting the interaction between a disordered material such as NBT and the influence of PT. For that reason, understanding the origin of these properties can give an insight into the role of lead (Pb) and its ability to typically afford improved piezoelectric properties.

In this chapter the structural properties of NBT-PT are studied for compositions at and around the MPB, namely x = 0.08, 0.14 and 0.18 at ambient temperatures and temperatures up to and beyond their Curie point Tc, which ranges from 200 to 350 °C depending on composition. Principally, a comparison between the average and local structure is drawn using synchrotron X-ray diffraction (XRD) and total scattering X-ray pair distribution function (PDF) analysis.

Permittivity as a function of temperature measurements are also included as they can give an indication of any temperature dependent phase transitions taking place and can therefore corroborate structural transitions observed by XRD [2], [16]. These measurements can also give an indication as to the ferroelectric nature of the material e.g. does it follow classical Curie-Weiss ferroelectric or is there frequency dispersive behaviour, which is typically associated with relaxor ferroelectrics and attributed to the existence of regions of localised polar order [38].

3.2 Material synthesis

Solid solutions of $(1-x)(Na_{0.5}, Bi_{0.5})TiO_3 - xPbTiO_3$ ($x = 0.08$, 0.14 and 0.18) were fabricated via a mixed oxide route. The reagent powders used were: Bismuth (III) oxide (Bi_2O_3), titanium dioxide (TiO_2), sodium carbonate (Na_2CO_3) and lead (II) oxide (PbO) (99.9% purity, Sigma-Aldrich). The reagents were dried at 150 °C to remove any moisture, then weighed and mixed in their stoichiometric ratios for $x = 0.08 - 0.18$. The mixture was ball milled (Capco Test Equipment) in acetone $(CH_3)_2CO$ for 6 hours to ensure the breakup of agglomerates and uniform distribution of reagents. The slurry was dried under continuous agitation to prevent denser reagents, such as PbO, settling. The dried powder was then sieved through a 100 μm mesh. Phase formation was achieved via calcination of the powders at 700 °C for 6 hours in closed alumina crucibles. The calcined powder was ball milled again in acetone for 6 hours during which 1 wt% binder (Glascol HA-40) was added to aid the pellet forming process.

Powder samples were uniaxially pressed (Apex) into 10 mm by 1mm thickness pellets at 1 MPa and then further isostatically (Stansted) pressed at 200 MPa. The pellets were placed on a powder bed of the same powder composition and sintered at 1100 °C for 3 hours. An initial slow ramp rate of 50 °C/hour up to 600 °C was used to burn off the binder after which the rate was increased to 300 °C/hour up to the sintering temperature. For the permittivity measurements the pellets were ground and polished and silver electrodes (Gwent) were deposited onto opposing faces and fired on at 550 °C.

3.3 Experimental methods

Sintered ceramic pellets for compositions $x = 0.08$, 0.14 and 0.18 were crushed into powders and annealed at 500 °C to reduce any stresses induced during crushing. The powders were placed in 1 mm diameter Kapton capillaries. Data were collected for 5 minutes at a range of temperatures. At room temperature (25 °C), then from $100 - 400$ °C in 25 °C steps. Resistive heating coils were used to heat the sample environment shown in **Figure 3.1** [129].
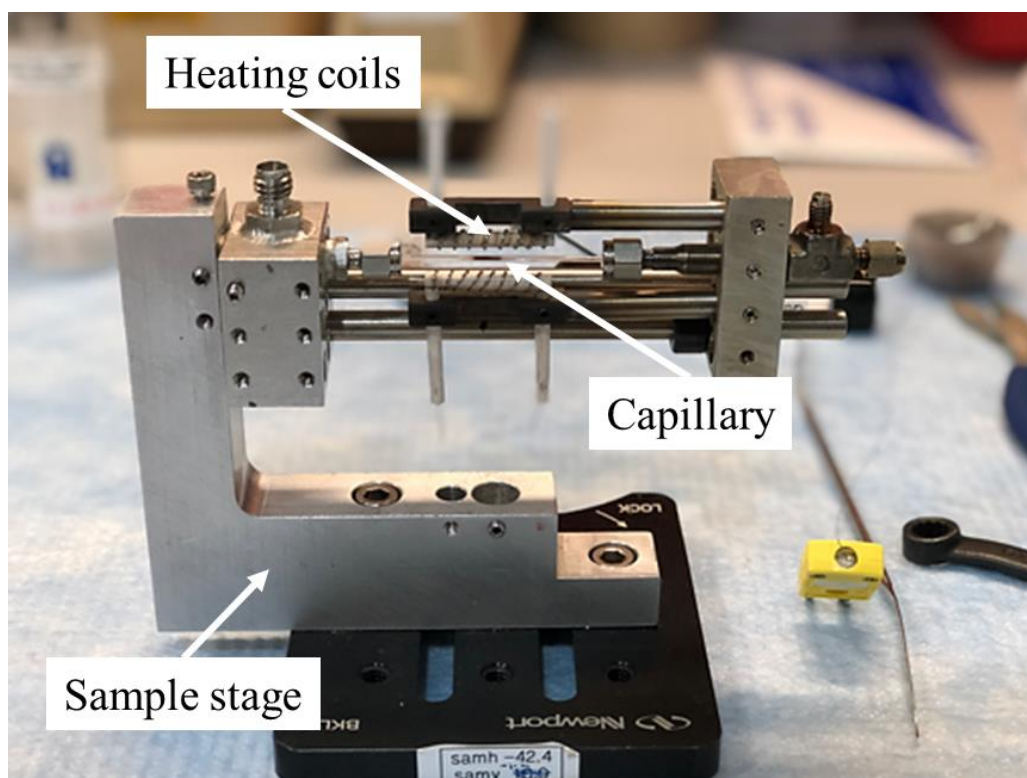
Figure 3.1 Heating stage at 11-ID-B. Heating is achieved via resistive heating of coils near the capillary.

X-ray scattering data were collected at 11-ID-B at the Advanced Photon Source (APS) at Argonne National Laboratories in Illinois, USA. An incident wavelength of 0.143 Å (86.5 keV) was used with sample to detector distances set in two positions: 1) long distance (950 mm) for conventional X-ray diffraction measurement which provides an insight into the average structure of a material, and 2) a short distance (250 mm) which coupled to the wavelength produced a usable Q_{max} of 23.4 Å^{-1} which is suitable for pair distribution function (PDF) analysis obtained from the Fourier transform (FT) of the total scattering structure function. This has been previously covered in detail in Section 2.3.

Shown in **Figure 3.2** the effect of sample-detector distance is illustrated. Q_{max}, a parameter typically desired to be high for PDF analysis, is inversely proportional to the distance. For long sample-detector distances however, there is the benefit of improved resolution i.e. detector pixels per unit of Q space or scattering angle θ.

$$\frac{Pixels}{\theta} \propto d$$

$$Q_{max} \propto \frac{1}{d}$$

Detector

θ

d

Detector

θ

d
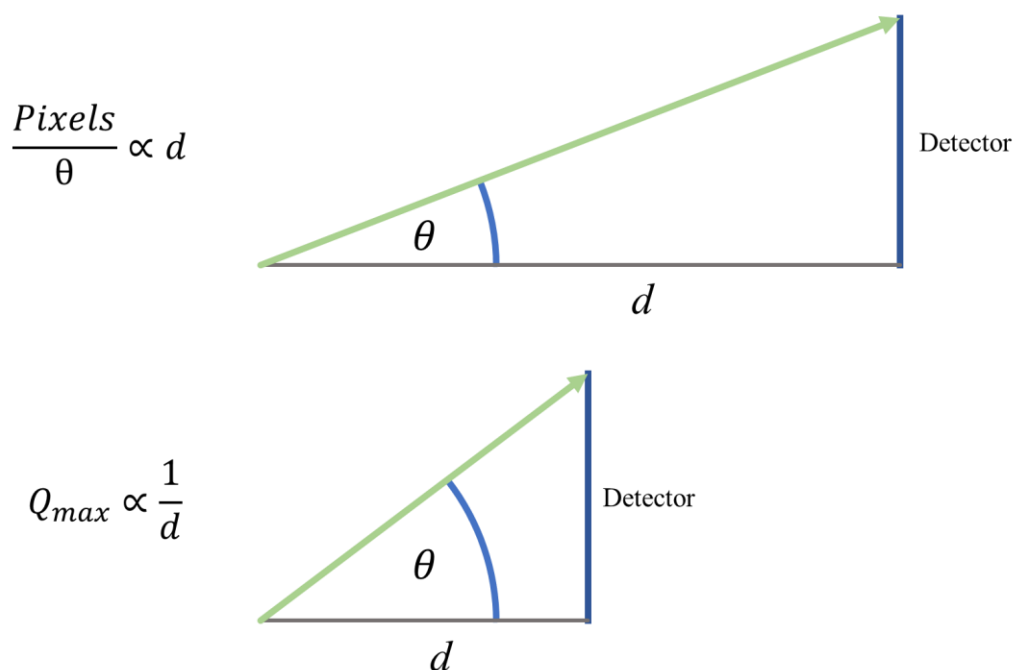
Figure 3.2 Schematic representation of sample-detector distance and its effects on Q_{max} and resolution.

Fit2D software was used to process the 2D diffraction data by integrating full 360° sector of the detector [130]. In the long detector distance regime diffraction data was analysed by peak fitting software and full profile refinement using the Le Bail method (HighScore Plus). Pair distribution function was converted from diffraction data in the short detector distance regime with the PDFgetX3 software [131]. To obtain the total scattering structure function $S(Q)$ the empty capillary was used for background subtraction and subsequent PDF extraction.

PDF profile refinements were carried out with PDFgui software [132] for full profile and range dependent refinements. This approach is very similar to Rietveld refinement which involves a least squares regression fit, previously covered in Section 2.5.1. Refined parameters include: Scale factors, lattice parameters, atomic fractional positions, anisotropic thermal parameters and peak broadening parameters.

Permittivity temperature data were measured on sintered pellet samples with a HP 4192A LF (Agilent, USA) impedance analyser for temperatures ranging from 20 - 500 °C at a broad range of frequencies (10 Hz – 10MHz). For clarity only 10 kHz, 100 kHz and 1000 kHz (1 MHz) will be shown. The heating and cooling rates were 3 °C per minute. The measurements were taken upon heating and cooling from the maximum temperature

(500 °C). The temperature was measured with a K-type (-200 to 1100 °C) thermocouple in a tube furnace alongside the mounted sample. Temperature and permittivity data were collected with LabVIEW software via a GPIB (IEEE) interface.

3.3.1 Note on error and standard deviation of results

As with any result it is important to know its statistical significance, which is typically represented by error bars. These error bars by convention signify the standard deviation of said result. This is no different for structural analysis results, for example lattice parameters, be they obtained by structural refinement methods or individual peak fitting methods. If any calculations are performed on results it is important to propagate the errors associated with those results, for example in a tetragonal structure the unit cell parameters a and c will have values and associated errors. When plotting the commonly quoted measure of tetragonal strain c/a it is important to also ascribe an error to that result. In this case the quadrature method of error calculation can be used as the calculation is simple division. However, in other cases this is non-trivial. A key example is the calculation of the rhombohedral angle from the hexagonal unit cell a and c lattice parameters. The calculation is not simple and contains several trigonometric functions. For this reason, in the work presented here the error of parameters derived from calculations will represent their upper and lower bounds instead of a true standard deviation. This is to say that in the example of the rhombohedral angle, the errors in a and c will be used to calculate the range of possible values of the rhombohedral angle and use this range to represent the error in the measurement. In plot figures this is represented by a shaded area around the data points.

3.4 Results

3.4.1 Permittivity temperature measurements

Permittivity temperature measurements were used to observe ferroelectric to paraelectric transitions characterised by a peak in the relative permittivity and loss tangent. The relative permittivity maxima (T_{max}) associated with the ferroelectric-paraelectric transition observed in classical ferroelectric material following Curie-Weiss behaviour occurs at the transition temperature. Frequency dispersive behaviour i.e. a

change in the T_{max} and maximum relative permittivity (ε_{max}) as a function of frequency, and a broad or diffuse ε_{max} peak is typically associated with relaxor-ferroelectric behaviour.

Data for $x = 0.08$ are shown in **Figure 3.3**. A sharp increase in relative permittivity is observed around 240 °C upon heating, and around 220 °C upon cooling. T_{max} occurs around 280 °C and 270 °C upon heating and cooling respectively, though the maxima peak is quite broad. T_{max} increases with frequency, whilst ε_{max} decreases with frequency. The combination of the sharp transitions and frequency dependent behaviours indicate that the two regimes of classical and relaxor ferroelectric behaviour, as discussed previously, are present in this composition. Tan δ measurements follow similar trends. The negative values observed at 1000 kHz occur due to induction in the measurement leads and improper compensation. However, the general trend observed reflects real results.
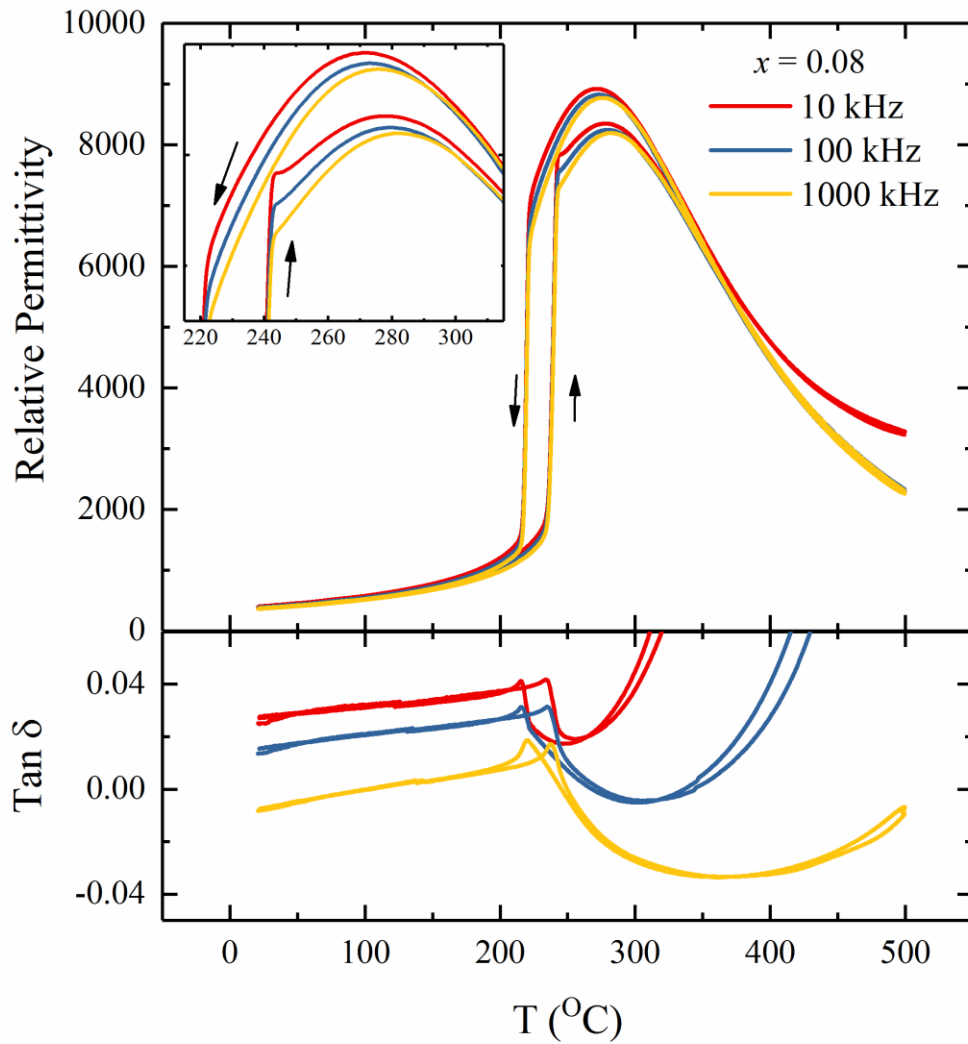
Figure 3.3 Relative permittivity and loss tangent measurements for x = 0.08. Inset shows a close-up of the transition temperature and T_{max} for the relative permittivity.

For x = 0.14 (**Figure 3.4**) the sharp transition is observed at higher temperatures of approximately 305 °C and 295 °C upon heating and cooling respectively. Around 375 °C a small knee is observed in the permittivity, more observable in Tan δ. Relaxor ferroelectric behaviour is still apparent from the frequency dispersive behaviour, however T_{max} occurs far closer to the sharp transition with a difference of approximately 10 °C, instead of 40 – 50 °C observed for x = 0.08. Additionally, the difference between the heating and cooling of T_{max}, or hysteresis in the permittivity is approximately 10 °C instead of 20 °C for x = 0.08. This shows that increasing PbTiO$_3$ (PT) content in NBT-PT is inducing a decrease in relaxor behaviour. Again, there appears to have been poor compensation of the sample stage.
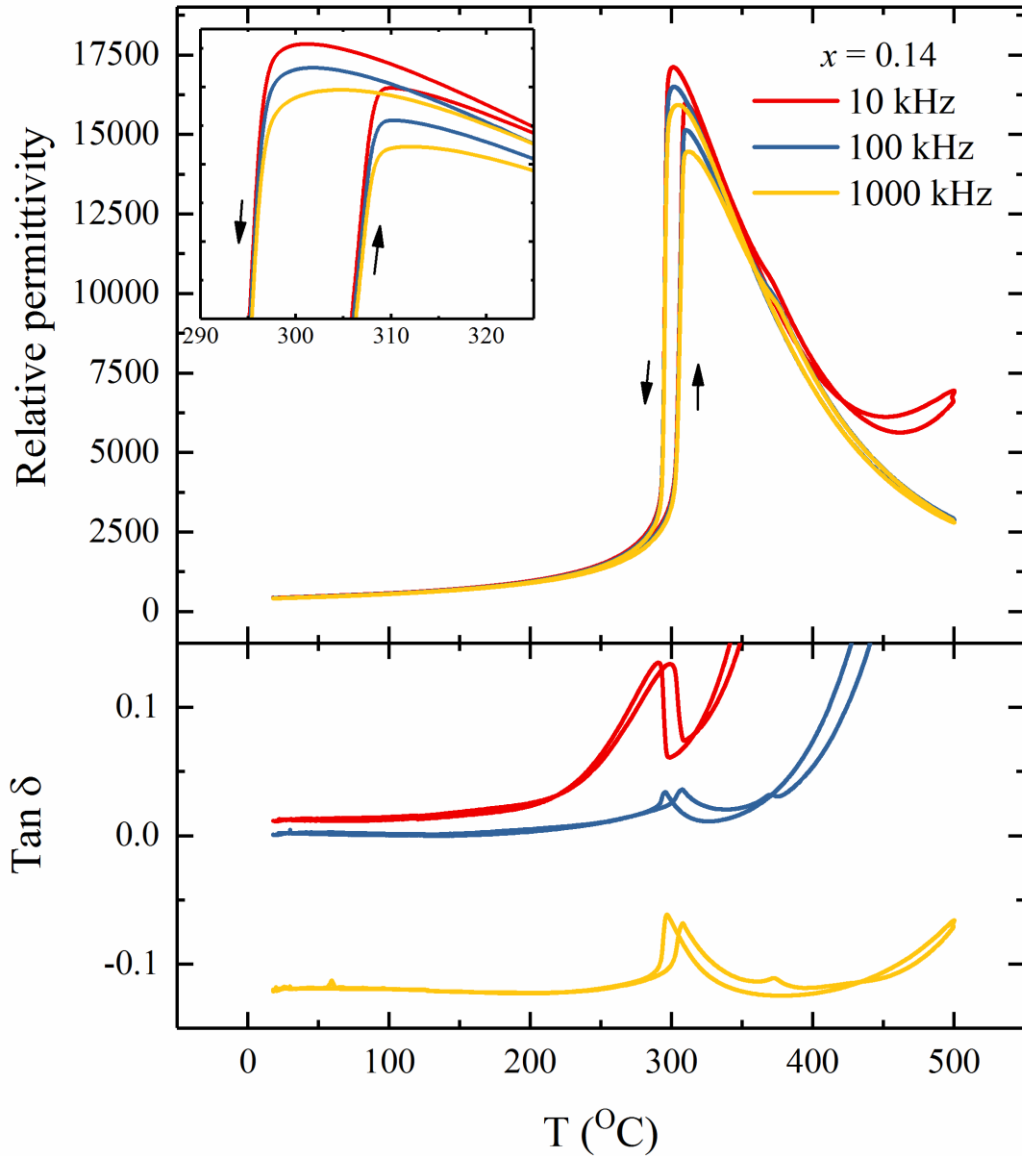
Figure 3.4 Relative permittivity and loss tangent measurements for $x = 0.14$. Inset shows a close-up of the transition temperature of the relative permittivity.

Measurements for $x = 0.18$ are shown in **Figure 3.5.** The hysteretic behavior reduces to approximately 5 °C and the frequency dispersive behaviour is less apparent with smaller changes in T_{max}, though changes in ε_{max} can still be seen. In this case T_{max} could be considered the Curie temperature T_C. The transition occurs around 330 °C
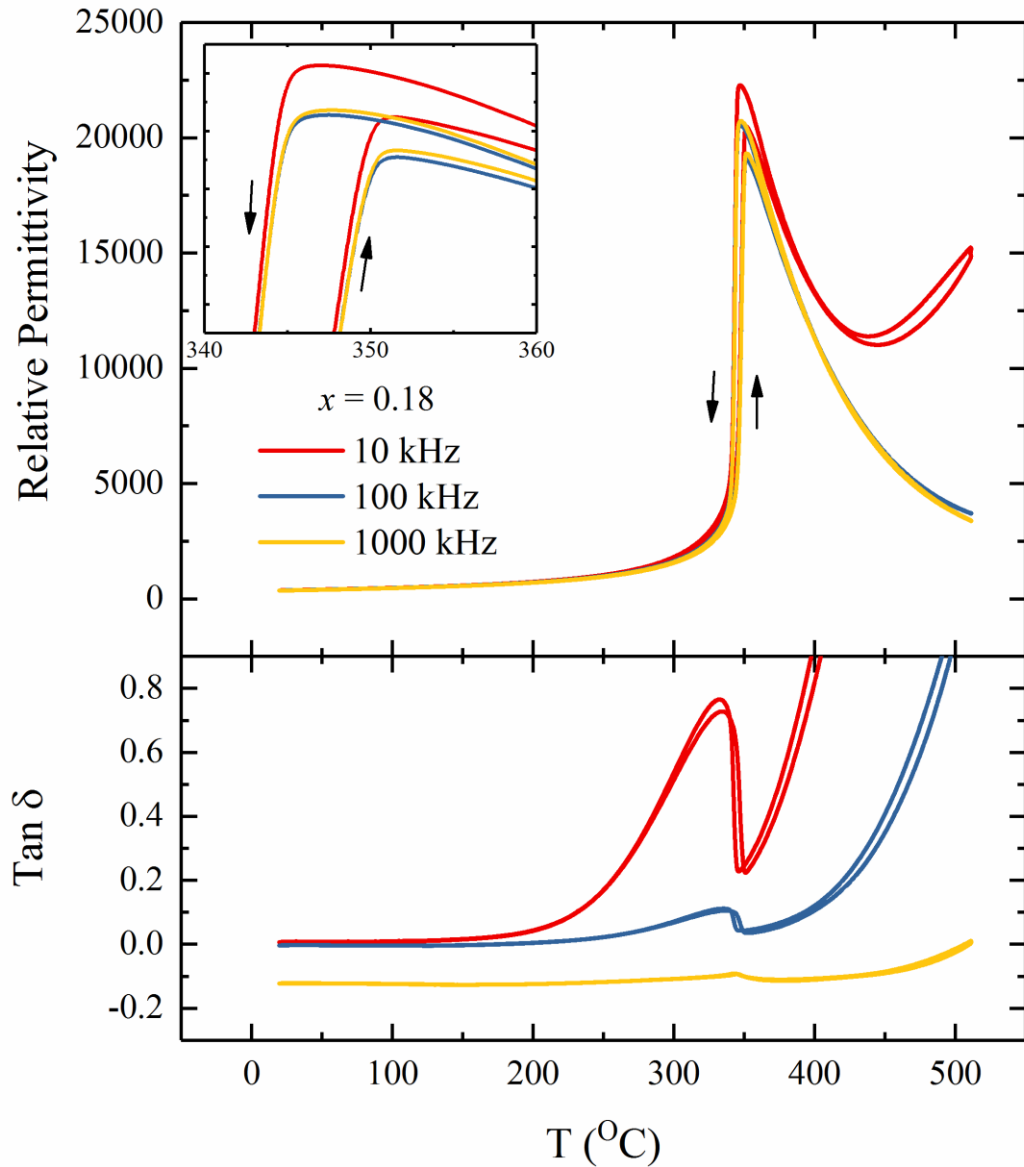
Figure 3.5 Relative permittivity and loss tangent measurements for *x* = 0.18. Inset shows a close-up of the transition temperature of the relative permittivity.

Permittivity measurements at 100 kHz for *x* = 0.08, 0.14 and 0.18 are shown together in **Figure 3.6** to highlight the compositional differences and trends. The transition from relaxor-like to classical ferroelectric is clear. Lead titanate is a highly strained and ordered material. It is suggested that with greater PT content a greater degree of ferroelectric order is induced which disrupts the presence of localized ferroelectric order or polar nanoregions found in NBT related materials.
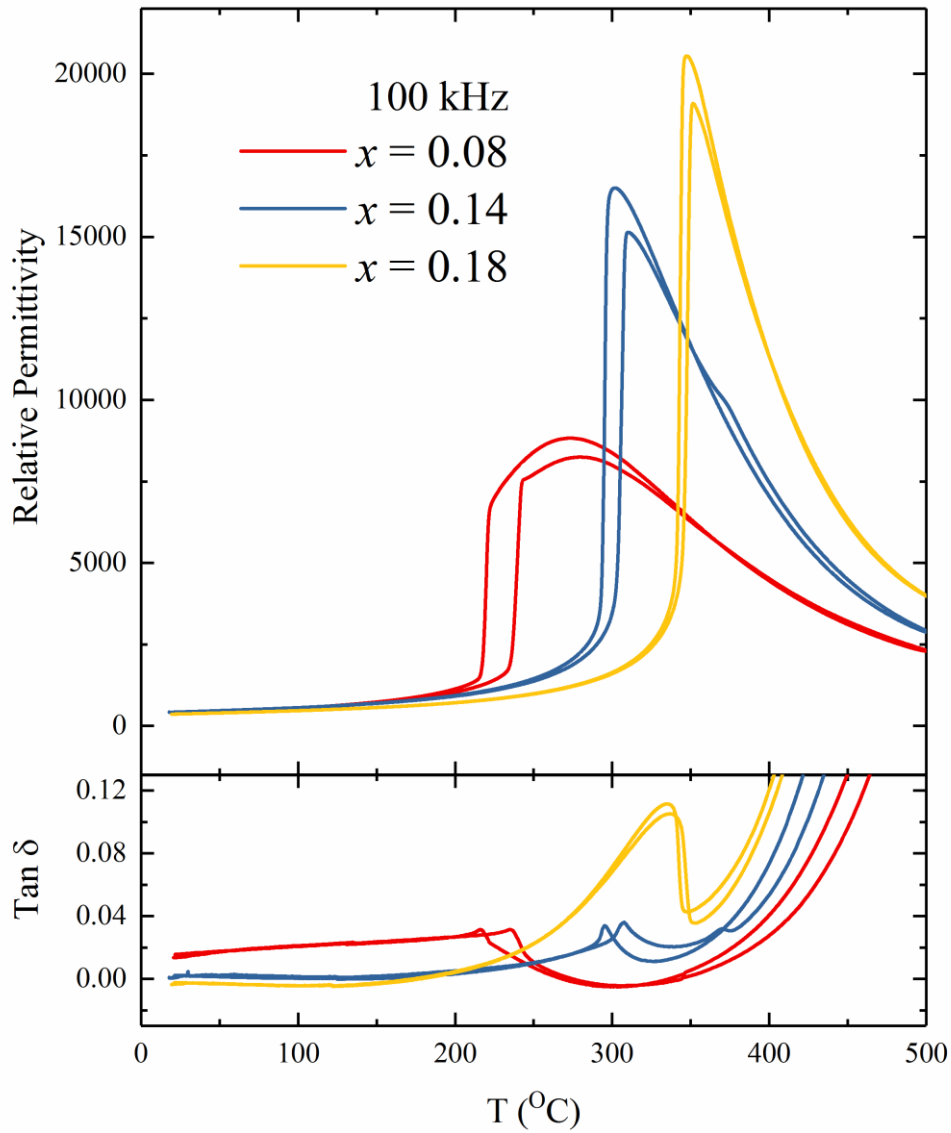
Figure 3.6 Permittivity and loss tangent measurements for all compositions at 100 kHz.

The ferroelectric or relaxor character can be further interpreted by plotting the inverse permittivity. As previously discussed in Section 1.8.2 a ferroelectric material follows the Curie-Weiss law for which above the transition temperature the permittivity is inversely proportional to the temperature. In this case the inverse permittivity would therefore follow a straight line. **Figure 3.7** shows the inverse permittivity for all the compositions. A linear regression fit was taken from the 450 – 500 °C range. The point at which the linear fit intercepts the x-axis i.e. infinite permittivity is the theoretical temperature at which the transition from paraelectric to ferroelectric would occur. The

difference between this point and the measured transition decreases with increasing PT content. This further illustrates the decreasing ferroelectric character with increased $PbTiO_3$ content. Interestingly however, the inverse permittivity appears to diverge from the linear fit at around 430 °C for all compositions, which suggests that nanoregion formation temperatures is not determined by composition.
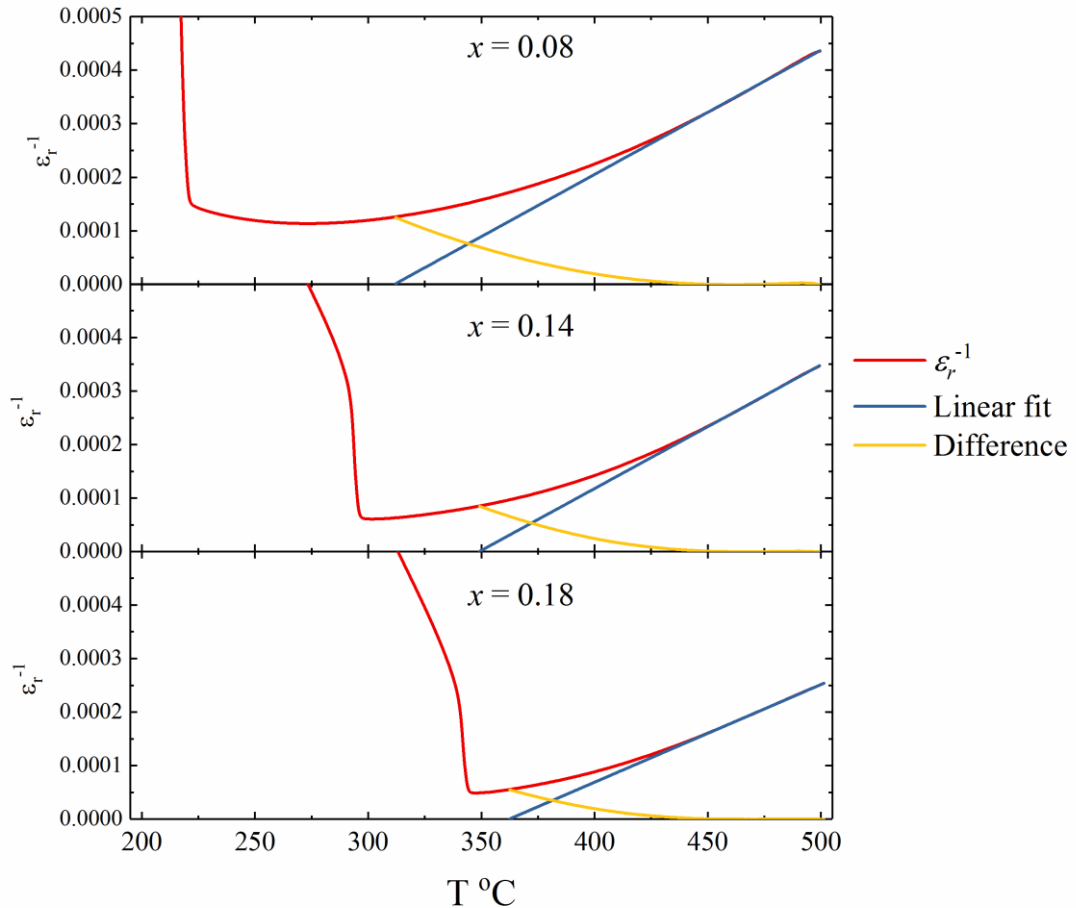
Figure 3.7 Inverse permittivity as a function of temperature for all compositions. The linear fit and difference plots are also shown.

3.4.2 Synchrotron X-ray Diffraction

X-ray diffraction data were collected as a function of temperature from ambient temperature (25 °C) and then from 100 - 400 °C in 25 °C steps. **Figure 3.8** shows ambient temperature data for all compositions, showing peak positions and intensities characteristic of a perovskite structure. All peaks in this figure are indexed in the pseudocubic form. For $x = 0.18$ clear splitting of the {100}, {200}, {210}, {220} and

{300} peaks indicate a tetragonal structure. The {110} peak also exhibits splitting but this is not clear in the figure. The same peak families exhibit peak doublets for $x = 0.14$. The lowest $PbTiO_3$ content composition $x = 0.08$ has peak splits corresponding to the rhombohedral structure, e.g. {111}. However, in the figure only {220} is clear. Peak analysis of the {222} splitting associated with a rhombohedral distortion is shown more clearly in **Figure 3.13**.
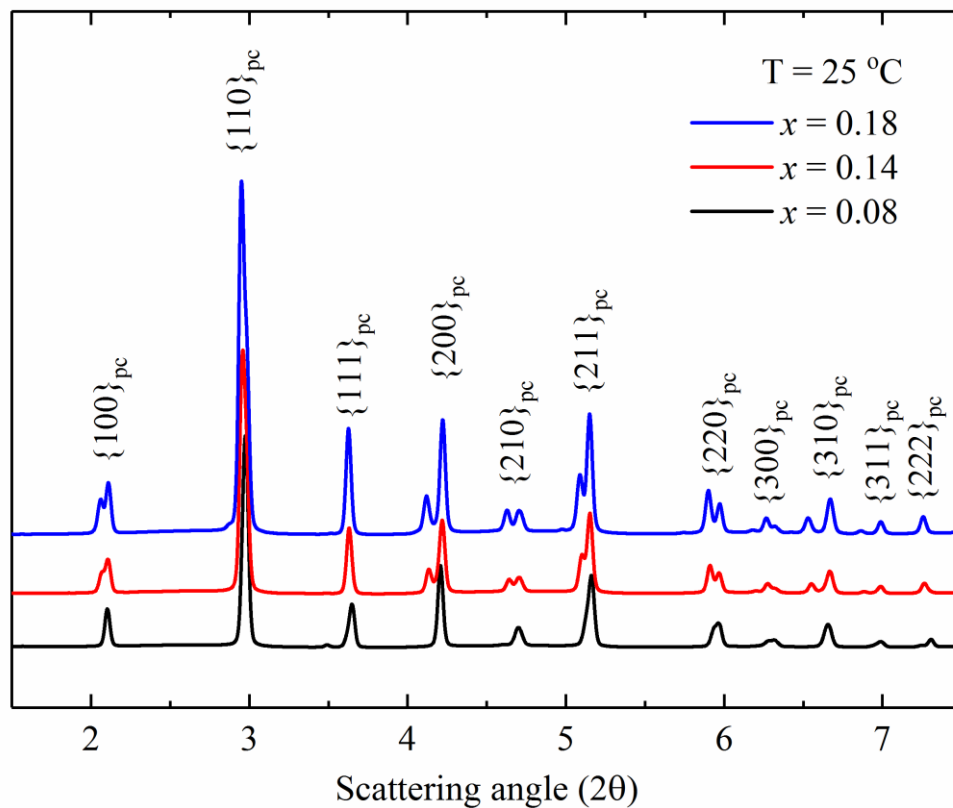
Figure 3.8 Synchrotron X-ray diffraction patterns for $x = 0.08$, 0.14 and 0.18 at 25 °C.

X-ray diffraction data is shown for the highest temperature (400 °C) in **Figure 3.9** where all compositions should exhibit a cubic structure. Peaks are indexed in the pseudocubic setting. The lack of peak doublet presence for any of the peaks confirms this. Permittivity measurements for $x = 0.14$ and 0.18 indicate that 400 °C is above T_C, where a paraelectric cubic structure would be expected.
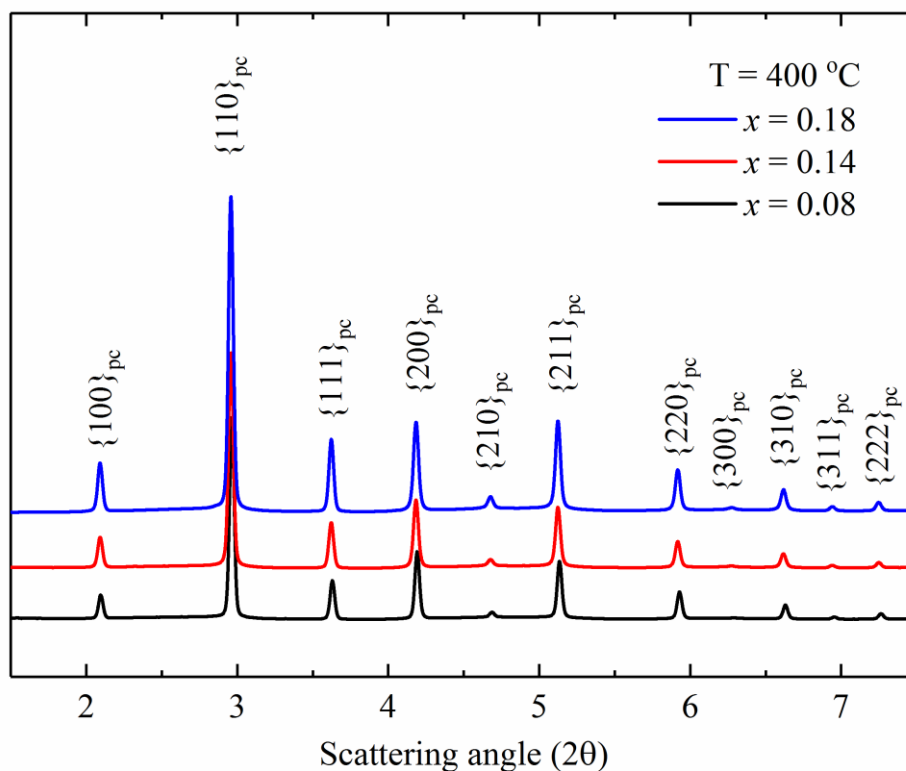
Figure 3.9 Synchrotron X-ray diffraction patterns for *x* = 0.08, 0.14 and 0.18 at 400 °C. The lack of any observable peak splitting indicate that all phases have adopted and average cubic structure.

3.4.2.1 Room temperature refinements

Structure analysis was performed with the Le Bail whole profile refinement method. This method is somewhat simpler than the Rietveld refinement method, focusing primarily on peak positions which it derives from the selected space group phase model. Unlike the Rietveld method peak intensities are not refined. For the purposes of this work i.e. obtain an average structural benchmark from which to compare local structure data, this is a suitable approach. The parameters refined were the background, scale factors, lattice parameters and peak shape parameters. The fit results are shown in Error! Reference source not found.. These errors represent statistical standard deviations, not experimental errors which would be larger.

Figure 3.10 shows the X-ray pattern for *x* = 0.08 with an *R3*c fit. The relatively small difference curve shows good agreement. Vertical black tick marks indicate peak positions of the *R3c* space group. The refinement was done using a hexagonal unit cell.

For clarity the peaks are labelled (a) – (n) and are indexed in the hexagonal and pseudocubic forms in **Table 3-1** for references when comparing to the tetragonal unit cells used in the refinements of $x = 0.14$ and $x = 0.18$.

Peaks labelled (a), (d) and (i) correspond to superlattice reflections caused by unit-cell doubling created by octahedral tilting (Section 0). As it is the oxygen atoms which form the octahedra, these reflections appear to be very weak when using X-ray scattering due to the relatively small atomic number of oxygen, in particular in the presence of bismuth and lead. For this reason, neutron diffraction is preferentially suited to observing octahedral tilts. Nevertheless, though very weak, the peak labelled (d) is visible and corresponds to the superlattice peak of reflection $\{311\}_{pc}$ i.e. $\{3/2\ 1/2\ 1/2\}_{pc}$. The behaviour of this peak with temperature is explored later (**Figure 3.18**). Le Bail refinements fits for $x = 0.14$ and 0.18 are shown in **Figure 3.11** and **Figure 3.12**. Both display good fitting with the *P4mm* tetragonal space group. The peaks are indexed in the conventional manner for a tetragonal unit cell.
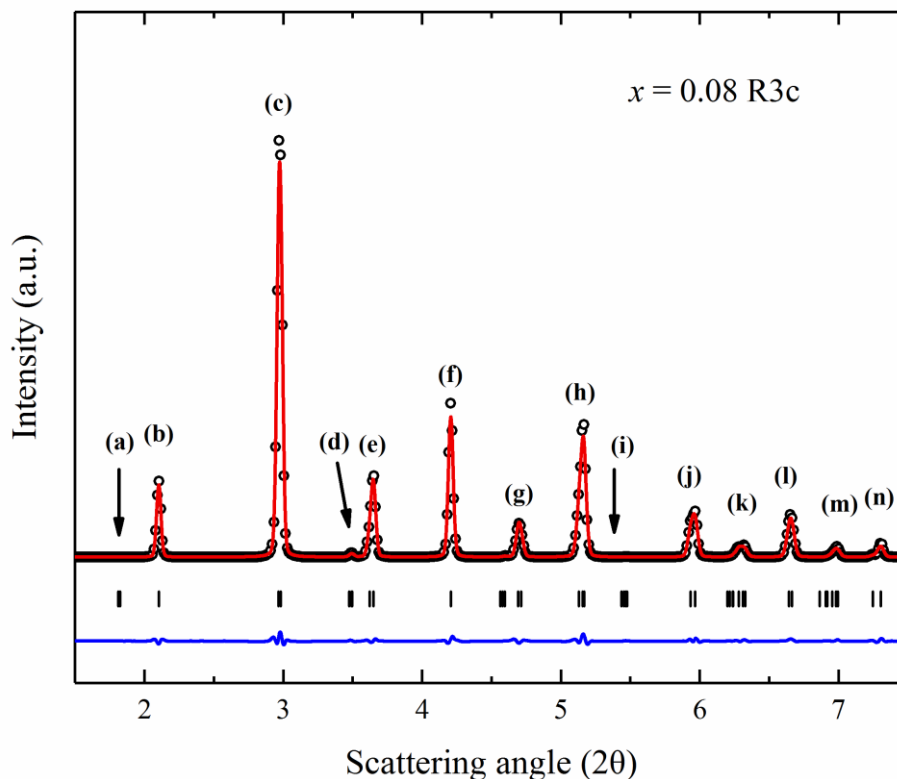
Figure 3.10 X-ray diffraction pattern for $x = 0.08$ with an *R3c* fit. All reflections shown are labeled (a) – (n) in Table 3-1.

Table 3-1 Indexed peaks for _R3c_ refinement of _x_ = 0.08 for hexagonal and pseudocubic settings

Peal label	Hexagonal peak index	Pseudocubic peak index
(a)	(003)	Superlattice reflection
(b)	(012)	{001}
(c)	(110)	{110}
(d)	(021)	{311}/2 Superlattice reflection
(e)	(202)/(006)	{111}
(f)	(024)	{200}
(g)	(116)	{210}
(h)	(003)	{211}
(i)	(009)	Superlattice reflection
(j)	(220)	{220}
(k)	(312)	{300}
(l)	(134)	{310}
(m)	(226)	{311}
(n)	(404)/(00 12)	{222}
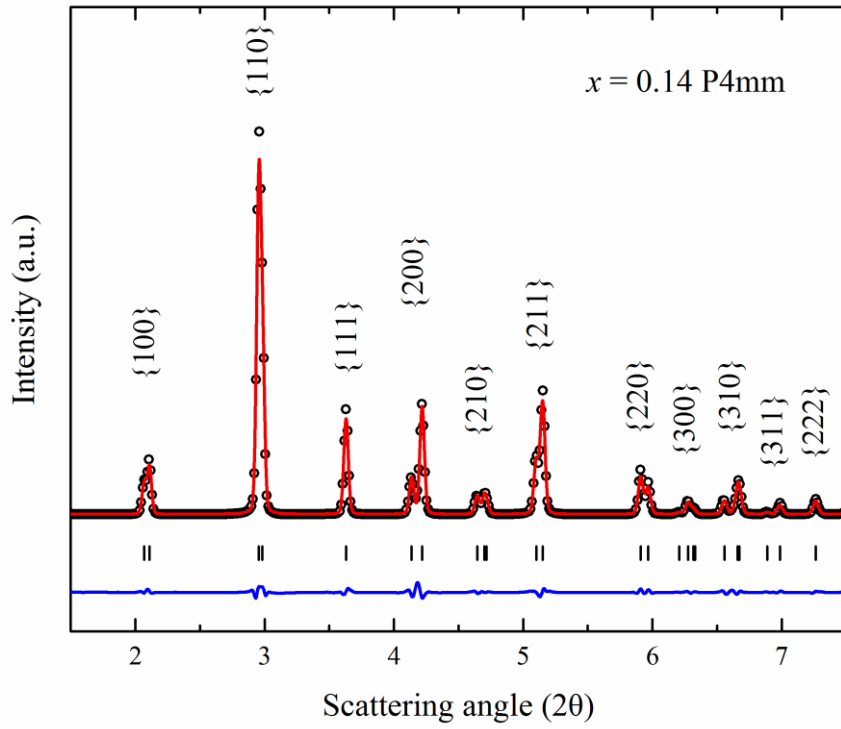
Figure 3.11 X-ray diffraction pattern for *x* = 0.14 with a *P4mm* fit.
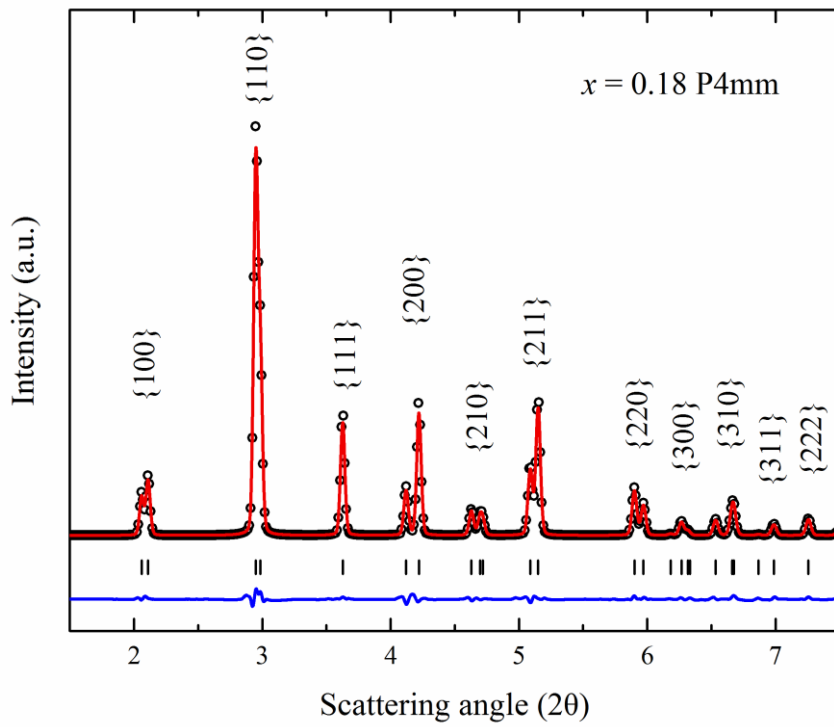
Figure 3.12 X-ray diffraction pattern for *x* = 0.18 with a *P4mm* fit.

Table 3-2 Room temperature Le-Bail fit results.

x	0.08	0.14	0.18
Space group	R3c	P4mm	P4mm
R$_{wp}$	4.628	4.071	3.955
a (Å)	5.49421 (19)	3.884982 (99)	3.882839 (93)
b (Å)			
c (Å)	13.57221 (98)	3.96141 (19)	3.97738 (17)
α (°)	90	90	90
β (°)			
γ (°)	120		

3.4.2.2 Evolution of peak profiles

To better understand these temperature dependent transitions, the behaviour of peaks characteristic to rhombohedral and tetragonal structures, namely {100} and {111}, can give an indication of the changing structure. Typically, the {200} peaks are chosen over {100} as they are at higher Q-space and therefore the differences in their positions Q-space or scattering angle 2θ are greater i.e. they are easier to identify. In many rhombohedral materials the {111} peaks are used for similar analysis, however in the case of $x = 0.08$ the {111}$_{pc}$ peaks lack definition so, for the same reason as stated before, the focus was laid on the {222}$_{pc}$ peaks. The {222}$_{pc}$ peaks for $x = 0.08$ and the {200} peaks for $x = 0.14$ and 0.18 are shown in **Figure 3.13** as a function of temperature. A clear transition from two peaks to one peak can be observed in all cases.
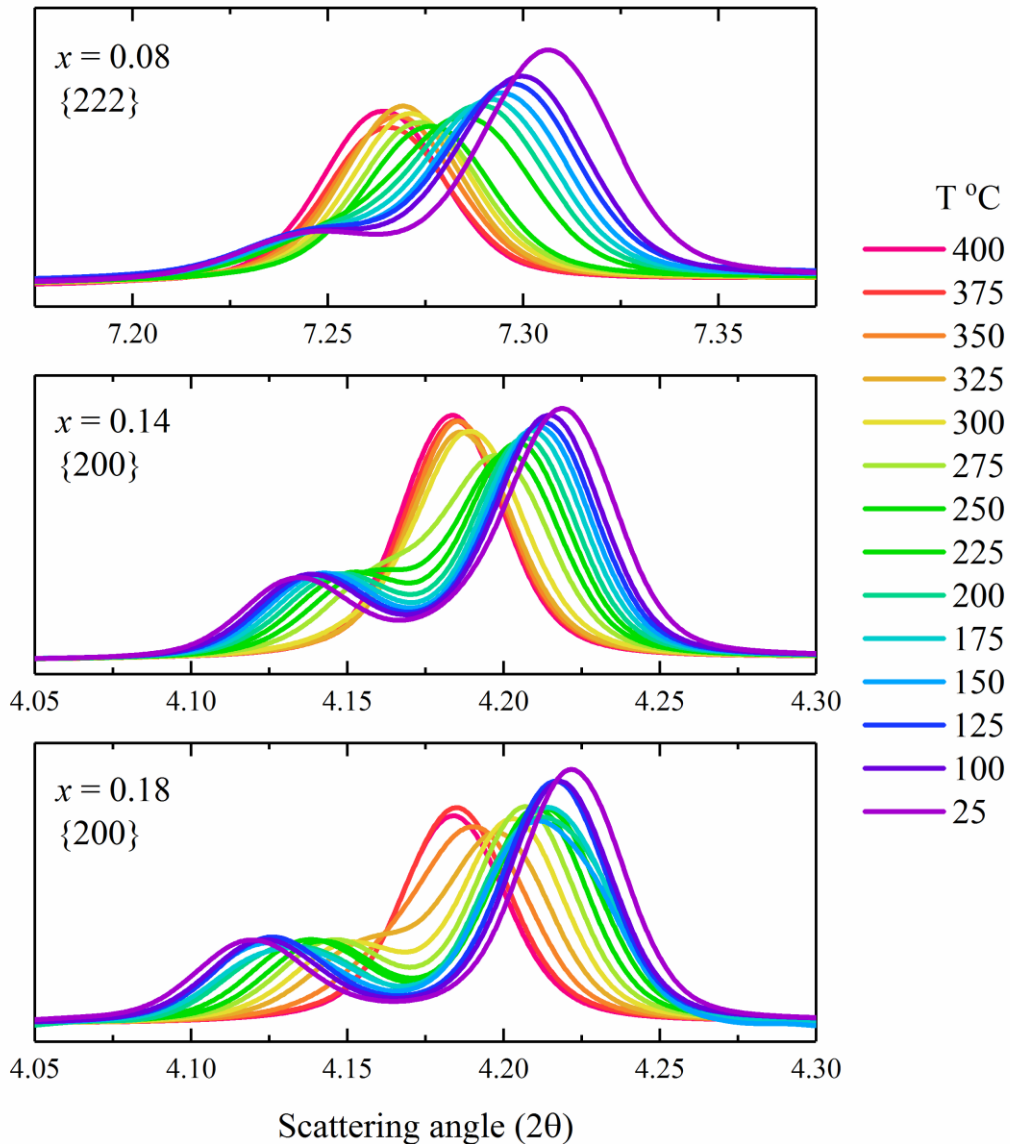
Figure 3.13 Peak behavior in *x* = 0.08, 0.14 and 0.18 as a function of temperature.

Peak analysis was carried out by peak fitting using Gaussian functions and are shown in **Figure 3.14**, **Figure 3.15** and **Figure 3.16** for *x* = 0.08, 0.14 and 0.18 respectively.

For clarity only fits of certain temperatures are shown which highlight key changes along the temperature range. In all cases two peaks were used in the fits at all temperatures. For *x* = 0.08 the rhombohedral angle (α_R) gives an indication of the extent of the rhombohedral distortion. It is calculated from the {222} peak positions ((404) and (00 12)). Shown in **Equation 3.1** is the entire calculation. This calculation is obtained from Appendix 2 in B. D. Cullity and S. R. Stock's *Elements of X-ray Diffraction* [9].

The hexagonal cell parameters a_H and c_H are first calculated from (404) and (00 12) peak positions respectively. For clarity the equation is broken down in to two parts where the constant ϕ is then calculated. This is in turn used to calculate the rhombohedral angle α_R when considering the pseudocubic unit cell.

Equation 3.1

$$a_H = (404)_H * 6\sqrt{\frac{2}{3}}$$

$$c_H = (00\ 12)_H * 6\sqrt{\frac{2}{3}}$$

$$\phi = \cos^{-1}\left(1 - \frac{9}{6 + 2\left(\frac{c_H}{a_H}\right)^2}\right)$$

$$\alpha_R = \cos^{-1}\left(\frac{1 - 2\cos\phi}{2\cos\phi - 3}\right)$$

The rhombohedral angle as a function of temperature is shown in **Figure 3.17**. Angle calculations from both the Le Bail fit and {222} peak fits are shown, and both follow a similar trend. From 25 - 225 °C there is a gradual increase in the angle from around 89.7° to 89.825°. From 225 – 250 °C there is a sharp increase in the angle up to 89.957°, after which it increases steadily. This coincides with the sharp transition observed in the relative permittivity measurements. In both calculations the angle approaches 90°. Both methods show that the angle has a lower limit of 89.975° but not quite 90° expected of the cubic structure. There are a few factors to which this is attributed: 1) the peak fitting method requires the use of two peaks and therefore if the peaks are not exactly in the same position would result in a non-90° angle result. 2) inhomogeneities in the sample would result in volumes of higher $PbTiO_3$ which possess a higher transition temperature (490 °C) thereby resulting in peak asymmetry.

$x = 0.08$ {222}
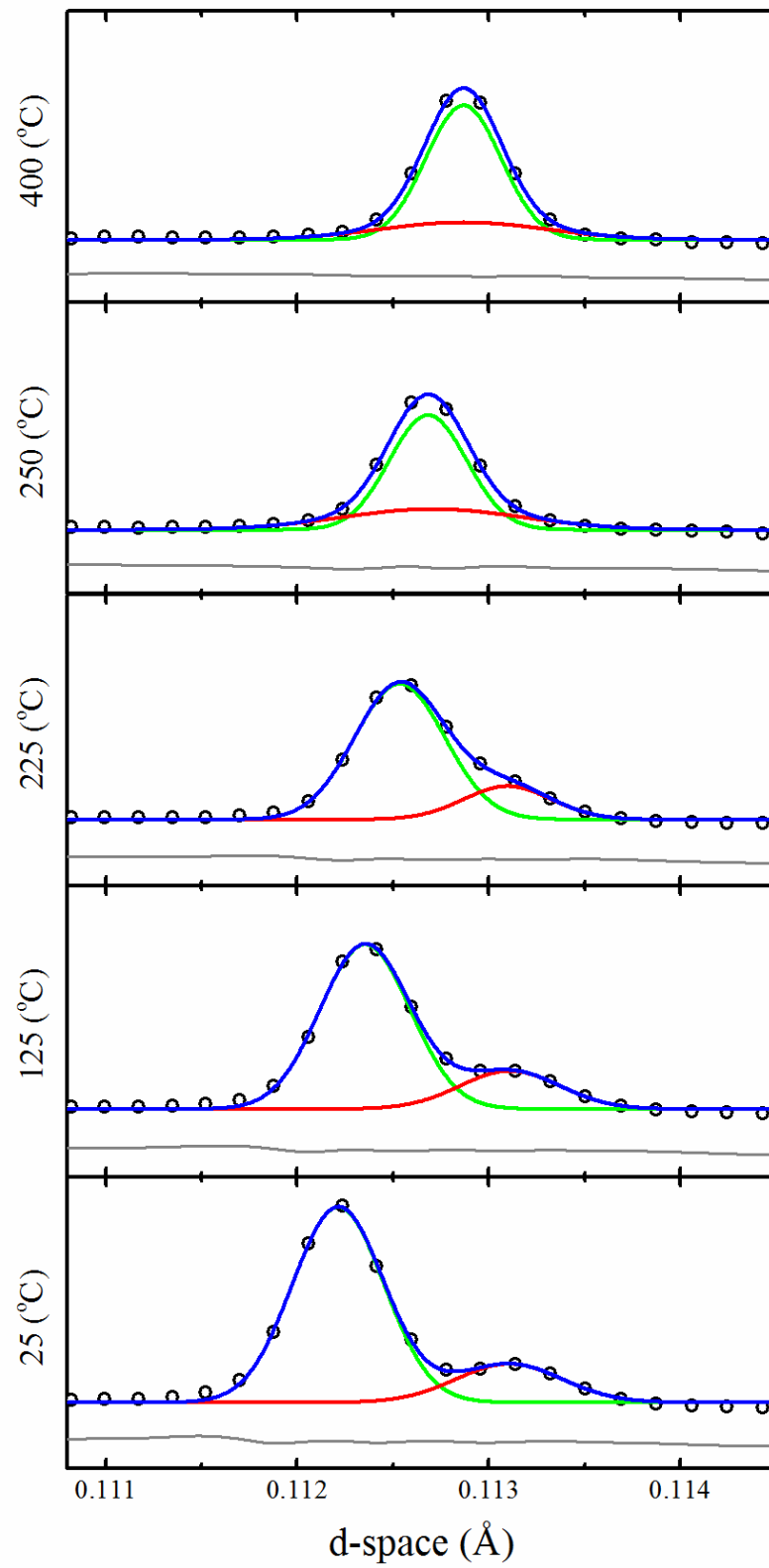
Figure 3.14 Gaussian fit of the {222}$_{pc}$ peaks for $x = 0.08$.
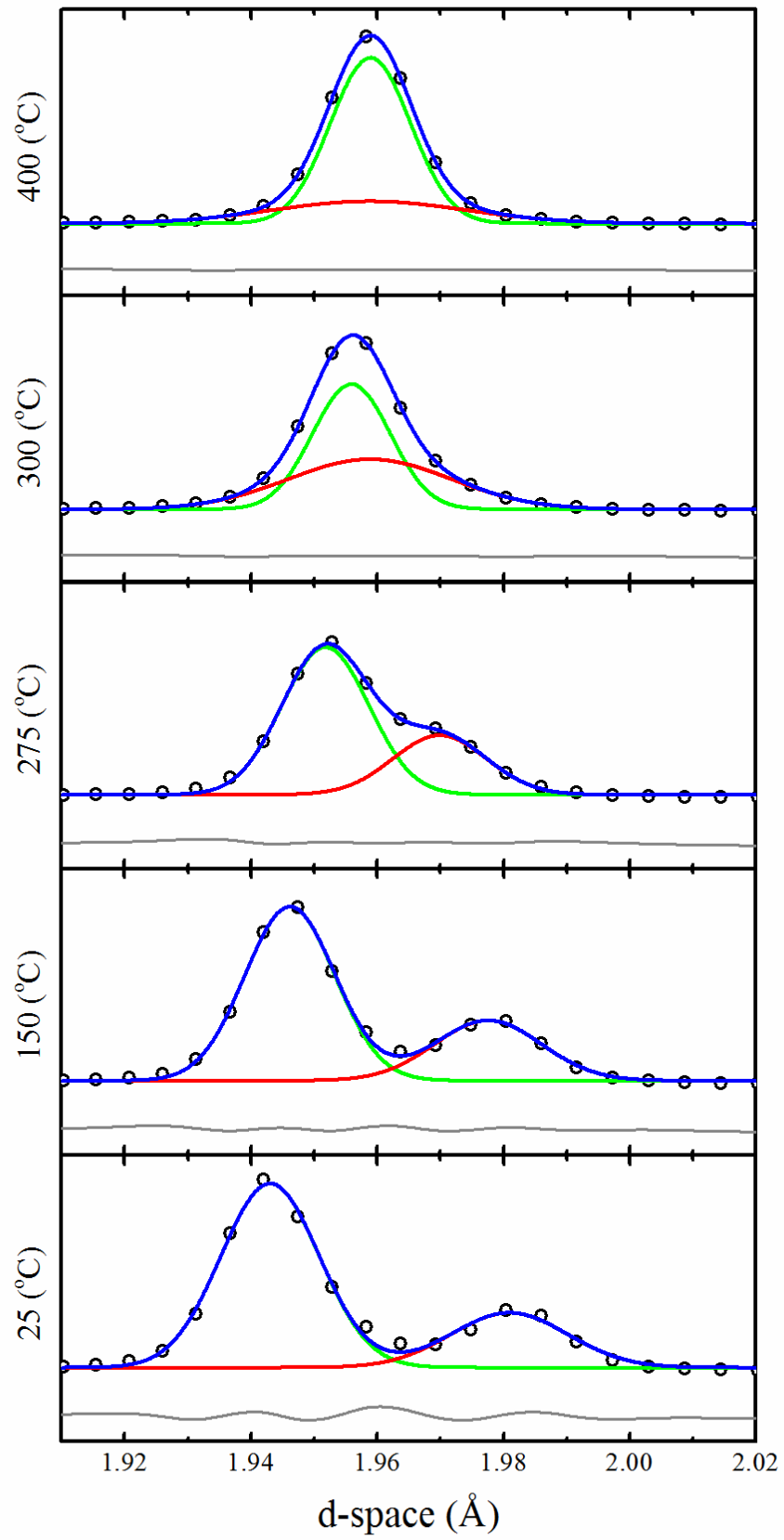
Figure 3.15 Gaussian fit of the {200} peaks for *x* = 0.14.

$x = 0.18\ \{200\}$
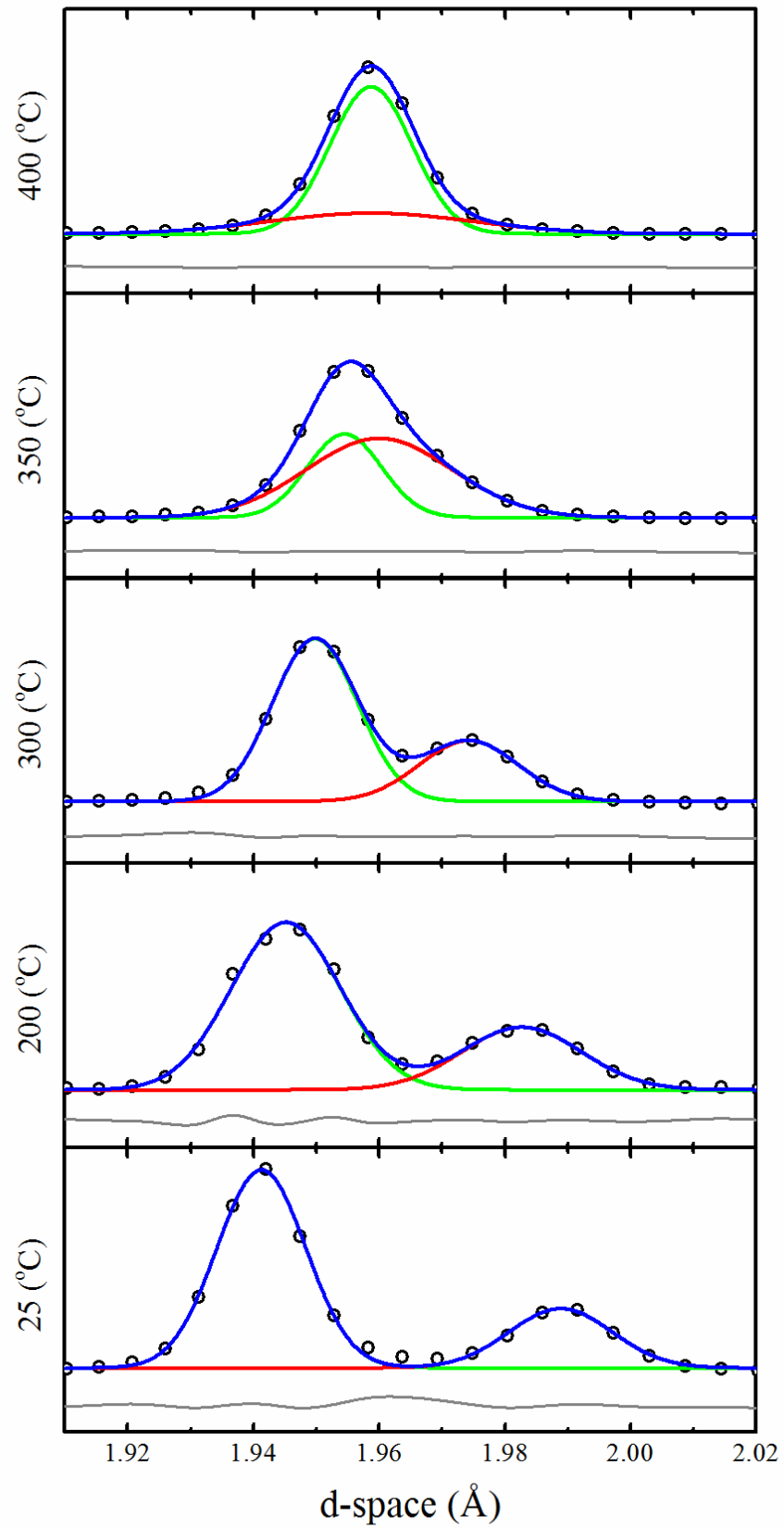
Figure 3.16 Gaussian fit of the {200} peaks for *x* = 0.18.
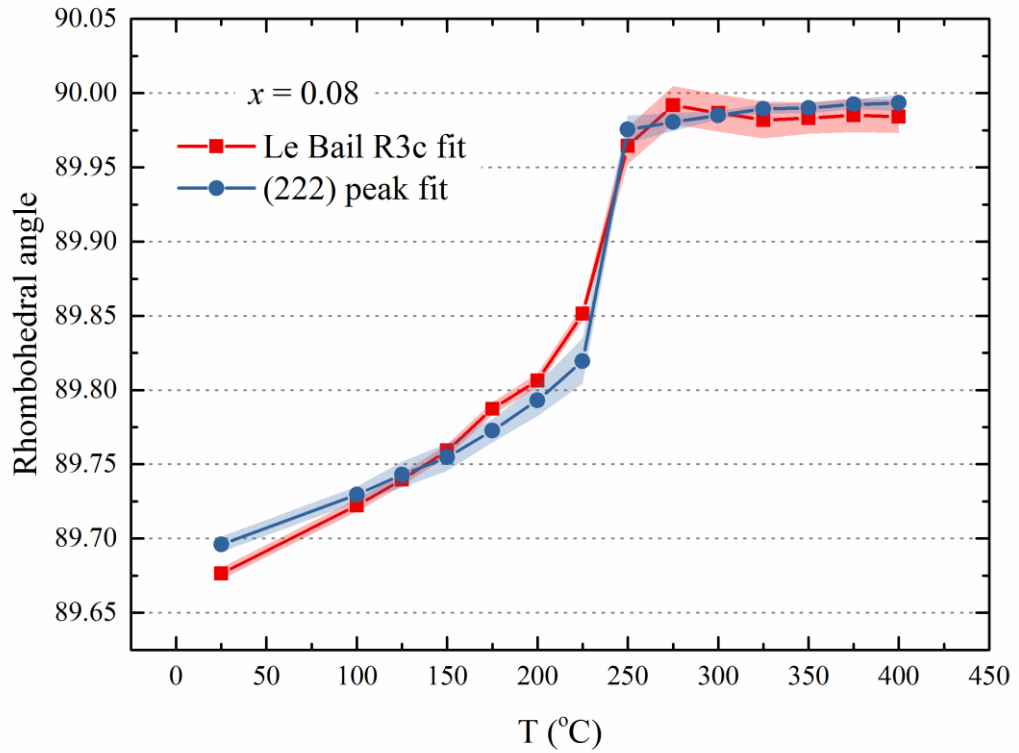
Figure 3.17 Rhombohedral angle calculated from {222}$_{pc}$ peaks for *x* = 0.08. Shaded area represents upper and lower fit results.

Previously discussed are the superlattice reflections in $x = 0.08$, of which only one is observable due to the inherent weak scattering intensity associated with the oxygen octahedron. **Figure** 3.18 shows the superlattice peak corresponding to the {311} reflection i.e. {3/2 1/2 1/2}. This peak corresponds to the $a^- a^- a^-$ octahedral tilt system in the *R3c* space group [14]. A clear extinction of the peak with increasing temperature can be observed, disappearing abruptly at 250 °C, indicating a transition from a tilted to an un-tilted structure.
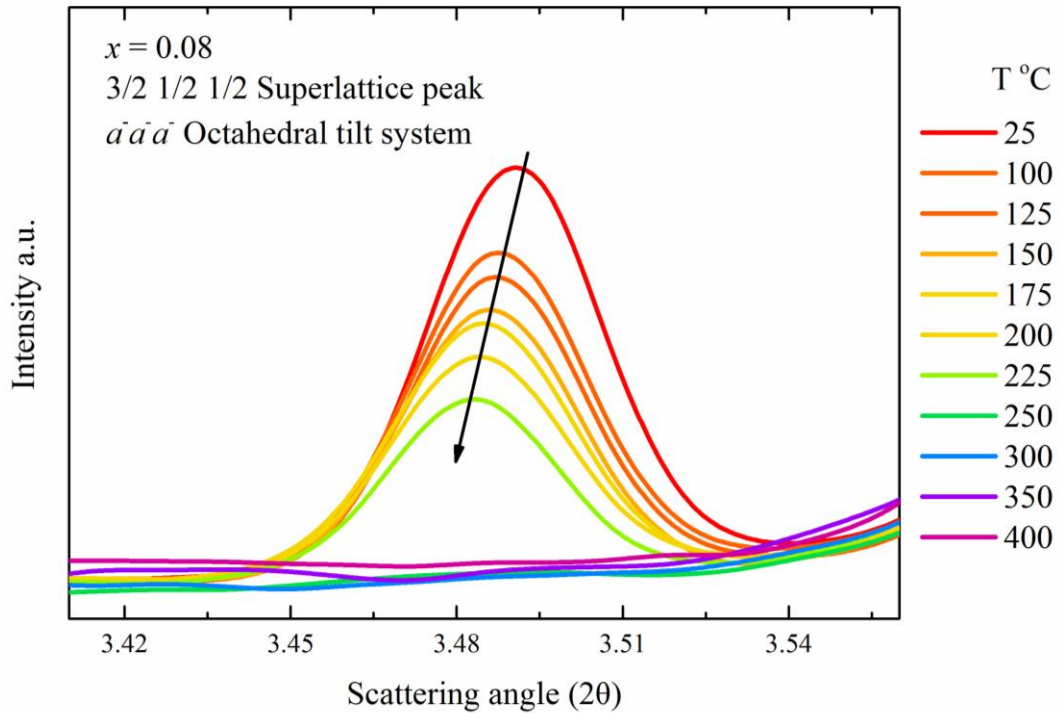
Figure 3.18 Superlattice {3/2 1/2 1/2} peak in x = 0.08 as a function of temperature.

For $x = 0.14$ and 0.18 the degree of tetragonal distortion can be simply calculated as a ratio of the unit cell parameters c and a, in turn calculated from the (002) and (200) peak positions, shown in **Figure 3.19**. For $x = 0.14$ a room temperature c/a of 1.019 is observed which steadily decreases with temperatures up to 275 °C above which a sharp decrease in c/a can be seen. Above 300 °C c/a = 1 indicating a lack of tetragonal distortion and therefore a cubic structure. For $x = 0.18$ a greater room temperature c/a of 1.024 can be seen. This is expected of a higher PT content composition. This also pushes the sharp decrease in c/a up to 325 °C, after which c/a = 1 can be observed from 375 °C. For both $x = 0.14$ and 0.18 the sudden decrease in c/a coincides with the permittivity measurement discussed, however the cubic structure indicated by c/a = 1 is not observable until higher temperatures are reached. This is again attributed to effects observed for $x = 0.08$.
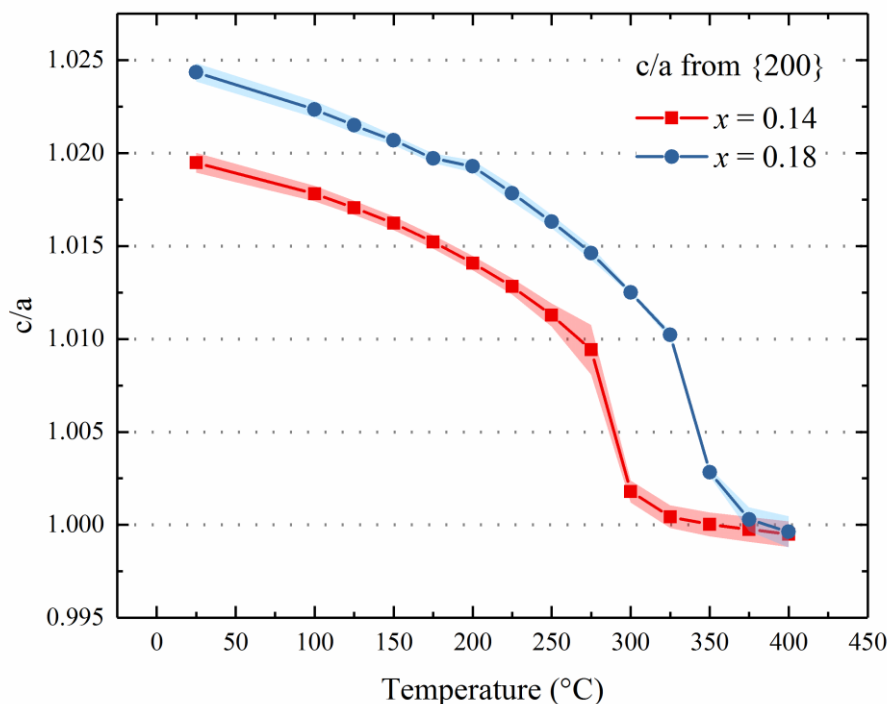
Figure 3.19 c/a ratio calculated from (002/200) peaks for $x = 0.14$ and 0.18. Shaded area represents upper and lower fit results.

3.4.3 Pair distribution function

X-ray diffraction results have described the average structure and the temperature dependent behaviour of compositions $x = 0.08$, 0.14 and 0.18 which is also observed in permittivity measurements (Section 3.4.1). However, NBT based materials have structural features which require further analysis [85]. This is already evidenced by the permittivity results for $x = 0.08$ which exhibit relaxor-ferroelectric features associated with structural disorder (**Figure 3.3**). Here the pair distribution function technique is used to characterise the local structure and draw a comparison with the average structure measurements.

3.4.3.1 Whole profile fits

In the first instance the $G(r)$ data obtained for $x = 0.08$, 0.14 and 0.18 at room temperature was refined. This is a full profile refinement which uses almost the entire PDF range of 5 – 60 Å. The refined parameters were: scale factors, lattice parameters,

atomic positions, atomic displacement parameters and broadening factors which are associated with finite instrument resolution effects at high-r. **Figure 3.20** shows R_{wp} values for PDF fits for space groups *R3c* (rhombohedral), *Cc* (monoclinic) and *P4mm* (tetragonal). An optimal *R3c* fit can be seen for $x = 0.08$. The parameters are expressed in the hexagonal form. Composition $x = 0.18$ exhibits a preferential *P4mm*. For $x = 0.14$ the *Cc* and *P4mm* phases have near identical R_{wp} values different by less than 2%. Currently this suggests structural behaviour similar to other MPB materials where a monoclinic structure exists as a lower symmetry parent phase to rhombohedral and tetragonal phases, acting as a 'bridge' between them. A mixed phase refinement is not possible with the current software.

Figure 3.21, **Figure 3.22** and **Figure 3.23** show $G(r)$ data with the optimal fits $G(calc)$ associated with the R_{wp} values shown in **Figure 3.20** and difference plot $G(diff)$. For **Figure 3.22** only the *Cc* fit is shown. The difference curve in all cases shows that at low-r the fit is worse. This may be due to very short length scale disorder exhibiting a lower symmetry. Fit results are summarised in **Table 3-3**. The errors shown in brackets represent statistical errors in the standard deviation of the refined parameters, not experimental errors. There are some differences in the whole PDF profile fit results and the Le Bail refinement results. These do not exceed 0.2% and are as low as 0.01%.
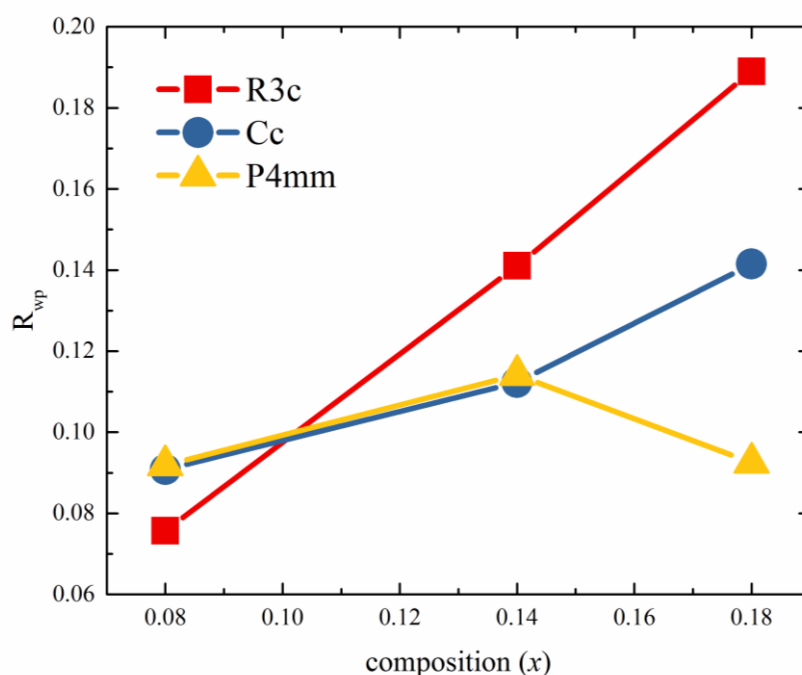
Figure 3.20 Whole profile R$_{wp}$ PDF fit values for $x = 0.08, 0.14$ and 0.18
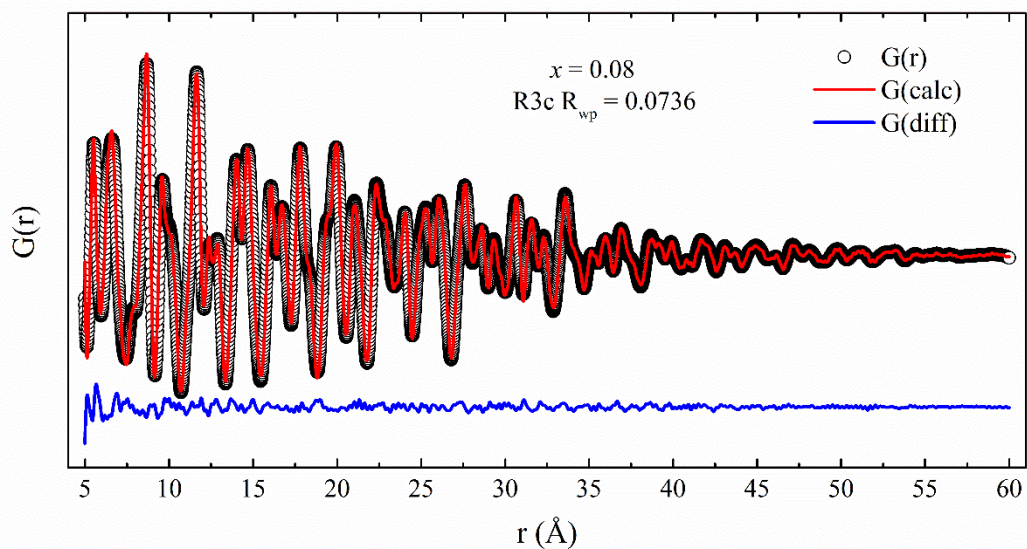
Figure 3.21 *R3c* **refinement of** *G(r)* **for** *x* **= 0.08**
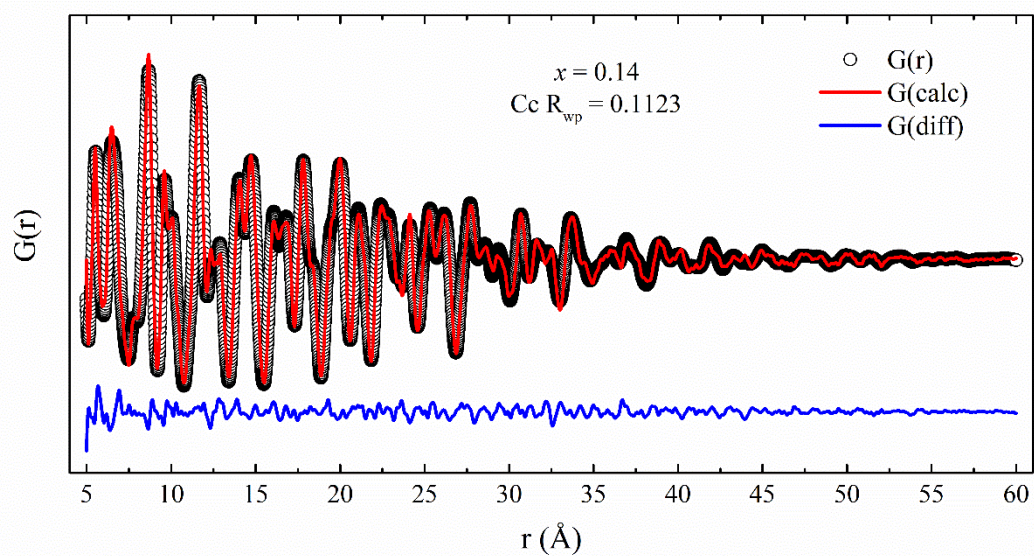
Figure 3.22 *Cc* **refinements of** *G(r)* **for** *x* **= 0.14**
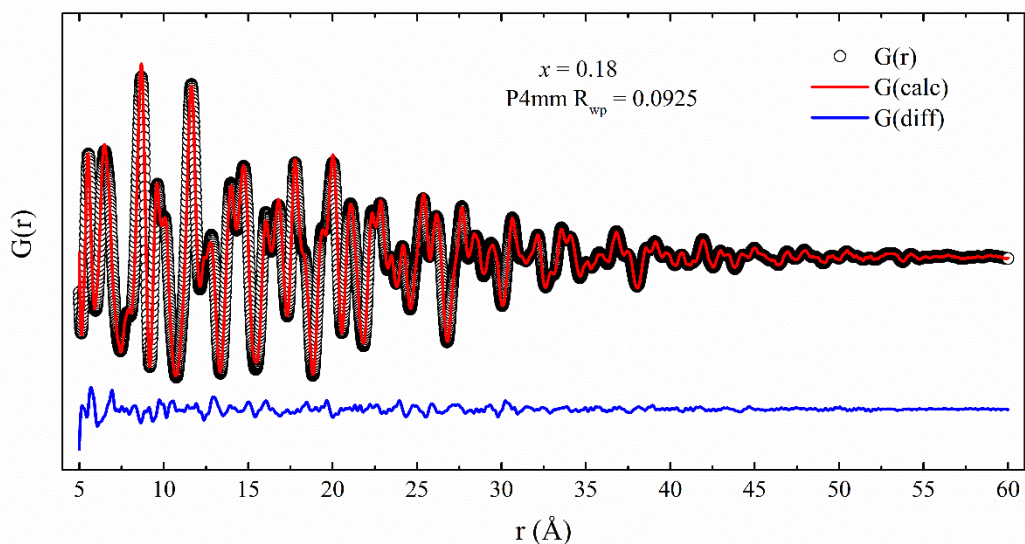
Figure 3.23 *P4mm* refinement of *G*(*r*) for *x* = 0.18

Table 3-3 Full *G*(*r*) profile (5 – 60 Å) PDF refinement results

x	0.08	0.14		0.18
Space group	R3c	Cc	P4mm	P4mm
R$_{wp}$	0.0757	0.1123	0.1141	0.0925
a (Å)	5.4918 (13)	9.521 (13)	3.884982 (99)	3.882839 (93)
b (Å)		5.5301 (41)		
c (Å)	13.5898 (57)	5.5832 (54)	3.96141 (19)	3.97738 (17)
α (°)	90	89.871 (83)	90	90
β (°)		125.54 (10)		
γ (°)	120	89.871 (83)		

3.4.3.2   Range dependent fits

A PDF contains real space structural data, and therefore offers the useful feature of selecting a specific PDF range to analyse. Results obtained from a given PDF range will therefore reflect structural features occurring at those length scales. A schematic illustration of this analysis method is shown in **Figure 3.24**. Similar analysis methods have been previously shown to be suitable to determine length scale dependent structural behaviour [133]

Here the PDFs obtained were analysed using the 'box-car', method whereby only a 10 Å region is selected and analysed and this is then shifted up by 5 Å where the same analysis is repeated. The box start is at 2 Å, therefore the first box is 2 – 12 Å, the next one is at 7 – 17 Å and so on up to 47 Å. Results obtained from refinements of the box regions will be plotted as data points centred on the midpoint of each box. For example, in the 2 – 12 Å box the result is plotted at data point 7 Å. Range dependent refinements of the same three space groups *R3c*, *Cc* and *P4mm* are performed in the 2 – 47 Å range. **Figure 3.25** shows R_{wp} values for all compositions as a function of box centres. In some cases, smaller box shifts are used to obtain refinement values between two points.
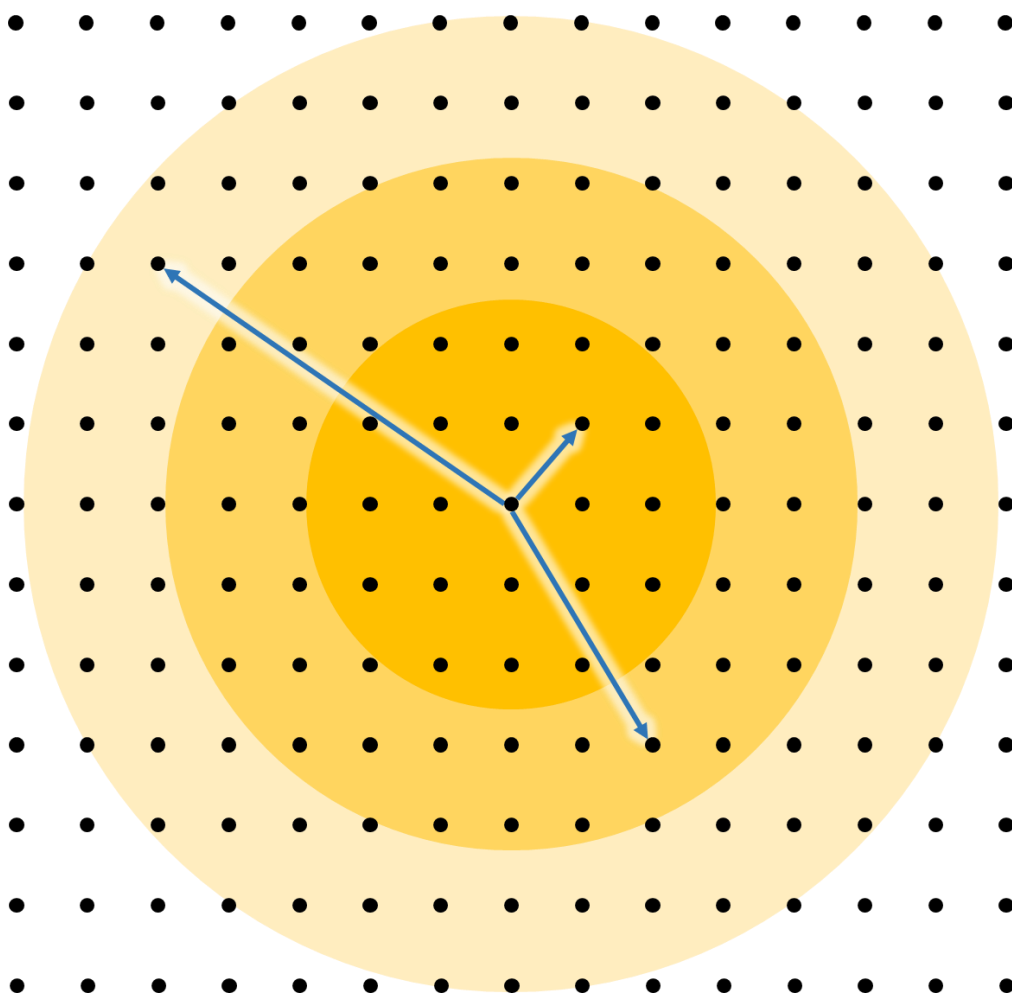
Figure 3.24 'Box-car' PDF refinement method illustrated in real space 2D lattice. Different PDF ranges are analysed separately.

For $x = 0.08$ both the monoclinic and rhombohedral phases appear to be equally suitable across all r values with a slightly more preferential rhombohedral phase at high-r. The $G(r)$ fit is shown in **Figure 3.26**. The difference plot reflects the relatively high R_{wp} at low-r. This is likely due to intrinsic lower resolution of low-r which is dependent on the experimentally determined Q_{max}. For $x = 0.14$ at low-r all phases appear to be almost equally suitable. Above 12 Å a tetragonal and monoclinic fit is almost identical up to 27 Å, above which only the tetragonal phase is suited (**Figure 3.27**). Similar behaviour is apparent for $x = 0.18$, however the region over which tetragonal and monoclinic phases have a similar fit is far smaller, where the divergence occurs between 12 Å and 17 Å, after which only the tetragonal phase is suitable (**Figure 3.28**). For clarity the figures only contain one structural model for every range section. In ranges where two models have equivalent fits the monoclinic fit data is used.

Several features merit discussion here: Generally, the low-r regions experience good fits with all space groups. This indicates that the local structure length scale of up to three unit-cells has a low symmetry structure. For $x = 0.08$ the structure still seems rather ambiguous at greater length scales as the *R3c* and *Cc* fits are very similar. This can be expected of the lowest PT content composition which exhibits the most NBT-like behaviour. For $x = 0.14$ and 0.18 the tetragonal structure emerges as the best fit at greater length scales, though for $x = 0.18$ this occurs at a lower r value than for $x = 0.14$. This indicates that the local structural coherence length of the monoclinic phase is larger for $x = 0.14$. It is only beyond 27 Å that the best fit phase represents the average structure as observed with XRD. For $x = 0.18$ the coherence length of the local scale structure is much shorter. As a lower symmetry phase *Cc* represents a deviation from the average structure. With an increase in PT content, the lower symmetry monoclinic phase becomes increasingly supressed and diminished in size to give rise to higher symmetry phases. Here the order inducing properties of the highly strained $PbTiO_3$ can be observed.
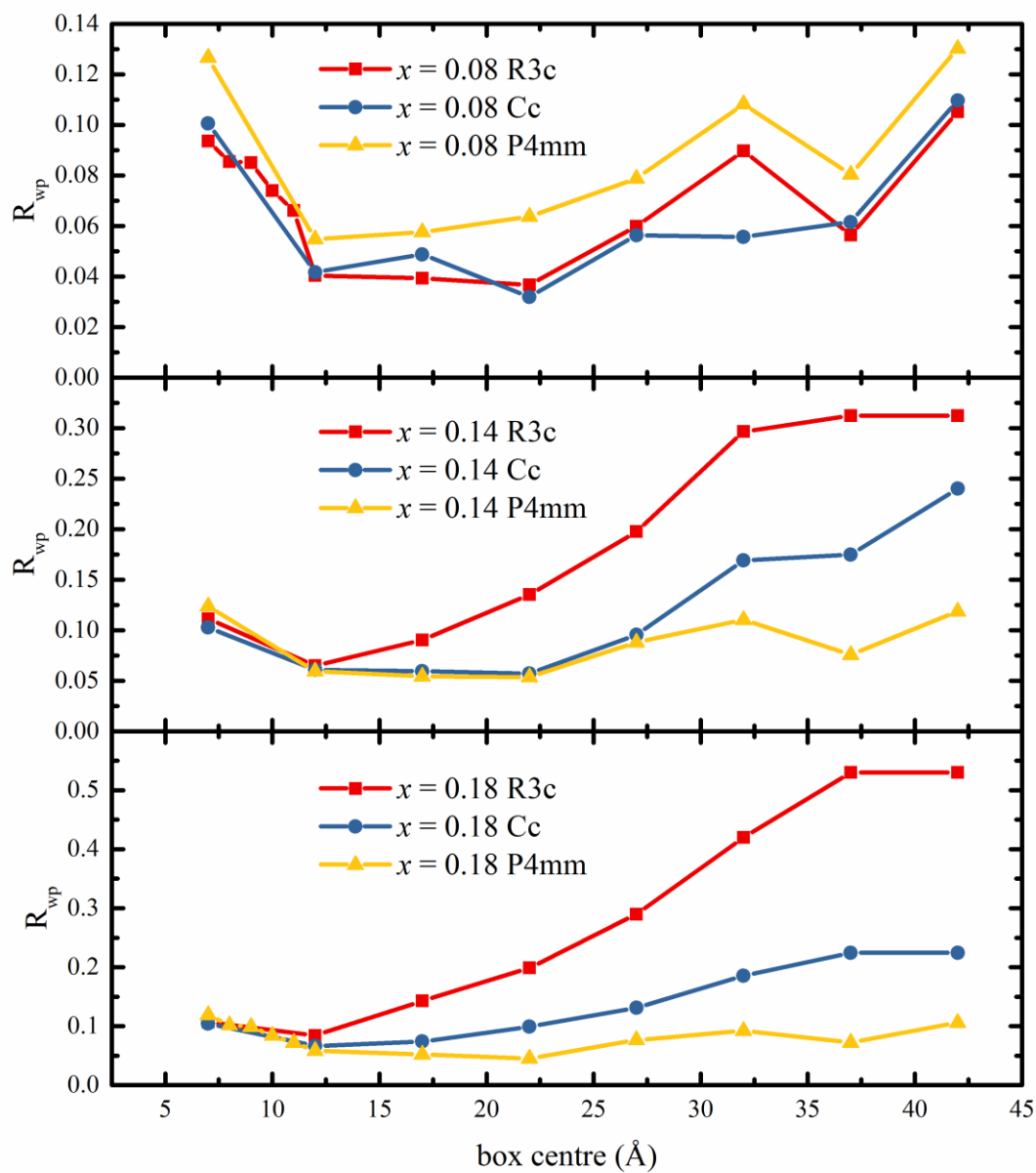
Figure 3.25 R$_{wp}$ values for x = 0.08, 0.14 and 0.18 as a function of PDF range fits for the space groups *R3c*, *Cc* and *P4mm*.
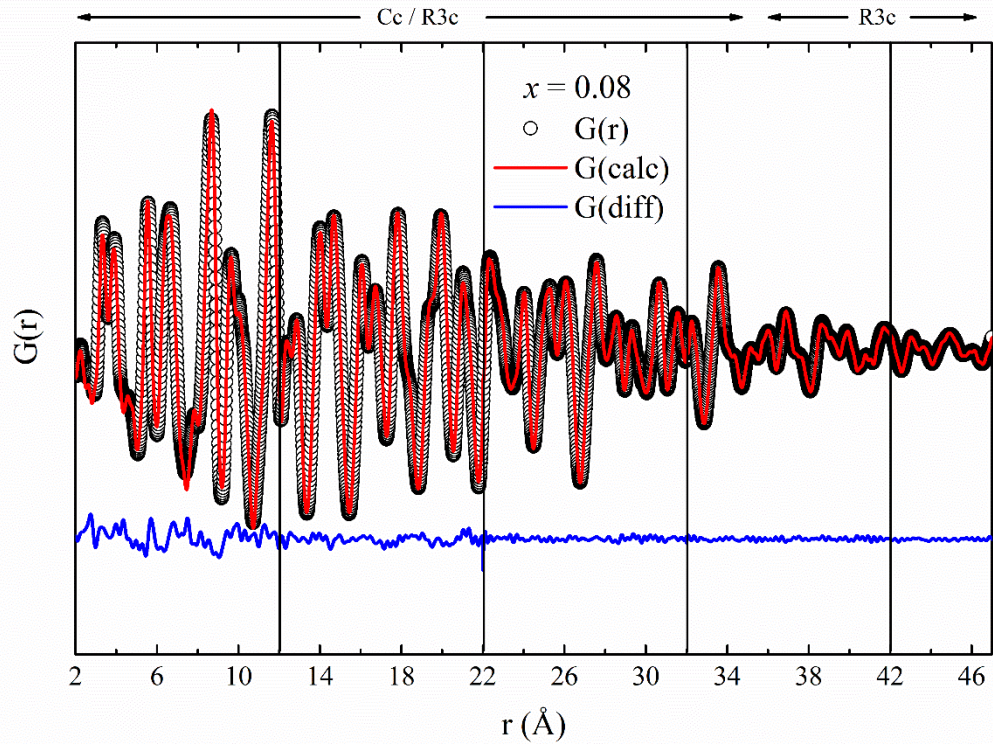
Figure 3.26 PDF for *x* = 0.08 composed of combined 'box-car' refinements (vertical black lines). Region of *Cc* and *R3c* fit extend to approximately 35Å.
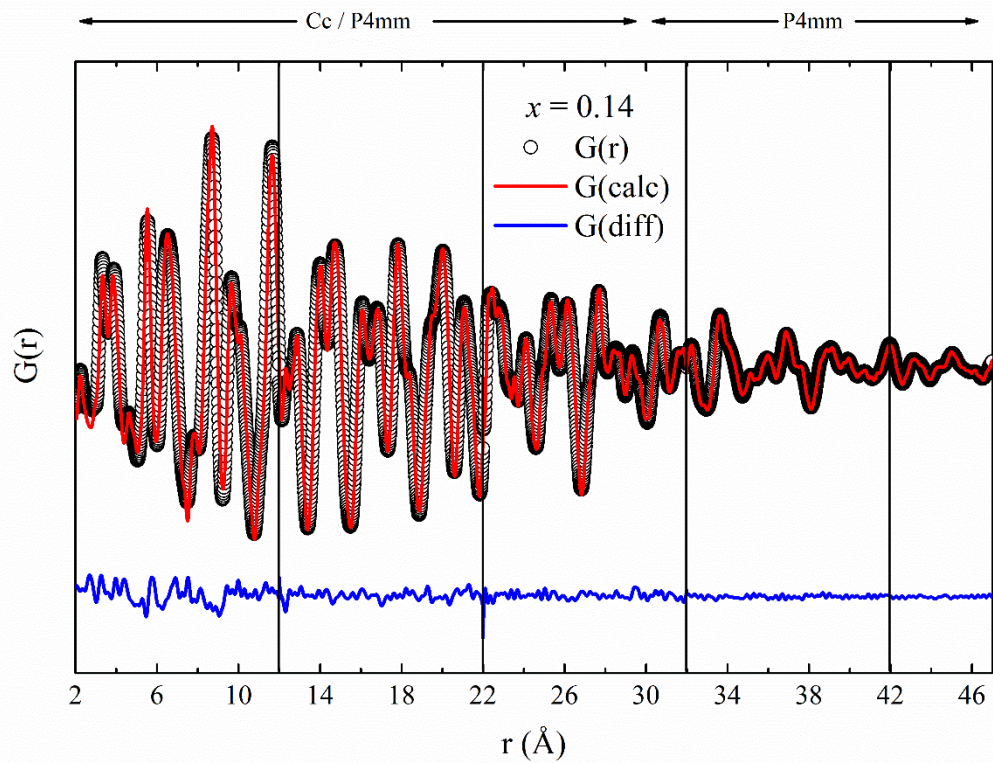
Figure 3.27 PDF for *x* = 0.14 composed of combined 'box-car' refinements (vertical black lines). Region of *Cc* and *P4mm* fit extend to approximately 30Å.
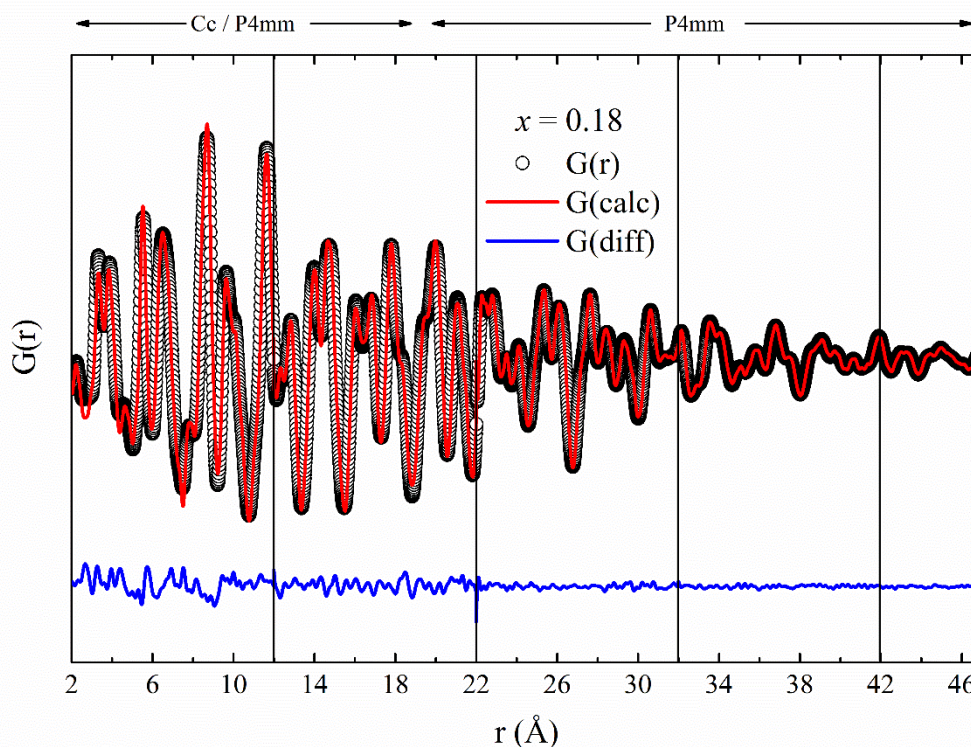
Figure 3.28 PDF for _x_ = 0.18 composed of combined 'box-car' refinements (vertical black lines). Region of Cc and _P4mm_ fit extend to approximately 20Å.

3.4.3.3 Range dependent fit parameters

Fit parameters from the box-car refinements were used to calculate useful structural features such as the rhombohedral angle and c/a ratio as a function of PDF range. For $x = 0.08$ (**Figure 3.29**) the rhombohedral angle is shown as a function of PDF range at 25 °C (black) and 400 °C (red) measurements. Measurements of rhombohedral angle from the average structure calculations at 25 °C and 400 °C are shown as horizontal blue (25 °C) and pink (400 °C) lines respectively. Vertical black and red lines indicate the range at which the parameters obtain from PDF analysis and XRD analysis become equivalent (within the error margin as shown by the shaded regions, see Section 3.3.1). The rhombohedral angle was calculated (**Equation 3.1**) using the hexagonal cell parameters a_H and c_H from the _R3c_ space group.

Room temperature angle calculations show significant range dependence. At low-_r_ the rhombohedral distortion is more extreme. At greater ranges it gradually decreases and only becomes equal to the average rhombohedral distortion at 27 – 32 Å, indicating the presence of a more distorted local volume of approximately 30 Å in size. The high

temperature measurements also show a highly distorted low-*r* structure. Above 22 Å the rhombohedral angle uncertainty is within the 90° line expected from average structure measurements. This suggests that for *x* = 0.08 there are relatively large localised regions, more distorted than the average structure. These persist at temperatures where the average structure is considered cubic i.e. non-distorted, albeit their coherence length is smaller. The vertical dotted lines indicate the range at which the rhombohedral angle matches that of the average structure and therefore the size of the nanoscaled region.
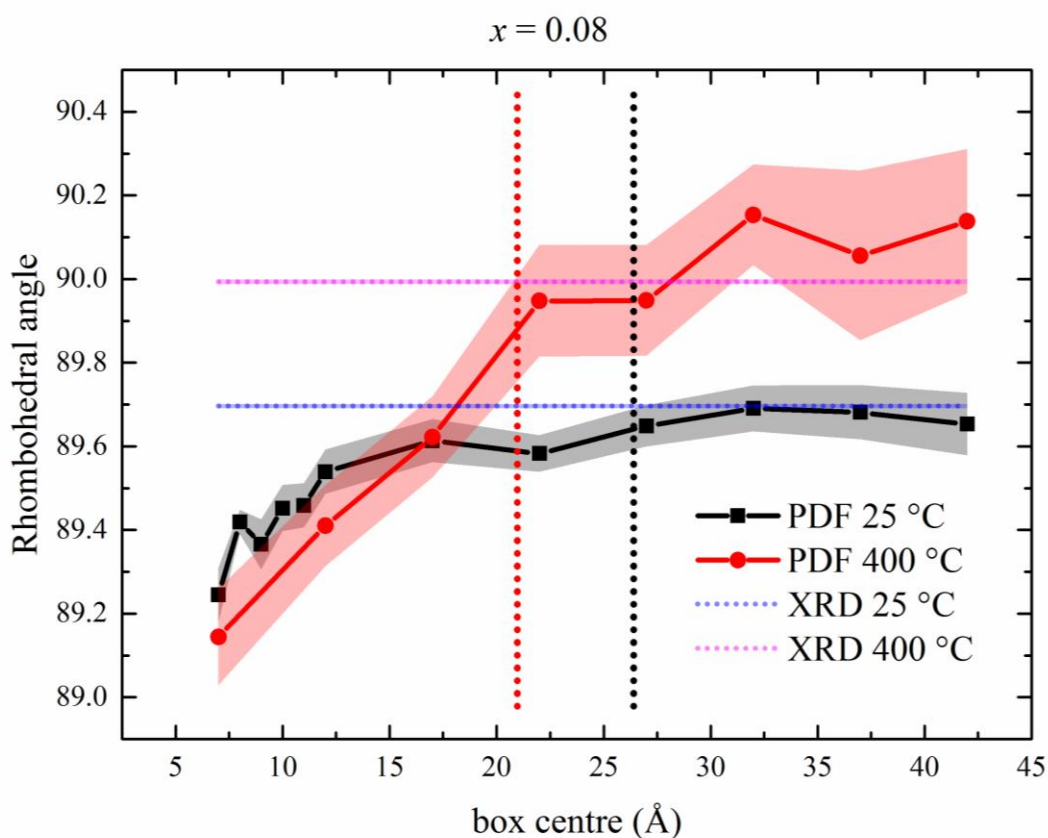
Figure 3.29 Rhombohedral angle as a function of PDF range for *x* = 0.08 at 25 (red) and 400 °C (black). Horizontal lines indicate rhombohedral angle measurements from average structure calculations. Vertical lines indicate suggested nanoregion size (coloured the same as PDF measurements)

For *x* = 0.14 and 0.18 the *c* and *a* parameters of the *P4mm* PDF refinement were used to calculate the *c/a* ratio as a function of range. These are shown in **Figure 3.30** and **Figure 3.31** for *x* = 0.14 and *x* = 0.18 respectively. The elements in the figures follow the same format as in **Figure 3.29**. Similar range dependent behaviour can be observed. Low-*r* regions have a higher c/a and are therefore significantly more distorted than the average

structure. Above 20 Å the c/a ratio resembles the average value for each composition. High temperature measurements show a non-cubic tetragonal distortion persists where average measurements show the structure to be cubic. These high temperature distortions have a coherence length of approximately 17 Å. The vertical dotted lines are used to represent the range at which the c/a values match those of the average structure and therefore the size of the nanoscaled region.
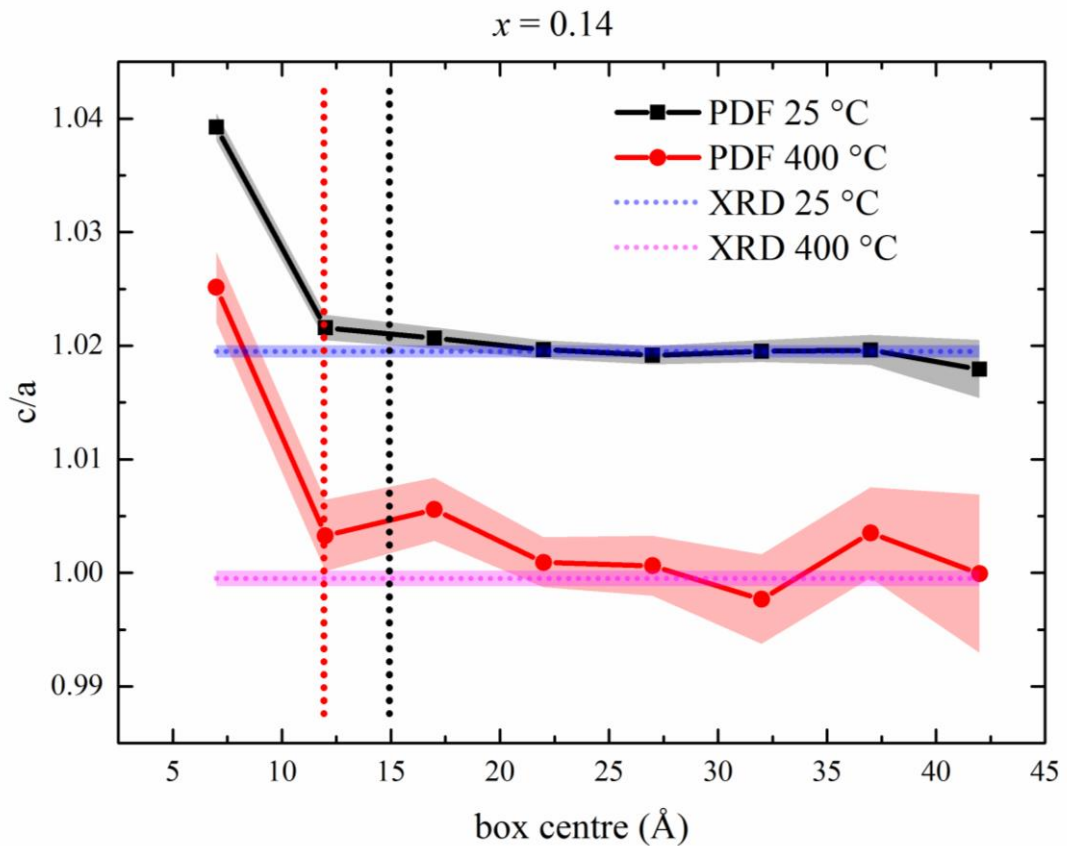
Figure 3.30 c/a ratio as a function of PDF range for $x = 0.14$ at 25 (red) and 400 °C (black). Horizontal lines indicate c/a ratio measurements from average structure calculations. Vertical dotted lines indicate nano region size.
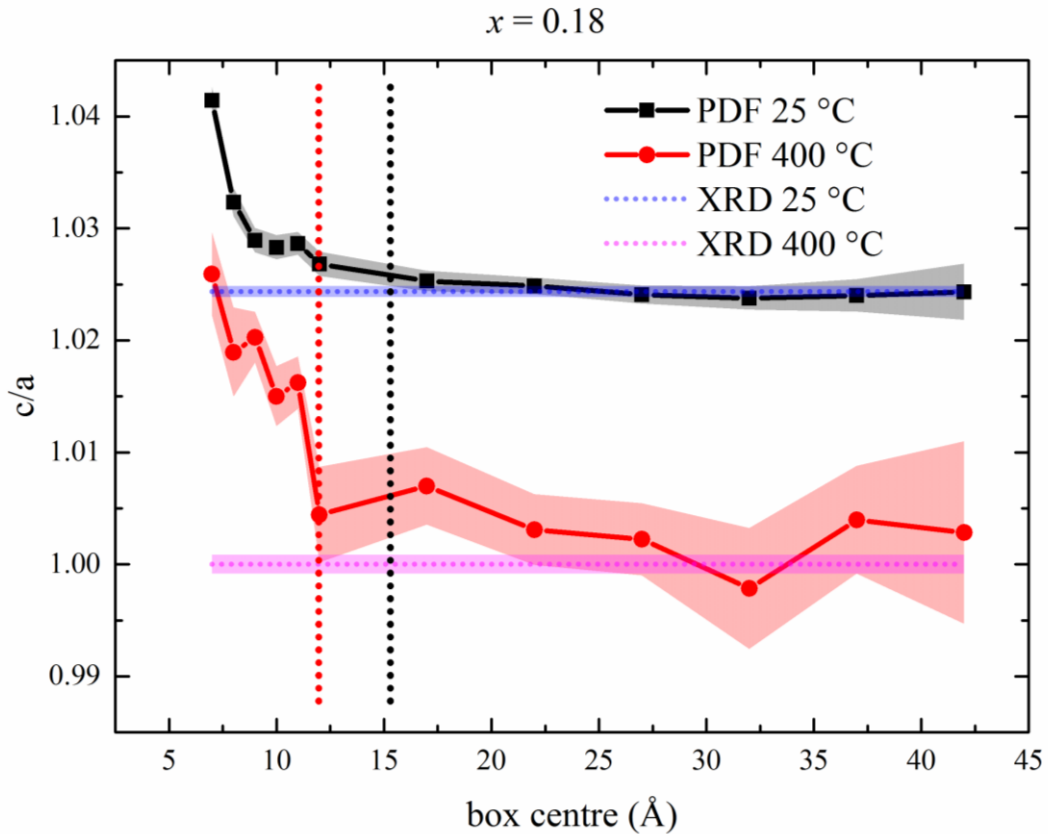
Figure 3.31 c/a ratio as a function of PDF range for *x* = 0.18 at 25 (red) and 400 °C (black). Horizontal lines indicate c/a ratio measurements from average structure calculations. Vertical dotted lines indicate nano region size.

3.5 Conclusions

A combination of average and local structural characterisation techniques have been used to study $(1-x)(Na_{0.5}, Bi_{0.5})TiO_3$-$xPbTiO_3$ (NBT-PT) for $x = 0.08$, 0.14 and 0.18; compositions which inhabit the rhombohedral, MPB and tetragonal regions respectively. Permittivity-temperature measurements were used in conjunction to verify any phase transitions observed and investigate ferroelectric behaviour.

Average structure X-ray diffraction measurements coincide with studies in the literature where $x = 0.08$ exhibits a rhombohedral *R3c* phase and $x = 0.14$ and 0.18 exhibit tetragonal *P4mm* phases. Temperature dependent measurements show a transition to a cubic phase by the merging of peak doublets associated with rhombohedral and tetragonal phases. Additionally, $x = 0.08$ exhibits an extinction the {3/2 1/2 1/2} octahedral tilt peak indicative of an un-tilted structure. Permittivity temperature measurements show abrupt transitions correlating with XRD measurements. Additionally, the measurements

illustrate the relaxor-like characteristics of $x = 0.08$ which decrease and evolve into a more classical ferroelectric-like behaviour with increasing $PbTiO_3$ content.

Local structure analysis via pair distribution function shows the presence of a monoclinic *Cc* phase in the MPB composition $x = 0.14$. For $x = 0.08$ and 0.18 *R3c* and *P4mm* phases were observed respectively. For further insight range dependent analysis was performed which revealed a more complex and range dependent structure. At room temperature and at low-*r* length scales all compositions show good fit agreement with the monoclinic phase. With increasing x, the length scale over which the monoclinic phase showed good agreement decreased systematically. This suggests that the monoclinic phase has only a short-range existence which is suppressed with increased $PbTiO_3$ content.

Furthermore, measurement of the refinement parameters shows local structure volumes of greater distortion with respect to the average structure. It is only at greater length scales that the rhombohedral or tetragonal distortions are the same as those measured via XRD. The size of these volumes decreases with increasing $PbTiO_3$ content. At high temperature these distortions persist at low-*r* and resemble the average structure at greater length scales, however the size of these regions is smaller than at room temperature. Nevertheless, the effects of $PbTiO_3$ are still apparent.

$PbTiO_3$ has been shown to have strong order-inducing properties by the decrease or suppression of nanoscale coherence length. In doing so NBT-PT transforms from a relaxor-like material to a material more closely resembling a classical ferroelectric. This presents a novel understanding of NBT-PT and the influence of order inducing materials on poorly crystalline materials.

4 Field-dependent local structure of $(K_x Na_{1-x})_{0.5} Bi_{0.5} TiO_3$

4.1 Introduction

As previously discussed there has been extensive research into the $(K_x Na_{1-x})_{0.5}$ $Bi_{0.5} TiO_3$ (KNBT) system (Section 1.14.5), revealing the structural complexities associated with its NBT end member [83], [92] and its promising MPB properties [45], [96] making this system a potentially viable option for the lead-free piezoelectric industry.

To help realise the piezoelectric potential of KNBT several *in situ* electric field, XRD studies have been conducted which show phase transformation behaviour beneficial to improved piezoelectric properties. Specifically, a transition to a tetragonal phase from a rhombohedral or mixed phase structure at the MPB [99]. The structurally ambiguous nature of KBT-NBT due to the NBT end member, necessitates the use of analysis techniques which are able to differentiate local from average structural behaviour, namely pair distribution function (PDF) analysis [52].

In this section, an *in situ* electric-field PDF experiment on KBT-NBT compositions near the MPB is described and the results discussed. This work has been published [117]. This work primarily investigates the contribution of compositional differences to the observed PDF data and the field induced structural changes over short and long PDF ranges.

4.2 Material synthesis

Solid solutions of $(K_x Na_{1-x})_{0.5} Bi_{0.5} TiO_3$ ($x = 0.15$, 0.18 and 0.2) were fabricated via the conventional mixed oxide route first detailed in Royles *et al.* [99].

The reagent powders used were: bismuth (III) oxide (Bi_2O_3), titanium dioxide (TiO_2), potassium carbonate (K_2CO_3) and sodium carbonate (Na_2CO_3) (99.9% purity, Sigma-Aldrich). The potassium and sodium reagents were required to be in carbonate form as they are oxides are reactive with water. The reagents were dried at 150 °C to remove any moisture, then weighed and mixed in stoichiometric ratios for $x = 0.10 - 0.30$.

The mixture was ball milled in isopropyl alcohol (C_3H_8O) or IPA for 24 hours to ensure the breakup of agglomerates and uniform distribution of reagents. The slurry was dried under continuous agitation to prevent denser reagents settling thereby losing the uniform distribution. The dried powder was then sieved through a 100 μm mesh. Phase formation was achieved via calcination of the powders at 850 °C for 4 hours in closed alumina crucibles, which were then attrition milled (Dyno-mill 70 KDL type-A) to further reduce particle size. The drying process was repeated during which 1-2 %wt binder (Glascol HA-40) was added to aid during the pellet forming process.

Large pellets measuring 20 mm in diameter by 3 mm thickness were uniaxially pressed at 50 MPa, then further pressed by isostatic press at 300 MPa to aid the densification process during sintering. The pellets were placed in a closed crucible on powder bed of the same composition to aid in reducing the loss of volatile species such as bismuth oxide. **Figure 4.1** shows the sintering profile used. An initial slow ramp of 50 °C/h up to 500 °C was used to burn off the binding agent, after which a ramp rate of 300 °C /h up to the sintering temperature 1150 °C which was maintained for 2 hours. The pellets cooled at 150 °C /h in order to relieve any stresses produced during sintering.
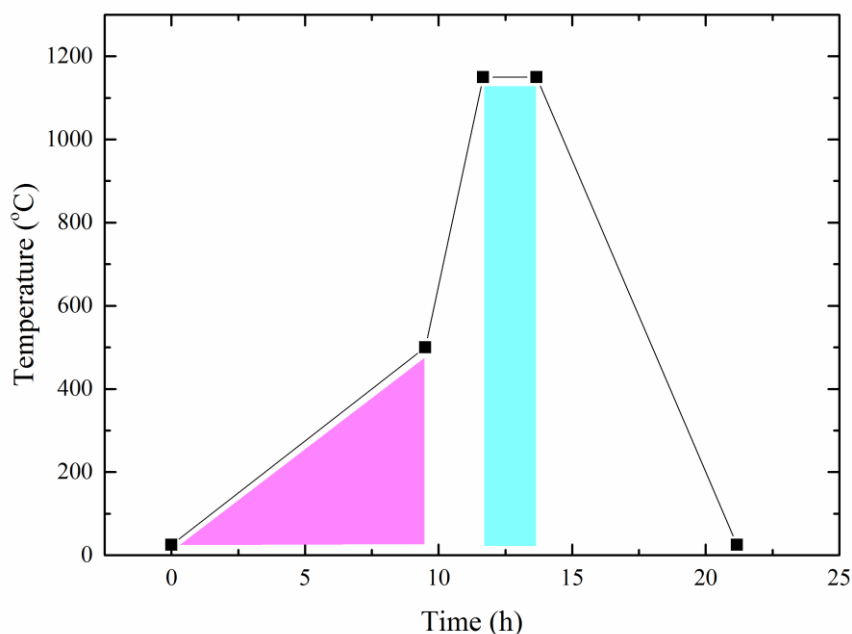
Figure 4.1 Sintering profile for (K_x Na_{1-x})$_{0.5}$ $Bi_{0.5}$ TiO_3. Binder burnout (magenta) and sintering (cyan) regions are highlighted.

The sintered pellets were ground and polished using silicon carbide into discs. Once a thickness of 1 mm was achieved silver electrodes were applied to the opposing large faces of the discs and fired at 550 °C. A diamond saw was used to cut the disc into multiple $1 \times 1 \times 5$ mm ceramic bars (**Figure 4.2**), which were annealed at 300 °C for 2 hours to minimise any internal stresses induced by the cutting.

a) Disc with silver electrodes   b) Cutting profile   c) Ceramic bar
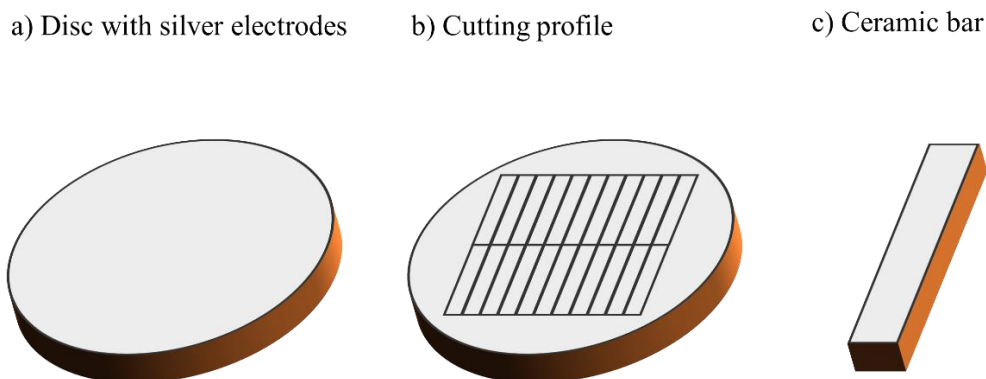
Figure 4.2 Ceramic processing route for *in situ* electric field synchrotron experiment.

4.3 Experimental methods

X-ray total scattering data were collected at ambient temperature using beamline 11-ID-B at the Advanced Photon Source (APS), Argonne National Laboratory, which is dedicated to PDF measurements [134]. An incident beam of wavelength 0.2114 Å (58.66 keV) was used with the sample to detector distance set to produce a usable Q_{max} of 23.6 Å^{-1}. **Figure 4.3** shows the experimental arrangement and the electric field vector. The sample was immersed in a Fluorinert (3M, USA) bath (electrically insulating liquid) in a Kapton (DuPont, USA) container. Total scattering data were collected simultaneous to the application of a static electric field. Samples were unpoled at the beginning of the experiment. The field was increased from 0 to 4000 V/mm in steps of 250 V/mm steps and held for 5 minutes at each field amplitude. The non-sample background scattering, including that from the Kapton container and Fluorinert liquid was measured separately and subtracted from the total signal.

The scattered photons were collected with a Perkin Elmer flat-panel amorphous-silicon 2D detector [134]. Fit2D software was used to process the diffraction data [135].

Total-scattering patterns incorporating contributions from crystallites having Q_{hkl} vectors parallel and perpendicular to the electric field were obtained by integrating ±10° sectors of the detector centred on the vertical and horizontal directions, respectively. As demonstrated previously [116], a conventional formalism involving the sine Fourier transform, as implemented in the PDFgetX3 software [131], is adequate for converting directional scattering functions, $S(Q)$ into their corresponding directional PDFs. Piezoelectric charge coefficient d_{33} were measured after the experiment with a Berlincourt meter (Piezo Systems).

There are important considerations to be had when applying an anisotropic field to a randomly orientated polycrystalline sample. Firstly, as previously stated, directional scattering arises from contribution from crystal grains with the appropriate Q_{hkl} vectors. Therefore it is important to remember that the measured structural changes occur in grains which experience elastic stresses from neighbouring grains. Secondly, the entire Q range cannot by definition correspond to Q vectors aligned or parallel to the electric field i.e. there will be some contribution to the structural data from structural responses not aligned to the vector. However, the majority of the Q range is within ±10° of the electric field vector.
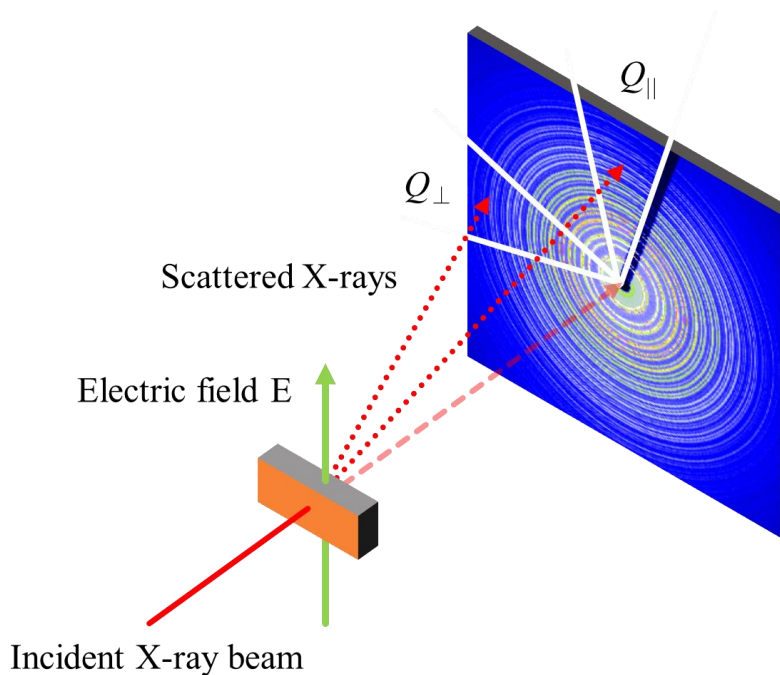
Figure 4.3 Schematic of experimental setup for X-ray total scattering, showing the applied field vector E and detector sectors of interest Q‖ and Q⊥.

4.4 Total scattering

Details of obtaining total scattering data are discussed previously (Section 2.3) however the principle requirements are knowledge of the material composition and measurement of any source scattering from non-sample sources e.g. insulating fluid and sample stage. Zero-field unpoled $S(Q)$ data parallel and perpendicular to the electric field is shown in **Figure 4.4**. Intensity differences are observable. These correspond to angular differences in the pixel sensitivity.

Total scattering with an applied field parallel and perpendicular to the electric field vector ($S_\parallel(Q)$ and $S_\perp(Q)$ respectively) is shown in **Figure 4.6** and **Figure 4.7**. Various features are apparent in the inset, namely suppression of the diffuse scattering between the diffraction peaks and shift in peak position. Parallel to the field, peaks shift to lower Q indicating an extension of the unit cell parameters indicating field-induced strain. Perpendicular to the field there is a contraction in the lattice spacing. This behaviour is typical of piezoelectric lattice strain where perpendicular contraction is required by the structure in response to the anisotropic applied field, following Poissons ratio. For both directions there is a clear suppression in the diffuse scattering thereby producing sharper peaks. This is characteristic of a crystal structure becoming more ordered. The scattering arising from periodic atomic planes (Bragg scattering) becomes more pronounced at the expense of scattering arising from the local deviations from the average scattering (diffuse scattering). At the local scale atoms diverge slightly from their average positions, however under an electric field they are constrained to more specific arrangements, and the distribution of atomic positions narrows. Composition $x = 0.20$ (MPB) shows a greater degree of diffuse scattering suppression and peak shift than the other two compositions, consistent with the conventional understanding of MPB materials which display a greater strain and possess greater lattice flexibility than neighbouring compositions.

Ferroelectric domain switching is not evident in these measurements as the experimental setup required of PDF analysis results in a reduction of scattering resolution in exchange for a greater Q_{max}. Prior *in situ* electric-field synchrotron X-ray diffraction experiments and polarisation measurements demonstrate domain switching under fields [44].

Unpoled S(Q) parallel and perpendicular to the field vector
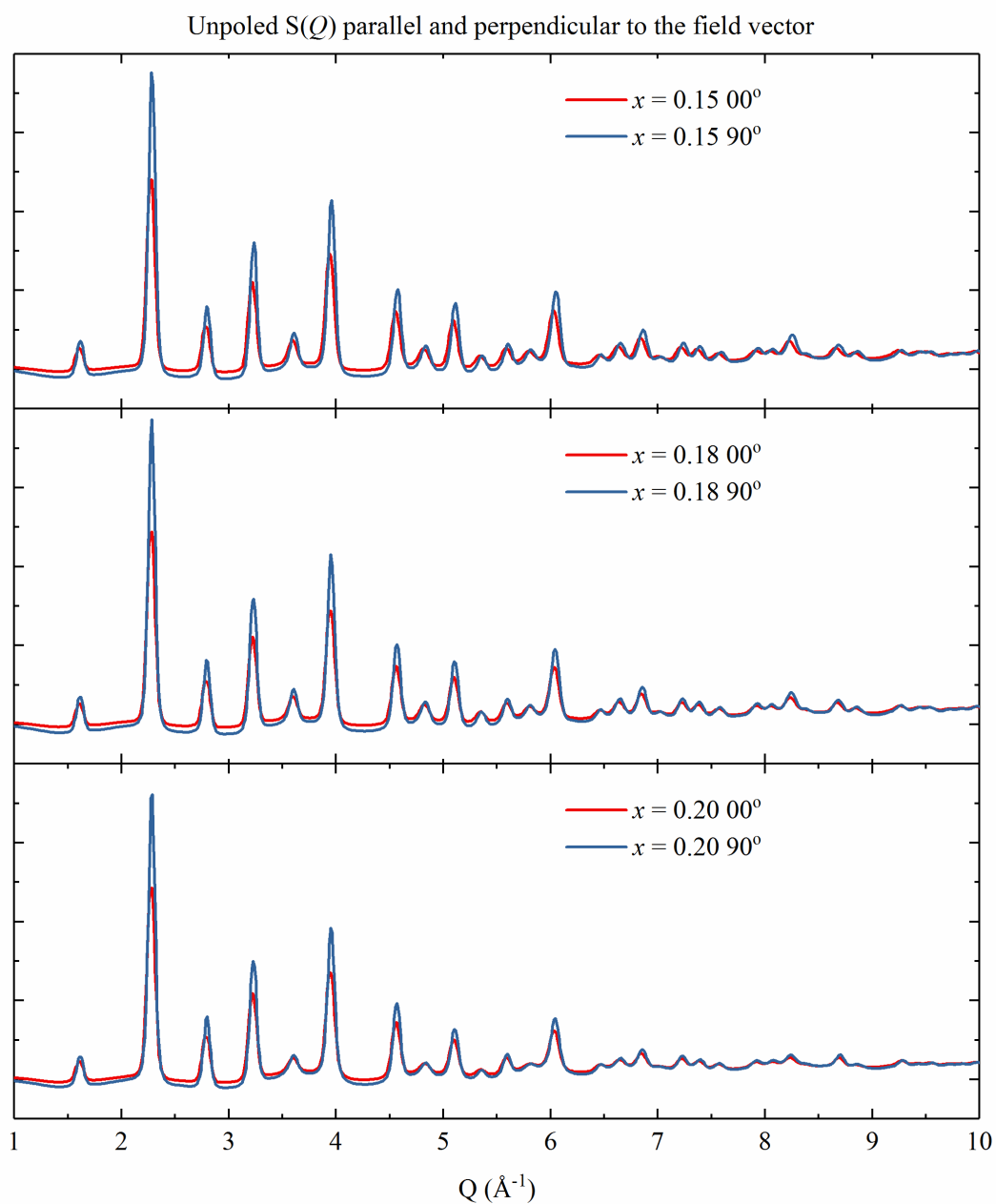
Figure 4.4 Zero-field (unpoled) S(Q) for x = 0.15, 0.18 and 0.20, parallel and perpendicular to the electric field vector.
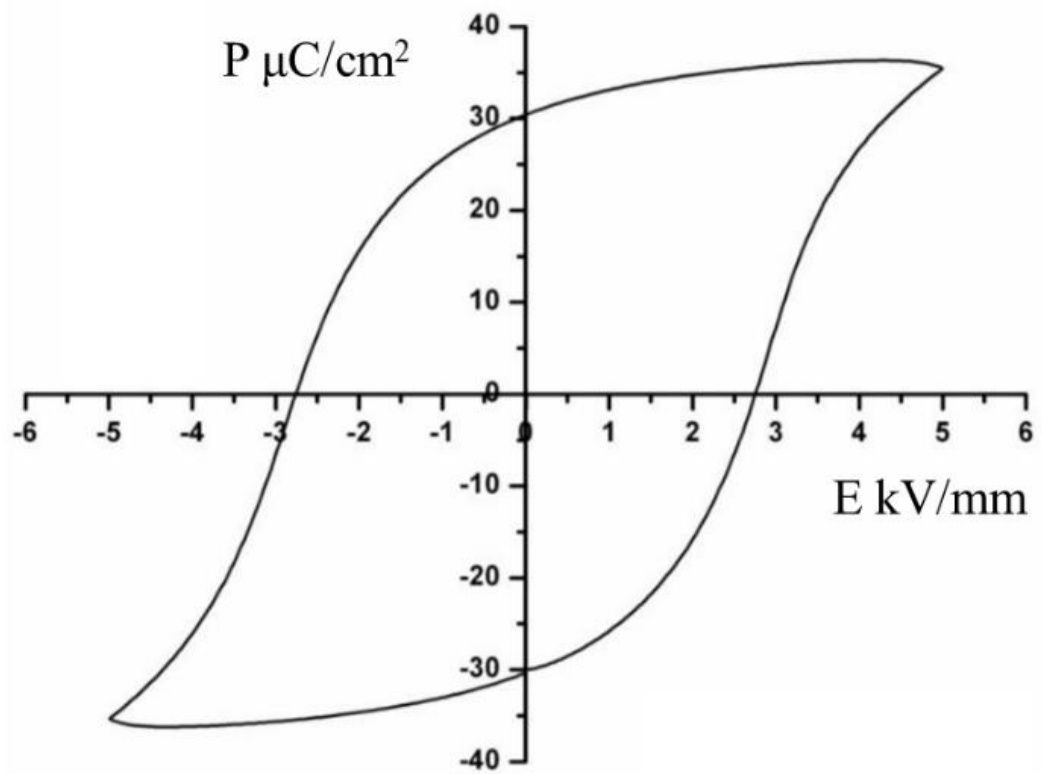
Figure 4.5 Polarisation-field hysteresis loop for x **= 0.20 showing ferroelectric behavior, from [44].**
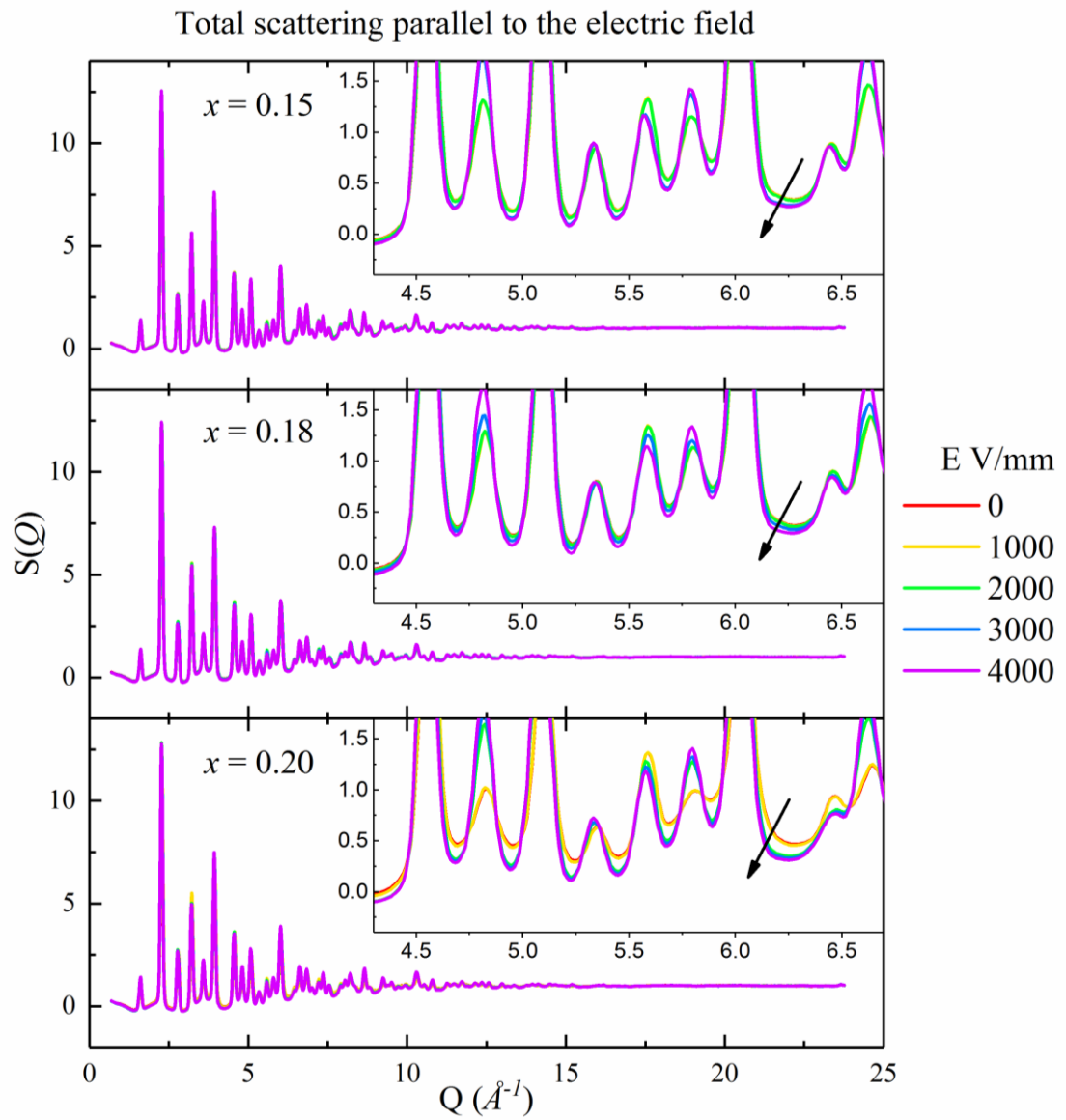
Figure 4.6 S||(Q) for *x* = 0.15, 0.18 and 0.20.
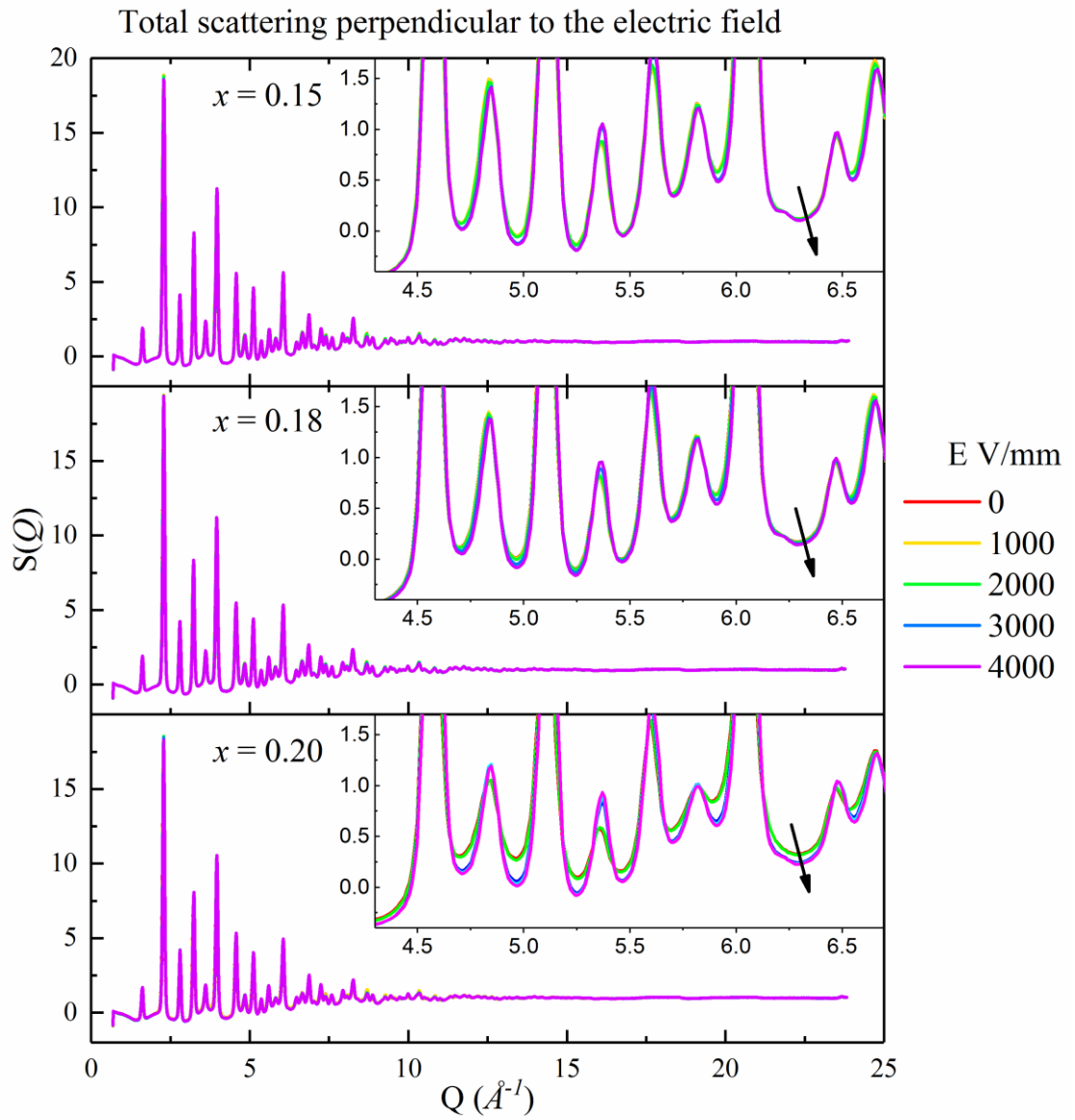
Figure 4.7 S⊥(Q) for *x* = 0.15, 0.18 and 0.20.

4.5 Pair distribution function

The reduced pair distribution function $G(r)$ is calculated as shown in **Equation 4.1** and discussed in greater detail in (Section 2.3.5.3). Here the directional PDFs are calculated from the parallel and perpendicular total scattering data and are denoted $G_{\parallel}(r)$ and $G_{\perp}(r)$ respectively. This enables measurement of the behaviour of interatomic distances parallel and perpendicular to the electric field vector.

Figure 4.8 and **Figure 4.9** show $G_{\parallel}(r)$ and $G_{\perp}(r)$ respectively for zero-field (black), 4000 V/mm (red) and difference (blue) data sets, with insets that show magnified sections of the PDFs to highlight subtle changes. Sharpening in the PDF peaks highlighted in the inset correlates to the decrease in diffuse scattering, indicating an increase in the spatial atomic order. The difference plot shows the overall structural changes are significant across all compositions and directions and are greatest for $x = 0.20$ suggesting the MPB has the greatest response to the electric field.

Equation 4.1

$$G(r) = \left(\frac{2}{\pi}\right) \int_{Q_{min}}^{Q_{max}} Q(S(Q) - 1) \sin(Qr) \, dQ$$
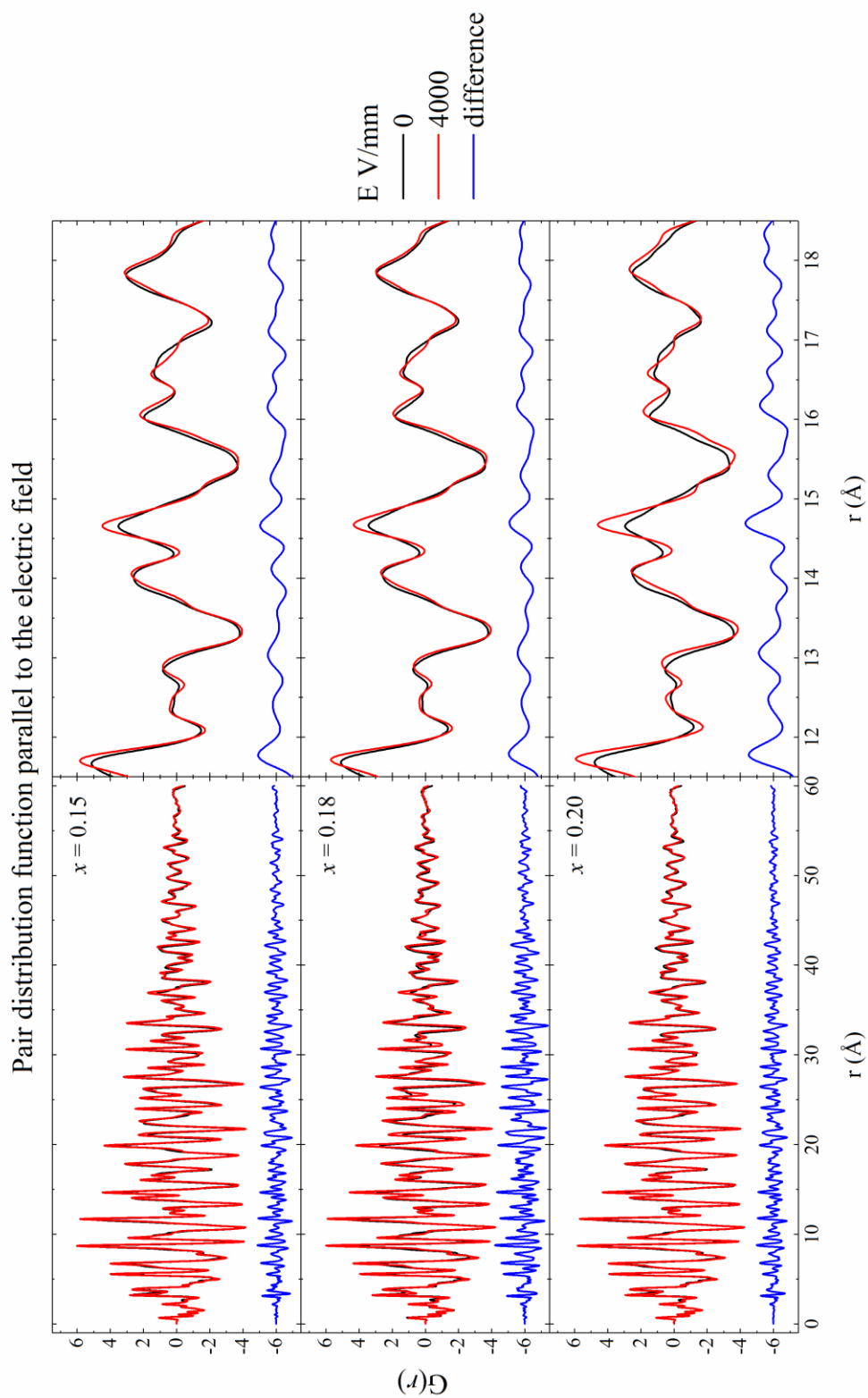
Figure 4.8 $G_\parallel(r)$ **for all compositions showing 0 V/mm (black) and 4000 V/mm (red), and difference (blue). Insets more clearly show the peak sharpening effects.**
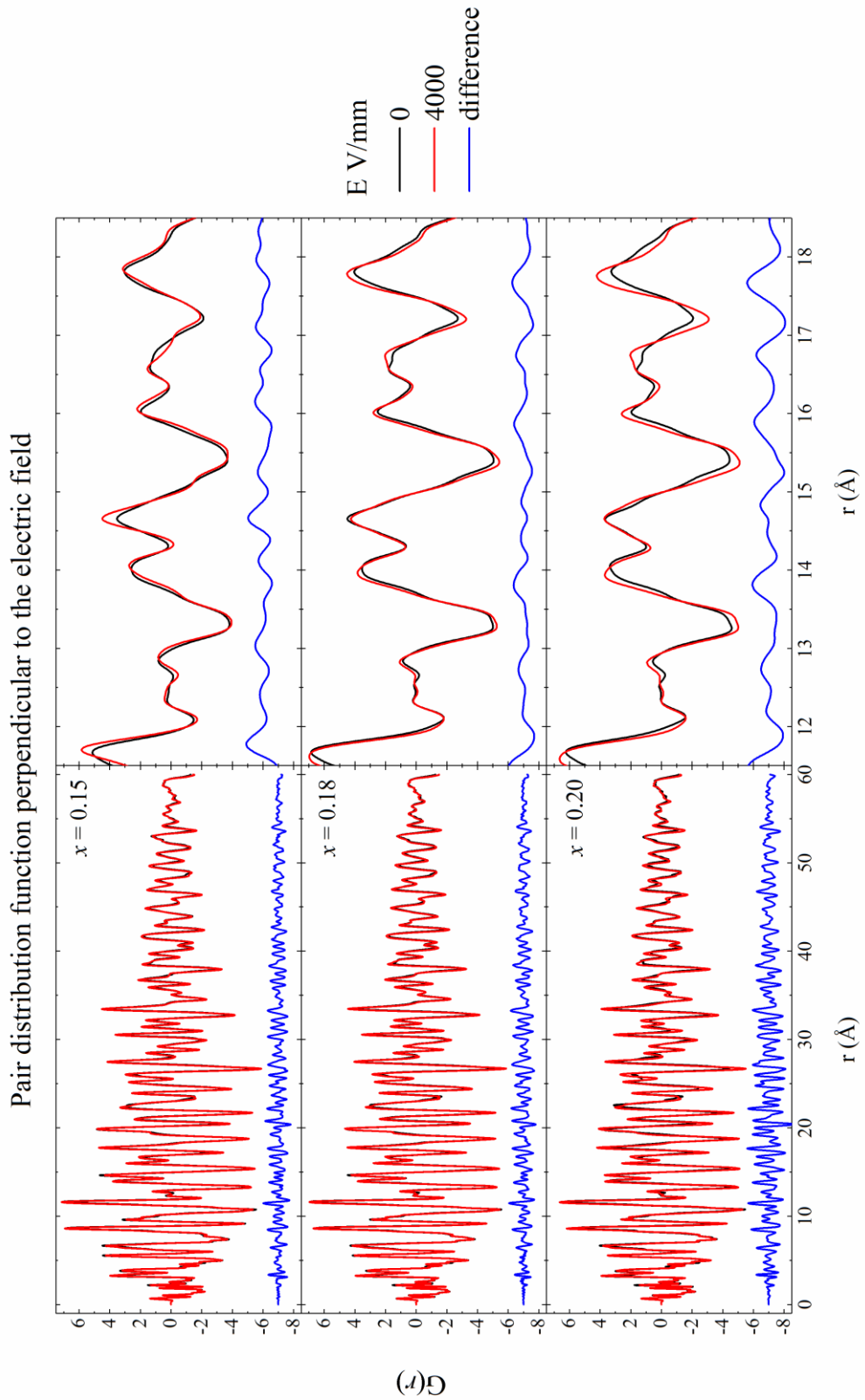
Figure 4.9 $G_\perp(r)$ **for all compositions showing 0 V/mm (black) and 4000 V/mm (red), and difference (blue). In the same manner as** $G_\parallel(r)$ **sharpening effects are shown in the inset, though less pronounced.**

To better understand the current data, it is more useful to look closely at certain ranges of r. In **Figure 4.10** low and high-r sections of the PDFs are shown for all compositions, parallel and perpendicular to the electric field. The low-r section ranges from 3 – 4.2 Å. This region contains the ABO_3 perovskite unit cell with A-B site distances in the 3.2 – 3.8 Å regions and the A-A/B-B site distances around 3.9 – 4 Å, typically called the cell parameter distance. The approximate position of peaks observable in this low-r range are highlighted by vertical black tick marks. The high-r range of the PDF shows distances at greater length-scales (41 - 47 Å), probing longer range order.

There are several observable changes exhibiting two distinct phenomena. High-r structural changes reflect expected electric-field induced piezoelectric lattice strain at higher fields, by the shift of peaks to greater r parallel to the field ($G_\parallel(r)$ in **Figure 4.10**). The lattice strain produces an extension of the lattice and thereby extension of the atomic distances. Perpendicular to the field high-r distances contract, again expected due to the lattice accommodating the anisotropic field ($G_\perp(r)$ in **Figure 4.10**). Conversely however, at low-r the opposite shift is observable with shifts to lower r parallel to the field and shifts to higher r perpendicular to the field. This is initially unexpected, requiring further analysis of the low-r range data.

The following two sections show the more in-depth analysis conducted on the low-r and high-r sections separately.
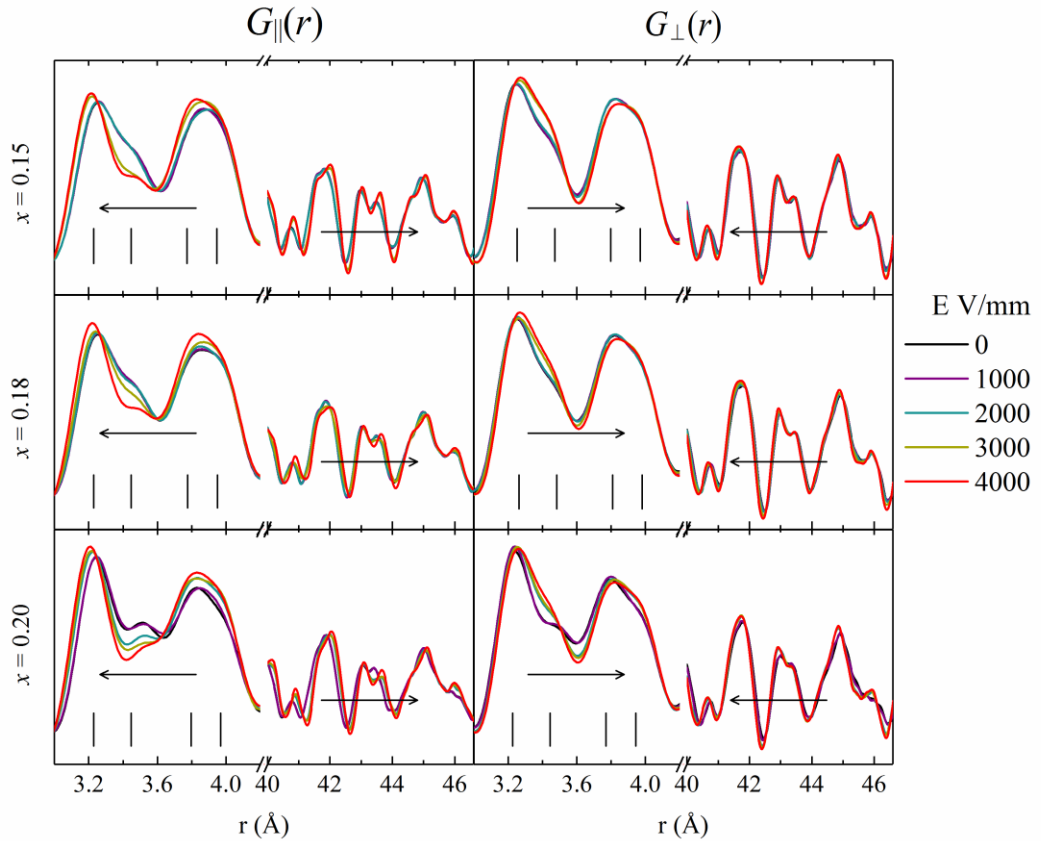
Figure 4.10 $G_{\parallel}(r)$ and $G_{\perp}(r)$ **for low and high** r **sections. Vertical black tick marks indicate low-**r **peak centres. Arrows indicate the general displacement of peak positions with applied field, showing a range dependent behaviour of interatomic spacings.**

4.5.1 Low-r peak analysis

To analyse the low-r behaviour, peak fitting in the $3 - 4$ Å range was performed. The shortest atom-pair distance corresponds to the Ti-O distance at 1.9 Å [136], however it is obscured by spurious oscillations induced by the relatively limited Q_{max} used in the Fourier transform. There are more atom-pairs corresponding to distances within the perovskite unit cell up to 7 Å e.g. the face diagonal around 5.4 Å, and the body diagonal around 6.9 Å. However, above 4 Å multiple atom-pairs contribute to a single peak and this peak overlap is non-trivial to analyse. Therefore the $3 - 4$ Å range is deemed suitable for analysis, corresponding to the A-B, A-A and B-B site distances. The perovskite ferroelectric structures studied here are characterised by off-centred displacements e.g. rhombohedral ‹111› or tetragonal ‹001› off-centring. This structural distortion results in the splitting of A-B site distances from the unified centrosymmetric cubic distance. For

KNBT this corresponds to Bi off-centering with respect to Ti giving a shortest distance of around 3.2 Å in good agreement with EXAFS measurements [136]. There is some contribution from the longest Bi-O distances that emerge for a rhombohedral distortion, however the effect is small and is spread across all Bi-Ti split distances.

Fixing the peak fitting areas in specific ratios enables structural determination as each distortion away from the centrosymmetric cubic structure has a corresponding set of peak area ratios. However, prior knowledge of these area ratios is required. To determine the ratios corresponding to different off-centre displacements a simple displacement model was constructed.

4.5.1.1   Displacement model

A simple displacement model was constructed as a foundation for some of the assumptions of the radial distribution function (RDF) fits. As discussed in Section 2.3.5.3, the RDF is perhaps the most intuitive atomic distribution function as the peak area corresponds to the coordination number. With this model, the coordination number ratios for various displacements can be inferred. The model consists of a unit cell with atoms in its eight corner positions representing Ti ions, and a central atom representing a Bi ion. It is justified to consider Bi as the displaced ion within the Ti ion frame as the disorder in NBT and related materials emerges from the localised Bi off-centre ordering [84].

Figure 4.11 shows a visual representation of this simple model, showing all atoms in the system, their 3D coordinates and the various displacement directions tested. This current model is still quite limited as the Ti ion frame is static i.e. it does not distort along with the Bi ion displacement and is therefore not realistic. For simple determination of the peak area ratios it is still useful however.

The Bi ion starting position is at the centre of the Ti frame (0.5, 0.5, 0.5) as shown in **Figure 4.11**. Here the distances to the corner Ti ions are evidently equivalent. The distance from Bi to each Ti can be calculated regardless of the position of Bi within the Ti frame. The Bi position is then modified depending on the displacement vector chosen, and is displaced along the vector in small incremental steps. At each step along a vector the Bi-Ti distances are then calculated. The distances were calculated on a Microsoft Excel spreadsheet.

The displacement directions tested were ‹001›, ‹111›, ‹110› and ‹112›, shown in **Figure 4.12**. The distances from the central Bi to the corner Ti are calculated as a function of Bi displacement. The Bi atom is displaced in small steps in a given direction.

In order to more realistically reflect these distances a deviation bounded at ±0.05 Å from the calculated positions was artificially added. The error follows a Gaussian distribution to reflect the physically realistic divergence of atomic positions. This also served to justify the requirement of the grouping of some distances into a larger set as the peaks in the raw data would be close enough to be represented by one. For example the rhombohedral ‹111› displacement requires a grouping of two groups of overlapping curves containing 3 atom-pair distances each; the peaks are broad and therefore contribute to a single peak with an area ratio of 6, out of a total area ratio of 8. This also reduces the number of peaks required for fitting facilitating the analysis, which in the small r range available would be non-trivial to differentiate.

The ‹001› and ‹111› displacements were chosen as they correspond to tetragonal and rhombohedral distortions which have been widely reported in KNBT [96]. ‹110› corresponds to a monoclinic displacement, reported in the NBT end member [108]. The ‹112› displacement was initially trialed as it reflects an averaging of tetragonal and rhombohedral displacements (that could emerge from locally coexisting tetragonal and rhombohedral domains). However it is also apparent that it could consist of an averaging of multiple monoclinic displacements e.g. ‹101› and ‹011› (emerging from monoclinic or orthorhombic domains). A final consideration of the ‹112› displacement is as an intrinsic displacement direction that would correspond to a lower symmetry distortion.
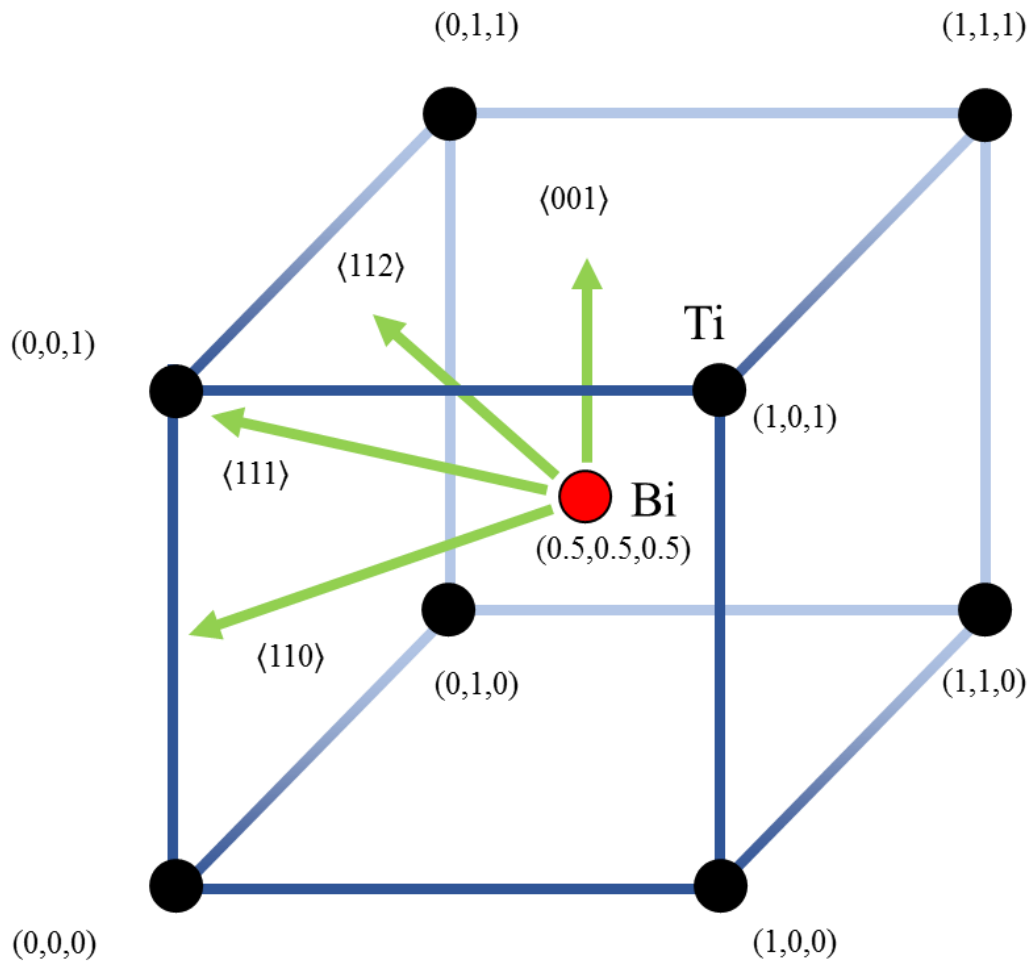
Figure 4.11 Simple cubic model with distances from central atom (red Bi) to corner atoms (black Ti) is measured as Bi is shifted along different directions (green arrows).
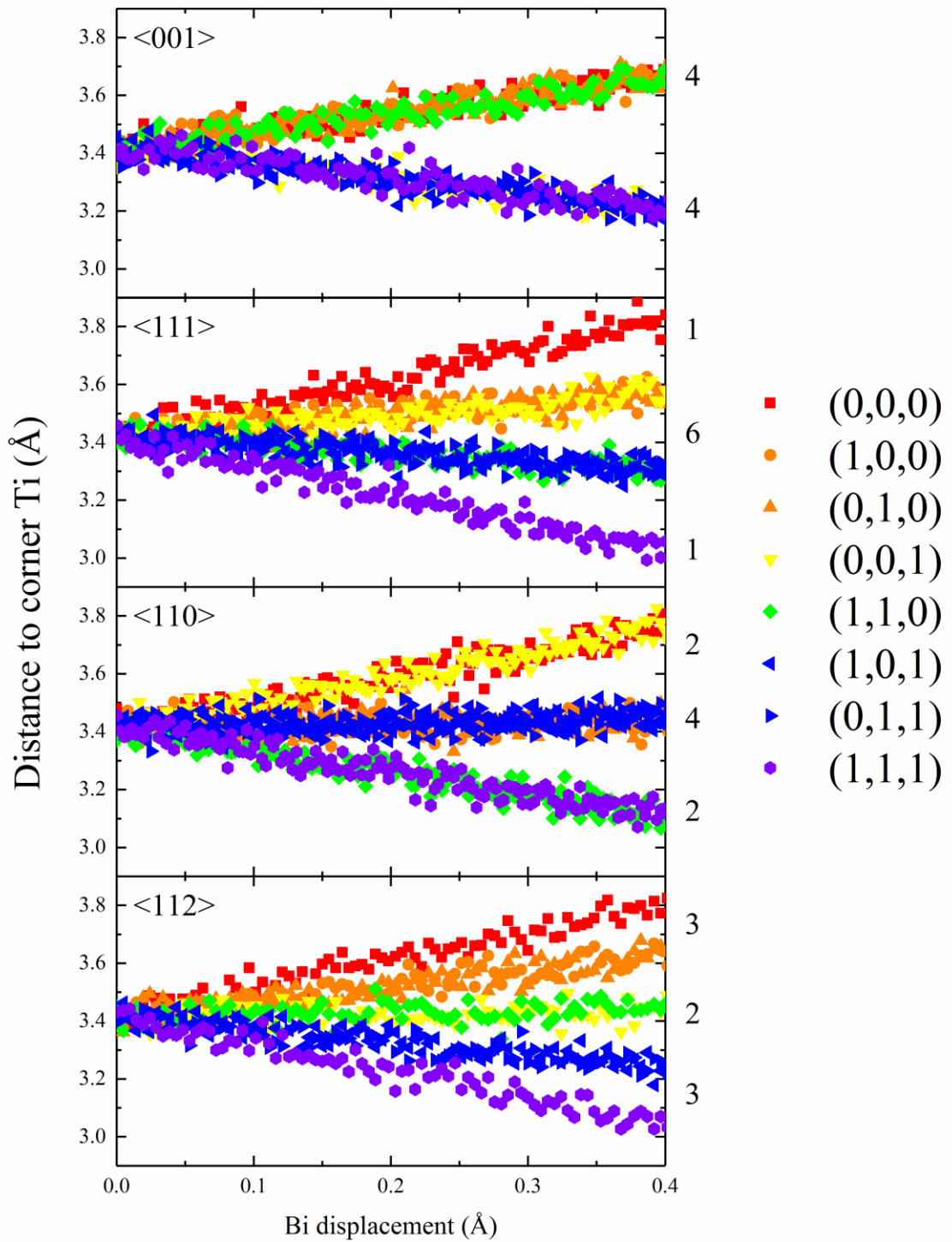
Figure 4.12 Distance of central Bi atom to 8 corner Ti atoms labeled by coordinates as a function of Bi displacement along various directions. Illustrated here are the various distances that emerge with different directions.

Table 4-1 summarises the displacement model results with clustering into the chosen groupings (**Figure 4.12**). **Figure 4.13** illustrates the splitting of the A-B site where the distances have been labelled short, intermediate and long, or R1, R2 and R3 respectively. Displacement directions such as ‹001› are relatively easy to visualise. A tetragonal distortion has 4 short A-B site distances and 4 long ones. Other displacements are more complex and have benefitted from the displacement model in order to determine their behaviour.

Table 4-1 Summary of atom pair distances arising from various displacement directions.

Displacement direction	Short: R1	Intermediate: R2	Long: R3
‹001›	4	-	4
‹111›	1	6	1
‹110›	2	4	2
‹112›	3	2	3
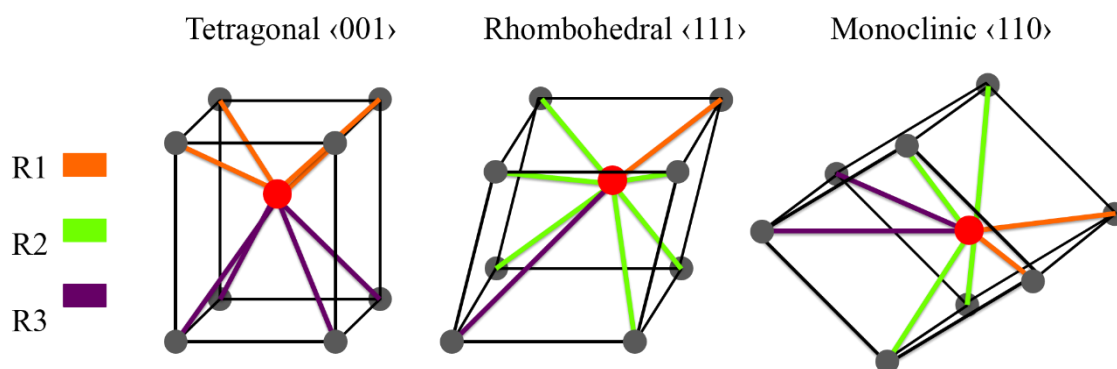
Figure 4.13 Schematics illustrating the structures related to different displacements and the subsequent interatomic distance $R1$ (short), $R2$ (intermediate) and $R3$ (long).

4.5.1.2   RDF fits

As previously discussed the radial distribution function (RDF) is more appropriate for low-r analysis with the added benefit that the peaks follow a Gaussian distribution. Furthermore, the RDF peak areas are proportional to the coordination number for a given

atom-pair. These features offer significant advantages to study a local structure which is distorted from the cubic structure and features A-B site distance splitting.

The RDF is calculated from the PDF as shown in **Equation 4.2**, and henceforth labelled by the symbol $G^*(r)$. The number density ρ_0, is obtained from the total scattering data. For each set of peaks, the areas were fixed in the ratios shown in **Table 4-1**. The peaks were then fit to the data by a least-squares method.

To validate this method, compositions away from the MPB, $x = 0.10$ and $x = 0.30$, were first fit with simpler rhombohedral and tetragonal models respectively, structures which are established and reported for these compositions. The reasoning here is that away from the MPB the atomic structure is less complex and therefore simpler models are suitable. Shown in **Figure 4.14** are the RDF fits for $x = 0.10$ and $x = 0.30$, showing peaks R1, R2, R3 and the Bi-Bi/Ti-Ti peak. These do indeed display the peak area ratios corresponding to rhombohedral ‹111› (R1 = 1, R2 = 6, R3 = 1) and tetragonal ‹001› (R1 = 4, R3 = 4) structures respectively.

Equation 4.2

$$G^*(r) = \big(G(r) + (4\pi r\rho_0)\big)r$$
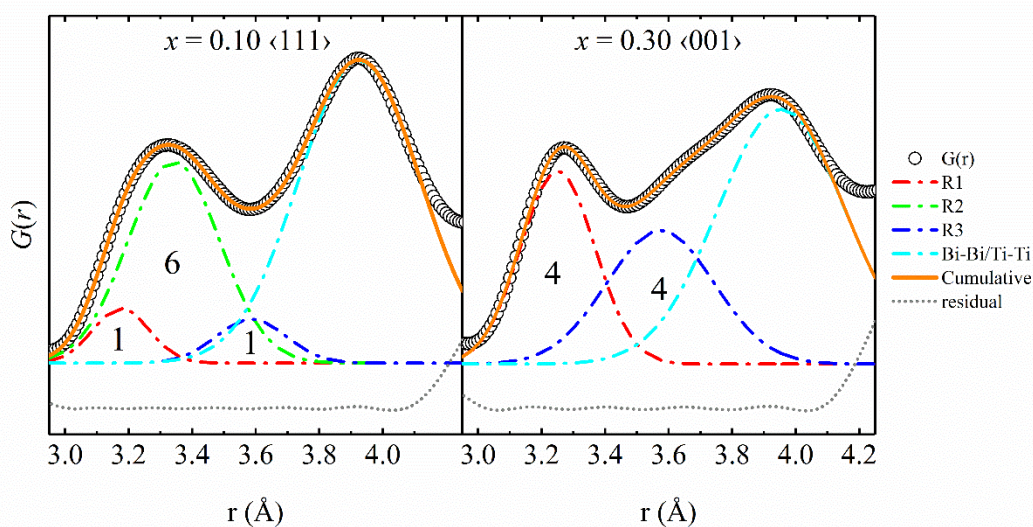
Figure 4.14 Displacement fits to RDF data for $x = 0.10$ (rhombohedral) and $x = 0.30$ (tetragonal) compositions.

The fits were performed on the compositions of interest: $x = 0.15$, $x = 0.18$ and $x = 0.20$, shown in **Figure 4.15** for the zero-field data sets. For $x = 0.15$ the ‹110› (R1 = 2, R2 = 4, R3 = 2) displacement was found to be best whilst $x = 0.20$ displayed a prefered ‹112› (R1 = 3, R2 = 2, R3 = 3) displacement fit. For $x = 0.18$ both displacement models appeared to show equally good fits. As shown in **Table 4-2** the goodness of fit (χ^2) confirms this behaviour. The difference in the fit for $x = 0.18$ is not sufficiently large to distinguish between the preferential suitability of the two displacement models. Additionally the fit value of ‹112› on $x = 0.18$ is significantly lower than for $x = 0.15$. What is apparent is a gradual transition from the ‹110› to the ‹112› displacement with increasing x.
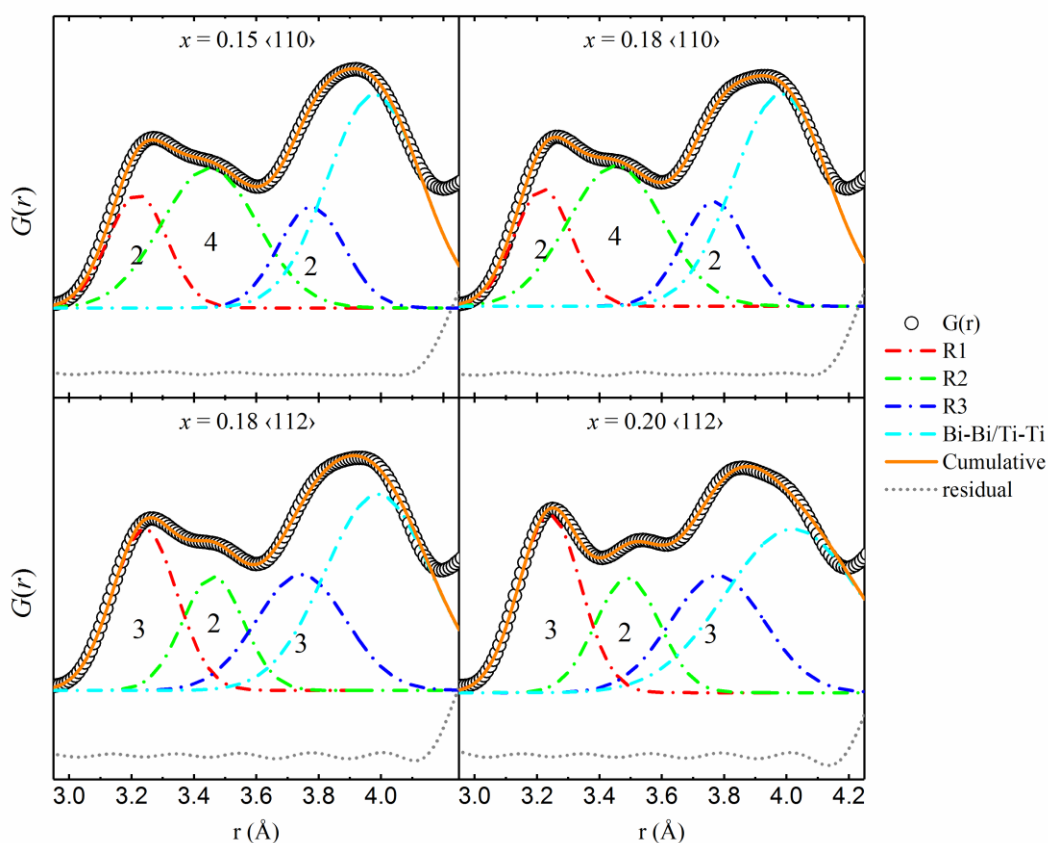
Figure 4.15 Displacement model fits to RDF data x = 0.15, 0.18 and 0.20. With increasing x a gradaual transition from the 2:4:2 ‹110› model to the 3:2:2 ‹112› model occurs.

Table 4-2 Goodness of fit for models shown in Figure 4.15 showing prefered ‹110› displacement for *x* = 0.15, a mixed fit for *x* = 0.18 and a ‹112› fit for *x* = 0.20

Goodness of fit: reduced χ^2			
Composition *x* =	<110>	<112>	Difference
0.15	0.008	0.385	0.377
0.18	0.008	0.025	0.017
0.20	0.119	0.023	0.096

The directional RDFs are shown in **Figure 4.16** at 4000 V/mm parallel and perpendicular to the electric field. To observe how the peaks behave as a function of electric field, the previously applied constraints were removed. Parallel to the field vector all compositions display a general increase in the intensity of R1 and R3 with a suppression of R2. Perpendicular to the vector the opposite effect can be observed showing a significant increase in the intensity of R2 and a suppression of R1 and R3, with a near extinction of R3.

These results suggest that the Bi^{3+} cation displacements are changing from a randomised arrangement, reorienting parallel to the electric field vector relative to the surrounding Ti^{4+} cations. Now more of the long and short (R1, R3) Bi-Ti distances are present along the field vector whereas the intermediate (R2) distances are more pronounced perpendicular to the field. This reorientation behaviour can be inferred because of the proportionality between peak area and coordination number. **Figure 4.17** is a schematic representation of a complete field induced Bi-Ti bond redistribution.

The displacement direction of data collected at 4000 V/mm cannot be readily determined. However the results can aid in narrowing down the possibilities. In the perpendicular direction R2 shifts to lower *r* which suggests the displacement is approaching monoclinic. Parallel to the field there is still a strong presence of R2 which excludes rhombohedral and tetragonal transitions which would be characterised by a lack of R2 altogether. These higher symmetry phases may be induced at greater fields.

Additionally, the previously observed low-*r* opposing shifts i.e. negative shifts parallel to the field and positive shifts perpendicular to the field can be explained as the exchange of peak intensities which give the appearance of a shift.
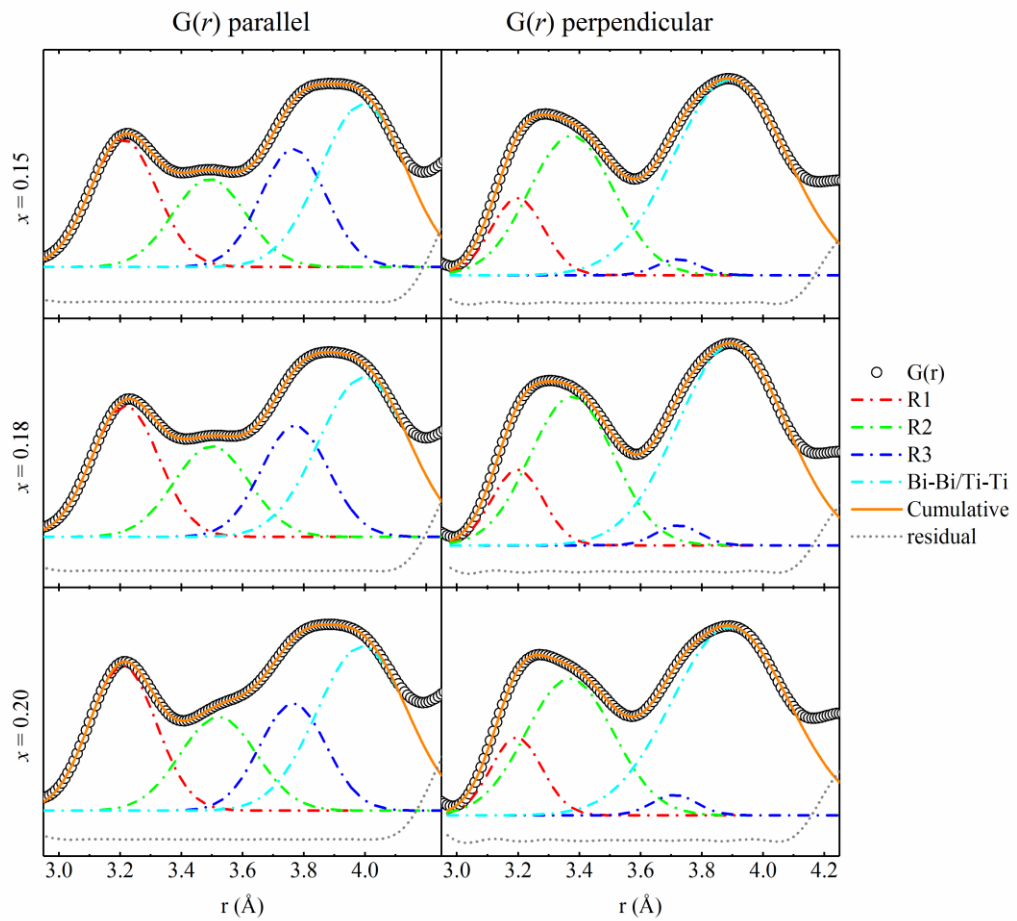
Figure 4.16 RDF parallel and perpendicular to the electric field vector at 4000 V/mm.
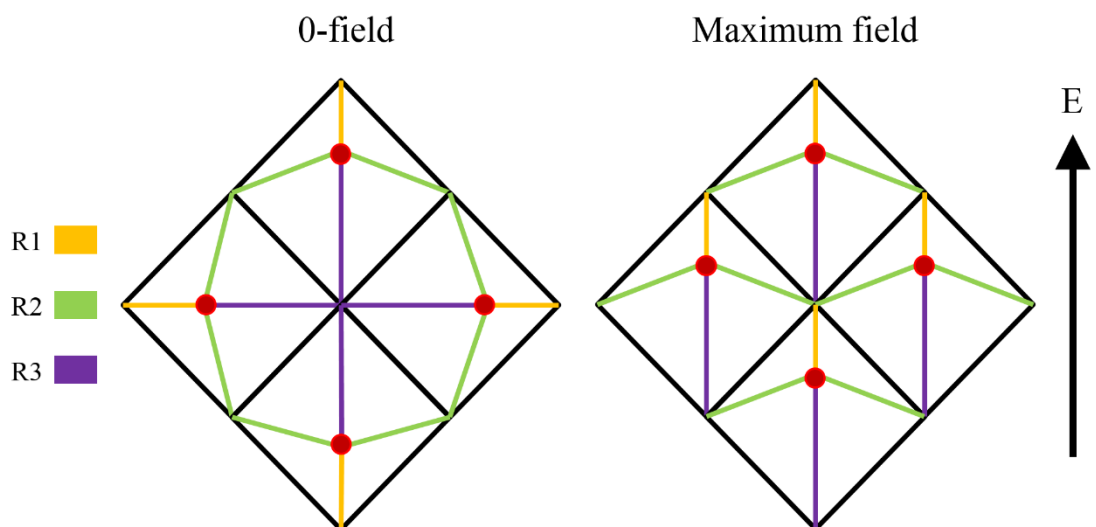
Figure 4.17 Schematic illustrating the field induced rearrangement of short, intermediate and long Bi-Ti resulting from the reorientation of the central Bi ion.

4.5.2 Piezoelectric strain analysis

To determine the high-r behaviour an approach previously described to calculate the effects of the electric-field on the PDF peak positions and changes to peak shape is employed here [137]. The following sections will show the features of this calculation and its application to the PDF data.

4.5.2.1 Peak shift calculation

The peak shift calculation functions by comparing the same small range in r (Δ) between zero-field PDF $E = 0$, and a PDF at field $E = \alpha$, where α is a non-zero field. The small section of $E = x$ is shifted in steps (δr) backwards in r whilst calculating the residual $\mathcal{R}^*$ is calculated at every step. When a minima in $\mathcal{R}^*$ is encountered this indicates that the peaks in the ranges are most similar and have shifted δr relative to $E = 0$. The value δr therefore indicates the amount of peak shift that has occurred for an electric field x. The minimum value R gives an indication of how much the peak shape has changed with the electric field.

This calculation is described in **Equation 4.3**, where $G(r)_{E=0}$ is the zero-field PDF, $G(r)_{E=\alpha}$ is the PDF at electric field α. $\mathcal{R}^*$ is the residual calculated between the two data sets in a fixed range Δ and δr is the shift in Δ, and N is the number of steps in the calculation. R^* is given by the magnitude of the summed differences between $G(r)_{E=0}$ and $G(r)_{E=\alpha}$ over a range Δ, divided by the magnitude of the sum of $G(r)_{E=0}$ over that same range. There are several important considerations required when using this method, particularly setting a reasonable Δ value. Generally, the range should be at least the breadth of one peak to accurately track the shifts. Additionally, the method is most reliable with well-defined peaks. At very high-r values the PDF signal decays significantly and this may produce unreasonable results.

Equation 4.3

$$\mathcal{R}^* = \frac{\sum_r^{r+\Delta} |G(r)_{E=0} - G(r \pm \delta r)_{E=\alpha}|}{\sum_r^{r+\Delta} |G(r)_{E=0}| / N}$$

To demonstrate this method in a simple manner the calculation was applied to two Gaussian peaks offset by 4α units as shown in **Figure 4.18 a)**. The peak representing $E = 0$ is in position 10 and the peak representing $E = \alpha$ represents a field induced peak shift of 4 units. Peak $E = \alpha$ is shifted back towards peak E = 0 and beyond its position. The residual values as a function of peak offset are shown in **Figure 4.18 b)** and the minimum value of $\mathcal{R}^*$ is at -4 indicating that the shift between the peaks is 4 units. In this modelled example the $\mathcal{R}^*$ value is exactly 0 as the chosen peaks are identical. Here is where peak shape change would be measured as a non-zero $\mathcal{R}^*$ value at the minima. The greater the value of $\mathcal{R}^*$ is at the minima the greater the peak shape has changed. In a real example this could correspond to peak broadening or sharpening.
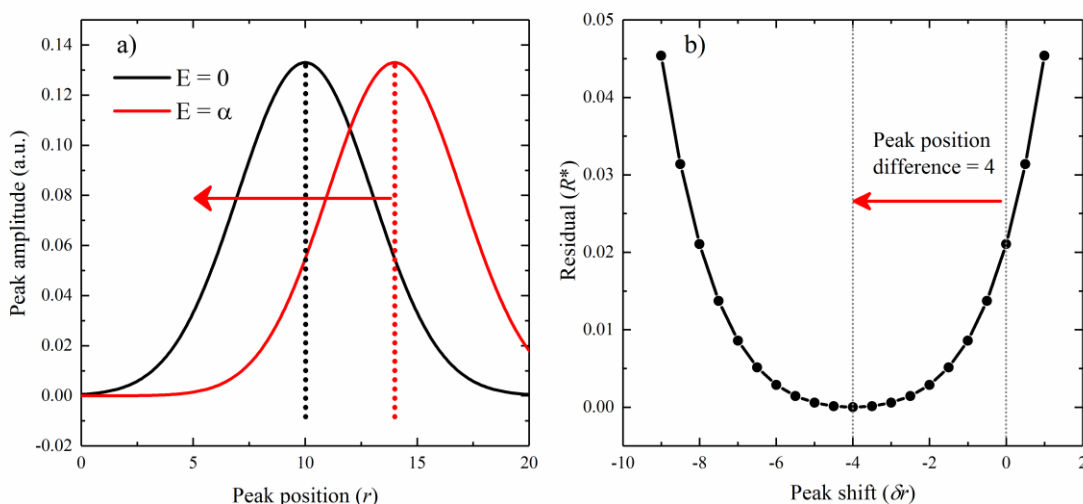
Figure 4.18 a) The peak from E = α is shifted back past the peak at E = 0 whilst calculating the residual. b) The residual is at its lowest at -4 indicating that at this point the peaks are in equal positions. Therefore this shows that the peak at E = α has shifted forward by 4 units.

4.5.2.2 Peak shift data

The calculated peak shift (δr) in the parallel and perpendicular directions for $x = 0.15$, 0.18 and 0.20, is shown in **Figure 4.19**. Here the calculation box or bandwidth Δ was set to 5 Å, sufficient to contain at least one peak and at most two. This allows for measurement of peaks that are very broad but not so large that displacement information

for any individual peak is lost, and ensures that there is always at least one peak within the box. The step size N was set to 0.5 Å.

The piezoelectric lattice strain effects can be clearly seen with an approximate linear increase in the peak shift with r observed at high fields. Parallel to the field the lattice extension increases the interatomic distances i.e. positive δr. Perpendicular to the field the extension strain is accommodated by a perpendicular contraction in the lattice i.e. negative δr. The overall magnitude of the shifts perpendicular to the field are also around half of those parallel. At low electric fields in the parallel direction the shift response to field is approximately constant across r and does not follow the linear piezoelectric behaviour as this is sub-coercive field. However, the shift is non-zero across r which suggests that the the initial low-field responses are not correlated and localised, only becoming macroscopic at greater fields. The greatest changes are observed for $x = 0.20$, reflecting the greater peak shifts apparent in **Figure 4.10**. Below 7 Å (atom-pair distances within the unit cell) the peak shifts oppose the general trend i.e. negative in the parallel direction and positive in the perpendicular direction. Here, unexpected low-r shifts previously shown in **Figure 4.10** are revealed. Above 40 Å artefacts in the calculation become more prominent due to the relatively small $G(r)$ signal at high-r values.
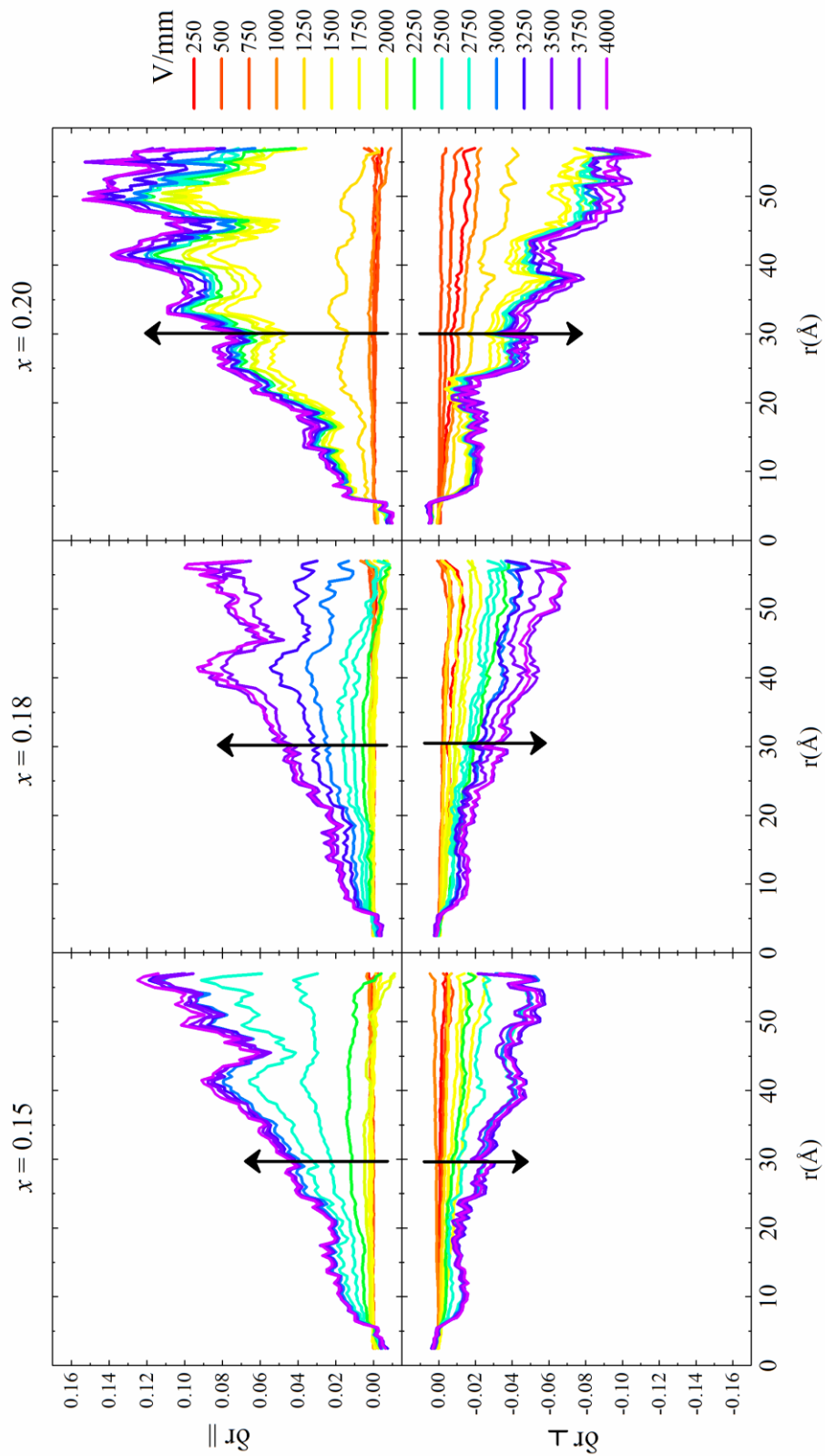
Figure 4.19 Peaks shifts (δr) parallel (∥) and perpendicular (⊥) to the electric field as a function of *r* and electric fields ranging from 0 – 4000 V/mm. Arrows indicate the general electric field trend.

The residuals $\mathcal{R}*$ are shown in **Figure 4.20**. For $x = 0.15$ and 0.18 the peak shape changes are slightly greater at high r than at low r. For $x = 0.20$ the changes are greater above 10 Å. This can be explained as field induced peak sharpening or ordering which becomes more apparent at greater ranges. The data does appear 'noisy', in particular for $x = 0.20$, again likely due to calculation artefacts related to small $G(r)$ signals at high r and the chosen parameters such as the calculation range Δ, and the step size N.
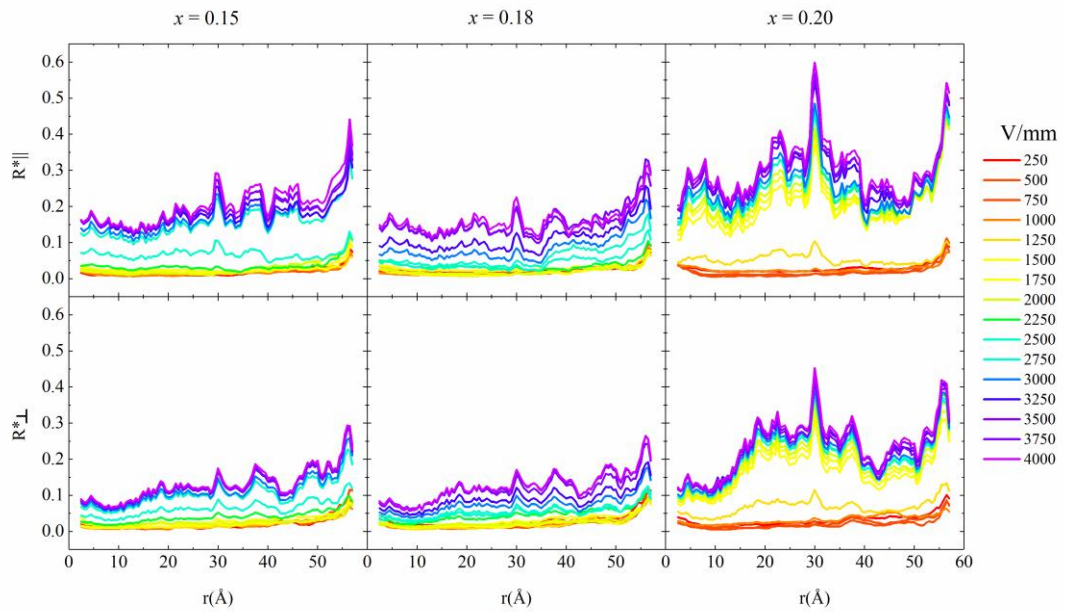
Figure 4.20 Residuals from the $\mathcal{R}*$ calculation as a function of eleictric field across all ranges of r.

4.5.2.3 Calculated strain

Field-induced strain was calculated from the gradient of $\delta r(r)$ with a linear regression fit over the 10 – 40 Å range, shown in **Figure 4.21**. This range was chosen to avoid the low-r effects previously discussed and the artefacts emerging above 40 Å. For $x = 0.20$ several features are prominent: 1) a region of little or no strain response from 0 – 1000 V/mm, 2) a rapid increase in strain from 1000 – 1500 V/mm and 3) a linear increase for the remainder of the applied fields. The rapid change observed correlates with phase transitions from pseudocubic to tetragonal previously reported [99], described as growth of tetragonal domains. The remaining significant contribution of R2 parallel to the PDF shown in **Figure 4.16**, suggests that a tetragonal phase transition is not observed

at short length scales. The linear increase in strain is however consistent with piezoelectric lattice strain, this is evidenced by a linear regression fit over this region, shown by the dotted blue line.

For $x = 0.15$ and 0.18 these features are far less prominent, showing a gradual increase in strain beginning around 2000 V/mm which plateaus around 3000 – 3500 V/mm. The perpendicular strain response is not as significant for all compositions, showing around half δr gradient compared to the parallel response. In the presence of an anisotropic stimulus this behaviour is expected and can be defined by Poisson's ratio.
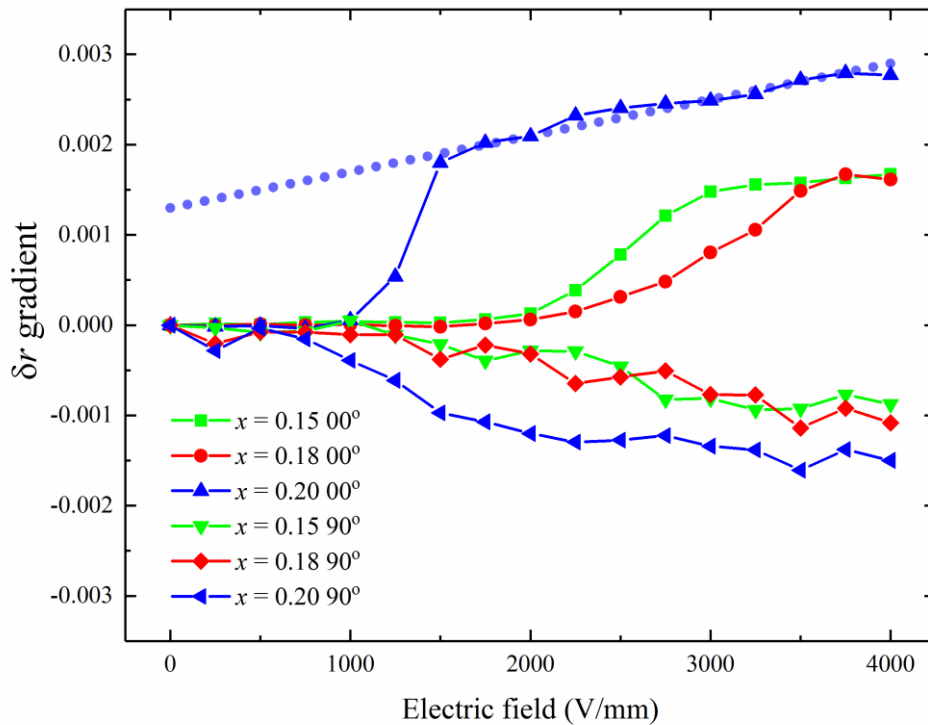
Figure 4.21 Gradient of peak shift δr or effectively piezoelectric strain as a function of electric field in the parallel and perpendicular directions relative to the electric-field vector. A linear regression fit on $x = 0.20$ (parallel) is shown to exhibit piezoelectric behavior.

4.5.2.3.1 d_{33} measurements

After the experiment was conducted, the piezoelectric charge coefficient d_{33} was measured using the Berlincourt method. The measurements are shown in **Table 4-3** and represents the average of three consecutive measurements. As the measurements were

taken from bars poled on their long faces the measurements are not representative of true d_{33} values. As per the IEEE measurement standard these would require disk samples with a diameter to thickness ratio greater than 10:1. In this case however the differences between the measurements still illustrate an increase in d_{33} as the MPB composition is approached.

Table 4-3 d_{33} measurements post-experiment

Composition (x)	d_{33} (pC/N)
0.15	119
0.18	130
0.20	161

4.6 Conclusions

The local Bi off-centre displacements relative to their nearest neighbour Ti atoms in $(K_x Na_{1-x})_{0.5} Bi_{0.5} TiO_3$ solid solutions near the MPB were measured using atomic pair distribution function (PDF) analysis derived from X-ray total scattering. The compositions measured were $x = 0.15$, 0.18 and 0.20. The analysis was divided between low-r and high-r ranges of the PDF.

In the low-r range the nearest three Bi-Ti distances were observed: short (R1), intermediate (R2) and long (R3). Parallel to the electric field vector R1 and R3 increase in amplitude with electric field at the expense of a decreasing R2. Perpendicular to the field vector R2 is more significant with a great decrease in R1 contribution and near extinction of R3. This suggests a Bi-Ti bond redistribution as a result of Bi displacing along the field vector with respect to Ti. This behaviour appears to be incipient to macroscopic piezoelectric lattice strain observed at high-r.

The high-r range was used to calculate field-induced strain. At the MPB ($x = 0.20$) there is an abrupt onset of Bi-Ti redistribution and lattice strain. For $x < 0.20$ the boundary between bond redistribution and piezoelectric lattice strain is less clear.

Generally, at low fields there is a constant non-zero strain. As this is a sub-coercive field regime there is no linear strain expected of piezoelectric behaviour. At greater fields (> 3000 V/mm) the behaviour becomes piezoelectric. This suggests an initial locally correlated strain which becomes macroscopic at high fields. The previously reported field induced transition to a tetragonal strain for $x = 0.20$ could therefore be explained as a macroscopic phenomenon initially mediated by local Bi-Ti reorientation [44]. The PDF technique is a low resolution scattering method due to the short sample-detector distance, and therefore the tetragonal transformation was not observed in the total scattering structure factor.

At zero-field the changes to the low-r behaviour were analysed as a function of composition. The Bi displacements undergo a transition from ‹110› to ‹112› with x increasing from 0.15 to 0.20. The ‹112› displacement can be interpreted in several ways: as an averaging of ‹001› and ‹111› or ‹101› and ‹011›, or an intrinsic ‹112› displacement. The averaging of two monoclinic/orthorhombic displacements ‹101› and ‹011› is favoured here because of the pseudosymmetric nature of NBT-KBT system where the rhombohedral and tetragonal phases have been reported to display local lower symmetry phases [138]. The increased number of displacement directions at the MPB appears to promote Bi-Ti redistribution under an electric field which is manifested as greater strain and improved piezoelectric properties. **Figure 4.22** summarises the Bi displacement directions at zero-field including results from $x = 0.10 - 0.30$, highlighting the monoclinic phase transition region at the MPB $x = 0.20$.
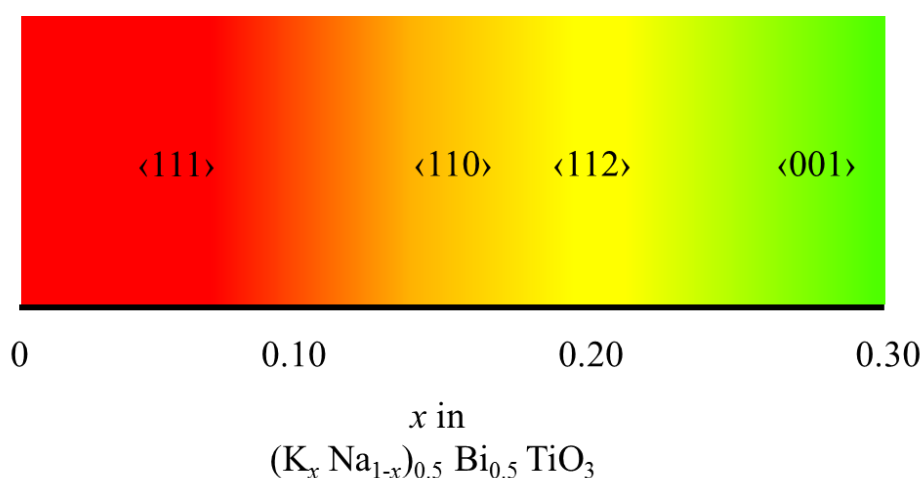
Figure 4.22 Proposed diagram of zero-field Bi displacement directions. Where ‹111› is indicated in red, ‹101› in orange, ‹112› in yellow and ‹001› in green.

5 Conclusions

The work presented here is a local structure analysis of two key materials in the (Na, Bi)TiO$_3$ (NBT) family of piezoelectric materials, namely x(K, Bi)TiO$_3$-(1-x)(Na, Bi)TiO$_3$ (KNBT) and (1-x)(Na, Bi)TiO$_3$-xPbTiO$_3$ (NBT-PT). The interest in these material is borne from two key motivators in this scientific field: 1) Observing the behaviour of potential lead-free candidates and their local structure origin for field-dependent behaviour, and 2) understanding the role and behaviour of lead (Pb) in these materials and the mechanisms by which it affords improved piezoelectric properties.

NBT-based materials possess chemical disorder, which manifests as significant local structural deviations from the average structure. The pair distribution function (PDF) method is particularly suited to the analysis of the local structure. Whilst the technique has been used for several decades it has only recently become readily available due to increased computing power and improved experimental methods. Here both conventional PDF analysis, such as structural refinement, and non-conventional approaches have been used, particularly to study *in situ* behaviour.

Fundamentally, this thesis explores two crystal structure ordering mechanisms in NBT-based materials:

1.   Order induced by the application of an electric field.
2.   Order induced by the addition of lead titanate.

1.   Field-dependent local structure of KNBT

The local structure of KNBT was studied for compositions near the MPB. *In situ* electric field measurements show the suppression of diffuse scattering, indicating an overall crystallographic ordering behaviour is taking place. This was analysed via PDF analysis where two range dependent regimes are observed. Analysis of the higher-r data in the 10 – 40 Å range reveals behaviour resembling previous average field dependent studies. Using a PDF peak shift analysis technique the changes in interatomic distances as a function of PDF range and electric field can be observed. Across all compositions low-field response is flat across r, only adapting a linear trend at higher fields. For x =

0.20 this occurs around 1 – 1.5 kV/mm where the material becomes poled and piezoelectric behaviour is observed. This effect is begins around 2 kV/mm for $x = 0.15$ and 0.18 but the linear piezoelectric behaviour does not emerge until 3 kV/mm. The non-zero sub-coercive field peak shifts observed also suggest that the emergence of piezoelectric behaviour begins at the local scale becomes macroscopic at greater fields.

Below 4 Å atomic distances appeared to behave in a contrary manner to what is expected of field induced behaviour. Parallel to the electric field atomic distances appeared to contract whilst the opposite behaviour was observed perpendicular to the field. Analysis of the low-r data revealed a field-induced redistribution of Bi-Ti interatomic distances. This was ascertained by measurement of the contributions of the various Bi-Ti distances present within the pseudocubic unit cell. A simple displacement model of the Bi-Ti environment also revealed zero-field local distortion direction which transitioned from a rhombohedral ‹111› displacement for $x = 0.10$, to a monoclinic ‹110› displacement for $x = 0.15$. This gradually transitioned to a ‹112› displacement for $x = 0.20$ which is suggested to emerge as a combination of multiple monoclinic distortions at the MPB. These complex displacement directions finally collapse to a tetragonal ‹001› dispalcement for $x = 0.30$. The complex character of the displacement directions present at the MPB are suggested enable greater response to the electric field and therefore produce the observed improved piezoelectric properties.

2.   Local and average structure study of NBT-PT

The local structure of NBT-PT was studied for compositions near and around the MPB as a function of temperature. Supplementary to PDF analysis were average structure X-ray diffraction (XRD) and permittivity temperature measurements. Permittivity temperature results showed the transition from relaxor like to classical ferroelectric with increasing $PbTiO_3$ content from $x = 0.08$ to 0.18. This is evidenced by the decrease in the frequency dispersion broad permittivity maxima and permittivity hysteresis. These properties can be attributed to the presence of nanoregions, whose presence or influence decreases with increasing x. XRD measurements corroborate the observed temperature dependent transitions which increase in temperature with increasing $PbTiO_3$ content.

Comparisons of full profile PDF refinement to average structure measurements showed a local monoclinic phase for $x = 0.14$ whilst $x = 0.08$ and 0.18 displayed similar

local structures to the average. However, significant structural differences emerged when range dependent analyses were performed. Refinement values show the presence of a monoclinic *Cc* phase across all ranges of $x = 0.08$ with similar fits to *R3c* which displayed a slightly improved fit at ranges above 37 Å. The region of structural ambiguity decreased with increasing *x*. For $x = 0.14$ *Cc* and *P4mm* display equal fitting values up to 27 Å, above which only the tetragonal phase shows optimal fitting. This becomes more constricted for $x = 0.18$ where *P4mm* becomes optimal above 17 Å. Calculated structure parameters also revealed a significant deviation from the average structure at low *r* ranges where the structure is more distorted, be it tetragonality c/a ratio or rhombohedral angle. The length scales at which the structure represented the average increased from around 27 Å for $x = 0.08$ to 15 Å for $x = 0.18$. This has been interpreted as the presence of nanoregions of greater distortion than the average, as well as displaying lower symmetry structural characteristics. This effect persisted at high temperatures, however the effective size of the nanoregions decreased to 22 Å and 12 Å for $x = 0.08$ and $x = 0.18$ respectively.

The measurements for NBT-PT all clearly illustrate the effects of increased $PbTiO_3$ content. This can be generalised as a transition from a material with the presence of nanoregions, exhibiting relaxor-like properties, to a material more characteristic of a ferroelectric which retains some relaxor characteristics which are far more subdued. This is particularly evidenced by the decrease in the nanoregion size. $PbTiO_3$ is a highly strained and ordered material and its presence in the solid solution induces long range crystallographic order and suppresses the formation of nanoregions.

6 Further work

Following the presented studies a clear scope for further work and development of experimental and analysis approaches is apparent. The relative infancy of the PDF analysis method, particularly when applied to ferroelectric materials has benefited from a variety of analysis approaches, some of which are presented in this thesis:

- The current PDF analysis on $(K_x, Na_{1-x})_{0.5}Bi_{0.5}TiO_3$ would benefit from analysis on scattering directions between the 0° and 90° directions relative to the electric field vector already presented. For the low-r analysis of the Bi-Ti peas the exchange in $R1$, $R2$ and $R3$ intensities as a function of angle to the electric field would provide further insight in to the Bi-Ti reorientation mechanisms. Similarly analysis of the strain calculated from the PDF peak is useful in characterising the nano domain reorientation behaviour. This analysis method is comparable to stain analysis by calculation of the {200} peak intensity ratios applied to average structure *in situ* measurements.

- The current study on $(1-x)(Na_{0.5}, Bi_{0.5})TiO_3-xPbTiO_3$ provided an insight in to the behaviour of lead (Pb) in an effort to understand the improved properties typically observed on lead based piezoelectric materials. It would be highly useful to measure the nanoregion size in the same manner presented here on other materials in which Pb is added, for example bismuth ferrite lead titanate (BFPT). The presence of nanoregions has been observed in bismuth ferrite potassium bismuth titanate (BF-KBT), in a pseudocubic compositional region. Average structure studies show the suppression of the nanoregions with the addition of $PbTiO_3$. Measurement of their size via could therefore be achieved via the range dependent PDF method.

- The inherent chemical disorder in KNBT and other NBT based materials is fundamentally linked to the observed structural disorder. Analysis techniques such as X-ray absorption fine structure (XAFS) would therefore be highly useful as it provides greater resolution at very short length scales i.e. first coordination shell or nearest neighbour atom-pairs, and chemical information such as oxidation state. Coupled with a technique such as electron energy loss spectroscopy (EELS) which

provides elemental information, the chemical order could be suitably described.

- Novel computational methods have recently permitted advanced PDF analysis via the Reverse Monte Carlo (RMC) method using RMCprofile [139], which has been used successfully in a number of complex perovskite systems [5], [84], [85], [140]. RMCprofile is a large box modelling technique which consists of a supercell which can contain up to 10000 atoms, in contrast to the single cell or 'small-box' method used by PDFgui [132]. The supercell can be initialised with a specified position for all atoms. Within a window of constraints the atoms are allowed to displace from their original positions. A PDF is calculated for the supercell and the atomic positions are refined to PDF data. The large box enables the extraction of useful information such as distribution of atomic positions or bond angles of specific atomic species. The RMC approach is envisaged to be highly useful for the NBT-PT system. In the first instance distinguishing between the local Bi and Pb bonding environments for different compositions is expected to aid in describing the ordering effects afforded by Pb in contrast to Bi as discussed in Chapter 3.

6.1 Field rate-dependence of the local structure in $(K_x Na_{1-x})_{0.5} Bi_{0.5} TiO_3$

In conjunction to the *in situ* electric field synchrotron experiment, measurements were taken as a function of electric field ramp rate to a maximum electric field of 4 kV/mm. The motivation for this was the observation of rate dependent phase transitions, where above 0.25 kV mm^{-1} s^{-1} resulted in a transition to a tetragonal phase (Royles .et al 2011). However when strain-field measurements were conducted, no significant difference in the high-field d_{33} was observable, suggesting other effects are taking place. This prompted an investigation into the local structure behaviour.

A range of ramp rates (0.01 to 100 kV mm^{-1} s^{-1}) were applied to KNBT samples though only results for $x = 0.20$ (MPB composition) are shown. The electric field was ramped to a maximum at 4 kV/mm, after which it was maintained for 5 minutes. During

this time the scattering data were collected. The obtained PDF is shown in **Figure 6.1** for scattering parallel to the electric field vector. The higher r PDF range appears to show a general increase in peak positions with increase ramp rate. This initial observation contrasts with the aforementioned observations reported by Royles *et al*. This behaviour is also accompanied by an increase in PDF peak sharpening, indicative of induced crystallographic ordering. The peak shift calculation previously detailed Section 4.5.2.1 was applied to the PDF ramp data and is shown in **Figure 6.2**. The overall linear trend in all the curves indicates piezoelectric lattice strain behaviour. Though an overall increase in the extent of the peak shift with increasing ramp rate is apparent it is clear that a consistent trend does not exist. This is clearly shown in **Figure 6.3**, which shows the peak shift slope as a function of electric field ramp rate. This also corresponds to strain. A linear regression fit indicates overall increase in the strain with the ramp rate following a logarithmic trend; however there are significant outliers to the trend, particularly in the $0.1 - 0.3$ kV mm^{-1} s^{-1} range.

These results are initially unexpected. Given the time dependent nature of the experiment, it is expected that the slowest ramps would produce the greatest strain. The greater amount of time available would allow a greater degree of domain reorientation to occur. The opposite effect can be observed. This suggests other strain mechanisms are taking place. A preliminary suggestion is the behaviour of oxygen vacancies acting as domain wall pinning regions. As temporal response of vacancies is slower than intrinsic strain it is suggested that slower rates allow pinning regions to migrate and inhibit the strain. At fast rates the vacancies are not able to respond the field and therefore their inhibiting effect does not take place.

Here, clear time dependent strain response behaviour is illustrated. A greater understanding of this behaviour would be obtained by repeating these measurements at higher temperatures where lattice flexibility is greater. Further analysis of the low-r behaviour would more clearly elucidate the effect of rate on Bi-Ti orientation. Additionally polarisation-field and strain-field measurements via conventional means would offer further insight into the behaviour.
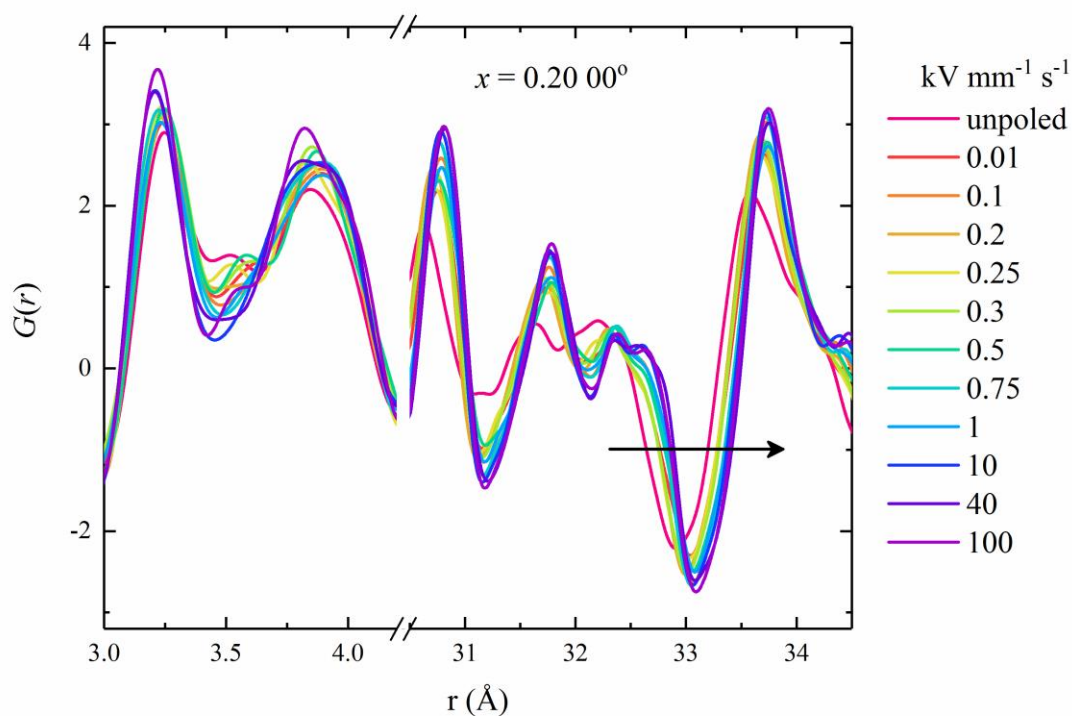
Figure 6.1 PDF as a function of electric field ramp rate for *x* = 0.20, parallel to the electric field vector. Low-*r* and high-*r* regions are shown.
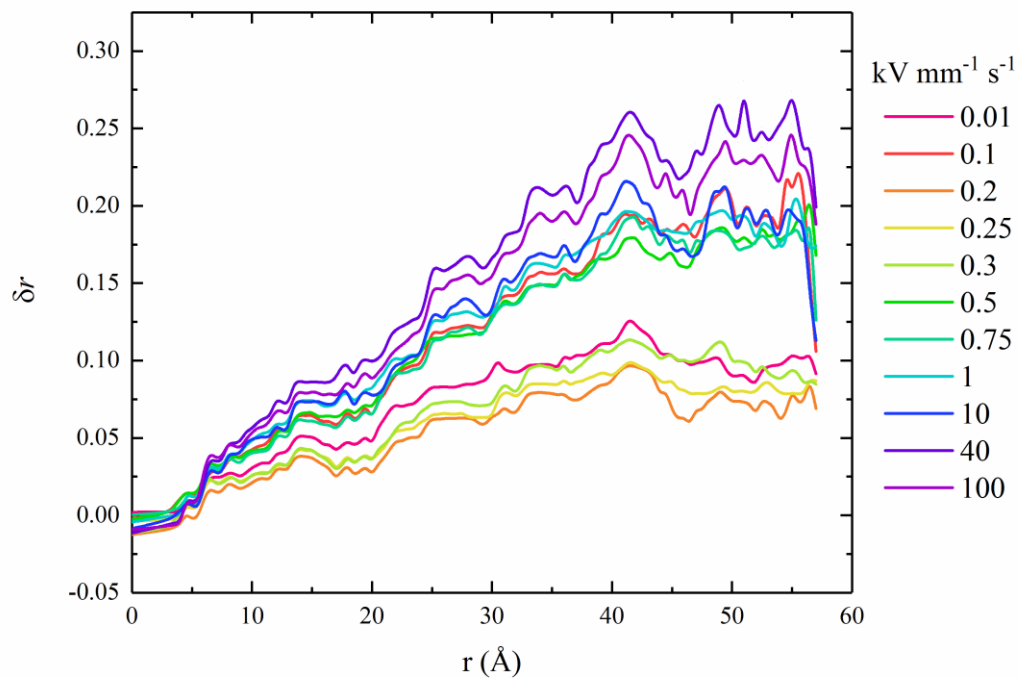
Figure 6.2 PDF Peak shift measurements for *x* = 0.20 as a function of electric field ramp rate.
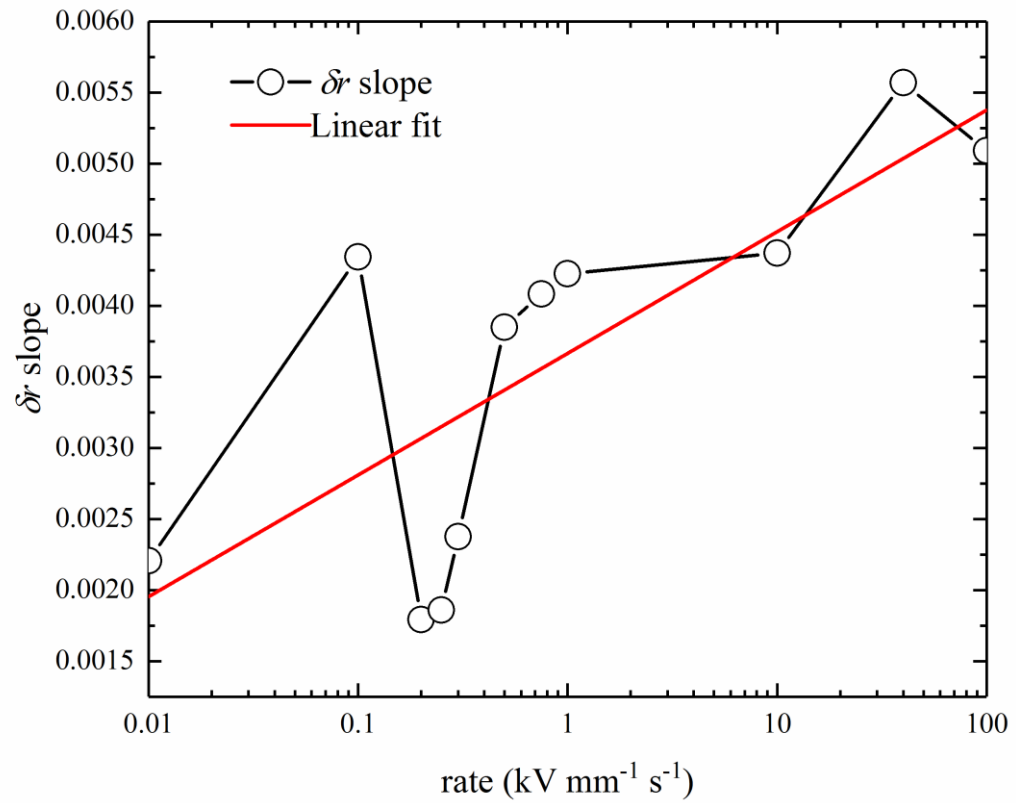
Figure 6.3 Peak shift (δr) slope or effective strain as a function of electric field ramp rate. A linear regression fit is shown in red.

7 References

[1]   A. J. Bell, "Ferroelectrics: The role of ceramic science and engineering," *J. Eur. Ceram. Soc.*, vol. 28, no. 7, pp. 1307–1317, Jan. 2008.

[2]   B. Jaffe, W. R. Cook Jr., and H. Jaffe, *Piezoelectric Ceramics*, vol. 3. Academic Press, London, 1971.

[3]   T. Stevenson, D. G. Martin, P. I. Cowin, A. Blumfield, A. J. Bell, T. P. Comyn, and P. M. Weaver, "Piezoelectric materials for high temperature transducers and actuators," *J. Mater. Sci. Mater. Electron.*, vol. 26, no. 12, pp. 9256–9267, 2015.

[4]   J. J. Rödel, K. G. Webber, R. Dittmer, W. Jo, M. Kimura, and D. Damjanovic, "Transferring lead-free piezoelectric ceramics into application," *J. Eur. Ceram. Soc.*, vol. 35, no. 6, pp. 1659–1681, 2015.

[5]   M. S. Senn, D. A. Keen, T. C. A. Lucas, J. A. Hriljac, and A. L. Goodwin, "Emergence of Long-Range Order in BaTiO3 from Local Symmetry-Breaking Distortions," *Phys. Rev. Lett.*, vol. 116, no. 20, pp. 1–5, 2016.

[6]   N. Zhang, H. Yokota, A. M. Glazer, Z. Ren, D. A. Keen, D. S. Keeble, P. A. Thomas, and Z. G. Ye, "The missing boundary in the phase diagram of PbZr1-xTixO3," *Nat. Commun.*, vol. 5, no. May, p. 5231, Jan. 2014.

[7]   G. H. Haertling, "Ferroelectric ceramics: History and technology," *J. Am. Ceram. Soc.*, vol. 82, no. 4, pp. 797–818, Apr. 1999.

[8]   T. Egami, "Local Structure of Ferroelectric Materials," in *Annual Review of Materials Research*, vol. 37, 2007, pp. 297–315.

[9]   B. D. Cullity, *Elements of X-ray Diffraction*, 2nd ed. Addison-Wesley Publishing Company Inc., 1956.

[10]   C. Hammond, *The Basics of Crystallography and Diffraction (2nd edn)*, Third edit., vol. 13. Oxford University Press, 2002.

[11]   M. De Graef, M. E. McHenry, and V. Keppens, "Structure of materials: An introduction to crystallography, diffraction, and symmetry," *J. Acoust. Soc. Am.*, vol. 124, no. 3, p. 1385, 2008.

[12] M. Nespolo, "Fundamentals of Crystallography, 3rd edition. By Carmelo Giacovazzo (ed.)," *Massimo Nespolo Acta Cryst*, vol. 67, pp. 561–563, 2011.

[13] T. Hahn, *International Tables for Crystallography: Space-group Symmetry.*, vol. A. 2005.

[14] A. M. Glazer, "The classification of tilted octahedra in perovskites," *Acta Crystallogr. Sect. B Struct. Crystallogr. Cryst. Chem.*, vol. 28, no. 11, pp. 3384–3392, Nov. 1972.

[15] V. M. Goldschmidt, "The laws of crystal chemistry," *Naturwissenschaften*, vol. 14, pp. 477–485, 1926.

[16] A. J. Moulson and J. M. Herbert, *Electroceramics: Materials, Properties, Applications. 2nd Edition*. England: John Wiley & Sons, 2003.

[17] C. Kittel, *Introduction to Solid State Physics*, vol. 8th editio. 2004.

[18] X. Y. Wei and X. Yao, "Preparation, structure and dielectric property of barium stannate titanate ceramics," *Mater. Sci. Eng. B-Solid State Mater. Adv. Technol.*, vol. 137, no. 1–3, pp. 184–188, 2007.

[19] J. L. Jones, E. B. Slamovich, and K. J. Bowman, "Domain texture distributions in tetragonal lead zirconate titanate by x-ray and neutron diffraction," *J. Appl. Phys.*, vol. 97, no. 3, p. 34113, 2005.

[20] J. L. Jones, M. Hoffman, and K. J. Bowman, "Saturated domain switching textures and strains in ferroelastic ceramics," *J. Appl. Phys.*, vol. 98, no. 2, p. 24115, 2005.

[21] D. A. Hall, J. D. S. Evans, E. C. Oliver, P. J. Withers, and T. Mori, "In-situ neutron diffraction study of the rhombohedral to orthorhombic phase transformation in lead zirconate titanate ceramics produced by uniaxial compression," *Philos. Mag. Lett.*, vol. 87, no. 1, pp. 41–52, 2007.

[22] D. a. Hall, T. Mori, P. J. Withers, H. Kungl, M. J. Hoffmann, and J. Wright, "Domain switching in rhombohedral PZT ceramics under electrical and mechanical loading," *Mater. Sci. Technol.*, vol. 24, no. 8, pp. 927–933, Aug. 2008.

[23] J. L. Jones, "The use of diffraction in the characterization of piezoelectric materials," *J. Electroceramics*, vol. 19, no. 1, pp. 67–79, 2007.

[24] J. L. Jones, J. C. Nino, A. Pramanick, and J. E. Daniels, "Time-Resolved, Electric-Field-Induced Domain Switching and Strain in Ferroelectric Ceramics and Crystals," in *Studying Kinetics with Neutrons: Prospects for Times-Resolved Neutron Scattering*, vol. 161, G. Eckold, H. Schober, and S. E. Nagler, Eds. 2010, pp. 149–175.

[25] D. a. Hall, a. Steuwer, B. Cherdhirunkorn, T. Mori, and P. J. Withers, "A high energy synchrotron x-ray study of crystallographic texture and lattice strain in soft lead zirconate titanate ceramics," *J. Appl. Phys.*, vol. 96, no. 8, p. 4245, 2004.

[26] D. A. Hall, A. Steuwer, B. Cherdhirunkorn, P. J. Withers, and T. Mori, "Micromechanics of residual stress and texture development due to poling in polycrystalline ferroelectric ceramics," *J. Mech. Phys. Solids*, vol. 53, no. 2, pp. 249–260, 2005.

[27] D. A. Hall, A. Steuwer, B. Cherdhirunkorn, P. J. Withers, and T. Mori, "Texture of poled tetragonal PZT detected by synchrotron X-ray diffraction and micromechanics analysis," *Mater. Sci. Eng. A*, vol. 409, no. 1–2, pp. 206–210, 2005.

[28] B. Jaffe, "Piezoelectric Properties of Lead Zirconate-Lead Titanate Solid-Solution Ceramics," *J. Appl. Phys.*, vol. 25, no. 6, p. 809, 1954.

[29] W. Liu and X. Ren, "Large piezoelectric effect in Pb-free ceramics," *Phys. Rev. Lett.*, vol. 103, no. 25, 2009.

[30] M. Ahart, M. Somayazulu, R. E. Cohen, P. Ganesh, P. Dera, H. K. Mao, R. J. Hemley, Y. Ren, P. Liermann, and Z. Wu, "Origin of morphotropic phase boundaries in ferroelectrics," *Nature*, vol. 451, no. 7178, pp. 545–548, Jan. 2008.

[31] K. Z. Baba-Kishi and A. M. Glazer, "Local structure of Pb(Zr 0.53 Ti 0.47)O 3," *J. Appl. Crystallogr.*, vol. 47, no. 5, pp. 1688–1698, Sep. 2014.

[32] B. Noheda, D. E. Cox, G. Shirane, J. a. Gonzalo, L. E. Cross, and S.-E. E. Park, "A monoclinic ferroelectric phase in the Pb(Zr[sub 1−x]Ti[sub x])O[sub 3] solid solution," *Appl. Phys. Lett.*, vol. 74, no. 14, p. 2059, 1999.

[33] R. Guo, L. E. Cross, S. E. Park, B. Noheda, D. E. Cox, and G. Shirane, "Origin of the high piezoelectric response in PbZr1-xTixO3," *Phys. Rev. Lett.*, vol. 84, no.

23, pp. 5423–5426, Jun. 2000.

[34] A. M. Glazer, K. Z. Baba-Kishi, G. K. H. Pang, and C. W. Tai, "Influence of short-range and long-range order on the evolution of the morphotropic phase boundary in Pb(Zr_1−xTi_x)O_3}," *Phys. Rev. B*, vol. 70, no. 18, p. 184123, Nov. 2004.

[35] M. G. Tucker, M. T. Dove, D. A. Keen, Tucker, M. G., M. T. Dove, and D. A. Keen, "Direct measurement of the thermal expansion of the Si-O bond by neutron total scattering," *J. Physics-Condensed Matter*, vol. 12, no. 26, pp. L425–L430, 2000.

[36] D. A. Keen and M. T. Dove, "Local structures of amorphous and crystalline phases of silica , SiO2 , by neutron total scattering Local structures of amorphous and crystalline phases of silica , SiO 2 , by neutron total scattering," *J Am Chem Soc*, vol. 11, pp. 9263–9273, 1999.

[37] R. A. Cowley, S. N. Gvasaliya, S. G. Lushnikov, B. Roessli, G. M. Rotaru, P. Road, and D. House, "Relaxing with relaxors: a review of relaxor ferroelectrics," *Adv. Phys.*, vol. 60, no. 2, pp. 229–327, 2011.

[38] L. E. Cross, "Relaxor ferroelectrics," *Ferroelectrics*, vol. 76, no. 1, pp. 241–267, Dec. 1987.

[39] A. A. Bokov and Z. G. Ye, "Recent progress in relaxor ferroelectrics with perovskite structure," *J. Mater. Sci.*, vol. 41, no. 1, pp. 31–52, Jan. 2006.

[40] S. Prosandeev, D. Wang, a. R. Akbarzadeh, B. Dkhil, and L. Bellaiche, "Field-Induced Percolation of Polar Nanoregions in Relaxor Ferroelectrics," *Phys. Rev. Lett.*, vol. 110, no. 20, p. 207601, May 2013.

[41] G. Smolenskii, "Ferroelectrics with diffuse phase transition," *Ferroelectrics*, vol. 53, no. 1, pp. 129–135, 1984.

[42] G. Xu, Z. Zhong, Y. Bing, Z.-G. G. Ye, and G. Shirane, "Electric-field-induced redistribution of polar nano-regions in a relaxor ferroelectric," *Nat. Mater.*, vol. 5, no. 2, pp. 134–140, Feb. 2006.

[43] B. Burton, E. Cockayne, and U. Waghmare, "Correlations between nanoscale chemical and polar order in relaxor ferroelectrics and the lengthscale for polar nanoregions," *Phys. Rev. B*, vol. 72, no. 6, p. 64113, Aug. 2005.

[44] A. Royles, "Electric-field-induced phase transformations in lead-free piezoelectric ceramics," University of Leeds, University of Leeds, 2010.

[45] M. Otonicar, J. Park, M. Logar, G. Esteves, J. L. Jones, and B. Jancar, "EXTERNAL FIELD-INDUCED CRYSTAL STRUCTURE AND DOMAIN TEXTURE IN Na0.5Bi0.5TiO3-K0.5Bi0.5TiO3 PIEZOCERAMICS," *Acta Mater.*, vol. 127, pp. 319–331, 2017.

[46] S. Roberts, "Dielectric Properties of Lead Zirconate and Barium-Lead Zirconate," *J. Am. Ceram. Soc.*, vol. 33, no. 2, pp. 63–66, 1950.

[47] R. Bechmann, "Elastic, Piezoelectric, and Dielectric Constants of Polarized Barium Titanate Ceramics and Some Applications of the Piezoelectric Equations," *J. Acoust. Soc. Am.*, vol. 28, no. 3, pp. 347–350, 1956.

[48] D. Berlincourt and H. Jaffe, "Elastic and Piezoelectric Coefficients of Single-Crystal Barium Titanate," *Phys. Rev.*, vol. 111, no. 1, pp. 143–148, 1958.

[49] H. F. F. Kay and P. Vousden, "Symmetry changes in barium titanate at low temperatures and their relation to its ferroelectric properties," *London, Edinburgh, Dublin Philos. Mag. J. Sci.*, vol. 40, no. 309, pp. 1019–1040, 1949.

[50] G. H. Kwei, A. C. Lawson, S. J. L. Billinge, and S. W. Cheong, "Structures of the ferroelectric phases of barium titanate," *J. Phys. Chem.*, vol. 97, no. 10, pp. 2368–2377, 1993.

[51] R. Comes, M. Lambert, and A. Guinier, "The chain structure of BaTiO3 and KNbO3," *Solid State Commun.*, vol. 6, no. 10, pp. 715–719, 1968.

[52] T. Egami and S. J. L. Billinge, "Underneath the Bragg Peaks: Structural Analysis of Complex Materials, 2nd Edition," in *Underneath the Bragg Peaks: Structural Analysis of Complex Materials, 2nd Edition*, vol. 16, 2012, pp. 1–481.

[53] G. H. Kwei, S. J. L. Billinge, S.-W. Cheong, and J. G. Saxton, "Pair-distribution functions of ferroelectric perovskites: Direct observation of structural ground states," *Ferroelectrics*, vol. 164, no. 1, pp. 57–73, 1995.

[54] J. B. Goodenough and M. Longo, "Distortions due to core polarization: Pb2+and Bi3+," in *Group III - Condensed Matter*, K.-H. Hellwege and A. M. Hellwege, Eds. Springer Materials, 1970.

[55] R. E. Cohen, "Origin of ferroelectricity in perovskite oxides," *Nature*, vol. 358, no. 6382, pp. 136–138, 1992.

[56] G. Shirane, S. Hoshino, K. Suzuki, and a. Et, "CRYSTAL STRUCTURES OF LEAD TITANATE AND OF LEAD-BARIUM TITANATE," *J. Phys. Soc. Japan*, vol. 5, no. 6, pp. 453–455, 1950.

[57] E. Sawaguchi, "FERROELECTRICITY VERSUS ANTIFERROELECTRICITY IN THE SOLID SOLUTIONS OF PBZRO3 AND PBTIO3," *J. Phys. Soc. Japan*, vol. 8, no. 5, pp. 615–629, 1953.

[58] J. Frantti, J. Lappalainen, S. Eriksson, V. Lantto, S. Nishio, M. Kakihana, S. Ivanov, and H. Rundlof, "Neutron diffraction studies of Pb(ZrxTi1-x)O-3 ceramics," *Japanese J. Appl. Phys. Part 1-Regular Pap. Short Notes Rev. Pap.*, vol. 39, no. 9B, pp. 5697–5703, 2000.

[59] B. Noheda, J. A. Gonzalo, R. Guo, S. E. Park, L. E. Cross, D. E. Cox, and G. Shirane, "The monoclinic phase in PZT: New light on morphotropic phase boundaries," in *Fundamental Physics of Ferroelectrics 2000*, vol. 535, R. E. Cohen, Ed. 2000, pp. 304–313.

[60] A. J. Bell, "Factors influencing the piezoelectric behaviour of PZT and other 'morphotropic phase boundary' ferroelectrics," *J. Mater. Sci.*, vol. 41, no. 1, pp. 13–25, Jan. 2006.

[61] D. L. Corker, A. M. Glazer, R. W. Whatmore, A. Stallard, and F. Fauth, "A neutron diffraction investigation into the rhombohedral phases of the perovskite series PbZr1-xTixO3," *J. Physics-Condensed Matter*, vol. 10, no. 28, pp. 6251–6269, 1998.

[62] A. J. Bell and E. Furman, "An alternative thermodynamic model for PZT," *Isaf 2002 Proc. 13th Ieee Int. Symp. Appl. Ferroelectr.*, pp. 19–24, 2002.

[63] D. Cao, I.-K. K. Jeong, R. Heffner, T. Darling, J.-K. K. Lee, F. Bridges, J.-S. S. Park, and K.-S. S. Hong, "Local structure study of the off-center displacement of Ti and Zr across the morphotropic phase boundary of PbZr1−xTixO3 (x=0.40,0.47,0.49,0.55)," *Phys. Rev. B*, vol. 70, no. 22, p. 224102, Dec. 2004.

[64] K. a. Schönau, L. a. Schmitt, M. Knapp, H. Fuess, R.-A. A. Eichel, H. Kungl, and

M. J. Hoffmann, "Nanodomain structure of Pb[Zr(1−x)Ti(x)]O3 at its morphotropic phase boundary: Investigations from local to average structure," *Phys. Rev. B*, vol. 75, no. 18, p. 184117, May 2007.

[65] T. Takenaka and H. Nagata, "Current status and prospects of lead-free piezoelectric ceramics," *J. Eur. Ceram. Soc.*, vol. 25, no. 12, pp. 2693–2700, Jan. 2005.

[66] E. Aksel and J. L. Jones, "Advances in Lead-Free Piezoelectric Materials for Sensors and Actuators," *Sensors (Peterboroug*, vol. 10, no. 3, pp. 1935–1954, Jan. 2010.

[67] K. Sakata and Y. Masuda, "Ferroelectric and antiferroelectric properties of (Na 0.5 Bi 0.5)TiO3-SrTiO3 solid solution ceramics," *Ferroelectrics*, vol. 7, no. 1, pp. 347–349, 1974.

[68] S. Zhao, G. Li, A. Ding, T. Wang, and Q. Yin, "Ferroelectric and piezoelectric properties of (Na, K) 0.5 Bi 0.5 TiO 3 lead free ceramics," *J. Phys. D. Appl. Phys.*, vol. 39, no. 10, pp. 2277–2281, May 2006.

[69] Y. Hiruma, H. Nagata, and T. Takenaka, "Thermal depoling process and piezoelectric properties of bismuth sodium titanate ceramics," *J. Appl. Phys.*, vol. 105, no. 8, p. 84112, 2009.

[70] G. A. Smolenskii, V. A. Isupov, A. I. Agranovskaya, and N. N. Krainik, "New ferroelectrics of complex composition .4," *Sov. Physics-Solid State*, vol. 2, no. 11, pp. 2651–2654, 1961.

[71] I. P. Pronin, P. P. Syrnikov, V. A. Isupov, V. M. Egorov, and N. V Zaitseva, "Peculiarities of phase transitions in sodium-bismuth titanate," *Ferroelectrics*, vol. 25, no. 1, pp. 395–397, 1980.

[72] J. A. Zvirgzds, P. P. Kapostin, J. V. Zvirgzde, and T. V. Kruzina, "X-ray study of phase transitions in effroelectric Na0.5Bi0.5TiO3," *Ferroelectrics*, vol. 40, no. 1, pp. 75–77, 1982.

[73] Y. Imry and S. K. Ma, "Random-field instability of the ordered state of continuous symmetry," *Phys. Rev. Lett.*, vol. 35, no. 21, pp. 1399–1401, 1975.

[74] J. Suchanicz and W. S. Ptak, "On the phase transition in Na0.5 Bi0.5 TiO3,"

Ferroelectrics, vol. 12, no. March 2012, pp. 71–78, 1990.

[75]   G. O. Jones and P. a. Thomas, "Investigation of the structure and phase transitions in the novel A-site substituted distorted perovskite compound Na 0.5 Bi 0.5 TiO 3," *Acta Crystallogr. Sect. B Struct. Sci.*, vol. 58, no. 2, pp. 168–178, Apr. 2002.

[76]   E. Aksel, J. S. Forrester, B. Kowalski, J. L. Jones, and P. a. Thomas, "Phase transition sequence in sodium bismuth titanate observed using high-resolution x-ray diffraction," *Appl. Phys. Lett.*, vol. 99, no. 22, p. 222901, 2011.

[77]   V. Dorcet, G. Trolliard, and P. Boullay, "Reinvestigation of Phase Transitions in Na 0.5 Bi 0.5 TiO 3 by TEM. Part I: First Order Rhombohedral to Orthorhombic Phase Transition," *Chem. Mater.*, vol. 20, no. 15, pp. 5061–5073, 2008.

[78]   G. Trolliard and V. Dorcet, "Reinvestigation of Phase Transitions in Na0.5Bi0.5TiO3 by TEM. Part II. Second Order Orthorhombic to Tetragonal Phase Transition," *Chem. Mater. F. Full J. TitleChemistry Mater.*, vol. 20, pp. 5074–5082, 2008.

[79]   R. Beanland and P. a. A. Thomas, "Imaging planar tetragonal sheets in rhombohedral Na0.5Bi0.5TiO3using transmission electron microscopy," *Scr. Mater.*, vol. 65, no. 5, pp. 440–443, Sep. 2011.

[80]   S. Gorfman and P. A. Thomas, "Evidence for a non-rhombohedral average structure in the lead-free piezoelectric material Na0.5Bi0.5TiO3," *J. Appl. Crystallogr.*, vol. 43, no. 6, pp. 1409–1414, Oct. 2010.

[81]   S. Gorfman, A. M. Glazer, Y. Noguchi, M. Miyayama, H. Luo, and P. a. Thomas, "Observation of a low-symmetry phase in Na 0.5 Bi 0.5 TiO 3 crystals by optical birefringence microscopy," *J. Appl. Crystallogr.*, vol. 45, no. 3, pp. 444–452, Mar. 2012.

[82]   B. N. Rao, A. N. Fitch, and R. Ranjan, "Ferroelectric-ferroelectric phase coexistence in Na1/2Bi1/2TiO3," *Phys. Rev. B*, vol. 87, no. 6, 2013.

[83]   I. Levin and I. M. Reaney, "Nano- and Mesoscale Structure of Na0.5Bi0.5TiO3: A TEM Perspective," *Adv. Funct. Mater.*, vol. 22, no. 16, pp. 3445–3452, Aug. 2012.

[84]   D. S. Keeble, E. R. Barney, D. a. Keen, M. G. Tucker, J. Kreisel, and P. a. Thomas,

"Bifurcated Polarization Rotation in Bismuth-Based Piezoelectrics," *Adv. Funct. Mater.*, vol. 23, no. 2, pp. 185–190, Jan. 2013.

[85] E. Aksel, J. S. Forrester, J. C. Nino, K. Page, D. P. Shoemaker, and J. L. Jones, "Local atomic structure deviation from average structure of Na0.5Bi0.5TiO3: Combined x-ray and neutron total scattering study," *Phys. Rev. B*, vol. 87, no. 10, p. 104113, Mar. 2013.

[86] Y. Hiruma, R. Aoyagi, H. Nagata, and T. Takenaka, "Ferroelectric and piezoelectric properties of (Bi1/2K1/2)TiO3 ceramics," *Japanese J. Appl. Phys. Part 1-Regular Pap. Br. Commun. Rev. Pap.*, vol. 44, no. 7A, pp. 5040–5044, 2005.

[87] Y. Hiruma, H. Nagata, and T. Takenaka, "Phase diagrams and electrical properties of (Bi1/2Na1/2)TiO3-based solid solutions," *J. Appl. Phys.*, vol. 104, no. 12, 2008.

[88] T. Takenaka, H. Nagata, Y. Hiruma, and a. Et, "Phase Transition Temperatures and Piezoelectric Properties of (Bi1/2Na1/2)TiO3- and (Bi1/2K1/2)TiO3-Based Bismuth Perovskite Lead-Free Ferroelectric Ceramics," *Ieee Trans. Ultrason. Ferroelectr. Freq. Control*, vol. 56, no. 8, pp. 1595–1612, 2009.

[89] C. F. Buhrer, "Some Properties of Bismuth Perovskites," *J. Chem. Phys.*, vol. 36, no. 3, pp. 798–803, 1962.

[90] A. Sasaki, T. Chiba, Y. Mamiya, and E. Otsuki, "Dielectric and piezoelectric properties of (Bi0.5Na0.5)TiO3-(Bi0.5K0.5)TiO3 systems," *Japanese J. Appl. Phys. Part 1-Regular Pap. Short Notes Rev. Pap.*, vol. 38, no. 9B, pp. 5564–5567, 1999.

[91] M. Otoničar, S. D. Škapin, B. Jančar, and D. Suvorov, "Structural diversity of the (Na1−xKx)0.5Bi0.5TiO3 perovskite at the morphotropic phase boundary," *J. Appl. Phys.*, vol. 113, no. 2, p. 24106, 2013.

[92] I. Levin, I. Reaney, E.-M. Anton, W. Jo, J. Rödel, J. Pokorny, L. Schmitt, H.-J. Kleebe, M. Hinterstein, and J. Jones, "Local structure, pseudosymmetry, and phase transitions in Na1/2Bi1TiO3-K1/2Bi1/2TiO3," *Phys. Rev. B*, vol. 87, no. 2, p. 24113, Jan. 2013.

[93] Y. Hiruma, H. Nagata, and T. Takenaka, "Depolarization temperature and

piezoelectric properties of (Bi1/2Na1/2)TiO3-(Bi1/2Li1/2)TiO3-(Bi1/2K1/2)TiO3 lead-free piezoelectric ceramics," *Ceram. Int.*, vol. 35, no. 1, pp. 117–120, 2009.

[94] J. Kreisel, B. Chaabane, P. Bouvier, B. Chaabane, B. Dkhil, A. Thomas, M. Glazer, R. Welberry, and M. Mezouar, "High-pressure x-ray scattering of oxides with a nanoscale local structure: Application to Na1/2Bi1/2TiO3," *Phys. Rev. B - Condens. Matter Mater. Phys.*, vol. 68, no. 1, pp. 1–7, 2003.

[95] X. X. Wang, S. H. Choy, X. G. Tang, and H. L. W. Chan, "Dielectric behavior and microstructure of (Bi1/2Na1/2)TiO3-(Bi1/2K1/2)TiO3-BaTiO3 lead-free piezoelectric ceramics," *J. Appl. Phys.*, vol. 97, no. 10, 2005.

[96] M. Otoničar, S. D. D. Škapin, M. Spreitzer, and D. Suvorov, "Compositional range and electrical properties of the morphotropic phase boundary in the Na0.5Bi0.5TiO3–K0.5Bi0.5TiO3 system," *J. Eur. Ceram. Soc.*, vol. 30, no. 4, pp. 971–979, Mar. 2010.

[97] J. F. Carroll, D. A. Payne, Y. Noguchi, and M. Miyayama, "Field-induced strain behavior for potassium sodium bismuth titanate ceramics," *IEEE Trans. Ultrason. Ferroelectr. Freq. Control*, vol. 54, no. 12, pp. 2516–2521, 2007.

[98] T. Takenaka, H. Nagata, and Y. Hiruma, "Phase Transition Temperatures and Piezoelectric properties oj (Bi0.5Na0.5)TiO3- and (Bi0.5K0.5)TiO3-Based Bismuth Perovskite Lead-Free Ferroelectric Ceramics," *IEEE Trans. Ultrason. Ferroelectr. Freq. Control*, vol. 56, no. 8, pp. 1595–1612, 2009.

[99] A. J. Royles, A. J. Bell, A. P. Jephcoat, A. K. Kleppe, S. J. Milne, and T. P. Comyn, "Electric-field-induced phase switching in the lead free piezoelectric potassium sodium bismuth titanate," *Appl. Phys. Lett.*, vol. 97, no. 13, p. 132909, 2010.

[100] A. J. Royles, A. J. Bell, J. E. Daniels, S. J. Milne, and T. P. Comyn, "Observation of a time-dependent structural phase transition in potassium sodium bismuth titanate," *Appl. Phys. Lett.*, vol. 98, no. 18, pp. 2011–2014, 2011.

[101] K. Sakata, T. TAkenaka, and Y. Naitou, "Ferroelectrics Phase relations , dielectric and piezoelectric properties of ceramics in," *Ferroelectrics*, vol. 131, no. May 2013, pp. 219–226, 1992.

[102] S.-E. Park and K. S. Hong, "Phase relations in the system of (Na1/2Bi1/2)TiO3–PbTiO3. I. Structure," *J. Appl. Phys.*, vol. 79, no. 1, p. 383, 1996.

[103] S. P. Singh, R. Ranjan, A. Senyshyn, D. Trots, and H. Boysen, "Structural phase transition study of the morphotropic phase boundary compositions of Na(0.5)Bi(0.5)TiO(3)-PbTiO(3).," *J. Phys. Condens. Matter*, vol. 21, no. 37, p. 375902, Sep. 2009.

[104] O. Elkechai, P. Marchet, P. Thomas, M. Manier, J. Mercurio, A. Albert-t, and L. Cedex, "Structural and dielectric study of the Na Bi TiO – PbTiO and K Bi TiO – PbTiO systems," *J. Mater. Chem.*, vol. 7, no. 1, pp. 91–97, 1997.

[105] J.-K. Lee, K. S. Hong, C. K. Kim, and S.-E. Park, "Phase transitions and dielectric properties in A-site ion substituted (Na[sub 1/2]Bi[sub 1/2])TiO[sub 3] ceramics (A=Pb and Sr)," *J. Appl. Phys.*, vol. 91, no. 7, p. 4538, 2002.

[106] J. C. Brooks-Bartlett and E. F. Garman, "The Nobel Science: One Hundred Years of Crystallography," *Interdiscip. Sci. Rev.*, vol. 40, no. 3, pp. 244–264, 2015.

[107] G. O. Jones, J. Kreisel, V. Jennings, M. A. Geday, P. A. Thomas, and A. M. Glazer, "Investigation of a peculiar relaxor ferroelectric: Na0.5Bi0.5TiO3," *Ferroelectrics*, vol. 270, pp. 191–196, 2002.

[108] E. Aksel, J. S. Forrester, J. L. Jones, P. A. Thomas, K. Page, and M. R. Suchomel, "Monoclinic crystal structure of polycrystalline Na0.5 Bi 0.5 TiO3," *Appl. Phys. Lett.*, vol. 98, no. 15, pp. 12–15, 2011.

[109] V. Petkov, I.-K. Jeong, J. S. Chung, M. F. Thorpe, S. Kycia, and S. J. L. Billinge, "High Real-Space Resolution Measurement of the Local Structure of Gasub1-x/subInsubx/subAs Using X-Ray Diffraction," *Phys. Rev. Lett.*, vol. 83, no. 20, pp. 4089–4092, 1999.

[110] P. Debye and H. Menke, "The determination of the inner structure of liquids by X-ray means.," *Phys. Z.*, vol. 31, pp. 797–798, 1930.

[111] L. P. Tarasov and B. E. Warren, "X-Ray Diffraction Study of Liquid Sodium," *J. Chem. Phys.*, vol. 4, no. 4, pp. 236–238, 1936.

[112] B. H. Toby and T. Egami, "Accuracy of pair distribution function analysis applied to crystalline and non-crystalline materials," *Acta Crystallogr. Sect. A Found.*

Crystallogr., vol. 48, no. 3, pp. 336–346, May 1992.

[113] S. Bates, G. Zografi, D. Engers, K. Morris, K. Crowley, and A. Newman, "Analysis of amorphous and nanocrystalline solids from their X-ray diffraction patterns," *Pharm. Res.*, vol. 23, no. 10, pp. 2333–2349, Oct. 2006.

[114] R. Harrington, R. B. Neder, and J. B. Parise, "The nature of x-ray scattering from geo-nanoparticles: Practical considerations of the use of the Debye equation and the pair distribution function for structure analysis," *Chem. Geol.*, vol. 329, pp. 3–9, Nov. 2012.

[115] J. Bednarcik, S. Michalik, V. Kolesar, U. Rutt, H. Franz, U. Rütt, and H. Franz, "In situ XRD studies of nanocrystallization of Fe-based metallic glass: a comparative study by reciprocal and direct space methods," *Phys. Chem. Chem. Phys.*, vol. 15, no. 22, pp. 8470–8479, Jun. 2013.

[116] T.-M. M. Usher, I. Levin, J. E. Daniels, and J. L. Jones, "Electric-field-induced local and mesoscale structural changes in polycrystalline dielectrics and ferroelectrics.," *Sci. Rep.*, vol. 5, no. April, p. 14678, Jan. 2015.

[117] A. J. Goetzee-Barral, T.-M. Usher, T. J. Stevenson, J. L. Jones, I. Levin, A. P. Brown, and A. J. Bell, "Electric field dependent local structure of (K x N a 1- x) 0.5 B i 0.5 Ti O 3," *Phys. Rev. B*, vol. 96, no. 1, p. 14118, 2017.

[118] J. F. James, *A Student's Guide to Fourier Transforms*. 2011.

[119] T. Proffen, S. J. L. Billinge, T. Egami, and D. Louca, "Structural analysis of complex materials using the atomic pair distribution function – a practical guide," *Zeitschrift FÜR Krist.*, vol. 218, no. 2, pp. 132–143, 2003.

[120] T. Egami and S. J. L. Billinge, *Underneath the Bragg Peaks: Structural Analysis of Complex Materials*. Pergamon, 2003.

[121] T. Proffen, S. J. L. Billinge, P. F. Peterson, E. S. Bozin, T. Proffen, and S. J. L. Billinge, "research papers Improved measures of quality for the atomic pair distribution function research papers," *J. Appl. Crystallogr.*, vol. 36, no. 1, pp. 53–64, 2003.

[122] P. J. Chupas, X. Qiu, J. C. Hanson, P. L. Lee, C. P. Grey, and S. J. L. Billinge, "Rapid-acquisition pair distribution function (RA-PDF) analysis," *J. Appl.*

Crystallogr., vol. 36, no. 6, pp. 1342–1347, 2003.

[123] D. A. Keen, "A comparison of various commonly used correlation functions for describing total scattering," *J. Appl. Crystallogr.*, vol. 34, no. 2, pp. 172–177, Apr. 2001.

[124] T. Proffen, "Total neutron scattering: The key to the local and medium range structure of complex materials," *Pramana-Journal Phys.*, vol. 71, no. 4, pp. 713–719, 2008.

[125] J. Als-Nielsen and D. McMorrow, *Elements of Modern X-ray Physics: Second Edition*. 2011.

[126] D. Attwood, *Soft X-Rays and Extreme Ultraviolet Radiation*. 2013.

[127] H. M. Rietveld, "A profile refinement method for nuclear and magnetic structures," *J. Appl. Crystallogr.*, vol. 2, no. 2, pp. 65–71, 1969.

[128] L. B. Mccusker, R. B. Von Dreele, D. E. Cox, D. Louër, P. Scardi, D. Louer, and P. Scardi, "Rietveld refinement guidelines," *J. Appl. Crystallogr.*, vol. 32, no. 1, pp. 36–50, 1999.

[129] P. J. Chupas, K. W. Chapman, C. Kurtz, J. C. Hanson, P. L. Lee, and C. P. Grey, "A versatile sample-environment cell for non-ambient X-ray scattering experiments," *J. Appl. Crystallogr.*, vol. 41, no. 4, pp. 822–824, 2008.

[130] A. P. Hammersley, "FIT2D: An Introduction and Overview ESRF Internal Report," 1997.

[131] P. Juhás, T. Davis, C. L. Farrow, and S. J. L. Billinge, "PDFgetX3: a rapid and highly automatable program for processing powder diffraction data into total scattering pair distribution functions," *J. Appl. Crystallogr.*, vol. 46, no. 2, pp. 560–566, Mar. 2013.

[132] C. L. Farrow, P. Juhas, J. W. Liu, D. Bryndin, E. S. Boin, J. Bloch, T. Proffen, S. J. L. L. Billinge, E. S. Božin, J. Bloch, T. Proffen, S. J. L. L. Billinge, E. S. Bozin, J. Bloch, T. Proffen, S. J. L. L. Billinge, E. S. Božin, J. Bloch, T. Proffen, and S. J. L. L. Billinge, "PDFfit2 and PDFgui: Computer programs for studying nanostructure in crystals," *J. Phys. Condens. Matter*, vol. 19, no. 33, p. 335219, Aug. 2007.

[133] D. Hou, T.-M. Usher, H. Zhou, N. Raengthon, N. Triamnak, D. P. Cann, J. S. Forrester, and J. L. Jones, "Temperature-induced local and average structural changes in BaTiO$_{3-x}$Bi(Zn$_{1/2}$Ti$_{1/2}$)O$_3$ solid solutions: The origin of high temperature dielectric permittivity," *J. Appl. Phys.*, vol. 122, no. 6, p. 064103, 2017.

[134] P. J. Chupas, K. W. Chapman, and P. L. Lee, "Applications of an amorphous silicon-based area detector for high-resolution, high-sensitivity and fast time-resolved pair distribution function measurements," *J. Appl. Crystallogr.*, vol. 40, no. 3, pp. 463–470, 2007.

[135] A. P. Hammersley, S. O. Svensson, M. Hanfland, A. N. Fitch, and D. Hausermann, "Two-dimensional detector software: From real detector to idealised image or two-theta scan," *High Press. Res.*, vol. 14, no. 4–6, pp. 235–248, 1996.

[136] V. A. Shuvaeva, D. Zekria, A. M. Glazer, Q. Jiang, S. M. Weber, P. Bhattacharya, and P. A. Thomas, "Local structure of the lead-free relaxor ferroelectric (KxNa1-x)(0.5)Bi0.5TiO3," *Physical Review B*, vol. 71, no. 17. pp. 1–8, 2005.

[137] I. Levin, V. Krayzman, J. C. Woicik, F. Bridges, G. E. Sterbinsky, T. M. Usher, J. L. Jones, and D. Torrejon, "Local structure in BaTi O3-BiSc O3 dipole glasses," *Phys. Rev. B*, vol. 93, no. 10, pp. 1–12, 2016.

[138] I. Levin, I. Reaney, E. M. Anton, W. Jo, J. Rödel, J. Pokorny, L. Schmitt, H. J. Kleebe, M. Hinterstein, and J. Jones, "Local structure, pseudosymmetry, and phase transitions in Na1/2Bi1/2TiO3–K1/2Bi1/2TiO3 ceramics," *Phys. Rev. B*, vol. 87, no. 2, 2013.

[139] M. G. Tucker, D. A. Keen, M. T. Dove, A. L. Goodwin, and Q. Hui, "RMCProfile: Reverse Monte Carlo for polycrystalline materials," *J. Phys. Condens. Matter*, vol. 19, no. 33, 2007.

[140] S. T. Norberg, M. G. Tucker, and S. Hull, "Bond valence sum: A new soft chemical constraint for RMCProfile," *J. Appl. Crystallogr.*, vol. 42, no. 2, pp. 179–184, Feb. 2009.

8 Appendices

8.1 Appendix A – Notes on low-r RDF fits on KNBT

8.1.1 Poor fits

Figure 8.1 shows examples of fits determined to be 'poor'. The ‹111› fit for x = 0.15 and 0.18 can be seen to offer very good fits with low χ^2 values. Nevertheless they are determined to not be suitable due to the significant overlap of peak $R2$ which is so broad that it fully engulfs $R1$. This suggests that the intermediate interatomic distance has a huge distribution of positions which can be significantly shorter than $R1$ and therefore is not considered not to be physically realistic or meaningful.
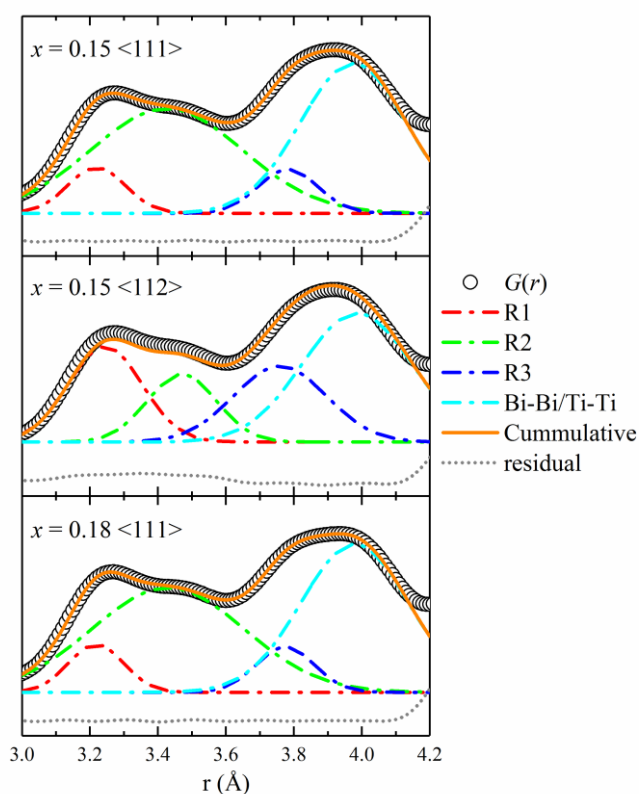

Figure 8.1 Examples of poor model fits. ‹111› on x = 0.15 and 0.18 produces a good fit but there is a significant overlap of R2 over R1 which is not physically meaningfull. ‹112› for x = 0.15 did not produce a suitable fit for the data.

8.1.2 Bi-O contribution

The reason for choosing the Bi-Ti contribution for this analysis has been previously justified. Although oxygen has a lower X-ray scattering length it is more abundant in the perovskite unit cell (O_3) and so it is important to determine what its contribution to the peak areas is. A partial PDF was obtained to show only the Bi-O contribution. **Figure 8.2** shows the contribution to be around 15% relative to the total area of the peak around 3.3 Å. Although not insignificant its contribution is several times smaller than Bi-Ti, and the peak is quite broad so its effect is shared across multiple peaks ($R1$, $R2$ and $R3$). This may also explain why the reorientation behaviour is more apparent perpendicular to the field than parallel to the field.
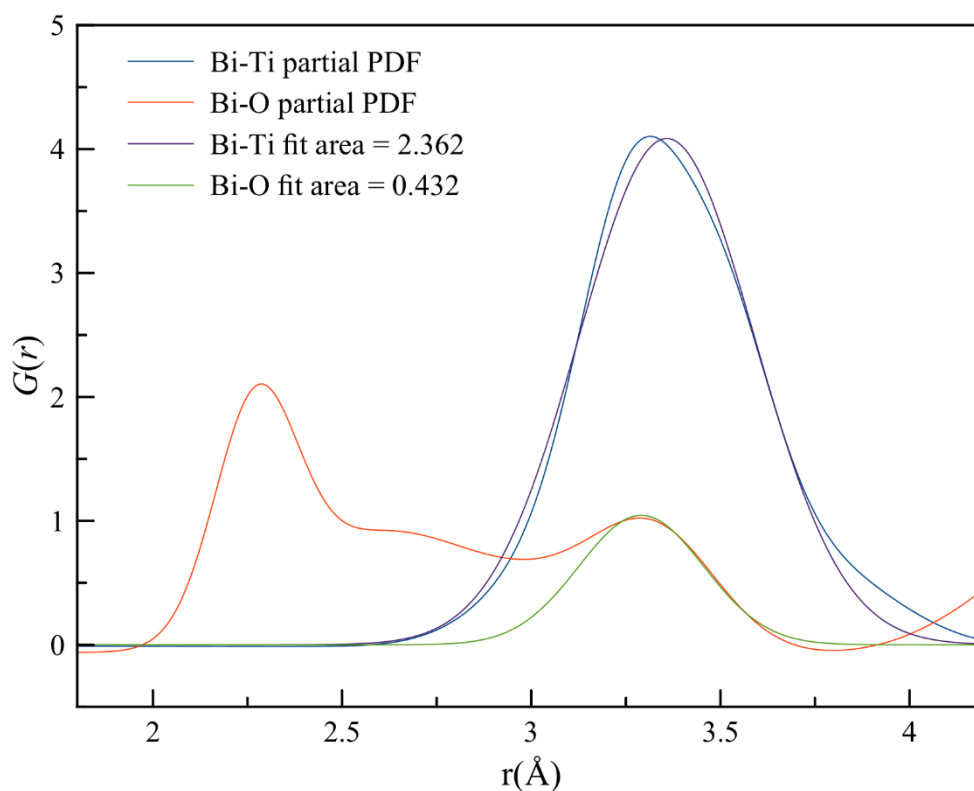

Figure 8.2 Percentage contribution to the RDF peak at 3.3 Å of the Bi-O and Bi-Ti atom-pairs. Values represent percentage of integrated intensity relative to the total peak.

8.2 Appendix B – Conference attendance

1. 2013 Joint IEEE – International Symposium on the Applications of Ferroelectrics, (ISAF/PFM/IUS/IFCS/EFTF).
   July 2013, Prague, Czech Republic.

2. 2014 Joint IEEE – International Symposium on the Applications of Ferroelectrics, (ISAF/IWATMD/PFM).
   Oral presentation – Investigating local order in Potassium Sodium Bismuth Titanate
   May 2014, State College, Pennsylvania, United States of America.

3. 2015 Joint IEEE – International Symposium on the Applications of Ferroelectrics, (ISAF/ISIF/PFM).
   Oral presentation – Investigating local order in $(K_x, Na_{1-x})_{0.5} Bi_{0.5} TiO_3$
   May 2015, Singapore.

4. Sustainable Functional Materials 2016
   Poster – Pair distribution function analysis of lead free piezoelectric materials
   April 2016, Scarborough, United Kingdom.

5. 2016 Joint IEEE – International Symposium on the Applications of Ferroelectrics, (ISAF/ECAPD/PFM).
   Oral presentation – Nanoscale ordering and bond redistribution in $(K_x, Na_{1-x})_{0.5} Bi_{0.5} TiO_3$
   August 2016, Darmstadt, Germany.

6. School of Chemical and Process Engineering Research Event
   Oral presentation, 1st place in presentation competition – The structure of piezoelectric materials.
   December 2017, Leeds, United Kingdom.

7. 1-DRAC Meeting

   Oral presentation – Local structure of $Na_{0.5}Bi_{0.5}TiO_3$-based materials

   April 2018, Manchester, United Kingdom.

8. 2018 Joint IEEE – International Symposium on the Applications of Ferroelectrics, (ISAF/FMA/AMF/AMEC/PFM).

   Oral presentation – Local and average structure study of $(1-x)(Na_{0.5}, Bi_{0.5})TiO_3$-$xPbTiO_3$

   May 2018, Hiroshima, Japan.